UNIVERSITY OF CALIFORNIA,
IRVINE

Theory and Applications of Exceptional Points of Degeneracy in Microwave and High-Power Devices

DISSERTATION

submitted in partial satisfaction of the requirements
for the degree of

DOCTOR OF PHILOSOPHY

in Electrical and Computer Engineering

by

Tarek Khedr Abdalla Mealy

Dissertation Committee:
Professor Filippo Capolino , Chair
Professor Michael Green
Professor Ozdal Boyraz

2022

DEDICATION

TO MY LITTLE ONES...ZAIN AND GAMILA

TABLE OF CONTENTS

LIST OF FIGURES

LIST OF TABLES

ACKNOWLEDGMENTS

First, I would like to express my appreciation and gratitude to my PhD advisor, Professor Filippo Capolino, for supporting me during the past five years. I have learnt a lot of things from Professor Capolino that helped to develop my way of thinking such as asking myself questions to understand, being precise when I speak or write, and being patient to learn new topics and improve things. Without the guidance and persistent help of Prof. Capolino, this dissertation would not have been possible. In addition, I would like to thank the committee members, Professor Michael Green and Professor Ozdal Boyraz who have provided helpful feedback and insights.

I would like to thank my colleagues who were involved in research. I thank Dr. Mohamed Othman who helped me a lot during my first year of PhD. I thank Dr. Ahmed Abdelshafy, Dr. Mohamed Nada and Dr. Hamidreza Kazemi for working with me and for supporting me. I am happy and appreciative of that teamwork. I thank also all my lab mates Alireza Nikzamir, Robert Marosi, Kasra Rouhi, Nathaniel Furman, Albert Parareda, Miguel Melo, Shafiqul Islam, Ehsan Hafezi and Enrico Renzi.

I am also grateful for the funding, the Air Force Office of Scientific Research (AFOSR) and the National Science Foundation. The research work in this dissertation was mainly supported by the AFOSR under Award FA9550-18-1-0355 and Award FA9550-20-1-0409, and NSF ECCS-1711975.

Most importantly, I am deeply and sincerely grateful to my mom who was always there for me at every step and gave me the strength and confidence to pursue my goals. I would like to express my thanks to my elder brothers Mohamed Mealy and Yasser Mealy for their continuous support and care.

Last but not least, I would like to thank my wife who was very supportive to me during my PhD journey. It would have been very difficult to reach this accomplishment without her.

VITA

Tarek Khedr Abdalla Mealy

EDUCATION

Doctor of Philosophy in Electrical and Computer Eng. **2022**
University of California, Irvine *Irvine, California, USA*

Masters of Science in Electronics and Communications Eng. **2017**
Cairo University *Cairo, Egypt*

Bachelor of Science in Electronics and Communications Eng. **2013**
Cairo University *Cairo, Egypt*

RESEARCH EXPERIENCE

Graduate Research Assistant **2017–2022**
University of California, Irvine *Irvine, California*

TEACHING EXPERIENCE

Teaching Assistant **2014–2017**
Cairo University *Cairo, Egypt*

Teaching Assistant **2018–2018**
University of California, Irvine *Irvine, California*

JOURNAL PUBLICATIONS

[1] H. Kazemi, M. Y. Nada, **T. Mealy**, A. F. Abdelshafy and F. Capolino, "Exceptional points of degeneracy induced by linear time-periodic variation,"in *Physical Review Applied*, vol. 11, no. 1, p. 014007, 2019.

[2] **T. Mealy** and F. Capolino, "General conditions to realize exceptional points of degeneracy in two uniform coupled transmission lines,"in *IEEE Transactions on Microwave Theory and Techniques*, vol. 68, no. 8, pp. 3342–3354, 2020.

[3] **T. Mealy**, A. F. Abdelshafy and F. Capolino, "Exceptional Point of Degeneracy in Backward-Wave Oscillator with Distributed Power Extraction,"in *Physical Review Applied*, vol. 14, no. 1, p. 014078, 2020.

[4] M. Y. Nada*, **T. Mealy***, and F. Capolino, "Frozen mode in three-way periodic microstrip coupled waveguide,"in *IEEE Microwave and Wireless Components Letters*, vol. 31, no. 3, pp. 229–232, 2020. ** These authors contributed equally to the work.*

[5] **T. Mealy**, A. F. Abdelshafy, and F. Capolino, "High-power x-band relativistic backward-wave oscillator with exceptional synchronous regime operating at an exceptional point,"in *Physical Review Applied*, vol. 15, no. 6, p. 064021, 2021.

[6] **T. Mealy**, A. F. Abdelshafy, and F. Capolino, "High Power Backward Wave Oscillator using Folded Waveguide with Distributed Power Extraction Operating at an Exceptional Point,"in *IEEE Transactions on Electron Devices*, vol. 68, no. 7, pp. 3588-3595, 2021.

[7] A. F. Abdelshafy, **T. Mealy**, E. Hafezi, A. Nikzamir, and F. Capolino, "Exceptional Degeneracy in a Waveguide Periodically Loaded with Discrete Gain and Radiation Loss Elements,"in *Applied Physics Letters*, vol. 118, no. 22, p. 224102, 2021.

[8] K. Rouhi, R. Marosi, **T. Mealy**, A. F. Abdelshafy, A Figotin, and F. Capolino, "Exceptional Degeneracies in Traveling Wave Tubes with Dispersive Slow-Wave Structure Including Space-Charge Effect,"in *Applied Physics Letters*, vol. 118, no. 26, p. 263506, 2021.

[9] **T. Mealy** and F. Capolino, "Traveling Wave Tube Eigenmode Solution for Beam-Loaded Slow Wave Structure Based on Particle-in-Cell Simulations,"in *IEEE Transactions on Plasma Science*, vol. 50, no. 3, pp. 635-648, 2022.

[10] F. Yazdi, **T. Mealy**, A. Nikzamir, R. Marosi, and F. Capolino, "Third Order Modal Exceptional Degeneracy in Parity-Time Glide-Symmetric Three-Way Waveguide,"in *Physical Review A*, 2022.

[11] F. Yazdi, A. Nikzamir, **T. Mealy**, M. Y. Nada, and F. Capolino, "Triple Ladder Lumped Circuit with Sixth Order Modal Exceptional Degeneracy,"in *IEEE Transactions on Circuits and Systems I: Regular Papers*, 2022.

[12] F. Yazdi, D. Oshmarin, **T. Mealy**, A. T. Almutawa, and F. Capolino, "Experimental

Demonstration of Sixth Order Degenerate Band Edge in Coupled Microstrip Waveguides,"in *Physical Review Applied*, 2022.

[13] H. Kazemi, A. Nikzamir, **T. Mealy**, A. Abdelshafy, and F. Capolino, "High-Sensitive Parity-Time Symmetric Oscillator in Coupled Transmission Lines with Nonlinear Gain", in *IEEE Journal of Microwaves*, 2022.

[14] R. Marosi, **T. Mealy**, A Figotin, and F. Capolino, "Three-Way Coupled Waveguide Slow-Wave Structures with Stationary Inflection Point,"in *arXiv:2203.05641*, 2022.

[15] **T. Mealy**, R. Marosi, and F. Capolino, "Reduced Plasma Frequency Calculation Based on Particle-In-Cell Simulations,"in *arXiv:2205.05806*, 2022.

[16] **T. Mealy**, and F. Capolino, "Degenerate Distributed Feedback Photonic Structure with Double Grating Exhibiting Degenerate Band Edge,"in *arXiv:2205.05639*, 2022.

[17] **T. Mealy**, and F. Capolino, "Exceptional Points of Degeneracy with Indirect Bandgap Induced By Mixing Forward and Backward Propagating Waves,"in *arXiv:2205.06844*, 2022.

ABSTRACT OF THE DISSERTATION

Theory and Applications of Exceptional Points of Degeneracy in Microwave and High-Power Devices

By

Tarek Khedr Abdalla Mealy

Doctor of Philosophy in Electrical and Computer Engineering

University of California, Irvine, 2022

Professor Filippo Capolino , Chair

Electromagnetic (EM) structures are crucial for high-speed communications and radar systems. Enhancing the performance of such components sometimes is a game changer for some applications that require unique features such as ultra-high sensitivity to perturbations, high output power, precise oscillation frequency, or high-power conversion efficiency. The performance of EM components is often limited by the regime of operation. This dissertation focuses on a new class of EM devices, whose architecture relies on dispersion engineering principles exploiting the so-called exceptional points of degeneracy (EPD) operational condition. The use of EPD regime allows to push the boundaries of the performance for some devices such as, for example, millimeter and terahertz frequencies high-power sources.

EPD is a singularity point at which two or more spectral components of the EM field spatial distribution coalesce. In this dissertation, the degeneracy conditions in microwave, optical and electron beam devices are investigated where the remarkable physical properties of such devices, operating at the EPD regime, are studied.

We have discovered an EPD that is induced in a system made of a linear electron beam interacting with an electromagnetic guided mode in a vacuum tube. This enables a degenerate synchronous regime in backward wave oscillators (BWOs) where power is extracted in

distrusted fashion rather than at the end of the structure. The proposed concept is applied to BWOs operating at X-band and millimeter wave frequencies. We demonstrate using particle in cell simulations (PIC) that EPD-BWOs have much higher output power and power conversion efficiency compared to standard BWOs.

Finally, we propose a method that finds the eigenmodes in the interactive system of a travelling-wave tube (TWT). The proposed solver is based on accurate PIC simulations of finite length hot structure. The determination of wavenumbers and eigenvectors of the hot modes supported in a TWTs is useful to study hot-mode degeneracy conditions in hot slow wave structure. Furthermore, the proposed method is applied to study electron beams in tunnels with complicated geometries, with the goal of estimating the reduced plasma frequency and understanding the degeneracy conditions.

Chapter 1

Introduction

1.1 Motivation of This Work

Electromagnetic (EM) components are very crucial for high-speed communications and radar systems. This dissertation focuses on proposing new class of EM devices that exploit exceptional points of degeneracy (EPD) to enhance the performance. Applications of EPDs have been already proposed in the area of solid state oscillators [1, 2, 3], oscillators and amplifiers using electron beam devices [4, 5], delay lines [6], small antennas [7], pulse generators and compressors [8], high-Q resonators, sensors , and lasers [9, 10, 11].

Most of the designs exhibiting EPD proposed in literature are state of art. Proposed designs are based on geometry optimization to have EPD. Sometimes it takes very long optimization time to realize that some structures never satisfy EPD conditions for any geometry. We study the condition that lead to EPD phenomenon in both uniform and periodic waveguides which help understand the physics that lead to EPD phenomenon. Moreover, we study the degeneracy conditions for a system supporting EM wave and space-charge wave supported by plasma medium. The discovery of such EPD is employed to find new regime of EM

sources that generates high power and frequency very efficiently.

1.2 History of Exceptional Points of Degeneracy (EPD)

An EPD is a point in the parameter space of a system at which the system's eigenvalues and eigenvectors coalesce [12, 13, 14, 15]. The term exceptional point (EP) was already mentioned in Kato's book in 1966 [15]. The phenomenon of degeneracy of both eigenvalues and eigenvectors is a stronger degeneracy condition compared to the traditional degeneracy that often refers to only the degeneracy of two wavenumbers of waveguides without necessarily the coalescence of the eigenvectors that describe the polarization state. Because the main physical feature of this phenomenon is the strong degeneracy of at least two eigenmodes [16], the letter 'D' is added to EP, to form EPD.

Non-Hermitian Hamiltonian can possess entirely real spectra when the system obeys parity-time (PT) symmetry condition [17]. A system is said to be partiy-time (PT) symmetric if the PT operator commutes with the Hamiltonian [18, 19], where PT operator applies a parity reflection and time reversal [17]. When the time reversal operator is applied to physical systems, energy changes from damping to growing and vice versa [20]. Based on this simple concept, two symmetrical coupled waveguides with balanced gain and loss satisfy PT symmetry [21, 22, 23], where the individual application of each of the space or time reversal would swap the gain and loss, therefore the simultaneous application of space and time reversal operator to the system would end up with the same system. The point separating the complex and real spectra of PT-symmetric system is called a transition point. The fact that the eigenvalues transitions from being entirely real valued to be complex, by the tuning of one of the system variables such as frequency, gain and loss parameters, coupling factor, etc., actually implies the occurrence of EPD, therefore, a transition point is an EPD. The concepts of PT symmetry have been then expanded to optics, where it was found that

coupled waveguides and resonators satisfy PT-symmetry condition when when the system's refractive index obeys $n(x) = n^*(x)$ [21, 22, 23, 24], where x is a coordinate in the system and * implies complex conjugate. EPDs are also linked to bifurcation theory [25, 26] where it was observed that they also represent points in the configuration space where multiple branches of spectra connect and are basically branch points (BPs) in the space of control variables [27, 28]. EPDs also the critical points one finds them in multilayer waveguiding systems [29, 30, 31, 32, 33].

One of the simplest second-order EPDs is found in uniform (i.e., longitudinally invariant) waveguides at the modal cutoff frequency [34]. Second-order EPDs in the form of band edges also occur in lossless periodic waveguides and photonic crystals [35, 36, 37]. EPDs also occur in coupled waveguides by introducing PT symmetry [22, 38, 23, 39, 40, 41] which implies using a balanced and symmetrical distribution of gain and loss. The occurrence of EPDs in coupled waveguides does not necessarily require a system to exactly satisfy the PT symmetry condition or to simultaneously have gain and loss in general [40, 41]. Furthermore, EPDs may occur in coupled waveguides that are lossless and gainless. For instance, different orders of EPD, especially the degenerate band edge (DBE) which is an EPD of order four in a lossless guiding medium, have been engineered in various types of periodic guiding structures in [42, 43, 44, 36, 45, 46, 47, 48, 41, 49]. Pioneering work on EPDs of order two, three, and four, namely the regular band edge, the stationary inflection point (SIP), and the degenerate band edge (DBE), respectively, have been presented in [35, 42, 43, 44, 50, 36, 51, 52] . The existence of SIP has been theoretically shown in microwave waveguides [53, 54, 55] and optical waveguides [47, 56, 6]. An experimental demonstration of the existence of the SIP (also called "frozen mode") at microwave frequencies, in reciprocal microstrip waveguides, has been provided in [55]. Experimental demonstrations of the existence of the DBE at microwave frequencies has been provided in both circular metallic waveguides with periodic loading [48] and in microstrip technology [41, 49]. The concepts we present in this work can be very beneficial to implement EPDs in realistic waveguides, conventionally used at

microwave frequencies.

1.3 EPD From Linear Algebra Perspective

1.3.1 Eignmode Analysis

We present here the analysis that is done to obtain the eigenmodes for uniform or periodic waveguide that supports N coupled modes. We show the condition that lead to degeneracy based on the eigenvalue problem.

Uniform Waveguide

A system of coupled uniform waveguides that supports N modes is described using a multi-dimensional first order differential equation [57], [31] as

$$\frac{d\mathbf{\Psi}(z)}{dz} = -j\underline{\mathbf{M}}\mathbf{\Psi}(z), \tag{1.1}$$

where $\underline{\mathbf{M}}$ is $N \times N$ system matrix and $\mathbf{\Psi}(z)$ is a multidimensional state vector that includes the equivalent voltages and currents at a coordinate z that represent the electromagnetic fields in the actual waveguides [58, 59, 57, 41].

The eigenmodes supported by the system described by (1.1) are found by assuming a state vector that is proportional to wave function as $\mathbf{\Psi}(z) \propto e^{-jkz}$ to obtain $-jk\ \mathbf{\Psi}(z) = -j\underline{\mathbf{M}}\mathbf{\Psi}(z)$ [57], yet simplified to an eigenvalue problem as

$$\underline{\mathbf{M}}\boldsymbol{\Psi}(z) = k\boldsymbol{\Psi}(z). \tag{1.2}$$

Periodic Waveguide

The evolution of the state vector of the periodic structure is described by

$$\boldsymbol{\Psi}(z+d) = \underline{\mathbf{T}}_u \boldsymbol{\Psi}(z), \tag{1.3}$$

where d is the structure period and $\underline{\mathbf{T}}_u$ is the $N \times N$ unit-cell transfer matrix (T-matrix). According to Floquet-Bloch theory, we look for periodic solutions of the state vector as e^{-jkd} where k is the Floquet-Bloch complex wavenumber, that satisfy $\boldsymbol{\Psi}(z+d) = \lambda\boldsymbol{\Psi}(z)$, with $\lambda \equiv e^{-jkd}$. The eigenvalue problem is then formulated as

$$\underline{\mathbf{T}}_u \boldsymbol{\Psi} = \lambda\boldsymbol{\Psi}, \tag{1.4}$$

where the eigenvalues $\lambda_n \equiv e^{-jk_n d}$, with $n = 1, 2, \ldots, N$ are obtained by solving the dispersion characteristic equation $D(k,\omega) \equiv \det[\underline{\mathbf{T}}_u - \lambda\underline{\mathbf{1}}]$, with $\underline{\mathbf{1}}$ being the $N \times N$ identity matrix.

An EPD of order m occurs when m eigenmodes of the eigenvalue problem (1.2), for uniform case, or (1.4), for periodic case, coalesce in both their eigenvalues and eigenvectors.

1.3.2 Dispersion Relation

The dispersion relation of electromagnetic eigenmodes in a waveguide that exhibits an EPD with order m has the behavior of $(\omega - \omega_e) \propto (k - k_e)^m$ in the vicinity of an EPD (ω_e, k_e) [42, 43, 44]. In the previously mentioned papers, the term EPD was not used, but the concept and the mathematics of an EPD was fully developed for guided waves. Here, ω and k are the angular frequency and the wavenumber, respectively, and the EPD is denoted by the subscript e. Such dispersion behavior is accompanied by a severe reduction in group velocity of the waves propagating in those structures resulting in a giant increase in the loaded quality factor and the local density of states which is beneficial for various applications. Indeed for a lossless waveguide exhibiting an EPD of order order m not only the group velocity $v_g = \partial\omega/\partial k$ vanishes, but all of its derivatives $\partial v_g^i/\partial k^i$ with $i < m - 1$ vanish as well [42].

We show in Fig. 1.1 examples of dispersion diagrams for structures exhibiting different EPD orders when the angular frequency is swept. We show in Fig. 1.2 the corresponding complex-plane plot for wavenumbers (color code is matched between Fig. 1.1 and Fig. 1.2). Fig. 1.1a and Fig. 1.2a are for a structure that exhbits a 2nd order EPD which is also known as regular band edge (RBE). Fig. 1.1b and Fig. 1.2b are for a structure that exhibits a 3rd order EPD which is also known as stationary inflection point (SIP) or frozen mode. Fig. 1.1c and Fig. 1.2c are for a structure that exhibits a 4th order EPD which is also known as degenerate band edge (DBE). Fig. 1.1c and Fig. 1.2c are for a structure that exhibits a 6th order EPD which is known as sixth order degenerate band edge (6DBE).

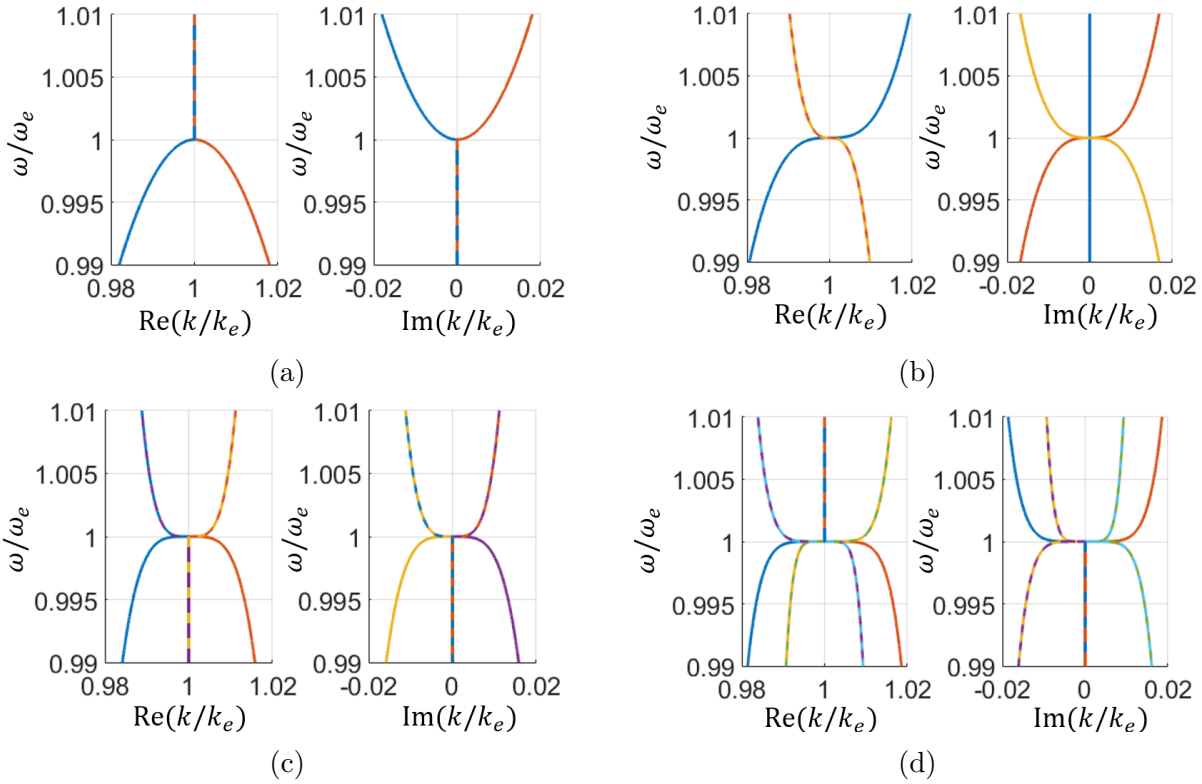

Figure 1.1: Examples of dispersion diagrams for structures exhibiting different EPD orders: (a) RBE (2nd order EPD), (b) SIP (3rd order EPD), (c) DBE (4th order EPD), and (d) 6DBE (6th order EPD). The figure shows the complex-valued normalized wavenumber versus normalized angular frequency. The corresponding complex-plane plots are shown in Fig. 1.2. The EPD occurs here at $k = k_e$ and $\omega = \omega_e$.

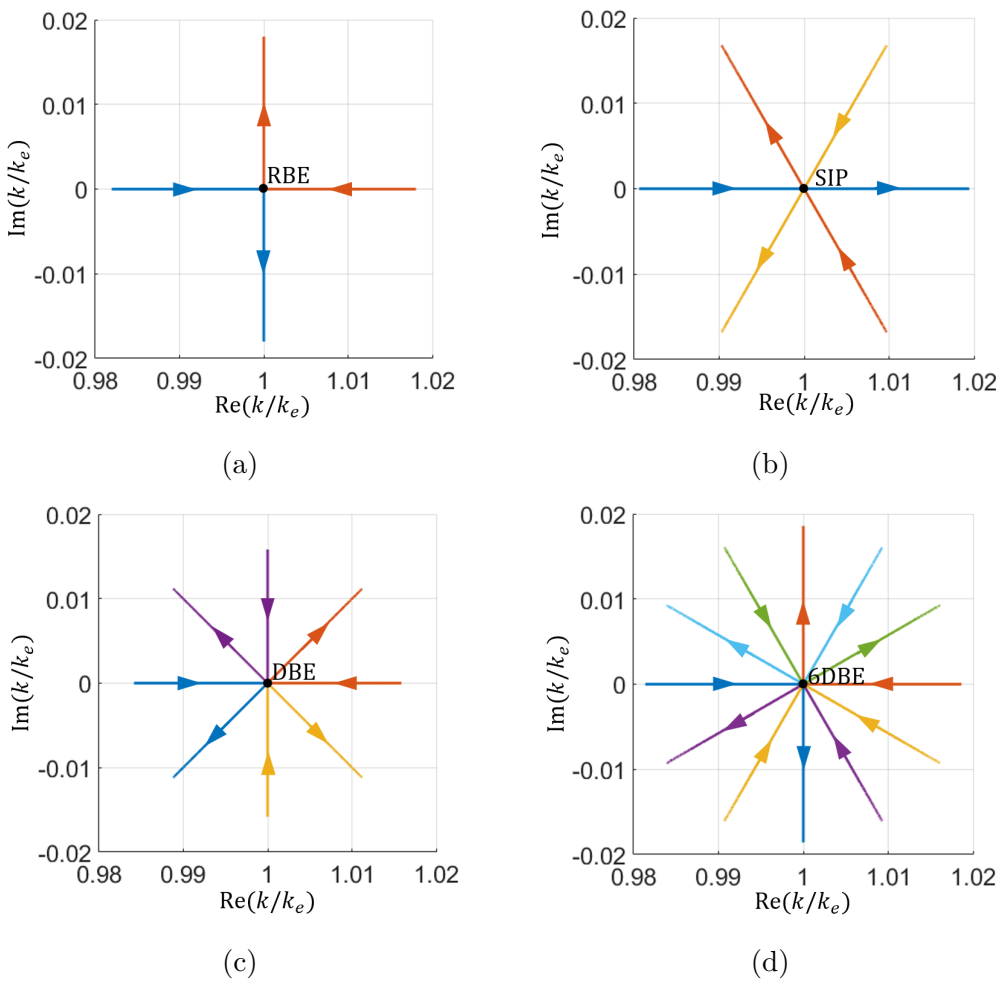

Figure 1.2: Complex-valued wavenumber plotted in the complex k-plane. The figure shows the trajectories of the wavenumbers of modes when increasing the frequency for different EPD orders: (a) RBE (2nd order EPD), (b) SIP (3rd order EPD), (c) DBE (4th order EPD), and (d) 6DBE (6th order EPD). Black Dots in the figure at $k = k_e$ are the EPDs where more than two eigenmodes coalesce. The color code used here matches the one used for the dispersion diagrams shown in Fig. 1.1.

1.3.3 Matrix Degeneracy and Field's Algebraic Growing Factor

In this subsection we consider uniform case, however, the same concepts can be found for periodic case. The general solution of (1.1) with an initial condition $\mathbf{\Psi}_{zo}$ at $z = 0$ is given by

$$\mathbf{\Psi}(z) = \exp(-j\underline{\mathbf{M}}z)\mathbf{\Psi}_{zo}. \tag{1.5}$$

Diagonalizable System Matrix

When the system matrix $\underline{\mathbf{M}}$ (same concepts apply to $\underline{\mathbf{T}}_u$ for periodic case) has distinct eigenvectors, i.e., none of of the eigenmode coalesce, it is diagonalized and represented as

$$\underline{\mathbf{M}} = \underline{\mathbf{U}}\ \underline{\mathbf{\Lambda}}\ \underline{\mathbf{U}}^{-1}, \tag{1.6}$$

where $\underline{\mathbf{U}}$ is the similarity transformation matrix containing all the eigenvectors of $\underline{\mathbf{M}}$ as columns and it is written in the form $\underline{\mathbf{U}} = [\mathbf{\Psi}_1|\mathbf{\Psi}_2|\dots\mathbf{\Psi}_N]$, whereas the matrix $\underline{\mathbf{\Lambda}}$ is a diagonal matrix containing all the eigenvalues of $\underline{\mathbf{M}}$, viz., $\Lambda_{nn} = k_n$ for $n = 1, 2, ..., N$. Since the eigenvectors of the system are distinct, they form a complete set to represent any state vector at any coordinate z. As a consequence, the initial condition $\mathbf{\Psi}_{zo}$ can be represented as a linear decomposition of the eigenvectors (See Ch.4 in [60]) as

$$\mathbf{\Psi}_{zo} = a_1\mathbf{\Psi}_1 + a_2\mathbf{\Psi}_2 + \ldots + a_N\mathbf{\Psi}_N = \underline{\mathbf{U}}\ \mathbf{a}, \tag{1.7}$$

where a_n are the the weights of each eigenvector, and the vector $\mathbf{a}$ is written in the form $\mathbf{a} = [\ a_1,\ \ a_2,\ \ \ldots\ \ a_N\ ]^{\mathrm{T}}$.

Substituting (1.6) and (1.7) in (1.5) yields

$$\begin{aligned}\boldsymbol{\Psi}(z) &= \underline{\mathbf{U}}\exp\left(-j\underline{\Lambda}z\right)\underline{\mathbf{U}}^{-1}\boldsymbol{\Psi}_{zo}. \\ &= \underline{\mathbf{U}}\exp\left(-j\underline{\Lambda}z\right)\mathbf{a} \\ &= [\boldsymbol{\Psi}_1 e^{-jk_1 z}|\boldsymbol{\Psi}_2 e^{-jk_2 z}|\ldots|\boldsymbol{\Psi}_N e^{-jk_N z}]\mathbf{a} \\ &= a_1\boldsymbol{\Psi}_1 e^{-jk_1 z} + a_2\boldsymbol{\Psi}_2 e^{-jk_2 z} + \ldots + a_N\boldsymbol{\Psi}_N e^{-jk_N z}.\end{aligned} \tag{1.8}$$

From (1.8), it is clear that the general solution of the wave equation is decomposed of N eigenmodes, where each mode independently evolves with z as $\Psi \propto e^{-jk_n z}$.

Non-Diagonalizable System Matrix with Full-order Degeneracy

At full order degeneracy, all the eigenvalues and the eigenvectors of the matrix $\underline{\mathbf{M}}$ coalesce, so $k_n = k_e$ and $\boldsymbol{\Psi}_n = \boldsymbol{\Psi}_e$ for $n = 1, 2, .., N$, where k_e and $\boldsymbol{\Psi}_e$ are the degenerate eigenvalue and eigenvector, respectively. For sake of simplicity we consider case of $N = 4$ but the same concepts can be applied to any other N. The system matrix $\underline{\mathbf{M}}$ is not diagonalizable, whereas, the matrix $\mathbf{U}$ constructed as described in the previous section will be singular exactly at the EPD (as a limit process). Hence the non-diagonizable $\mathbf{M}$ is similar to a matrix in Jordan normal form (See Ch. 7 in [60]) as

$$\underline{\mathbf{M}} = \underline{\mathbf{W}}\ \left(k_e\underline{\mathbf{1}} + \underline{\mathbf{N}}\right)\ \underline{\mathbf{W}}^{-\mathbf{1}} = k_e\underline{\mathbf{1}} + \underline{\mathbf{W}}\ \underline{\mathbf{N}}\ \underline{\mathbf{W}}^{-1}, \tag{1.9}$$

where $\underline{\mathbf{1}}$ is a $N \times N$ identity matrix, and $\underline{\mathbf{N}}$ is $N \times N$ Nilpotent matrix [60],

$$\underline{\mathbf{N}} = \begin{pmatrix} 0 & 1 & 0 & 0 \\ 0 & 0 & 1 & 0 \\ 0 & 0 & 0 & 1 \\ 0 & 0 & 0 & 0 \end{pmatrix}, \tag{1.10}$$

and it follows the property

$$\mathbf{N}^n = \mathbf{0}, \quad \forall\ n \geq 4\ . \tag{1.11}$$

The matrix $\underline{\mathbf{W}}$ contains the *generalized* eigenvectors of $\underline{\mathbf{M}}$ and is written in the form $\underline{\mathbf{W}} = [\mathbf{\Psi}_e|\mathbf{\Psi}_{e1}|\mathbf{\Psi}_{e2}|\mathbf{\Psi}_{e3}]$, where

$$\begin{aligned} \underline{\mathbf{M}}\mathbf{\Psi}_e &= \mathbf{0}, \\ \underline{\mathbf{M}}\mathbf{\Psi}_{e1} &= \mathbf{\Psi}_e, \\ \underline{\mathbf{M}}\mathbf{\Psi}_{e2} &= \mathbf{\Psi}_{e1}, \\ \underline{\mathbf{M}}\mathbf{\Psi}_{e3} &= \mathbf{\Psi}_{\mathrm{e2}}. \end{aligned} \tag{1.12}$$

Substituting (1.9) in (1.5) gives

$$\mathbf{\Psi}(z) = \exp\left(-jk_e z\underline{\mathbf{1}} - jz\underline{\mathbf{W}}\ \underline{\mathbf{N}}\ \underline{\mathbf{W}}^{-1}\right)\Psi_{zo}. \tag{1.13}$$

Since the matrix $k_e\underline{\mathbf{1}}$ and $\underline{\mathbf{W}}\ \underline{\mathbf{N}}\ \underline{\mathbf{W}}^{-1}$ commute (See Ch. 10 in [61]), then (1.13) is simplified to

$$\mathbf{\Psi}(z) = e^{-jk_e z}\exp\left(-jz\underline{\mathbf{W}}\ \underline{\mathbf{N}}\ \underline{\mathbf{W}}^{-1}\right)\mathbf{\Psi}_{zo}. \tag{1.14}$$

Using the Taylor series expansion of the exponential function (See Ch. 10 in [61]) and using the fact that $\left(\underline{\mathbf{W}}\ \underline{\mathbf{N}}\ \underline{\mathbf{W}}^{-1}\right)^n = \underline{\mathbf{W}}\ \underline{\mathbf{N}}^n\ \underline{\mathbf{W}}^{-1}$ for any integer n, (1.14) is expanded as

$$\mathbf{\Psi}(z) = e^{-jk_e z}\sum_{n=0}^{\infty}\frac{\underline{\mathbf{W}}\ (-jz\underline{\mathbf{N}})^n\ \underline{\mathbf{W}}^{-1}}{n!}\mathbf{\Psi}_{zo}, \tag{1.15}$$

and making use of (1.11), (1.15) is reduced to

$$\mathbf{\Psi}(z) = e^{-jk_e z}\underline{\mathbf{W}}\left(\underline{\mathbf{1}} - jz\underline{\mathbf{N}} - \frac{z^2\underline{\mathbf{N}}^2}{2} + \frac{jz^3\underline{\mathbf{N}}^3}{6}\right)\underline{\mathbf{W}}^{-1}\mathbf{\Psi}_{zo} \tag{1.16}$$

At a fourth order EPD the state vector $\mathbf{\Psi}_{zo}$ at at $z = 0$ is represented as a series combination of the generalized eigenvectors as

$$\mathbf{\Psi}_{zo} = a_e\mathbf{\Psi}_e + a_{e1}\mathbf{\Psi}_{e1} + a_{e2}\mathbf{\Psi}_{e2} + a_{e3}\mathbf{\Psi}_3 = \underline{\mathbf{W}}\ \mathbf{a}_e, \tag{1.17}$$

where a_{en} are the the weights of the generalized eigenvectors, and the vector $\mathbf{a}_e$ is written in the form $\mathbf{a}_e = [\ a_e \quad a_{e1} \quad a_{e3} \quad a_{e3}\ ]^T$.

Substituting (1.17) into (1.15), the general solution at fourth order EPD is obtained as

$$\begin{aligned}\boldsymbol{\Psi}(z) &= e^{-jk_e z}\underline{\mathbf{W}}\left(\underline{\mathbf{1}} - jz\underline{\mathbf{N}} - \frac{z^2\underline{\mathbf{N}}^2}{2} + \frac{jz^3\underline{\mathbf{N}}^3}{6}\right)\mathbf{a}_e \\ &= e^{-jk_e z}\underline{\mathbf{W}}[\ a_e\ ,\ \ a_{e1}\ ,\ \ a_{e2}\ ,\ \ a_{e3}\ ]^T \\ &\quad -jze^{-jk_e z}\underline{\mathbf{W}}[\ a_{e1}\ ,\ \ a_{e2}\ ,\ \ a_{e3}\ ,\ \ 0\ ]^T \\ &\quad -\frac{z^2}{2}e^{-jk_e z}\underline{\mathbf{W}}[\ a_{e2}\ ,\ \ a_{e3}\ ,\ \ 0\ ,\ \ 0\ ]^T \\ &\quad -jz^3e^{-jk_e z}\underline{\mathbf{W}}[\ a_{e3}\ ,\ \ 0\ ,\ \ 0\ ,\ \ 0\ ]^T\end{aligned} \tag{1.18}$$

Simplifying (1.18), the general solution of (1.1) casts in the form

$$\begin{aligned}\boldsymbol{\Psi}(z) = \ & a_e\boldsymbol{\Psi}_e e^{-jk_e z} \\ & +a_{e1}\left(\boldsymbol{\Psi}_{e1} - jz\boldsymbol{\Psi}_e\right)e^{-jk_e z} \\ & +a_{e2}\left(\boldsymbol{\Psi}_{e2} - jz\boldsymbol{\Psi}_{e1} - \frac{z^2}{2}\boldsymbol{\Psi}_e\right)e^{-jk_e z} \\ & +a_{e3}\left(\boldsymbol{\Psi}_{e3} - jz\boldsymbol{\Psi}_{e2} - \frac{z^2}{2}\boldsymbol{\Psi}_{e1} + j\frac{z^3}{6}\boldsymbol{\Psi}_e\right)e^{-jk_e z}.\end{aligned} \tag{1.19}$$

From (1.19), we conclude that only one mode preserve the proportionality $\boldsymbol{\Psi} \propto e^{-jkz}$ at the fourth order EPD, while the other three modes have algebraic growth with z as $\boldsymbol{\Psi} \propto \mathbf{P}(z)e^{-jkz}$, where $\mathbf{P}(z)$ is a polynomial vector function of maximum order of 3.

1.4 Organization of the Dissertation and Contents

The dissertation is organized into Chapters that involve the theory and applications of dispersion engineering in the microwave, RF and electron beam devices. We explore the conditions

for various orders of EPDs to exist in different structures.

Chapter 2: we present in this chapter a transmission line theory of EPD in two coupled-mode uniform guiding structures. We have also experimentally demonstrated the occurrence of a fourth order EPD (the DBE) in microstrip coupled transmission lines (CTL) at microwave frequencies, first through four-port measurements of a unit cell leading to the DBE dispersion relation and then through the transmission characteristics of a finite-length CTL.

Chapter 3: we present special EPD condition that is obtained in two coupled waveguides without resorting to gain and loss. We employ coupled mode theory to study the general conditions for two coupled waves to exhibit an EPD. We show the that coupled forward and backward exhibit EPDs. We also demonstrate how to realize indirect bandgaps in guiding systems supporting a backward and a forward wave.

Chapter 4: we show the relation between mirror symmetry in periodic coupled waveguides and the possible occurrence of various orders of EPDs. The EPDs we consider in this chapter are for waveguides that are lossless and gainless where the role of mirror symmetry of the structure on the occurrence of EPDs is explored.

Chapter 5: we use the concept presented in Ch. 4 to design a photonic structure that exhibits DBE. We propose a degenerate version of the Bragg condition that operates at DBE. We show that a double grating waveguide with broken symmetry supports a DBE.

Chapter 6: we investigate the physics of EPD resulting from the interaction between an electron beam and an EM mode. We propose to use such EPD to conceive high power sources. We use a generalization of the well established Pierce model to account for the interaction of the EM wave in the slow wave structure (SWS) and the electron beam, assuming small signal modulation of the beam.

Chapter 7: we show how the proposed physic phenomenon of “degenerate synchronism” pre-

sented in Ch. 6 is used to greatly improve the performance of a realistic high-power X-band relativistic BWO, based on a linear electron beam in a corrugated circular metallic waveguide. We achieve high power efficiency and output power levels, showing a very significant improvement compared to standard BWO.

Chapter 8: we propose and utilize degenerate synchronization regime presented in Ch. 6 to increase the output power and power conversion efficiency of millimeter wave BWOs. Degenerate synchronization regime is achieved through altering the folded waveguide by adding periodic power extraction ports. This allows the interactive system to work at an EPD which implies a maintained synchronism for any desired level of power extraction.

Chapter 9: we propose for a method to obtain the eigenmodes in interactive system of a travelling-wave tube (TWT) based on particle-in-cell (PIC) simulation. The proposed tool is based on simulation of finite length hot structure considering the precise waveguide geometry, materials' electromagnetic properties, electron beam cross-section area, confinement magnetic field and space charge effect. The proposed tool is used to assess the occurrence of EPD in Ch. 7 and Ch. 8.

Chapter 10: we utilize the method presented in Ch. 9 to calculate the reduced plasma frequency of a cylindrical-shaped electron beam flowing inside of a cylindrical tunnel. The occurrence of EPD in such system is investigated.

Chapter 11: we propose an analytic method for computing the eigenmodes of a double-stream electron beam, consisting of a solid inner cylindrical stream and a co-axial outer annular stream, contained within a cylindrical metallic waveguide. We show that such system exhibits EPDs that result in amplification of the space-charge wave supported by the structure.

Chapter 2

General Conditions to Realize Exceptional Points of Degeneracy in Two Uniform Coupled Transmission Lines

We present the general conditions to realize a fourth order exceptional point of degeneracy (EPD) in two *uniform* (i.e., invariant along z) lossless and gainless coupled transmission lines (CTLs), namely, a degenerate band edge (DBE). Until now the DBE has been shown only in periodic structures. In contrast, the CTLs considered here are uniform and subdivided into four cases where the two TLs support combinations of forward propagation, backward propagation and evanescent modes (when neglecting the mutual coupling). We demonstrate for the first time that a DBE is supported in *uniform* CTLs when there is proper coupling between: (i) propagating modes and evanescent modes, (ii) forward and backward propagating modes, or (iii) four evanescent modes (two in each direction) [49]. We also show that the loaded quality factor of *uniform* CTLs exhibiting a fourth order EPD at $k = 0$ is

robust to series losses due to the fact that the degenerate modes do not advance in phase. We also provide a microstrip possible implementation of a uniform CTL exhibiting a DBE using periodic series capacitors with very sub-wavelength unit-cell length. Finally, we show an experimental verification of the existence DBE for a microstrip implementation of a CTL supporting coupled propagating and evanescent modes.

2.1 Motivation and State of the Art

Exceptional points of degeneracy (EPDs) are points in parameters space where two or more eigenmodes of a waveguide coalesce into a single eigenmode. The dispersion relation of eigenmodes in a waveguide that exhibits an EPD with order m, where m is the number of coalescing eigenmodes, has the behavior of $(\omega - \omega_e) \propto (k - k_e)^m$ near the EPD at (ω_e, k_e) [44, 47]. Here ω and k are the angular frequency and the wavenumber, respectively, and the EPD is denoted by the subscript e. Such dispersion behavior is accompanied by a severe reduction in the group velocity of waves propagating in those structures and a tremendous increase in local density of states [9] resulting in a giant increase in the loaded quality factor of the structure [43, 62]. Indeed for a lossless waveguide exhibiting an EPD of order order m not only the group velocity $v_g = \partial\omega/\partial k$ vanishes, but all of its derivatives $\partial v_g^i/\partial k^i$ with $i < m - 1$ vanish as well [42].

In general, EPDs occur in coupled resonator systems and in coupled-multimode waveguides. Recently the occurrence of EPDs has been shown in a *single* resonator where one of its elements is time modulated [63]. In this chapter we focus on EPDs occurring in multimode waveguides. Furthermore, there are a few types of EPDs, some involve the simultaneous presence of loss and gain, like in parity time (PT) symmetric systems [22, 39, 57]. Here however we focus on EPDs that do not require loss and gain to occur, namely we focus on the regular band edge and on the degenerate band edge (DBE), that is a fourth order EPD

introduced a few years ago by Figotin and Vitebskiy in layered anisotropic crystals [44], [43].

Recent work has shown that the DBE can be engineered in various types of *periodic* guiding systems. The DBE is a fourth order EPD existing in periodic waveguides without loss and gain. It has been shown to exist in photonic crystals [44, 64, 9], circular waveguides with periodic inclusions [65], two coupled substrate integrated waveguides [66], two coupled periodic transmission lines [67, 8], ladder circuits [68], and integrated coupled optical waveguides [47, 46]. The first experimental demonstration of the existence of the DBE in periodic waveguides at radio frequency was shown in [48], and recently extended to periodic coupled microstrips [41]. Structures exhibiting DBEs have been proposed recently for a wide range of applications such as, for example, high quality factors photonic crystals [62], high power electron-beam devices [69, 5], RF oscillators [1] and lasers [11].

There are only a few ways to obtain EPDs in *uniform* waveguides. The simplest second order EPD is found in uniform waveguides at the modal cutoff frequency where two modes, the forward and backward modes, coalesce at $k = 0$, forming an EPD of order 2 that is called "regular" band edge [70]. Another way to realize second order EPDs in *uniform* coupled transmission lines (CTLs) is based on PT-symmetry [22], [17] which implies using a balanced and symmetrical distribution of gain and loss [57]. In contrast to these two types of second order EPD, in this chapter we show there are other ways to realize EPDs of fourth order in two lossless/gainless *uniform* CTLs at $k = 0$. Therefore this chapter shows for the first time how to realize a DBE at $k = 0$ in uniform transmission lines (Fig. 2.1) since previously the DBE was shown only in periodic waveguides [44, 47, 65, 46, 41]. This chapter also shows how to locate a regular band edge (an EPD of order 2) at any k, in *uniform* waveguides (Fig. 2.1).

In Section II, we discuss briefly all possible EPDs that may exist in two *uniform* CTLs, and their general necessary and sufficient conditions. In Section III, we show the necessary and sufficient conditions to realize fourth order EPD in two uniform, lossless, CTLs in term

of their per-unit-length parameters and we show all possible typologies that may support a fourth order EPD, namely a DBE, at $k = 0$. We also show that CTLs of finite length make formidable resonators that exhibit an L^5 scaling of the quality factor with the CTL length L. Finally we show the effect of CTL losses on the occurrence of the DBE and on the quality factor and show that series losses affect the DBE much less than shunt losses. In Section IV, we present an example of *uniform* CTLs that support a DBE at $k = 0$ and we also provide a microstrip possible implementation of such uniform CTLs exhibiting the DBE using a series per-unit-length inductance realized with a very sub-wavelength unit-cell length. In Section V we show two experimental validations of the occurrence of the DBE in uniform CTLs, using periodic capacitive loading with subwavelength period, approximating (in a metamaterials sense) the uniform CTL. The findings in this chapter open up new ways to conceive distributed oscillators, leaky wave antennas, and radiating leaky wave antennas with extreme tunability, waveguide-based sensors, etc.

2.2 System Description of Uniform Coupled Waveguides

Consider the two *uniform* waveguides schematically shown in Fig. 2.1a, where each waveguide (when uncoupled) supports either a forward propagating mode, a backward propagating mode (where group velocity and phase velocity have opposite sign) or an evanescent mode; along each positive and negative z-direction due to reciprocity.

An equivalent CTL model is used to describe the coupled waveguides in Fig. 2.1a [58, 59] and this model can also be used to describe propagation in several other "two-ways" guiding geometries that support two waves in each direction. Let V_n and I_n , with $n =$

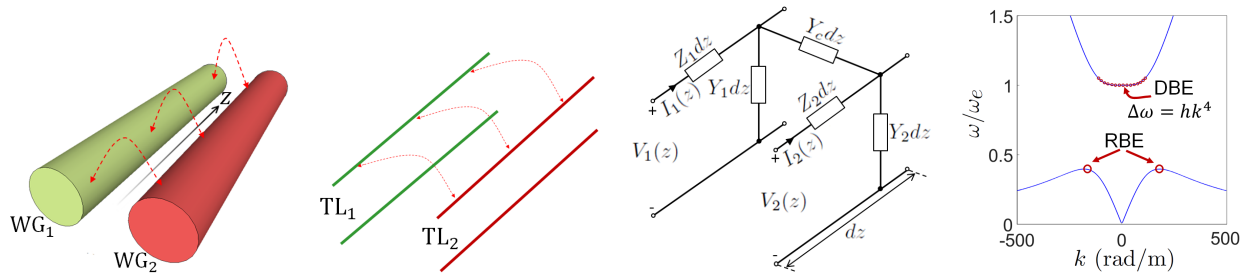

(a) (b) (c) (d)

Figure 2.1: (a) Two uniform coupled waveguides supporting four modes (two in each direction). Modes have wavenumbers satisfying the k and $-k$ symmetry, due to reciprocity. (b) Equivalent coupled transmission line (CTL) model describing the propagation of the four modes in the two uniform coupled waveguides. (c) Generalized per-unit-length distributed equivalent circuit model for the CTL. Coupling is represented by the distributed (i.e., per-unit-length) admittance Y_c . In this chapter we determine the necessary and sufficient conditions that the five reactances shall satisfy for the CTLs to exhibit a DBE, i.e., a fourth order degeneracy. (d) Representation of a dispersion diagram (showing only the branches of purely-real wavenumber) reporting two important features: the DBE at $k_e = 0$ and $\omega = \omega_e$ (that is a fourth order EPD), and a regular band edge at $\omega = 0.4\omega_e$, with a non-vanishing wavenumber of $k = \pm 147.5$ rad/m (a second order EPD).

$1, 2$, be the equivalent voltage and current in each TL of Fig. 2.1b, describing the spatial evolution of electromagnetic waves along the z-direction. It is convenient to introduce the two-dimensional vectors $\mathbf{V}(z) = [\ V_1(z)\ ,\ \ V_2(z)\ ]^{\mathrm{T}}$, $\mathbf{I}(z) = [\ I_1(z)\ ,\ \ I_2(z)\ ]^{\mathrm{T}}$, where the superscript T represents the transpose operation.

When the two transmission lines are not coupled they support four independent modes that are described by four distinct wavenumbers k_1', k_2' and $-k_1'$, $-k_2'$ and their voltage and current are written as

$$V_n(z) \propto e^{\pm jk_n' z}, \quad I_n(z) \propto e^{\pm jk_n' z}, \tag{2.1}$$

where, the modal wavenumbers k_n' , with $n = 1, 2$, are are generally written as $k_n' = \beta_n - j\alpha_n$, where β_n and α_n are the phase propagation and attenuation constants, respectively, and they determine the type of mode; for example, a wavenumber k' that possesses only the

imaginary part α is an evanescent mode. Forward modes are determined by $\beta\alpha > 0$, whereas "backward" propagating modes have $\beta\alpha < 0$ (hence, backward propagating modes have phase and group velocities with opposite directions).

The circuit *equivalent* model for an infinitesimal-length of a wavguide is represented by generic per-unit-length distributed parameters as shown in Fig. 2.1c. There, Z_1, Z_2, Y_1, Y_2 and Y_c may be inductive or capacitive impedances and admittances. In this chapter, for the sake of brevity, we do not consider magnetic induction coupling between the two TLs, i.e., we only consider shunt per-unit-length inductive or capacitive coupling Y_c shown in Fig. 2.1c. Coupling due to magnetic induction between two nearby lines could be investigated using the same mechanism and formulation used in this chapter and it is not treated here. It can be neglected in several cases, when the separation between the two lines is very large, for examples, or for the case studied in Sec. IV, where the coupling is due to the physical connection between the 1^{st} and 2^{nd} TL.

We assume that Z_1 and Z_2 may be either capacitive or inductive impedances, as well as Y_1, Y_2 can be either capacitive or inductive, where the subscripts 1 and 2 are used to describe the parameters in the first and second transmission line TL_1 and TL_2, respectively. We recall that a single TL (say TL_1 for example) supports backward waves if Z_1 is capacitive and Y_1 is inductive. Furthermore, a TL (say TL_1 for example) supports evanescent waves if both Z_1 and Y_1 have the same kind of reactance. An example of dispersion diagram with a DBE (a fourth order EPD) at $k = 0$ and a regular band edge (a second order EPD) at $k \neq 0$, is shown in Fig. 2.1d, using the CTL parameters provided in the next section. The DBE occurring at $k = 0$, which is the main focus of this chapter, has a dispersion characterized by the relation [44, 47]

$$(\omega - \omega_e) = hk^4, \tag{2.2}$$

in the vicinity of $k = 0$, where h is a geometry-dependent fitting parameter that controls the flatness of the dispersion.

Using the matrix notation as in [71] for the circuit *equivalent* model in Fig. 2.1c, the differential wave equations (telegrapher's equations) describing propagation in the two CTLs are

$$\begin{aligned} \frac{d\mathbf{V}(z)}{dz} &= -\underline{\underline{\mathbf{Z}}}(\omega)\mathbf{I}(z), \\ \frac{d\mathbf{I}(z)}{dz} &= -\underline{\underline{\mathbf{Y}}}(\omega)\mathbf{V}(z). \end{aligned} \tag{2.3}$$

Here $\underline{\underline{\mathbf{Z}}}$ and $\underline{\underline{\mathbf{Y}}}$ are the per-unit-length series-impedance and shunt-admittance matrices, respectively, describing the per-unit-length distributed parameters of the coupled transmission lines (CTLs) [71]. They are 2×2 symmetric matrices given by

$$\begin{aligned} \underline{\underline{\mathbf{Z}}}(\omega) &= \begin{pmatrix} Z_1(\omega) & 0 \\ 0 & Z_2(\omega) \end{pmatrix}, \\ \underline{\underline{\mathbf{Y}}} &= \begin{pmatrix} Y_1(\omega) + Y_c(\omega) & -Y_c(\omega) \\ -Y_c(\omega) & Y_2(\omega) + Y_c(\omega) \end{pmatrix}, \end{aligned} \tag{2.4}$$

where the coupling between the two TLs is due to $Y_c(\omega)$. For the sake of convenience, a four-dimensional state vector that includes voltages and currents at a coordinate z in the CTLs is defined as

$$\mathbf{\Psi}(z) = [\ V_1(z)\ ,\ \ V_2(z)\ ,\ \ I_1(z)\ ,\ \ I_2(z)\ ]^{\mathrm{T}}. \tag{2.5}$$

Therefore, the two telegrapher equations (2.3) representing wave propagation are cast in terms of a multidimensional first order differential equation [57, 31]

$$\frac{d\mathbf{\Psi}(z)}{dz} = -j\underline{\mathbf{M}}(\omega)\mathbf{\Psi}(z), \tag{2.6}$$

where $\underline{\mathbf{M}}(\omega)$ is a 4×4 system matrix given by

$$\underline{\mathbf{M}}(\omega) = \begin{pmatrix} \underline{\underline{\mathbf{0}}} & -j\underline{\underline{\mathbf{Z}}}(\omega) \\ -j\underline{\underline{\mathbf{Y}}}(\omega) & \underline{\underline{\mathbf{0}}} \end{pmatrix}, \tag{2.7}$$

and $\underline{\underline{\mathbf{0}}}$ is the 2×2 null matrix.

When the matrix $\underline{\mathbf{M}}(\omega)$ is diagonalizable all the four eigenmodes supported in the CTL have state vectors $\mathbf{\Psi}_n(z) \propto e^{-jk_n z}$, with $n = 1, 2, 3, 4$; however, when the matrix $\underline{\mathbf{M}}(\omega)$ is not diagonalizable (this is corresponding to the case exhibiting an EPD), some modes preserve the proportionality $\mathbf{\Psi}_n(z) \propto e^{-jk_n z}$, while the rest have algebraic growth with z as $\mathbf{\Psi}_n \propto \mathbf{P}(z)e^{-jk_n z}$, where $\mathbf{P}(z)$ is a vector polynomial function of maximum order 3 for systems made of two CTLs as considered in this chapter [49]. Therefore, when $\underline{\mathbf{M}}(\omega)$ is diagonalizable the eigenmodes supported by the uniform CTL described by (2.6) are fully represented by using $\mathbf{\Psi}(z) \propto e^{-jkz}$ in (2.6) to obtain $-jk\ \mathbf{\Psi}(z) = -j\underline{\mathbf{M}}(\omega)\mathbf{\Psi}(z)$ [57], yet

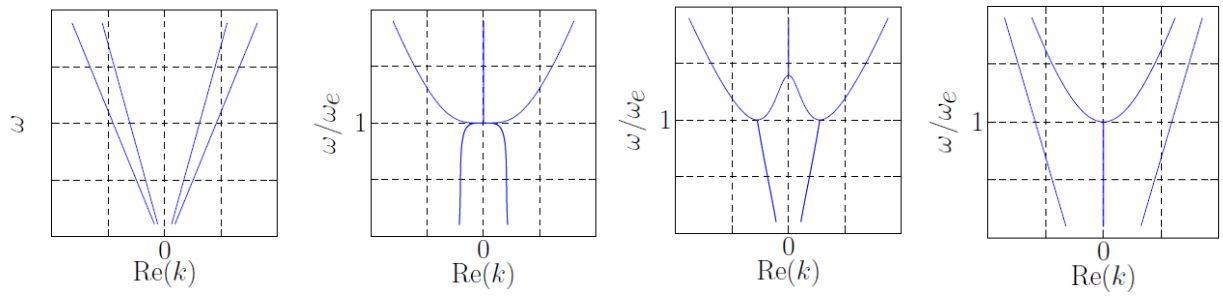

(a) (b) (c) (d)

Figure 2.2: Dispersion diagrams describing different EPDs at angular frequency ω_e: (a) CTLs where none of the EPD conditions are satisfied at any non-zero frequency; (b) CTLs exhibiting the 4^{th} order EPD (i.e., the DBE) at the angular frequency ω_e where $\mathrm{Tr}(\underline{\underline{\mathbf{Z}}}(\omega_\mathrm{e})\underline{\underline{\mathbf{Y}}}(\omega_\mathrm{e})) = 0$ and $\det(\underline{\underline{\mathbf{Z}}}(\omega_\mathbf{e})\ \underline{\underline{\mathbf{Y}}}(\omega_\mathbf{e})) = 0$. For uniform CTLs made of 2 TLs this condition necessarily occurs at $k = 0$; (c) CTLs exhibiting two exceptional points of 2^{nd} order degeneracy, where $\mathrm{Tr}(\underline{\underline{\mathbf{Z}}}(\omega_\mathrm{e})\underline{\underline{\mathbf{Y}}}(\omega_\mathrm{e}))^2 = 4\det(\underline{\underline{\mathbf{Z}}}(\omega_\mathbf{e})\ \underline{\underline{\mathbf{Y}}}(\omega_\mathbf{e}))$. For uniform CTLs made of 2 TLs this can occur at any k; (d) CTLs exhibiting a single 2^{nd} order EPD where $\det(\underline{\underline{\mathbf{Z}}}(\omega_\mathbf{e})\ \underline{\underline{\mathbf{Y}}}(\omega_\mathbf{e})) = 0$. This condition occurs at $k = 0$. In these plots we show only the real part of the four modal wavenumbers.

simplified to an eigenvalue problem as

$$\underline{\underline{\mathbf{M}}}\boldsymbol{\Psi}(z) = k\boldsymbol{\Psi}(z). \tag{2.8}$$

The four eigenvalues k_1, k_2, k_3 and k_4 and their corresponding eigenvectors (at $z = 0$) $\boldsymbol{\Psi}_1$, $\boldsymbol{\Psi}_2$, $\boldsymbol{\Psi}_3$ and $\boldsymbol{\Psi}_4$ of the above eigenvalue problem are written in their simplest form as [70, 49]

$$\begin{aligned} k_1 = -k_3 &= \frac{1}{\sqrt{2}}\sqrt{-T - \sqrt{T^2 - 4D}}, \\ k_2 = -k_4 &= \frac{1}{\sqrt{2}}\sqrt{-T + \sqrt{T^2 - 4D}}, \end{aligned} \tag{2.9}$$

where $T = \mathrm{Tr}(\underline{\underline{\mathbf{Z}}}\ \underline{\underline{\mathbf{Y}}})$ is the trace and $D = \det(\underline{\underline{\mathbf{Z}}}\ \underline{\underline{\mathbf{Y}}})$. The system vector is concisely and conveniently represented as

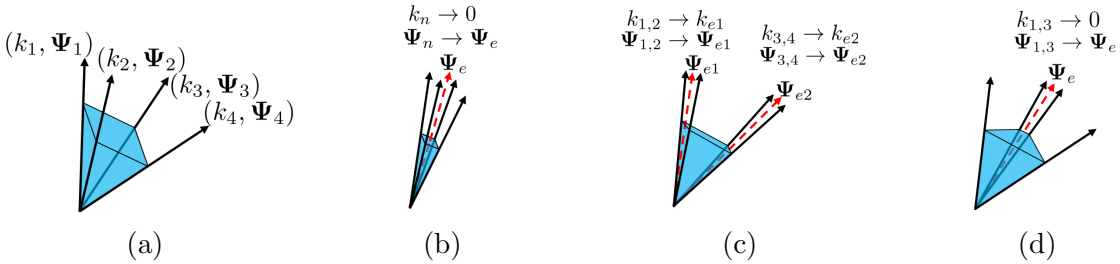

Figure 2.3: Schematic representation of the four eigenvectors of the four eigenmodes supported by a CTL as they approach different EPDs conditions: (a) no EPD, i.e., the four eigenvectors are four independent vectors in a four dimensional state space; (b) 4^{th} order EPD, i.e., the four eigenvectors tend to coalesce into a single eigenstate. When the structure is lossless and gainless such 4^{th} order EPD is called DBE; (c) two points of 2^{nd} order degeneracy, i.e, pairs of eigenvectors coalesce to two independent eigenstates at the so called RBE; and (d) a single 2^{nd} order EPD, i.e., only two eigenvectors coalesce at the so called RBE while the other two remain independent. The degree (i.e., the order) of degeneracy of a multimode EPD condition is given by the number of coalescing eigenvectors.

$$\mathbf{\Psi}_n = \psi_0 \begin{pmatrix} Z_1\left(k_n^2 + Z_2(Y_2 + Y_c)\right) \\ Z_1 Z_2 Y_c \\ jk_n\left(k_n^2 + Z_2(Y_2 + Y_c)\right) \\ jZ_1 k_n Y_c \end{pmatrix}, \tag{2.10}$$

where ψ_0 is arbitrary constant and it has a unit of Am^3.

The solutions (2.9) and (2.10) represent the four wavenumbers of the eigenmodes that propagate or attenuate along both the positive and negative z-directions (four modes), viz., $k_3 = -k_1$ and $k_4 = -k_2$.

In general, an EPD of order m occurs when m eigenomodes have the same eigenvalue and eigenvector. For a system of two uniform CTLs a 4^{th} order EPD (a full order EPD) occurs if all the 4 eigenvalues are equal [31], which implies that eigenvectors coalesce as well, as it is

obvious from (2.10). Therefore in such a uniform system the coalescence of four wavenumbers is a sufficient condition for an EPD to occurr.

The system made of two CTLs considered in this chapter exhibits three types of EPDs: (i) two points of second order degeneracy ($k_1 = k_2$ and $k_3 = k_4$) when $T^2 = 4D$. This can occur at any wavenumber k; (ii) A second order EPD ($k_1 = k_3$) or ($k_2 = k_4$) when $D = 0$. This occurs only at $k = 0$; and (iii) a fourth order EPD ($k_1 = k_2 = k_3 = k_4$) when both $T = 0$ and $D = 0$. This occurs only at $k = 0$. These three cases are illustrated in the dispersion diagram in Fig. 2.2 and in the schematic representation of the four eigenvectors in Fig. 2.3. Indeed, in a reciprocal systems ($k_1 = -k_3$), the equality ($k_1 = k_3$) in condition (ii) implies that ($k_1 = k_3 = 0$). Furthermore, still based on reciprocity, the condition ($k_1 = k_2 = k_3 = k_4$) in (iii) implies that ($k_1 = k_2 = k_3 = k_4 = 0$). Hence, these two conditions can be used also to design systems radiating at broadside and working at an EPD. Condition (ii) is usually refereed to as a cutoff condition (at $k = 0$) and indeed it occurs also in regular single mode waveguides. Condition (i) is interesting, because it sets a cutoff condition at any desired wavenumber $k \neq 0$. It is important to point out that a 3^{rd} order EPD cannot exist in two coupled transmission lines unless reciprocity is broken [54] which is out of the scope of this chapter; here we only consider reciprocal coupled transmission lines. The scope of this chapter is mainly to show the fourth order degeneracy (namely the DBE) described in condition (iii) and to show that condition (i) can be also easily engineered.

2.3 Fourth Order DBE in Uniform Waveguides

When modes are supported in uniform waveguides modeled by two uniform and coupled TLs, a fourth order EPD (DBE) occurs when all four independent eigenvectors coalesce and form one single eigenvector [44, 42] as schematically shown in Fig. 2.3b. This occurs when the impedance and admittance matrices that describe the per-unit-length parameters of the

system satisfy both conditions:

$$\begin{aligned} T &= \mathrm{Tr}(\underline{\underline{\mathbf{Z}}}\ \underline{\underline{\mathbf{Y}}}) = 0, \\ D &= \det(\underline{\underline{\mathbf{Z}}}\ \underline{\underline{\mathbf{Y}}}) = 0. \end{aligned} \tag{2.11}$$

Indeed from (2.11) these two conditions imply that $k_1 = k_2 = k_3 = k_4$ and consequently from (2.10) it implies that all four eigenvectors are identical. Substituting (2.4) into (2.11) and after some simplification, necessary and sufficient conditions to realize a fourth order EPD at radian frequency ω_e in term of the per-unit-length CTL parameters are obtained in their simplest form as

$$Z_1(\omega_e)Y_1^2(\omega_e) = -Z_2(\omega_e)Y_2^2(\omega_e), \tag{2.12}$$

$$Y_c(\omega_e) = \frac{-Y_1(\omega_e)Y_2(\omega_e)}{Y_1(\omega_e) + Y_2(\omega_e)}. \tag{2.13}$$

It is important to point out that the first condition in (2.12) represents a constraint on the parameters of the uncoupled TLs to have a DBE, whereas the second condition in (2.13) represents the constraint on the required coupling admittance to have a DBE. Therefore just fixing the coupling parameter is not enough to have a DBE since the two individual TLs (without considering coupling) need to satisfy the constraint (2.12). Both terms $Y_1^2(\omega_e)$ and $Y_2^2(\omega_e)$ in (2.12) have a negative sign (we do not consider losses so far in this ideal analysis) regardless of the type of Y_1 and Y_2 susceptance. Consequently, from (2.12) and (2.13) we deduce that two necessary conditions to realize a fourth order EPD at radian

frequency ω_e for lossless and gainless CTLs are

$$\begin{aligned} &\mathrm{Im}\left(Z_1\right)\mathrm{Im}\left(Z_2\right)\Big|_{\omega=\omega_e} < 0, \\ &\mathrm{Im}\left(Y_c^{-1}\right)\mathrm{Im}\left(Y_1^{-1}+Y_2^{-1}\right)\Big|_{\omega=\omega_e} < 0. \end{aligned} \tag{2.14}$$

This means that the a necessary condition to realize a DBE in uniform CTL is that the two series per-unit-length impedances Z_1 and Z_2 must be of different types, i.e., one should be capacitive and the other inductive. Furthermore, Y_c^{-1} and $Y_1^{-1}+Y_2^{-1}$ must also be of different types. Figure 2.4 shows all possible configurations of the per-unit-length parameters of CTLs that exhibit a fourth order DBE.

From Fig. 2.4, it is concluded that a fourth order DBE occurs in two uniform CTLs when there is a coupling between: a forward propagating mode and an evanescent mode (Fig. 2.4a), a forward and a backward propagating modes (Fig. 2.4b), two evanescent modes (Fig. 2.4c), or a backward propagating mode and an evanescent mode (Fig. 2.4d). For a rectangular waveguide structure, the configuration in Fig. 2.4a represents a coupling between a transverse electric (TE) or transverse magnetic (TM) propagating mode and a TM evanescent mode (below cutoff), whereas the configuration in Fig. 2.4c represents coupling between TE and TM evanescent modes, both below cutoff when considered without coupling [72].

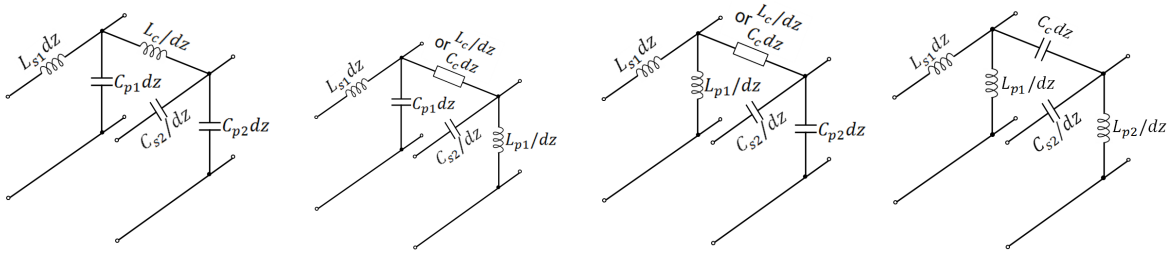

Figure 2.4: Different configurations of uniform CTLs that may exhibit a fourth order EPD, namely, the DBE when the CTLs are lossless. Here we show the combinations of distributed reactances that provide multi-mode degenerate conditions: Configuarion (a) shows that a fourth order EPD is obtained by a proper inductive coupling between a "forward" propagating mode in TL_1 and an evanescent mode in TL_2. Configuration (b) shows that a fourth order EPD is obtainable by a proper coupling between a forward mode in TL_1 and a "backward" mode in TL_2. Note that here we denote a mode to be "forward" when phase and group velocities have the same signs, whereas a "backward" mode has phase and group velocities with opposite signs. Configuration (c) shows that a four order EPD is obtainable also when proper coupling is designed between evanescent modes in TL_1 and TL_2. Finally, configuration (d) shows that an EPD can be obtained also by a capacitive coupling between an evanescent mode in TL_1 and a backward propagating mode in TL_2.

2.3.1 Example of Uniform CTL with Infinite Length

Two CTLs with circuit configuration as in Fig. 2.4a are designed to exhibit a fourth order EPD at frequency $f_e = 5$ GHz, i.e., to satisfy the DBE conditions in (2.12) and (2.13). The CTLs parameters are $C_{p1} = C_{p2} = 0.12$ nF/m, $L_{s1} = 200$ nH/m, $C_{s2} = 5.07$ fFm and $L_c = 16.89$ pHm, where the series and parallel per-unit-length components are designated with subscripts s and p, respectively. This is the case when one TL (without considering the coupling between the two TLs) supports two propagating modes (one in each direction) while the other TL supports evanescent waves. However the two TLs are coupled via the inductive subsceptance $Y_c = 1/(j\omega L_c)$ leading to the modal dispersion diagram in Fig. 2.5. There, both the real and imaginary parts of the wavenumber are shown versus real radian frequency. A fourth order DBE occurs at radian frequency $\omega_e = 31.42 \times 10^9$ rad/s at which $k_1 = k_2 = k_3 = k_4 = 0$. Note that the dispersion diagram also exhbits two second order EPDs which represent two regular band edges (RBEs) at $\omega = 0.4\omega_e$ (i.e., at $f \approx 2$GHz) at

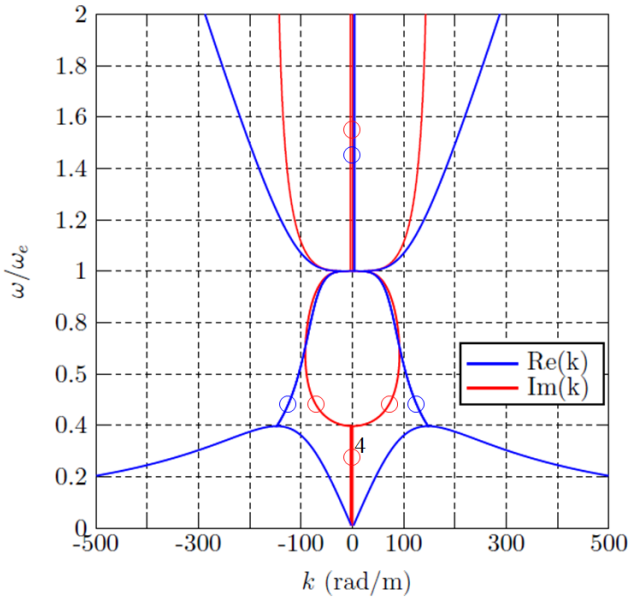

Figure 2.5: Dispersion diagram of modal complex wavenumbers k versus normalized frequency for two uniform CTLs with distributed circuit model as in 2.4a. The diagram shows a fourth order DBE $\omega = \omega_e$, i.e., at $f = f_e = 5$GHz, where all modes have $k = 0$. This CTL structure also exhibits two RBEs (EPDs of second order) at $\omega = 0.4\omega_e$, i.e., at $f = 2$GHz, with a non-vanishing wavenumber of $k = \pm 147.5$ rad/m. Branches that represent two modes are denoted by a red or a blue circle, the branch representing four modes is tagged by red circles with number 4. The dispersion diagram showing *only* the purely-real wavenumber branches is reported in Fig. 2.1d.

two distinct non-vanishing wavenumbers $k = \pm 147.5$ rad/m, where their sufficient condition $\mathrm{T}^2 = 4D$ is satisfied at this particular frequency. In the bandgap $0.4\omega_e < \omega < \omega_e$ the diagram has four wavenumbers with complex values that describe exponential decay. For $\omega > \omega_e$ two waves are propagating (purely real k) and two are evanescent (purely imaginary k). The same dispersion diagram showing *only* the branches with purely-real wavenumbers is reported in Fig. 2.1d. Therefore the CTL technique used in this chapter allows to put regular band edges at properly designed wavenumbers.

2.3.2 Uniform Waveguide with Finite Length

So far we have discussed modal propagation in infinitely long structures. We now consider two uniform CTLs with finite length L, Fig. 2.6a, operating in very close proximity of the DBE, and investigate the transmission properties in terms of scattering parameter $|S_{21}|$. Since this finite length CTL structure forms a resonator, we also investigate its quality factor. The CTL per-unit-length parameters are the same as those used in the previous subsection that led to Fig. 2.5. There are two ports, at the beginning and end of TL_1, whereas TL_2 is terminated on short circuits at both ends, as depicted in Fig. 2.6a. Figure 2.6b shows the transmission coefficient magnitude $|S_{21}|$ versus frequency, for different lengths L. The length is here given in terms of wavelengths of the propagating wave in TL_1, when uncoupled to TL_2, calculated at the EPD frequency $\lambda_{1,e} = 2\pi/k_{1,e}$= 40.8 mm, where $k_{1,e} = \omega_e\sqrt{L_{s1}C_{p1}}$. The pass band property is in agreement with that shown in Fig. 2.5, i.e., there is propagation for $f > f_e = 5$GHz. It is shown that the CTL exhibits a resonance (called DBE resonance) at a frequency almost coincident with the DBE one, regardless of the CTL length, at least for the two longer cases. The frequency of the other resonances at lower frequencies are strongly affected by the length of the structure. This resonator based on a multi-mode degeneracy exhibits a very interesting physical behavior of its quality factor. The loaded quality factor of the finite length and lossless CTL is plotted versus length L in Fig. 2.7, and it is concluded that such quality factor (blue line) follows the asymptotic trend proportional to L^5 as L increases, which is the same conclusion that was made in [68, 43, 62, 73], though in these references the DBE was obtained in periodic structures and at the edge of the Brillouin zone, whereas in this chapter we show for the first time a DBE at k=0. Here the quality factor has been evaluated as $Q = \omega_{res}\tau_g/2$, where ω_{res} is the resonance frequency associated with maximum transmission, i.e., where $|S_{21}|$ is maximum, and the group delay τ_g is calculated as the derivative of the phase of S_{21}, with respect to the angular frequency ω, i.e., $\tau_g = \partial\left(\angle S_{21}\right)/\partial\omega$ [74]. Note that high Q values are obtained while the TL_1 characteristic

impedance (without considering the coupling) is 50 Ohms and the termination load is also 50 Ohms; therefore TLs forming a cavity using the four mode degenerate condition (the DBE) do not need high reflection coefficients at the end of each TL. The strong reflection of the degenerate modes at the end of the CTL occurs because the characteristic impedance of a CTL made of two TLs is actually represented by a 2×2 impedance matrix, and therefore it is generally mismatched when two independent loads are used as termination as in Fig. 2.6a. Furthermore, exactly at the DBE frequency the group velocities of the four coalescing modes vanish and therefore the characteristic 2×2 matrix impedance shall describe absence of power flow (the characteristic impedance of a *single* TL at cutoff would be either zero or infinity). However one should note that the DBE *resonance* is slightly shifted from the DBE frequency and therefore power transfer to the load is actually occurring. It is important to point out that there are various resonance frequencies in the cavity, however, in this chapter we are focusing on the nearest one to the DBE frequency which we call it the first resonance frequency. Because of the DBE-like dispersion relation in (2.2), for long cavities the first DBE resonance frequency is approximated by the asymptotic formula

$$f_{res,1} = f_e + \alpha/L^4, \tag{2.15}$$

where α is a constant. This implies that the longer the CTL cavity, the closer the DBE resonance is to the DBE frequency, and hence the less power leakage occurs outside the resonator.

A further investigation is now conducted by studying the effect of series and parallel distributed losses in the CTL on the quality factor. Therefore we assume that each TL has either a per-unit-length series resistance R_s or a per-unit-length shunt conductance G_p. Accordingly, Fig. 2.7a plot the quality factor of the CTL versus length L for different values of the

series quality factor Q_s, where $Q_s = \omega_e L_{s1}/R_s = 1/(\omega_e C_{s2} R_s)$ is the quality factor (assumed the same) of the two series elements, which are an inductive distributed reactance in TL_1 and a capacitive distributed reactance in TL_2, and hence they satisfy $\omega_e L_{s1} = 1/(\omega_e C_{s2})$. In Fig. 2.7b instead we show the quality factor by considering losses in the two shunt (parallel) capacitive susceptances such that $Q_p = \omega C_{p1}/G_{p1} = \omega C_{p2}/G_{p2}$. Note that the same parallel capacitor and same loss is used in each of the two TLs. The two plots show a very important fact about *uniform* CTLs exhibiting a fourth order DBE: the quality factor of the CTLs is robust to the series losses, i.e., the series distributed resistance does not affect the total quality factor trend shown in Fig. 2.7a. This occurs because the wavenumbers of the four modes at DBE are such that $k_1 = k_2 = k_3 = k_4 = 0$, which means the voltage along the finite length CTL is basically constant resulting in an almost vanishing current through the series elements Z_1 and Z_2 . However, when losses are in the shunt (parallel) elements the quality factor of the structure tends to saturate to the quality factor of the used distributed parallel capacitors as shown in Fig. 2.7b. To obtain such plots, for each CTL length we have determined the resonant frequency and evaluated the required parameters at that frequency.

It is important to point out that the resonance mentioned in the previous study is not a conventional resonance due to two mode reflection, however, it is due to four modes which make it with very unique properties like quality factor and resonance frequency scaling with cavity length. Such properties can be used to make oscillator with a unique mode selection scheme that leads to a stable single-frequency oscillation, even in the presence of load variation [2, 1]. Moreover, the proposed DBE in this chapter exists at $k = 0$ which make good candidate for application like leaky wave antennas, and active leaky wave antennas that act as radiating oscillators.

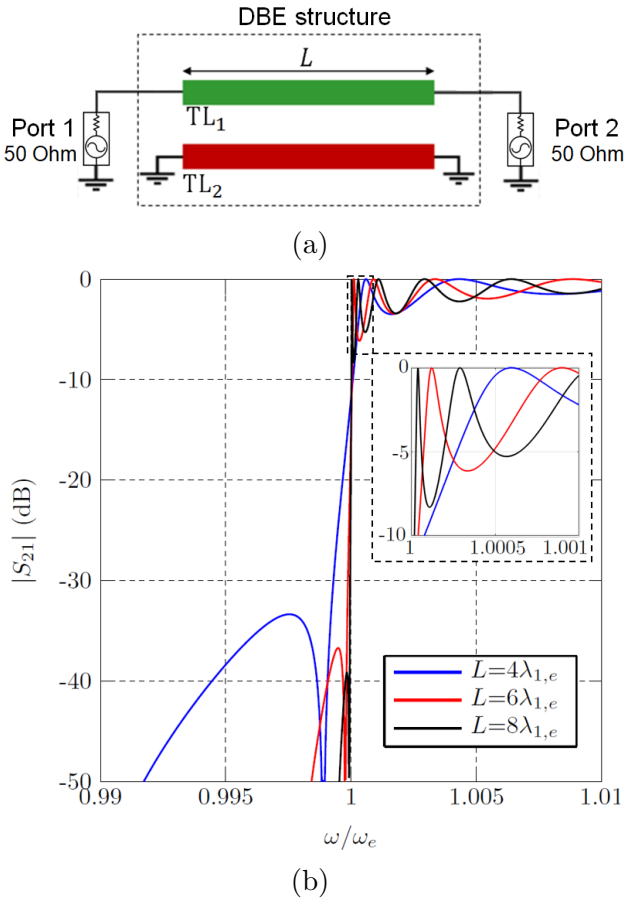

Figure 2.6: Magnitude of the transmission scattering parameter S_{21} for the waveguide consisting of two uniform microstrip CTLs with finite length L, with distributed circuit model as in 2.4a. The CTLs have a fourth order EPD (namely, a DBE) at the so called DBE frequency $f = f_e = 5$GHz . (a) Finite length CTL circuit setup. (b) Scattering parameter S_{21} for different lengths L revealing that this finite length CTL structure is a cavity despite the characteristic impedance of TL_1 is equal to the termination load. A clear transmission peak, called DBE resonance, is observed near the DBE frequency, and it gets narrower for increasing lengths. $\lambda_{1,e}$ is the wavelength of the propagating waves in TL_1, when it is uncoupled to TL_2, calculated at the EPD frequency $\lambda_{1,e} = 2\pi/k_{1,e} = 40.8$ mm, where $k_{1,e} = \omega_e\sqrt{L_{s1}C_{p1}}$.

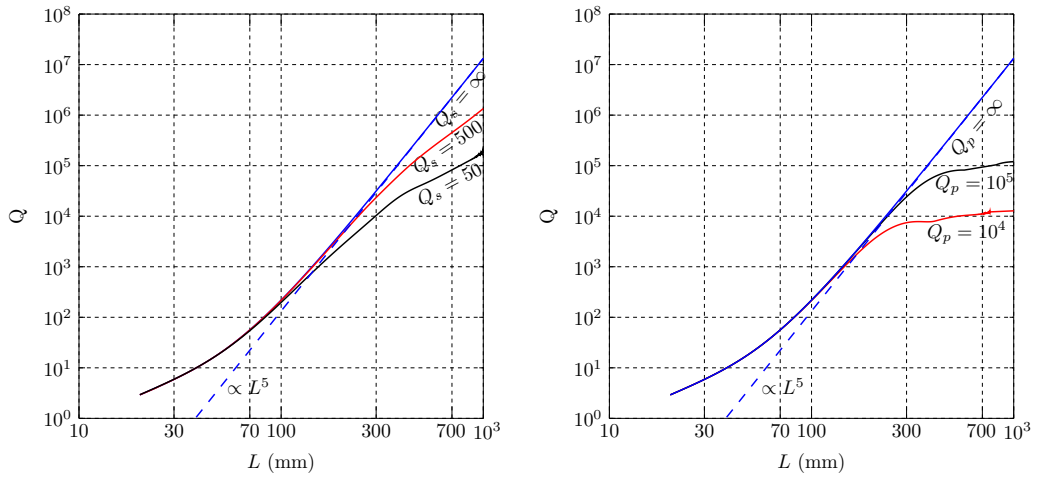

(a) (b)

Figure 2.7: Trend of the quality factor of a CTL cavity as in Figure 2.6a operating at the DBE resonance, in close proxinity of the DBE frequency, showing the L^5 scaling with cavity length L. When the CTL cavity has distributed losses, the quality factor trend is perturbed. Distributed series resistance and parallel conductance are assumed to be symmetrical, i.e., identical in each TL: (a) series losses only, and (b) parallel losses only. The legend $Q = \infty$ refers to the limit represented by a lossless CTL cavity and the blue dashed line is a fitting trend showing the L^5 growth with cavity length. These plots show that the Q factor of the CTL cavity is less sensitive to series losses.

2.4 Microstrip Implementation with Subwavelength Series Capacitors

A microstrip implementation of the uniform CTL in Fig. 2.4a is now considered where the series continuously distributed capacitance is approximated by a periodic capacitive loading with subwavelength period $d = \lambda_d/10$, where λ_d is wavelength in the substrate. Furthermore, the guided wavelength $\lambda_g = 2\pi/k$ in the proximity of the DBE at $k = 0$ is very large, and tends to infinity when k tends to zero. Therefore, because of the very subwavelength period $d \ll \lambda_g$, the CTL can be seen as a homogenized medium according to metamaterial homogenization concepts [75, 76].. Indeed we design the CTL such that the homogenized effective CTL parameters approximately equal those in the uniform case considered in the previous subsections. The grounded dielectric substrate has a relative dielectric constant of 2.2, loss tangent 0.001, and height of 0.75 mm. Metal layers have conductivity of 4.5×10^7 S/m and thickness of 35 μm. The series capacitance in each unit cell is implemented using an inter-digital capacitor and the coupling inductance in Fig. 2.4a is implemented using a folded short and thin microstrip between the two TLs as shown in Fig. 2.8. The two TL widths (i.e., when assumed uncoupled, and before introducing the series capacitors) are designed to have a characteristic impedance of 50 Ohms at f =5 GHz. All the dimensions (in mm) are reported in Fig. 2.8. The inter-digital capacitance is approximately C_d =1 pF, and since the period is $d = 5.1$ mm, then the effective distributed series capacitance is the same as the required one to get DBE, i.e., $C_{s1} = C_d d \approx 5.1$ fFm.

Figure 2.9a shows the modal dispersion obtained using full wave simulations based on the method of moments implemented in Keysight Technologies Advanced Design System (ADS). The used method of moments is based on the three-dimensional Green's function with all the dynamic terms, hence including radiation losses. The dispersion relation was calculated by determining the S-parameters of a single unit-cell, then converting them to a 4×4 unit-cell

transfer matrix $\mathbf{T}_U$ that relates voltages and currents at the beginning and end of the unit cell as in [41], and then using the Floquet theorem determining the eigenvalue problem that provides the four modal wavenumbers. Figure 2.9a shows the existence of a DBE in the dispersion diagram, and in proximity of ω_e it is in good agreement with the diagram of the uniform ideal CTL in Fig. 2.5.

We then observe the quality factor of a resonator made by a finite-length dual microstrip, shown in Fig. 2.8. The loading and excitation for calculating the quality factor are as shown in Fig. 2.6a , and the operating frequency is at the DBE resonance (the peak of the transfer function closest to the DBE frequency). The quality factor is estimated by the same formula considered in the previous section, i.e., by $Q = \omega_{res}\tau_g/2$, where the resonance frequency (the one closest to the DBE frequency) depends on the cavity length. The quality factor versus "cavity" length $L = Nd$, using N unit cells of the microstrip implementation in Fig. 2.8, is plotted in Fig. 2.9b. From this figure we note that the quality factor tends to saturate before exhibiting the asymptotic L^5 trend because of radiation, conduction and dielectric losses. Indeed the ideal $Q \propto L^5$ trend depicted in Fig. 2.7 (blue line) occurs only in the ideal case where losses are negligible, whereas in this case both series and shunt losses are present because of copper and dielectric losses. Note that here the TL_1 characteristic impedance is 50 Ohms and that the load is also 50 Ohms, therefore a cavity using the four mode degenerate condition (the DBE) does not need high reflection coefficients at the end of each TL that can be normally terminated at any load.

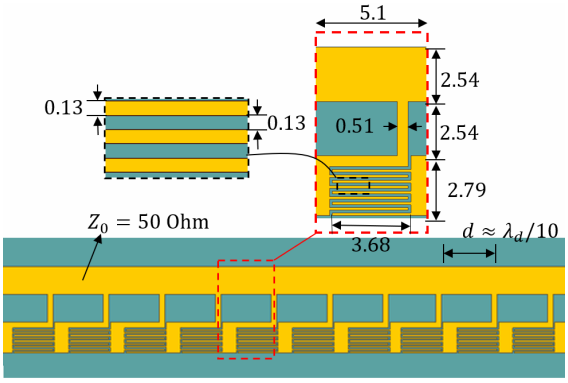

Figure 2.8: Microstrip implementation of two uniform CTLs over a grounded dielectric substrate, with circuit model as in Fig. 2.4a, i.e., with a distributed series capacitor (bottom line) that is here implemented by resorting to a periodic distribution of series inter-digital capacitors, with sub-wavelength period d. The bottom part of the figure shows the finite length CTLs, whereas the top part of the figure shows the unit cell with period d =5.1 mm. Dimensions are all in mm. This microstrip CTL implementation develops a fourth order EPD at $f = f_e = 5$GHz.

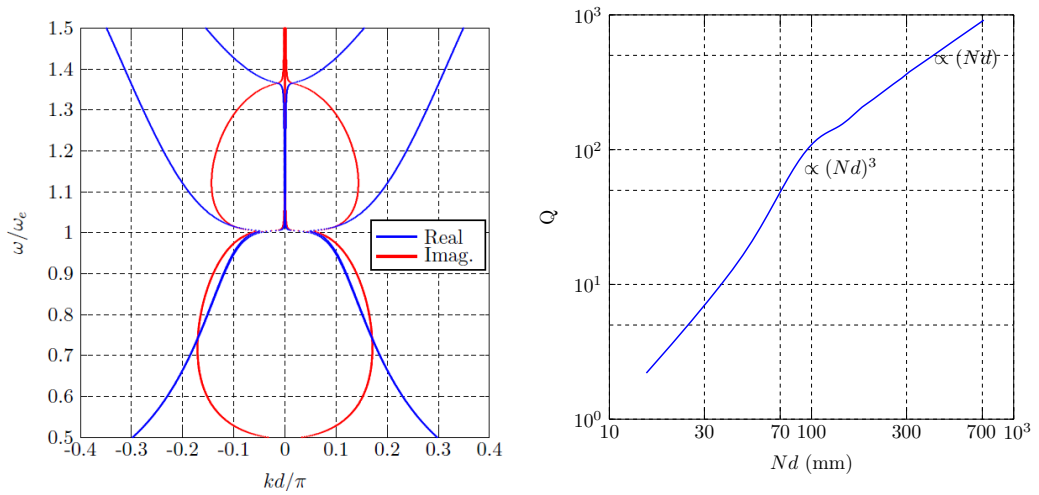

(a) (b)

Figure 2.9: Results relative to the microstrip implementation of the uniform CTLs using a periodic distribution of interdigital series capacitors in TL_2, with subwavelength period (Fig. 2.8). (a) Dispersion diagram obtained via full-wave simulation showing the complex modal wavenumbers versus frequency. The full-wave simulation reveals the existence of a DBE (a fourth order degeneracy) at $k = 0$. The simulation accounts for radiation, dielectric and copper losses. (b) Quality factor of the periodic CTLs versus resonant "cavity" length, showing its scaling with the number of unit cells N.

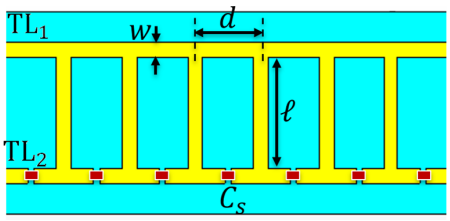

Figure 2.10: Microstrip implementation of a waveguide made of two coupled uniform TLs over a grounded dielectric substrate in Fig. 2.4a that exhibits DBE. TL_1 (when uncoupled from TL_2) supports propagation. Whereas TL_2(when uncoupled from TL_1) supports evanescent modes because it is loaded with distributed series capacitors mimicking a uniform series capacitive per-unit-length distribution. The capacitors in this structure are discrete components with value 3.1 pF. The inductive coupling between the two TLs is implemented using stubs connected between the transmission lines TL_1 and TL_2. The period is small compared to the guided wavelength.

2.5 Experimental Verification Using a CTL with Discrete Series capacitor

In this section we show an experimental verification of the existence of the DBE when and evanescent modes are coupled in the CTL. Figure 2.10 shows the microstrip implementation of the uniform CTL in Fig. 2.4a. The unit-cell is fabricated on a grounded dielectric substrate (Rogers substrate RT/duroid 5880) with a relative dielectric constant of 2.2, loss tangent of 0.001, and height of 0.79 mm. We use here discrete component capacitors to periodically load one TL to support evanescent modes. We use surface mount ceramic capacitors (manufactured by Murata Electronics, part number GJM1555C1H3R1BB01D) with capacitance of 3.1 pF and quality factor of $Q > 50$ for $f < 3$ GHz. All the TLs have width of $w = 2.4$ mm to have a characteristic impedance of 50 Ohm. The structure has period of $d = 10.5$ mm ($d \sim \lambda_d/10$) and stubs length $\ell = 19$ mm. As discussed in the previous section, the CTL can be seen as uniform, due to the subwavelength period.

To confirm the existence of EPDs in the periodic CTL, we analyze a unit-cell and perform scattering (S)-parameter measurements using a four-port Rohde & Schwarz vector network analyzer (VNA) ZVA 67. Figure 2.11a shows the fabricated unit-cell with 5 mm extension on

both sides to be able to solder the SMA connectors. The measured scattering matrix is then transformed into a 4×4 transfer matrix $\underline{\mathbf{T}}_A$. However this transfer matrix, of the microstip in Fig. 2.11a that includes extensions, is not the same as the transfer matrix of the one unit cell $\underline{\mathbf{T}}_U$, however it is a cascaded version of it. The total transfer matrix is $\underline{\mathbf{T}}_A = \underline{\mathbf{T}}_R\underline{\mathbf{T}}_U\underline{\mathbf{T}}_L$, where $\underline{\mathbf{T}}_R$ and $\underline{\mathbf{T}}_L$ account for the extra lengths constituting the extensions at both sides and the SMA connectors. In Fig. 2.11b we show the microstrip used in the two extensions, connected as a "through", for calibration purposes. The transfer matrix of the two connected extensions is $\underline{\mathbf{T}}_B = \underline{\mathbf{T}}_R\underline{\mathbf{T}}_L$. Now a matrix that is proportional to the unit-cell transfer matrix $\underline{\mathbf{T}}_U^{'}$ is obtained by de-embedding $\underline{\mathbf{T}}_B$ from $\underline{\mathbf{T}}_A$, i.e., $\underline{\mathbf{T}}_U^{'} = \underline{\mathbf{T}}_A\underline{\mathbf{T}}_B^{-1} = \underline{\mathbf{T}}_R\underline{\mathbf{T}}_U\underline{\mathbf{T}}_R^{-1}$. It is important to point out that although $\underline{\mathbf{T}}_U$ and $\underline{\mathbf{T}}_U^{'}$ are not identical but they share the same eigenvalues because $\underline{\mathbf{T}}_U^{'}$ is just a transformed version of $\underline{\mathbf{T}}_U$. An analogous procedure based on comparing transfer matrices of CTLs with 8 and 9 unit cells was adopted in [77]. Using Floquet theory, following [41], the dispersion relation of the four modes is obtained as $e^{jkd} = \text{eig}(\underline{\mathbf{T}}_U)$ (i.e., the four eigenvalues of $\underline{\mathbf{T}}_U$) and since $\underline{\mathbf{T}}_U$ and $\underline{\mathbf{T}}_U^{'}$ have identical eigenvalues, the dispersion is determined finally in the form of $e^{jkd} = \text{eig}(\underline{\mathbf{T}}_U^{'}) = \text{eig}(\underline{\mathbf{T}}_A\underline{\mathbf{T}}_B^{-1})$, where $\underline{\mathbf{T}}_A$ and $\underline{\mathbf{T}}_B$ are the transfer matrices for the two four-port microstips in Fig. 2.11a and Fig. 2.11b, respectively. The wavenumber dispersion diagram in Fig. 2.11c shows the four coalescing complex wavenumbers (only the real parts are shown for brevity, the imaginary parts is analogous to that in Fig. 2.5). In summary, the wavenumber dispersion diagram based on measurements is in good agreement with the results based on the S-parameters calculated via full-wave simulations based on the finite element method implemented in CST Studio Suite. The dispersion shows several frequencies at which EPD exists: a 4^{th} order EPD (the DBE) at f ≈1.85 GHz and two 2^{nd} order EPDs (the RBEs) at f ≈0.86 GHz. The perturbation due to ohmic, dielectric, and radiation losses seems negligible because it does not destroy the occurrence of the EPDs.

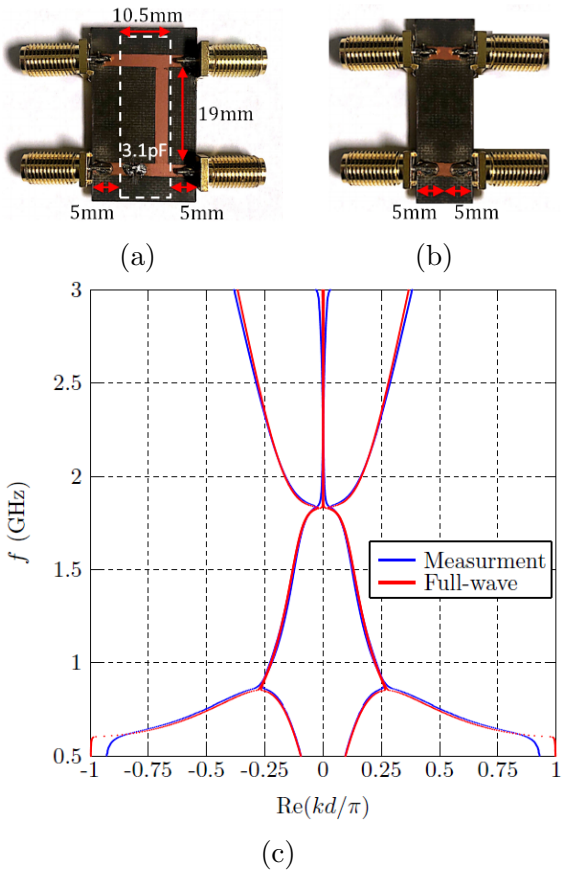

Figure 2.11: (a) Fabricated unit-cell for the CTL in Fig. 2.10 with 5mm extensions on both sides to be able to solder the SMA connectors. (b) Fabricated microstrip extensions used for calibration, i.e., to de-embed the effect of the extra extensions and SMA connectors from (a). (c) Wavenumber dispersion versus frequency showing the existence of the DBE around 1.85 GHz, and two 2^{nd} order EPDs (i.e., regular band edges) around 0.86 GHz. The measured result is in very good agreement with that from full-wave simulations.

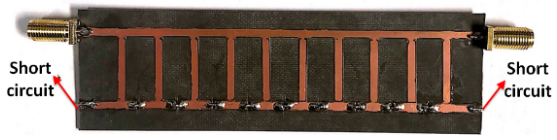

(a)

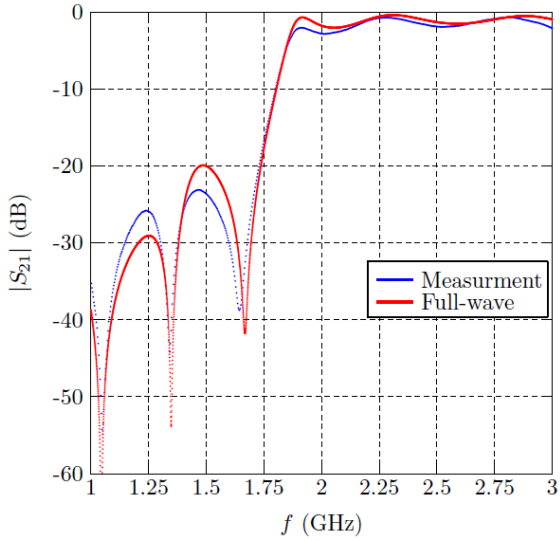

(b)

Figure 2.12: Measurements and simulations of the scattering parameter S_{21} for a nine-unit-cell CTL in (a). The result is consistent with the DBE observation in the dispersion diagram at f =1.85 GHz. The good agreement between full-wave simulations and measurements shows that there is a DBE resonance associated with the DBE.

Figure 2.11c shows a nine-unit-cell of the same DBE structure. The lower TL is connected to two short circuits, similarly to the setup shown in Fig. 2.6a. We show in Fig. 2.12b the measurement and full-wave simulation based on the finite element method, of the magnitude of the scattering parameter S_{21}. These results show good agreement between simulation and measurement. The results also demonstrate the occurrence of the DBE resonance at 1.9 GHz that is close to the DBE frequency of 1.85 GHz.

2.6 Conclusion

We have shown the general conditions demonstrating that a 4^{th} order EPD, namely a DBE, occurs at $k = 0$ in two *uniform* lossless and gainless CTLs when there is proper coupling between: (i) propagating modes and evanescent modes, (ii) forward and backward propagating modes, or (iii) four evanescent modes. We show that the resonance frequency of a cavity made of a finite-length CTLs exhibiting a DBE is very close to the DBE frequency, moreover, we show that the quality factor increases with the fifth power of the cavity length (in the lossless case) and such trend is robust to the occurrence of series losses. Furthermore, we have shown that by using the CTL concept, a *regular band edge* can be designed at non-vanishing wavenumbers. An example of CTLs supporting the EPD wave phenomena discussed in this chapter has been presented using a metamaterial-based CTLs where the period to realize series capacitances is sub-wavelength. We have provided the experimental demonstration of the occurrence of the DBE in two uniform CTLs using a metamaterial-like periodic CTL with subwavelength period, implemented in microstrips. Possible applications exploiting the physics of the DBE and the RBE are in high quality factor cavities [62], radio frequency oscillators [1] and distributed oscillators [2], leaky wave antennas [57], filters, pulse compression [8], sensors, high power electron-beam devices [5], and lasers [11].

Chapter 3

Exceptional Points of Degeneracy with Indirect Bandgap Induced By Mixing Forward and Backward Propagating Waves

In this chapter we demonstrate that exceptional points of degeneracy (EPDs) are obtained in two coupled waveguides without resorting to gain and loss [78]. We show the general concept that modes resulting from a proper coupling of forward and backward waves exhibit EPDs of order two and that there the group velocity vanishes [78]. We verify our insight by using coupled mode theory and also by fullwave numerical simulations of light in a dielectric slab coupled to a grating, when one supports a forward wave whereas the other (the grating) supports a backward wave [78]. We also demonstrate how to realize a photonic indirect bandgap in guiding systems supporting a backward and a forward wave, show its relations to the occurrence of EPDs, and offer a design procedure.

3.1 Motivation and State of the Art

An EPD is a point in the parameter space of a system at which the system's eigenvalues and eigenvectors coalesce [12, 13, 14, 15]. The term exceptional point (EP) and the associated perturbation theory where discussed in the well known Kato's book in 1966 [15]. The phenomenon of degeneracy of both eigenvalues and eigenvectors (polarization states), studied here, is a stronger degeneracy compared to the traditional degeneracy of only two eigenvalues.

Non-Hermitian Hamiltonian can possess entirely real spectra when the system obeys parity-time (PT) symmetry condition [17]. A system is said to be PT symmetric if the PT operator commutes with the Hamiltonian [18, 19], where PT operator applies a parity reflection and time reversal [17]. When the time reversal operator is applied to physical systems, energy changes from damping to growing and vice versa [20]. Based on this simple concept, two symmetrical coupled waveguides with balanced gain and loss satisfy PT symmetry [21, 22, 23], where the individual application of each of the space or time reversal would swap the gain and loss, therefore the simultaneous application of space and time reversal operator to the system would end up with the same system. The point separating the complex and real spectra regimes of PT-symmetric Hamiltonians has been called exceptional point (EP) [15], also known as transition point. Here, beside the mathematical aspects, we stress the role of degeneracy, as implied also in [16], hence include the 'D' in the EPD acronym.

In this chapter, we present a class of two coupled waveguides where EPDs exist without resorting to the presence of gain and loss. By using coupled mode theory [79, 80], we show that two coupled waveguides, where one waveguide supports forward propagation (i.e., where the phase and power propagate in the same direction) whereas the other one supports backward propagation (i.e., where the phase and power propagate in opposite direction), experience a phase transition as in the PT-symmetric case. We show the general conditions

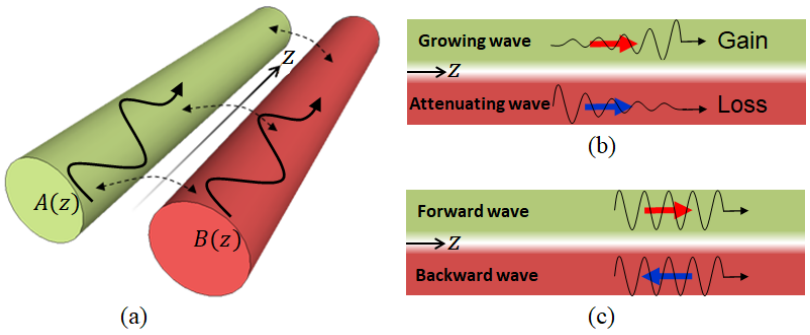

Figure 3.1: (a) Coupling between two electromagnetic waves whose complex amplitudes are A and B. Conditions that lead to EPDs are obtained by introducing proper coupling between: (b) two waveguides with PT symmetry where the two media have gain and loss supporting exponentially growing and attenuating waves; (c) two waveguides with forward and backward propagating waves, without resorting to PT symmetry (i.e., in this case the waveguides do not have gain and loss). The waves with black arrows represent the directions of propagation. The blue and red arrows represent the directions of power flow.

for modes resulting from coupling two coupled waves to exhibit an EPD looking at both the degenerate eigenvalues and eigenvectors. We show that the coupling of two waves, that carry power in opposite directions, leads to an EPD and we explain how this results in the vanishing of the group velocity of the degenerate mode. We illustrate the concepts in a simple system made of two coupled waveguides, i.e., a dielectric slab coupled to a grating, when one supports a forward wave whereas the other (the grating) supports a backward wave. Other general conditions that lead to exceptional degeneracies of two modes in uniform waveguide were studied in [49] using a transmission line approach. Finally, we relate the occurrence of EPDs to the presence of a photonic indirect bandgap.

3.2 Second Order EPD by Mixing Two Waves

We consider two coupled electromagnetic waves as shown in Fig. 3.1a. These two waves are described by the complex time-domain notation

$$
\begin{aligned}
a(\mathbf{r},t) &= A(z) f_a(\boldsymbol{\rho}) e^{i\omega t}, \\
b(\mathbf{r},t) &= B(z) f_b(\boldsymbol{\rho}) e^{i\omega t},
\end{aligned}
\tag{3.1}
$$

where $A(z)$ and $B(z)$ are the complex amplitudes of waves along the z direction, $\mathbf{r} = \boldsymbol{\rho} + z\hat{\mathbf{z}}$, and $\boldsymbol{\rho}$ is the transverse coordinate. $f_a(\boldsymbol{\rho})$ and $f_b(\boldsymbol{\rho})$ are the normalized modal field profile in the transverse direction for each mode. When the two waves are uncoupled, i..e., when their waveguides are far from from each other, the evolution of the amplitudes along the z direction is simply descried by $dA(z)/dz = -i\beta'_a A(z)$ and $dB(z)/dz = -i\beta'_b B(z)$, where β'_a and β'_b are the uncoupled propagation constants of each wave (that is also an eigenmode of the structure since there is no coupling). The solutions are $A(z) = A_0 \exp(-i\beta'_a z)$ and $B(z) = B_0 \exp(-i\beta'_a z)$. The power carried by each wave in the positive z direction is given by $p_a(z) = \pm|A(z)|^2$ and $p_b(z) = \pm|B(z)|^2$ where the sign depends on the type of the wave. The sign is positive when the wave is forward, i.e., when the power is carried in the same direction of wave propagation (i.e., when the phase and group velocity have the same directions). The sign is negative when the waves backward, i.e., when the phase propagates along the positive z direction whereas the power flows in the negative z direction (i.e., when the phase and group velocity have the opposite directions).

When coupling is introduced to those two waves, the system eigenmode is found by solving the spatial-evolution equation that, based on coupled mode theory [79, 80], is given by

$$
\frac{d}{dz}\begin{pmatrix} A(z) \\ B(z) \end{pmatrix} = -i \begin{pmatrix} \beta_a & \kappa_{ab} \\ \kappa_{ba} & \beta_b \end{pmatrix} \begin{pmatrix} A(z) \\ B(z) \end{pmatrix},
\tag{3.2}
$$

where β_a and β_b are "perturbed" propagation constants for the coupled system, and κ_{ab} and κ_{ba} are the coupling coefficients between the two modes. The relation between κ_{ab} and κ_{ba}

is determined by applying the power conservation principle. The total power carried in the coupled structure is $p_t(z) = |A(z)|^2 \pm |B(z)|^2$ assuming wave A is forward wave, and wave B to be either forward or backward, when taking the $+$ or the $-$ sign, respectively. Thus, there are two possible scenarios: (i) "codirectional coupling" when both waves carry power at the same direction and (ii) "contradirectional coupling" when the two waves carry power in the opposite direction [79].

When the system does not have gain and loss, conservation of energy states that $dp_t(z)/dz = 0$, and by using (3.2), one finds that the constraint $\mathrm{Re}\left(AB^*\left(\kappa_{ba} \mp \kappa_{ab}^*\right)\right) = 0$ should be satisfied. Therefore, we have $\kappa_{ab} = \kappa_{ba}^*$ in case of codirectional coupling where the two waves are forward, and $\kappa_{ab} = -\kappa_{ba}^*$ in case of contradirectional coupling where one wave is a forward and the other one is backward [79].

The mixing of the two waves constitutes what is called the guiding system's eigenmode (some call it "supermode") which is a weighted sum of the individual guided waves. The eigenmode propagation constant is determined by solving the characteristic equation of the coupled system in (3.2) assuming the wave amplitudes to be in the form of $[A(z), B(z)]^T \propto e^{-ikz}$ which yields $k^2 - k(\beta_a + \beta_b) + (\beta_a\beta_b - \kappa_{ab}\kappa_{ba}) = 0$. The characteristic equation has two solutions that are given by

$$k_n = \frac{\beta_a + \beta_b}{2} + (-1)^n \sqrt{\left(\frac{\beta_a - \beta_b}{2}\right)^2 - (-1)^p \kappa^2}, \tag{3.3}$$

where $\kappa = |\kappa_{ab}|$ and the indices $n = 1, 2$ denote the two modes of the coupled system. Furthermore, $p = 1$ and $p = 2$ represent the case of codirectional and contradirectional coupling, respectively. An EPD occurs when two eigenmodes coalesce, i.e., $k_1 = k_2 = k_e$, with $k_e = (\beta_a + \beta_b)/2$. This EPD occurs when $\beta_a - \beta_b = 2\sqrt{(-1)^p \kappa^2}$. At an EPD, the eigenvectors must coalesce, and in this simple system their coalescence follows from the coalescence of the

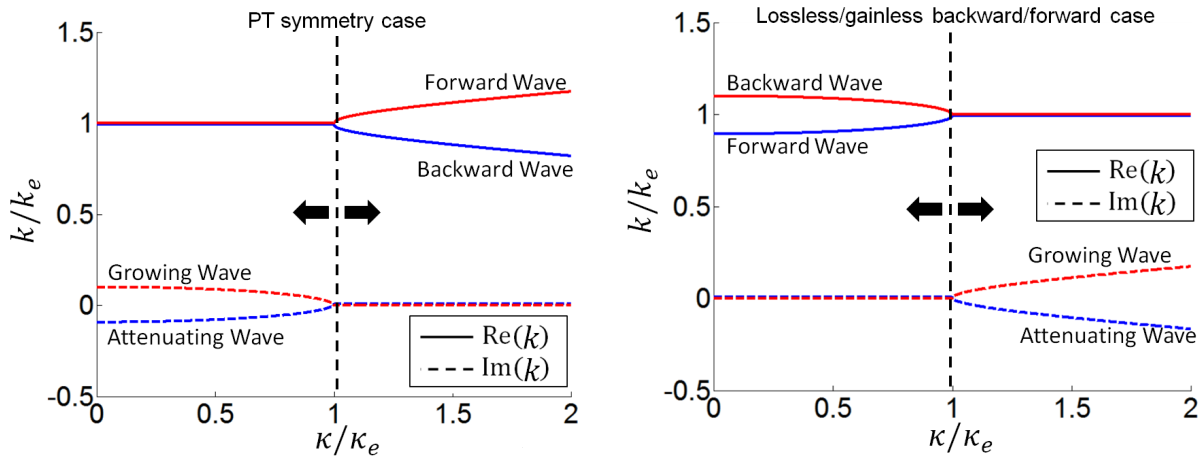

(a) (b)

Figure 3.2: The two wavenumbers of the guiding system versus the coupling parameter κ, showing the existence of an EPD. Two cases are examined: (a) coalescence of modes in PT-symmetrical waveguides, (b) coalescence of modes obtained by coupling a forward wave (phase and group velocities have the same direction) and a backward wave (phase and group velocities have opposite directions). Both cases exhibit an EPD, represented by the bifurcation point.

eigenvalues. Indeed, the two eigenvectors are $\left[\begin{array}{cc} A_n, & B_n \end{array}\right]^T = \left[\begin{array}{cc} 1, & (k_n - \beta_a)/\kappa_{ab} \end{array}\right]^T$ and it is easy to see that they coalesce when $k_1 = k_2$.

The group velocity of the eigenmode with wavenumber k_n is determined as (assuming k_n to be purely real)

$$v_{g,n} = \frac{1}{d_\omega k_n} = \frac{k_n - k_e}{2k_n d_\omega \left(\beta_a + \beta_b\right) + 2d_\omega \left(\beta_a \beta_b + (-1)^p \kappa^2\right)}. \tag{3.4}$$

where $d_\omega \equiv d/d\omega$ denotes the derivative with respect to angular frequency ω. It is clear from the expression that $v_{g,1,2} = 0$ when $k_1 = k_2 = k_e$,i.e., exactly at the EPD. Next, we also show what happens near the EPD.

3.2.1 Codirectional Coupling

For the case of codirectional coupling, $p = 1$, the EPD condition is simplified to $\beta_a - \beta_b = \pm 2i\kappa$. The EPD condition puts a constraint that the difference between the propagation constants of the uncoupled waves has to be purely imaginary in order to exhibit an EPD. Thus, we conclude that the EPD can never be obtained for any value of the coupling parameter κ in the case of a lossless/gainless system. If we resort to a PT symmetry, as in Fig. 3.1b, where the system has balanced gain and loss, we have $\beta_a = \beta_0 + i\alpha$ and $\beta_b = \beta_0 - i\alpha$, and an EPD is obtained when $\alpha = \kappa$ [21, 22, 23, 81, 57], and the degenerate wavenumber is $k_e = \beta_0$.

For this case, the two propagation constants of the coupled system in the vicinity of the EPD are $k_{1,2} = \beta_0 \pm \sqrt{\kappa^2 - \alpha^2}$ and their derivatives are $d_\omega k_{1,2} = d_\omega \beta_0 \pm (2\kappa d_\omega \kappa - 2\alpha d_\omega \alpha) / (k_2 - k_1)$. This is also illustrated by determining the eigenvector of the degenerate eigenmode from (3.2) (for codirectional coupling case where $p = 1$) as

$$\begin{pmatrix} A_e(z) \\ B_e(z) \end{pmatrix} = \begin{pmatrix} 1 \\ -ie^{-i\arg(\kappa_{ab})} \end{pmatrix} e^{-ik_e z}, \tag{3.5}$$

and one finds that the total power carried by the degenerate eigenmode is $p_t(z) = |A_e(z)|^2 - |B_e(z)|^2 = 0$ vanishes, in agreement with the vanishing of the group velocity. In the vicinity of an EPD we have $k_1 \approx k_2$ and by neglecting the $d_\omega \beta_0$, usually smaller than the other term, the group velocities of the two modes are $v_{g,1,2} \approx \pm (k_2 - k_1) / (2\kappa d_\omega \kappa - 2\alpha d_\omega \alpha)$ when $\kappa > \kappa_e$, i.e., where the two eigenmodes are propagating with purely real wavenumbers. Therefore we conclude that near an EPD in a PT-symmetric guiding system, the two modes of the coupled system are phase-synchronized ($k_1 \approx k_2$), i.e., with almost identical phase velocity, but have opposite group velocity ($v_{g,1} \approx -v_{g,2}$), which eventually results on having

a wave in the guiding structure with vanishing group velocity when the system is exactly at the EPD. As an example, for a system with PT symmetry where the uncoupled waveguides have, respectively, a growing wave with $\beta_a = 100 + 10i$ (1/m) and an attenuating wave with $\beta_b = 100 - 10i$ (1/m), an EPD is obtained when the coupling parameter is $\kappa = 10$ 1/m as shown in Fig. 3.2a.

3.2.2 Contradirectional Coupling

We consider coupling between forward wave with wavenumber $\beta_a > 0$ and $v_{g,a} > 0$ ($v_{g,a} = d_\omega \beta_a$) and backward wave with wavenumber $\beta_b > 0$ and $v_{g,b} < 0$ ($v_{g,b} = d_\omega \beta_b$). The two propagating waves carry power in opposite directions and therefore they exhibit contradirectional coupling, we use $p = 2$ in Eq. (3.3). The EPD condition ($k_1 = k_2$) for this case is simplified to $\beta_a - \beta_b = \pm 2\kappa$, which means that the difference between the propagation constants should be purely real to have an EPD, which is possible for a lossless/gainless system. Therefore, the EPD condition for this case is satisfied through the proper design of the coupling parameters, i.e, when $\kappa = |\beta_a - \beta_b| / 2$ (we recall that κ was defined as purely real positive). This means that there are two possible EPD conditions, $\beta_a - \beta_b = 2\kappa$ and $\beta_a - \beta_b = -2\kappa$, that may both occur when varying frequency. At those two frequencies one has $\beta_a > \beta_b$ and $\beta_b > \beta_a$, respectively. A more detailed discussion is provided later on when discussing the indirect bandgap.

In the *vicinity* of an EPD, the two propagation constants of the coupled system are given by Eq. (3.3), and the derivatives of the two wavenumbers with respect to the angular frequency are

$$d_\omega k_{1,2} = \frac{1}{2} d_\omega \left(\beta_a + \beta_b\right) \pm \frac{1}{2} \frac{\left(\beta_a - \beta_b\right) d_\omega \left(\beta_a - \beta_b\right) - 2\kappa d_\omega \kappa}{\left(k_2 - k_1\right)}. \tag{3.6}$$

When $\kappa < \kappa_e$, i.e., where the two eigenmodes are propagating with purely real wavenumbers, in the vicinity of an EPD we have $k_1 \approx k_2$ and by neglecting the term $d_\omega (\beta_a + \beta_b)$ with respect to the second one, the group velocities of the two modes are

$$v_{g,1,2} \approx \pm \frac{k_2 - k_1}{\frac{1}{2}(\beta_a - \beta_b)\left(v_{g,a}^{-1} - v_{g,b}^{-1}\right) - 2\kappa d_\omega \kappa}. \tag{3.7}$$

Therefore, we conclude that near an EPD, the coupled forward and backward waves are synchronized in phase, i.e., $k_1 \approx k_2$ but have nearly opposite group velocity ($v_{g,1} \approx -v_{g,2}$), which eventually results in having a wave in the guiding structure with vanishing group velocity when the system is exactly at an EPD.

This is also illustrated by determining the eigenvector of the degenerate eigenmode from (3.2) (for contradirectional coupling case where $p = 2$) as

$$\begin{pmatrix} A_e(z) \\ B_e(z) \end{pmatrix} = \begin{pmatrix} 1 \\ -e^{-i\arg(\kappa_{ab})} \end{pmatrix} e^{-ik_e z}, \tag{3.8}$$

and one finds that the total power carried by the degenerate eigenmode is $P_t(z) = |A_e(z)|^2 - |B_e(z)|^2 = 0$ vanishes, in agreement with the vanishing of the group velocity. At the EPD, the system matrix is not diagonalizable but rather similar to a 2×2 Jordan matrix. The fields in the two-waveguide system is represented using the degenerate and generalized eigenvectors as

$$\begin{pmatrix} A(z) \\ B(z) \end{pmatrix} = \begin{pmatrix} 1 \\ -e^{-i\arg(\kappa_{ab})} \end{pmatrix} (u_1 - jzu_2)\, e^{-ik_e z} + \begin{pmatrix} 1 \\ ie^{-i\arg(\kappa_{ab})}/\kappa_e \end{pmatrix} u_2 e^{-ik_e z}. \quad (3.9)$$

where u_1 and u_2 are proper coefficients that depend on the system excitation and boundary conditions.

The two waveguides with contradirectional coupling are schematically shown in Fig. 3.1c and the dispersion diagram is in Fig. 3.2 where we see a forward wave with $\beta_a = 110$ (1/m) and backward wave with $\beta_b = 90$ (1/m), and the EPD is obtained at $k = k_e = 100$ (1/m) , where $\kappa_e = 10$ (1/m) as shown in Fig. 3.2b.

The contradirectional coupling case can be realized is in two possible scenarios: (i) two modes exist in two separate waveguides where the first waveguide supports a forward wave and the second waveguide supports a backward wave and the coupling is introduced by bringing them near each other; (ii) two modes exist in the same waveguide having periodicity where the one wave (e.g., the forward) has the fundamental Floquet harmonic equal to $\beta_1 = \beta_0$ and the other wave (e.g., the backward) has its 1st harmonic Floquet harmonic equal to $\beta_2 = -\beta_0 + 2\pi/d$, where d is the waveguide period, and the EPD is only possible at the band edge $\beta_0 = \pi/d$. An example belonging to the first scenario, where the EPD is found in two coupled dielectric slab waveguides, is shown later on. The second scenario instead exists in conventional periodic waveguides and it is not further considered in this chapter.

We present an example of a guiding system that supports two waves carrying power in opposite directions and we show that it exhibits two EPDs. Consider the guiding system made of a Si substrate (supporting the forward wave) coupled to a Si grating waveguide as shown in Fig. 3.3a, with dimensions $w = p = h = 70$ nm and $d = 140$ nm. Silicon is modeled with a refractive index $n_{\mathrm{Si}} = 3.45$. We first show in Fig. 3.3b the dispersion of the two

wavenumbers β'_a and β'_b of the two uncoupled waveguides ($s \to \infty$) as red dashed (uniform waveguide) and blue dashed (grating waveguide). The figure shows that the structures support a forward wave where the group velocity is positive $v'_{g,a} = 1/(d_\omega \beta'_a) > 0$ and a backward wave where the group velocity is negative $v'_{g,b} = 1/(d_\omega \beta'_b) < 0$. In the same Figure 3.3b, we show the dispersion of the two wavenumbers k_1 and k_2 of the coupled guiding system, i.e., when the two waveguide are close to each other with a gap of $s = 70$ nm. The dispersion show the existence of two EPDs associated to a wavenumber (momentum) displacement. The dispersion diagrams we show are for modes with electric field polarized in the y direction. The dispersion diagrams have been found by using the finite element method-based eigenmode solver implemented in CST Studio Suite, by numerically simulating only one unit cell of the structure. The proposed condition allows to locate the EPDs at band edges that are not necessarily at the center or at the edge of a Brillioum zone, without using loss and gain. It also shows the capability to engineer an indirect bandgap in these simple structures.

3.3 Indirect Bandgap in the Contradirectional case

In the contradirectional case where coupling occurs between a forward and backward wave, as in Fig. 3.1c, an indirect bandgap is possible and we show here how it is formed. Since in this case one wave is forward and one is backward, the uncoupled propagation constants β'_a and β'_b have opposite slopes as schematically shown in Fig. 3.4 (see also dashed blue and red curves in Fig. 3.3b), and an analogous trend is expected for the parameters β_a and β_b of the coupled system. By looking at the dispersion diagram shown in Fig. 3.4, the red-dashed curve is the forward wave with wavenumber $\beta'_a(\omega)$ and the blue-dashed curve is the backward wave with wavenumber $\beta'_b(\omega)$. Assuming that the coupling it not so strong, one

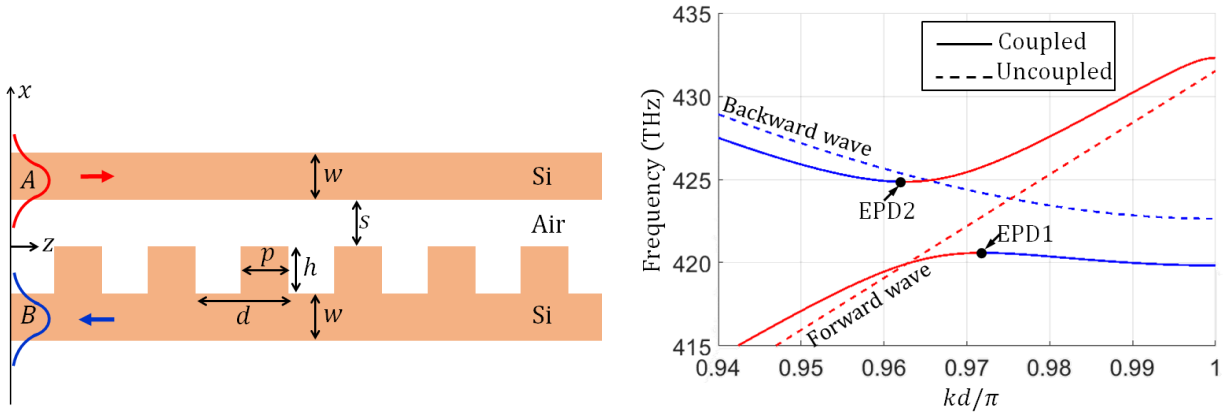

(a) (b)

Figure 3.3: Example of modal EPD of order 2 between a forward wave (phase and group velocities have the same direction) and backward wave (phase and group velocities have opposite directions). (a) Two coupled Si layers where the top one supports a forward wave (in red) while the bottom one is periodically corrugated to support a backward wave (positive phase velocity and negative group velocity, in blue). The red and blue arrows represent the direction of power flow. (b) Dispersion relation showing the propagating eigenmodes when the two waveguides are uncoupled (dashed) and when the are coupled (solid). The dispersion of modes in the coupled waveguides show the existence of two EPDs. The blue and red colors of the curves are related to the power flow directions. Note also that because two EPDs are found, an indirect bandgap is present between the upper and lower branches that can be designed ad-hoc. In the shown case we have $\Delta k_e \equiv k_{e2} - k_{e1} < 0$.

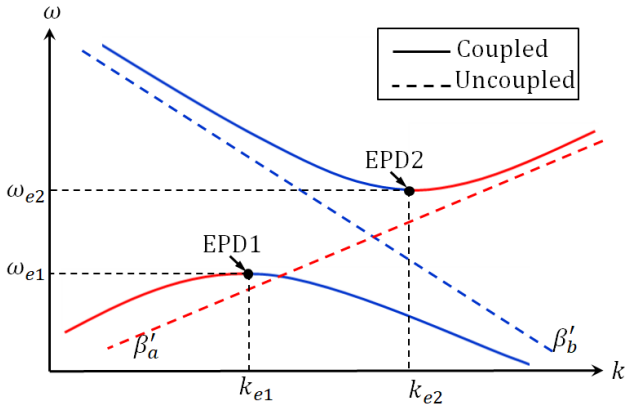

Figure 3.4: Schematic of a dispersion diagram showing the indirect bandgap that results from two EPDs based on contradirectional coupling. The red-dashed line represents the wavenumber of the forward wave β'_a whereas the blue-dashed line the one of the backward wave β'_b, when the waveguides are uncoupled. The coupling yields the two curves with two EPDs that are labeled as EPD1 and EPD2. The indirect bandgap width is $\Delta\omega_{IB}$. In the shown case $\Delta k_e \equiv k_{e2} - k_{e1} > 0$.

may assume that $\beta_a(\omega) \approx \beta_a'(\omega)$ and $\beta_b(\omega) \approx \beta_b'(\omega)$, at least in trend, hence, in slope. The forward wave has positive slope, $v_{g,a} = d\omega/d\beta_a > 0$, whereas the backward wave has negative slope $v_{g,b} = d\omega/d\beta_b < 0$, and the dispersion curves for β_a and β_b versus frequency should intersect at some frequency ($\beta_a = \beta_b$) because one wavenumber is increasing with frequency whereas the other is decreasing with frequency; an example with a grating is illustrated in Fig. 3.3b while a schematic is in Fig. 3.4. Let us approximate the dispersion curves locally, in the frequency range of interest, as straight lines, i.e., $\beta_a(\omega) \approx a + v_{g,a}^{-1}\omega$ and $\beta_b(\omega) \approx b + v_{g,b}^{-1}\omega$, where now $v_{g,a}$ and $v_{g,b}$ are assumed to have the local fixed value. Furthermore, assuming, for simplicity, that κ is constant within the frequency range of interest, one finds that EPDs occurs at two angular frequencies ω_{e1} and ω_{e2} such that $\beta_a(\omega_{e1}) - \beta_b(\omega_{e1}) = -2\kappa$ and $\beta_a(\omega_{e2}) - \beta_b(\omega_{e2}) = 2\kappa$, where $\omega_{e1} < \omega_{e2}$. Subtracting the previous two conditions leads to the indirect bandgap determination

$$\Delta\omega_{IB} \equiv \omega_{e2} - \omega_{e1} \approx \frac{4\kappa}{v_{g,a}^{-1} - v_{g,b}^{-1}}. \tag{3.10}$$

Note that $v_{g,a}^{-1} - v_{g,b}^{-1} > 0$, hence $\Delta\omega_{IB} > 0$. The bandgap width can be controlled by the slope of the two parameters β_a and β_b; indeed, when $v_{g,a}^{-1} \approx -v_{g,b}^{-1}$, the denominator of (3.10) is small and the bandgap is very wide, viceversa, the bandgap is narrow when $v_{g,a}^{-1}$ is very different from $-v_{g,b}^{-1}$. If we consider the dispersion of the coupling term κ, a more complicated picture may arise that could be determined by the reasoning just provided.

The degenerate wavenumbers at the two EPDs are $k_{e,1} = (\beta_a(\omega_{e1}) + \beta_b(\omega_{e1}))/2$ and $k_{e,2} = (\beta_a(\omega_{e2}) + \beta_b(\omega_{e2}))/2$. Using the linear approximation formulas for the wavenumbers $\beta_a(\omega)$ and $\beta_a(\omega)$, one finds that $k_{e1} \approx [a+b+\left(v_{g,a}^{-1} + v_{g,b}^{-1}\right)\omega_{e1}]/2$ and $k_{e2} \approx [a+b+\left(v_{g,a}^{-1} + v_{g,b}^{-1}\right)\omega_{e2}]/2$. The difference between the two degenerate wavenumbers is

$$\Delta k_e \equiv k_{e2} - k_{e1} \approx \frac{v_{g,a}^{-1} + v_{g,b}^{-1}}{2} \Delta\omega_{IB}. \tag{3.11}$$

Therefore, it is necessary that $v_{g,a}^{-1} + v_{g,b}^{-1} \neq 0$ in order to have indirect bandgap. When $|v_{g,a}^{-1}| > |v_{g,b}^{-1}|$ we get $k_{e2} > k_{e1}$,hence $\Delta k_e > 0$, i.e., the EPD that occurs at the smaller frequency ω_{e1} occurs also at the smaller degenerate wavenumber k_{e1} and this condition is depicted in Fig. 3.4. When $|v_{g,a}^{-1}| < |v_{g,b}^{-1}|$, we get $k_{e1} > k_{e2}$, hence $\Delta k_e < 0$, i.e., the EPD that occurs at the smaller frequency ω_{e1} occurs at larger degenerate wavenumber k_{e1} and this condition is depicted in Fig. 3.3b. Indeed, by looking at Fig. 3.3b, one finds by naked eye that $|v_{g,a}| > |v_{g,b}|$, (absolute change with frequency of dashed red curve is higher than the one of the dashed blue one), therefore $|v_{g,a}^{-1}| < |v_{g,b}^{-1}|$ resulting in $k_{e1} > k_{e2}$ according to (3.11) and the EPD at lower frequency, around 420 THz, occurs at higher degenerate wavenumber of $k_{e1} = 0.972\,\pi/d$.

3.4 Conclusion

We have demonstrated that EPDs are not only obtained in PT-symmetric waveguides but they are also obtained in two lossless and gainless waveguides when they support forward and backward waves that are properly coupled. We have shown a simple system that supports this condition made of a grating coupled to a dielectric layer. We have elaborated that the scheme discussed here exhibits a photonic indirect bandgap that can be controlled by changing the group velocities of the forward and backward modes along with the coupling coefficient. Two conditions may occur: the bandgap is associated either to a positive or negative momentum difference between the two energy levels. The finding in this chapter can be useful to design systems with EPDs whose use is of growing importance for enhancing light-matter interactions and nonlinear photonic phenomena.

Chapter 4

The Role of Parity Symmetry in the Occurrence of Exceptional Points of Degeneracy in Electromagnetic Waveguide

We show the relation between parity (P), i.e., mirror, and parity-time (PT) symmetries in periodic coupled waveguides and the possible occurrence of various orders of exceptional points of degeneracy (EPDs). We first consider the role of P symmetry on EPDs in waveguides that are lossless and gainless, like the stationary inflection point (SIP), degenerate band edge (DBE), and the sixth order EPD (6DBE), of respective degeneracy order of 3, 4 and 6. We use equivalent multi transmission line to model the periodic waveguides' electromagnetic modes. The following conclusions are derived analytically and numerically for waveguides that support N modes in each direction (i.e., $2N$ modes in total). In the case of even N, a periodic waveguide with P symmetry may exhibit EPDs of maximum order N. Hence, to obtain a full-order degeneracy (i.e., EPD of order $2N$) P symmetry must be

broken. Whereas for odd N, a periodic waveguide with P symmetry may exhibit EPDs of maximum order $N+1$ and an EPD of order N is not possible. We also demonstrate that PT symmetry (in contrast to P symmetry alone) does not prohibit the occurrence of a full order degeneracy in a system made of two coupled waveguides. We present two examples of coupled microstrip transmission lines. The first one is composed of two coupled microstrip TLs and we show that the occurrence of 4th order EPD (DBE) is only possible when the P symmetry is broken or when PT symmetry is introduced. The second example is composed of three coupled microstrip TLs and we show that by breaking P symmetry we enable the occurrence of EPDs as the SIP, which is an EPD of order three, and the 6DBE, which is an EPD of order six.

4.1 Motivation and State of the Art

Exceptional points of degeneracy (EPDs) are points in a system's parameters space where two or more eigenmodes coalesce into a single eigenmode [12, 13, 14, 15] (note that the term exceptional point (EP) was already used in Kato's book in 1966 [15]). Since the main physical feature of this phenomenon is the strong degeneracy of at least two eigenmodes [16], the letter "D" is added to EP, to form EPD. The dispersion relation of electromagnetic eigenmodes in a waveguide that exhibits an EPD with order m, where m is the number of coalescing eigenmodes, has the behavior of $(\omega - \omega_e) \propto (k - k_e)^m$ in the vicinity of an EPD (ω_e, k_e) [42, 43, 44] (in those papers, the term EPD was not used, but the concept and the mathematics of an EPD was fully developed for guided waves). Here, ω and k are the angular frequency and the wavenumber, respectively, and the EPD is denoted by the subscript e. Such dispersion behavior is accompanied by a severe reduction in group velocity of the waves propagating in those structures resulting in a giant increase in the loaded quality factor and the local density of states which is beneficial for various applications.

One of the simplest second-order EPDs is found in uniform (i.e., longitudinally invariant) waveguides at the modal cutoff frequency [34]. Second-order EPDs in the form of band edges also occur in lossless periodic waveguides and photonic crystals [35, 36, 37]. EPDs also occur in coupled waveguides by introducing parity-time (PT) symmetry [22, 38, 23, 39, 40, 41, 82] which implies using a balanced and symmetrical distribution of gain and loss. The occurrence of EPDs in coupled waveguides does not necessarily require a system to exactly satisfy the PT symmetry condition or to simultaneously have gain and loss in general [40, 41]. Furthermore, EPDs may occur in coupled waveguides that are lossless and gainless. For instance, different orders of EPD, especially the degenerate band edge (DBE) which is an EPD of order four in a lossless guiding medium, have been engineered in various types of periodic guiding structures in [42, 43, 44, 36, 45, 46, 47, 48, 41, 49]. Pioneering work on EPDs of order two, three, and four, namely the regular band edge, the stationary inflection point (SIP), and the DBE, respectively, have been presented in [35, 42, 43, 44, 50, 36, 51, 52]. The existence of SIP has been theoretically shown in microwave waveguides [53, 54, 55] and optical waveguides [47, 56, 6]. An experimental demonstration of the existence of the SIP (also called "frozen mode") at microwave frequencies, in reciprocal microstrip waveguides, has been provided in [55]. Experimental demonstrations of the existence of the DBE at microwave frequencies has been provided in both circular metallic waveguides with periodic loading [48] and in microstrip technology [41, 49]. The concepts we present in this chapter can be very beneficial to implement EPDs in realistic waveguides, conventionally used at microwave frequencies.

Applications of the SIP and DBE have been proposed in the area of solid state oscillators [1, 2, 3], oscillators and amplifiers using electron beam devices [4, 5], delay lines [6], small antennas [7], pulse generators and compressors[8], high-Q resonators, sensors , and lasers [9, 10, 11].

Symmetry in periodic waveguides plays an important role in the kind of modes that are

allowed to exist, and in the maximum order of EPD that can be obtained. In this chapter, we use theory and numerical examples to study how parity (P) symmetry in coupled waveguides determines the maximum orders of the EPDs that may occur. We show analytically that P symmetry, also called mirror symmetry, in waveguides, limits the maximum obtainable order of EPD. In contrast, we show that when adding time symmetry, i.e., using PT symmetry, in waveguides with loss and gain, the occurrence of full-order degeneracy is not prohibited. We use a transfer matrix formulation and we determine the properties that such matrices shall have to have full-order degeneracy. Some numerical examples involving microstrip lines are presented to verify the necessity for breaking P symmetry in order to achieve some EPD orders such as full order degeneracy. For CTLs with $N = 3$, we show that SIP and the sixth order DBE (6DBE), a full-order degeneracy, are both possible for the cases where P symmetry is broken.

4.2 Parity (Mirror) Symmetry

We consider a waveguide made of N periodically-coupled transmission lines (CTLs), e.g., microstrip lines. The presented concepts are general and they apply to multimode waveguides with or without P symmetry that are represented in terms of multi-transmission lines. In the following, the term transmission line (TL) refers either to the equivalent modeling or to real waveguide structures that are analogous to transmission line (like microstrip lines).

We investigate two cases, when N is even, as shown in Fig. 4.1 and when N is odd, as shown in Fig. 4.2. The type of symmetry is determined by the operator under which the fields are invariant. The transverse P reflection (also called reflection or mirror) operator acting on the fields is defined as

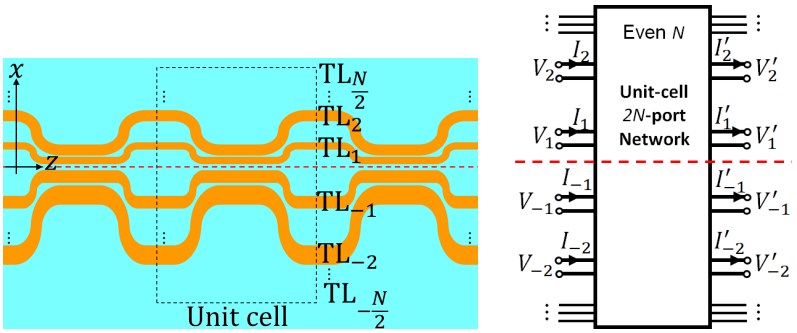

(a) (b)

Figure 4.1: (a) Periodic N coupled TLs consisting of coupled and uncoupled sections, where N is even. The structure consists of $N/2$ TLs that exist at $x < 0$ and other $N/2$ TLs that exist at $x > 0$. A multi TL structure has P symmetry when the TLs that exist at $x < 0$ and the ones that exist at $x > 0$ are mirrored to each other. (b) A $2N$-port circuit network model for a unit-cell of the structure in (a).

$$P : (x, z) \rightarrow (-x, z). \tag{4.1}$$

When the P-reflection operator is applied to electromagnetic fields, it results in mirroring the fields around the plane of symmetry. In the following subsections, we study the relation between P symmetry in coupled waveguides and the maximum obtainable orders of EPDs for both the cases of even and odd N.

4.2.1 Even Number of Periodically-Coupled TLs

Figure 4.1a shows N coupled-periodic TLs that may have P symmetry, where N is even.We describe the wave propagation in the periodic coupled TLs shown in Fig. 4.1a by defining ports at the beginning and the end of each unit cell. A unit cell of the periodic structure is modeled using an equivalent $2N$-port network as shown in Fig. 4.1b where voltages and

currents with negative indices are associated to TLs that exist at $x < 0$ whereas voltages and currents with positive indices are associated to the TLs that exist at $x > 0$.

For convenience, we define a state vector that describes the electromagnetic fields at the unit cell boundaries

$$\mathbf{\Psi} = \begin{bmatrix} \mathbf{\Psi}_{\mathrm{U}}^T, & \mathbf{\Psi}_{\mathrm{L}}^T \end{bmatrix}^T, \tag{4.2}$$

where the subscripts U and L are designated for the upper ($x > 0$) and lower ($x < 0$) state vectors, respectively, and the superscript T denotes the transpose operation. The upper and lower state vectors are defined as

$$\begin{aligned} \mathbf{\Psi}_{\mathrm{U}} &= \begin{bmatrix} \mathbf{\Psi}_1^T, & \mathbf{\Psi}_2^T, & \cdots & \mathbf{\Psi}_{N/2}^T \end{bmatrix}^T, \\ \mathbf{\Psi}_{\mathrm{L}} &= \begin{bmatrix} \mathbf{\Psi}_{-1}^T, & \mathbf{\Psi}_{-2}^T, & \cdots & \mathbf{\Psi}_{-N/2}^T \end{bmatrix}^T, \end{aligned} \tag{4.3}$$

where $\mathbf{\Psi}_n = \begin{bmatrix} V_n, & I_n \end{bmatrix}^T$, with $n = \pm 1, \pm 2, ..., \pm N/2$, is a two-dimensional column vector (with size 2×1) involving the voltage and the current of the n^{th} TL at the start of the unit cell as shown in Fig. 4.1. Note that the state vector Ψ has $2N$ components since each Ψ_n is of dimension 2. Based on the equivalent circuit network shown in Fig. 4.1b, the relation between the output and input state vectors of a given unit cell are defined by the forward transfer matrix such as

$$\mathbf{\Psi}' = \mathbf{T}\mathbf{\Psi}, \tag{4.4}$$

which is written in block matrix form as

$$\begin{bmatrix} \boldsymbol{\Psi}'_{\mathrm{U}} \\ \boldsymbol{\Psi}'_{\mathrm{L}} \end{bmatrix} = \begin{bmatrix} \mathbf{T}_{\mathrm{UU}} & \mathbf{T}_{\mathrm{UL}} \\ \mathbf{T}_{\mathrm{LU}} & \mathbf{T}_{\mathrm{LL}} \end{bmatrix} \begin{bmatrix} \boldsymbol{\Psi}_{\mathrm{U}} \\ \boldsymbol{\Psi}_{\mathrm{L}} \end{bmatrix}. \tag{4.5}$$

Note that here $\mathbf{T}$ dentotes the transfer matrix, since this symbol is routinely used and we have used it in several of our prior publications. For time reflection we will use the symbol $\mathbf{F}$. The prime symbol "$\prime$" is used to refer to the state vector at the right end of the unit cell.

By applying the P-reflection operator defined in (4.1) to the state vectors describing electromagnetic fields expressed as in (4.3), we get

$$\mathcal{P}\left(\boldsymbol{\Psi}\right) = \mathbf{P}\boldsymbol{\Psi} \ , \ \mathcal{P}\left(\boldsymbol{\Psi}'\right) = \mathbf{P}\boldsymbol{\Psi}' \ , \tag{4.6}$$

where

$$\mathbf{P} = \begin{bmatrix} \mathbf{0}_N & \mathbf{I}_N \\ \mathbf{I}_N & \mathbf{0}_N \end{bmatrix}, \tag{4.7}$$

is the $2N \times 2N$ matrix that swaps the states in the upper and lower half space, where $\mathbf{I}_N$ and $\mathbf{0}_N$ are the $N \times N$ identity and zero matrices, respectively, hence $\mathbf{P}\boldsymbol{\Psi}$ is a vector where the upper and lower fields of the waveguide in Fig. 4.1 are swapped. The P-reflection matrix is an involutory matrix [83] (Ch. 5) , i.e.,

$$\mathbf{P} = \mathbf{P}^{-1}. \tag{4.8}$$

Applying the P-reflection operator to $\mathbf{\Psi}' = \mathbf{T\Psi}$ yields $\mathcal{P}(\mathbf{\Psi}') = \mathcal{P}(\mathbf{T\Psi})$ which in matrix notation is written as

$$\mathbf{P\Psi}' = \mathbf{PT\Psi}. \tag{4.9}$$

For a waveguide with P symmetry, the propagation of the state vector transformed by the P-reflection operator is still described by the same transfer matrix $\mathbf{T}$, i.e, $\mathcal{P}(\mathbf{\Psi}') = \mathbf{T}\mathcal{P}(\mathbf{\Psi})$, which, in matrix notation, is expanded as

$$\mathbf{P\Psi}' = \mathbf{TP\Psi}. \tag{4.10}$$

By comparing (4.9) and (4.10), one finds that for structures with P symmetry, $\mathbf{T}$ and $\mathbf{P}$ commute, therefore, the unit-cell transfer matrix satisfies

$$\mathbf{TP} = \mathbf{PT}. \tag{4.11}$$

In other words, the block matrices that form the transfer matrix as in (4.5) satisfy $\mathbf{T}_{\mathrm{UU}} = \mathbf{T}_{\mathrm{LL}}$ and $\mathbf{T}_{\mathrm{UL}} = \mathbf{T}_{\mathrm{LU}}$.

It is beneficial to represent our system using even and odd modes to be able to interpret the

degeneracy of the modes. Hence, a new state vector based on such even and odd modes is given by

$$\mathbf{X} = \left[\left(\mathbf{\Psi}_{\mathrm{U}} + \mathbf{\Psi}_{\mathrm{L}}\right)^{T}, \ \ \left(\mathbf{\Psi}_{\mathrm{U}} - \mathbf{\Psi}_{\mathrm{L}}\right)^{T} \right]^{T} = \mathbf{t}\mathbf{\Psi}, \tag{4.12}$$

where $\mathbf{t}$ is a transformation matrix given by

$$\mathbf{t} = \begin{bmatrix} \mathbf{I}_N & \mathbf{I}_N \\ \mathbf{I}_N & -\mathbf{I}_N \end{bmatrix}, \tag{4.13}$$

the matrix $\mathbf{t}$ is expressed in terms of the refection symmetry matrix as

$$\mathbf{t} = \mathbf{P} + \mathbf{Q}, \tag{4.14}$$

where

$$\mathbf{Q} = \begin{bmatrix} \mathbf{I}_N & \mathbf{0}_N \\ \mathbf{0}_N & -\mathbf{I}_N \end{bmatrix}, \tag{4.15}$$

and its inverse is

$$\mathbf{t}^{-1} = \frac{1}{2}\mathbf{t} = \frac{1}{2}\left(\mathbf{P} + \mathbf{Q}\right). \tag{4.16}$$

By using the even and odd mode bases in (4.5), we obtain $\mathbf{X'} = \mathbf{T}_{\mathrm{X}}\mathbf{X}$, where $\mathbf{T}_{\mathrm{X}} = \mathbf{tTt}^{-1}$. Using (4.16) and (4.14), one obtains

$$\mathbf{T}_{\mathrm{X}} = \tfrac{1}{2}(\mathbf{PTP} + \mathbf{PTQ} + \mathbf{QTP} + \mathbf{QTQ}) \ . \tag{4.17}$$

By adding and subtracting the terms $\mathbf{T}$ and $\mathbf{TPQ}$ to Eq. (4.17) we obtain

$$\mathbf{T}_X = \tfrac{1}{2}(\mathbf{PTP} + \mathbf{PTQ} + \mathbf{QTP} + \mathbf{QTQ}) + \tfrac{1}{2}(\mathbf{T} - \mathbf{T}) + \tfrac{1}{2}(\mathbf{TPQ} - \mathbf{TPQ}), \tag{4.18}$$

which is then simplified to

$$\mathbf{T}_X = \tfrac{1}{2}\left(\mathbf{T} + \mathbf{TPQ} + \mathbf{QTP} + \mathbf{QTQ}\right) + \tfrac{1}{2}(\mathbf{PT} - \mathbf{TP})\left(\mathbf{P} + \mathbf{Q}\right). \tag{4.19}$$

By calculating the first term of the latter equation, $\mathbf{T}_{\mathrm{X}}$ reads as

$$\mathbf{T}_{\mathrm{X}} = \begin{bmatrix} \mathbf{T}_{\mathrm{UU}} + \mathbf{T}_{\mathrm{UL}} & \mathbf{0}_N \\ \mathbf{0}_N & \mathbf{T}_{\mathrm{LL}} - \mathbf{T}_{\mathrm{LU}} \end{bmatrix} + \tfrac{1}{2}(\mathbf{PT} - \mathbf{TP})\left(\mathbf{P} + \mathbf{Q}\right). \tag{4.20}$$

We recall that for waveguides with P symmetry the matrices $\mathbf{T}$ and $\mathbf{P}$ are always commutative, therefore the last term in (4.20) vanishes. This yields that the transmission matrix $\mathbf{T}_{\mathrm{X}}$ in (4.20) is a block diagonal matrix, made of four blocks of size $N \times N$. Under P symmetry,

clearly, the eigevectors associated to the bock $\mathbf{T}_{\mathrm{UU}}+\mathbf{T}_{\mathrm{UL}}$ cannot mix with those of the block $\mathbf{T}_{\mathrm{LL}}-\mathbf{T}_{\mathrm{LU}}$. This implies that there is no coupling between even and odd modes due to the introduced P symmetry and the system is described using

$$\begin{aligned}
\left[\boldsymbol{\Psi}'_{\mathrm{U}}+\boldsymbol{\Psi}'_{\mathrm{L}}\right] &= \left[\mathbf{T}_{\mathrm{UU}}+\mathbf{T}_{\mathrm{UL}}\right]\left[\boldsymbol{\Psi}_{\mathrm{U}}+\boldsymbol{\Psi}_{\mathrm{L}}\right], \\
\left[\boldsymbol{\Psi}'_{\mathrm{U}}-\boldsymbol{\Psi}'_{\mathrm{L}}\right] &= \left[\mathbf{T}_{\mathrm{LL}}-\mathbf{T}_{\mathrm{LU}}\right]\left[\boldsymbol{\Psi}_{\mathrm{U}}-\boldsymbol{\Psi}_{\mathrm{L}}\right].
\end{aligned} \tag{4.21}$$

Therefore, we conclude that when the waveguide exhibits P symmetry, the maximum order of EPD which can be obtained is N because to have a higher order we need more than N modes to be coupled.

As an important explanatory case, we apply these concepts to the case of $N = 2$, which is the one considered in [48, 41, 49], where the authors had to break the P symmetry in their proposed geometries without demonstrating that it was necessary to achieve a DBE. The above conclusions imply two periodically-coupled TLs with P symmetry cannot have a DBE, and only the second order EPD (i.e., an RBE) is possible to exist. The DBE may exist in two coupled TLs only if P symmetry is broken.

4.2.2 Odd Number of Periodically-Coupled TLs

In this section, we consider the other case when N is odd, with a waveguide example shown in Fig. 4.2a. The state vector is conveniently defined as

$$\boldsymbol{\Psi} = \left[\begin{array}{ccc} \boldsymbol{\Psi}_{\mathrm{U}}^{T}, & \boldsymbol{\Psi}_{0}^{T}, & \boldsymbol{\Psi}_{\mathrm{L}}^{T} \end{array}\right]^{T}, \tag{4.22}$$

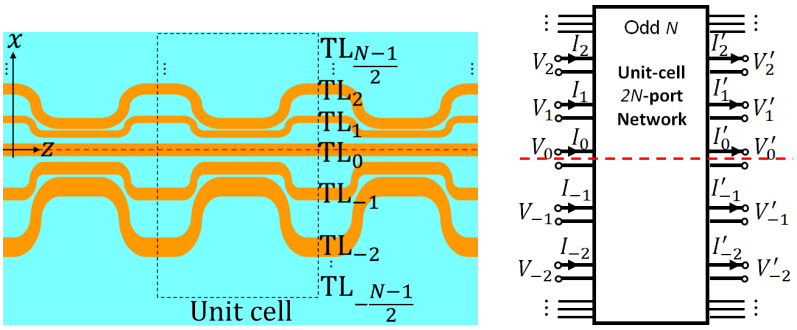

(a) (b)

Figure 4.2: (a) Periodically coupled N TLs, consisting of coupled and uncoupled sections, where the number of TLs is odd. (b) A 2N-port circuit network model for a unit-cell of structure in (a).

where

$$\begin{aligned} \boldsymbol{\Psi}_{\mathrm{U}} &= \begin{bmatrix} \boldsymbol{\Psi}_1^T, & \boldsymbol{\Psi}_2^T, & \cdots & \boldsymbol{\Psi}_{(N-1)/2}^T \end{bmatrix}^T, \\ \boldsymbol{\Psi}_{\mathrm{L}} &= \begin{bmatrix} \boldsymbol{\Psi}_{-1}^T, & \boldsymbol{\Psi}_{-2}^T, & \cdots & \boldsymbol{\Psi}_{-(N-1)/2}^T \end{bmatrix}^T, \end{aligned} \tag{4.23}$$

where the subscript 0 refers to the mode guided by the central TL in Fig. 4.2a. We assume that the central TL supports only a single mode in each direction, characterized by $\boldsymbol{\Psi}_0$, which is a two-dimensional column vector.

The relation between the output $\boldsymbol{\Psi}'$ and input $\boldsymbol{\Psi}$ state vectors of each unit cell is given in term of the unit-cell transfer matrix as $\boldsymbol{\Psi}' = \mathbf{T}\boldsymbol{\Psi}$, which is expanded as

$$\begin{bmatrix} \boldsymbol{\Psi}'_{\mathrm{U}} \\ \boldsymbol{\Psi}'_0 \\ \boldsymbol{\Psi}'_{\mathrm{L}} \end{bmatrix} = \begin{bmatrix} \mathbf{T}_{\mathrm{UU}} & \mathbf{T}_{\mathrm{U0}} & \mathbf{T}_{\mathrm{UL}} \\ \mathbf{T}_{0\mathrm{U}} & \mathbf{T}_{00} & \mathbf{T}_{0\mathrm{L}} \\ \mathbf{T}_{\mathrm{LU}} & \mathbf{T}_{\mathrm{L0}} & \mathbf{T}_{\mathrm{LL}} \end{bmatrix} \begin{bmatrix} \boldsymbol{\Psi}_{\mathrm{U}} \\ \boldsymbol{\Psi}_0 \\ \boldsymbol{\Psi}_{\mathrm{L}} \end{bmatrix}, \tag{4.24}$$

where all four corner blocks have dimensions $(N-1) \times (N-1)$, and the center block $\mathbf{T}_{00}$

that has 2×2 dimensions. Similarly to the even case, the waveguide's fields are represented in terms of even and odd modes as

$$\mathbf{X} = \left[\begin{array}{ccc} \left(\boldsymbol{\Psi}_{\mathrm{U}} + \boldsymbol{\Psi}_{\mathrm{L}}\right)^T, & \boldsymbol{\Psi}_0^T, & \left(\boldsymbol{\Psi}_{\mathrm{U}} - \boldsymbol{\Psi}_{\mathrm{L}}\right)^T \end{array} \right]^T = \mathbf{t}\Psi, \tag{4.25}$$

where

$$\mathbf{t} = \begin{bmatrix} \mathbf{I}_{N-1} & \mathbf{0}_{(N-1)\times 2} & \mathbf{I}_{N-1} \\ \mathbf{0}_{2\times(N-1)} & \mathbf{I}_2 & \mathbf{0}_{2\times(N-1)} \\ \mathbf{I}_{N-1} & \mathbf{0}_{(N-1)\times 2} & -\mathbf{I}_{N-1} \end{bmatrix}. \tag{4.26}$$

Also, the transformation matrix $\mathbf{t}$ is written as (4.14), i.e., $\mathbf{t} = \mathbf{P} + \mathbf{Q}$, where the matrices $\mathbf{P}$ and $\mathbf{Q}$ in the odd case are

$$\begin{aligned} \mathbf{P} &= \begin{bmatrix} \mathbf{0}_{N-1} & \mathbf{0}_{(N-1)\times 2} & \mathbf{I}_{(N-1)} \\ \mathbf{0}_{2\times(N-1)} & \mathbf{I}_2 & \mathbf{0}_{2\times(N-1)} \\ \mathbf{I}_{(N-1)} & \mathbf{0}_{(N-1)\times 2} & \mathbf{0}_{N-1} \end{bmatrix}, \\ \mathbf{Q} &= \begin{bmatrix} \mathbf{I}_{N-1} & \mathbf{0}_{(N-1)\times 2} & \mathbf{0}_{N-1} \\ \mathbf{0}_{2\times(N-1)} & \mathbf{0}_2 & \mathbf{0}_{2\times(N-1)} \\ \mathbf{0}_{N-1} & \mathbf{0}_{(N-1)\times 2} & -\mathbf{I}_{N-1} \end{bmatrix}. \end{aligned} \tag{4.27}$$

The inverse of the matrix $\mathbf{t}$ is expressed as

$$\mathbf{t}^{-1} = \frac{1}{2}(\mathbf{P} + \mathbf{Q} + \mathbf{W}), \tag{4.28}$$

where

$$\mathbf{W} = \begin{bmatrix} \mathbf{0}_{N-1} & \mathbf{0}_{(N-1)\times 2} & \mathbf{0}_{N-1} \\ \mathbf{0}_{2\times(N-1)} & \mathbf{I}_2 & \mathbf{0}_{2\times(N-1)} \\ \mathbf{0}_{N-1} & \mathbf{0}_{(N-1)\times 2} & \mathbf{0}_{N-1} \end{bmatrix}. \tag{4.29}$$

By applying the even and odd modes basis transformation to the system description in (4.24), we obtain $\mathbf{X}' = \mathbf{T}_{\mathrm{X}}\mathbf{X}$, where $\mathbf{T}_{\mathrm{X}} = \mathbf{t}\mathbf{T}\mathbf{t}^{-1}$. Using the property in (4.28), it is found that $\mathbf{T}_{\mathrm{X}} = \frac{1}{2}(\mathbf{P} + \mathbf{Q})\mathbf{T}(\mathbf{R} + \mathbf{Q} + \mathbf{W})$. After some mathematical manipulation, by adding and subtracting same extra terms $\mathbf{T}$ and $\mathbf{QPT}$, we obtain

$$\mathbf{T}_{\mathrm{X}} = \tfrac{1}{2}\left(\mathbf{T} + \mathbf{PTQ} + \mathbf{QTQ} + \mathbf{QPT} + \tfrac{1}{2}(\mathbf{P} + \mathbf{Q})\mathbf{TW}\right) + \tfrac{1}{2}(\mathbf{Q} + \mathbf{P})\left(\mathbf{TP} - \mathbf{PT}\right), \tag{4.30}$$

The transfer matrix $\mathbf{T}_{\mathrm{X}}$ is finally put in the following convenient form

$$\mathbf{T}_{\mathrm{X}} = \begin{bmatrix} \mathbf{T}_{\mathrm{UU}} + \mathbf{T}_{\mathrm{LU}} & \mathbf{T}_{\mathrm{U0}} + \mathbf{T}_{\mathrm{L0}} & \mathbf{0}_{N-1} \\ \mathbf{T}_{0\mathrm{U}} & \mathbf{T}_{00} & \mathbf{0}_{2\times(N-1)} \\ \mathbf{0}_{N-1} & \mathbf{0}_{(N-1)\times 2} & \mathbf{T}_{\mathrm{LL}} - \mathbf{T}_{\mathrm{LU}} \end{bmatrix} + \tfrac{1}{2}(\mathbf{Q} + \mathbf{P})\left(\mathbf{TP} - \mathbf{PT}\right). \tag{4.31}$$

For CTLs with P symmetry, one has $\mathbf{PT} = \mathbf{TP}$ (i.e., the two matrices $\mathbf{T}$ and $\mathbf{P}$ commute),

and therefore the last term in (4.31) vanishes. In this case, the transmission matrix is seen as a block matrix with blocks

$$\mathbf{T}_{\mathrm{X}} = \begin{bmatrix} [\mathbf{T}_{\mathrm{E}}]_{(N+1)\times(N+1)} & [\mathbf{0}]_{(N+1)\times(\mathrm{N}-1)} \\ [\mathbf{0}]_{(N-1)\times(\mathrm{N}+1)} & [\mathbf{T}_{\mathrm{O}}]_{(N-1)\times(N-1)} \end{bmatrix},$$

$$\mathbf{T}_{\mathrm{E}} = \begin{bmatrix} \mathbf{T}_{\mathrm{UU}} + \mathbf{T}_{\mathrm{LU}} & \mathbf{T}_{\mathrm{U0}} + \mathbf{T}_{\mathrm{L0}} \\ \mathbf{T}_{0\mathrm{U}} & \mathbf{T}_{00} \end{bmatrix}, \tag{4.32}$$

$$\mathbf{T}_{\mathrm{O}} = \mathbf{T}_{\mathrm{LL}} - \mathbf{T}_{\mathrm{LU}}.$$

Therefore, with reflection symmetry, the matrix $\mathbf{T}_{\mathrm{X}}$ has two diagonal blocks: $\mathbf{T}_{\mathrm{E}}$ with dimension $(N+1)\times(N+1)$ and $\mathbf{T}_{\mathrm{O}}$ with dimension $(N-1)\times(N-1)$,and the modes associated to these two distinct blocks cannot be mixed to create a degeneracy because the cross diagonal blocks of $\mathbf{T}_{\mathrm{X}}$ are full of zeros. In other words, the $N+1$ even modes and the 2 modes at the central TL are decoupled from the $N-1$ odd modes. Using this decomposition, the full system is equivalently described using the two subsystems:

$$\begin{bmatrix} \mathbf{\Psi}'_{\mathrm{U}} + \mathbf{\Psi}'_{\mathrm{L}} \\ \mathbf{\Psi}'_{0} \end{bmatrix} = \mathbf{T}_{\mathrm{E}} \begin{bmatrix} \mathbf{\Psi}_{\mathrm{U}} + \mathbf{\Psi}_{\mathrm{L}} \\ \mathbf{\Psi}_{0} \end{bmatrix}, \tag{4.33}$$

$$[\mathbf{\Psi}'_{\mathrm{U}} - \mathbf{\Psi}'_{\mathrm{L}}] = \mathbf{T}_{\mathrm{O}} [\mathbf{\Psi}_{\mathrm{U}} - \mathbf{\Psi}_{\mathrm{L}}].$$

This means that the maximum order of allowed EPD is $(N-1)+2 = N+1$ (which is the dimension of the larger block $\mathbf{T}_{\mathrm{E}}$).

Furthermore, we also derive another important property: that an EPD of order N cannot be obtained due to reciprocity because $\det(\mathbf{T}_{\mathrm{E}}) = 1$, hence the eigenvalues of the matrix $\mathbf{T}_{\mathrm{E}}$ are in pair form, i.e., both λ and $1/\lambda$ are eigenvalues (or equivalently, both k and $-k$ are wavenumbers). Indeed, the existence of an EPD of order N requires the system to have N coalescing modes paired by the other N reciprocal modes, as spectrum of the the system matrix of dimension $2N \times 2N$, however, the block $\mathbf{T}_{\mathrm{E}}$ can lead to only $(N+1)/2$ modes coalescing at k paired by the reciprocal $(N+1)/2$ modes coalescing at $-k$. The $\mathbf{T}_{\mathrm{O}}$ block describing the waves with odd distribution, can provide a maximum degeneracy of order $N-1$.

Let us consider now an important example of a waveguide made of three coupled TLs ($N = 3$) with P symmetry. It may exhibit EPDs of order 2 and 4, and based on the discussion above, but it can never exhibit EPDs of order 3 and 6. Indeed in [55, 47] the SIP was obtained in structures that do not have P symmetry; the geometry presented in [55] has glide symmetry whereas the one presented in [47] does not possess any kind of symmetry in the traverse direction. Furthermore, based on the shown analysis, using $N = 3$ CTLs, it is possible to obtain a DBE degenerate eigenmode (order $N + 1 = 4$),and this degenerate eigenmode has a voltage and current distribution in the transverse direction that is even symmetric. Still referring to the $N = 3$ case, we also conclude that from the $\mathbf{T}_{\mathrm{O}}$ block describing the waves with odd distribution, the maximum degeneracy involving an odd voltage and current distribution is $N - 1 = 2$. Of course, also the block $\mathbf{T}_{\mathrm{E}}$ describing the even wave distribution can provide a degeneracy of order 2.

For P-symmetric structures, the reduction of the evolution equations to the forms in Eq (4.31) and Eq. (4.32) can alternatively be found by introducing perfect electric conductor (PEC) and perfect magnetic conductor (PMC) walls at the symmetry plane.

4.3 Parity-Time (PT) Symmetry

Here, we investigate whether PT symmetry enables or not the existence of a full-order EPD. For sake of simplicity, we just focus on the case with $N = 2$, in analogy to the example in Fig. 4.5. The PT operator involves P-reflection and time reversal [17], as

$$PT : (t, x, z) \rightarrow (-t, -x, z). \tag{4.34}$$

The P-reflection operator was already discussed in the previous section together with its associated matrix $\mathbf{P}$ which is used to flip the state vector upside down. The time reversal operator involves complex conjugate operation in addition to flipping the direction of the current flow [20]. By applying the PT operator in (4.34) to the state vectors (4.2), we get

$$\mathcal{PT}\left(\Psi\right) = \mathbf{PF}\boldsymbol{\Psi}^{*}, \tag{4.35}$$

where * denotes the complex conjugate operation that swap j with $-j$, and

$$\mathbf{F} = \begin{bmatrix} \mathbf{f} & 0 \\ 0 & \mathbf{f} \end{bmatrix} = \begin{bmatrix} 1 & 0 & 0 & 0 \\ 0 & -1 & 0 & 0 \\ 0 & 0 & -1 & 0 \\ 0 & 0 & 0 & -1 \end{bmatrix}, \tag{4.36}$$

is the matrix that flips the direction of all the current elements in the state vector (4.2) [20].

Applying PT operator to $\mathbf{\Psi}' = \mathbf{T}\mathbf{\Psi}$ yields $\mathcal{PT}(\mathbf{\Psi}') = \mathcal{PT}(\mathbf{T}\mathbf{\Psi})$, which is written in matrix notation as

$$\mathbf{PF}\mathbf{\Psi}'^{*} = \mathbf{PFT}^{*}\mathbf{\Psi}^{*} \tag{4.37}$$

For a PT-symmetric structure, the propagation of the state vector transformed by the PT operator is still described by the same transfer matrix $\mathbf{T}$, i.e, $\mathcal{PT}(\mathbf{\Psi}') = \mathbf{T}\mathcal{PT}(\mathbf{\Psi})$, which in matrix notation is expanded as

$$\mathbf{PF}\mathbf{\Psi}'^{*} = \mathbf{PF}\mathbf{\Psi}^{*}. \tag{4.38}$$

By comparing (4.37) and (4.38), one finds that for structures with PT symmetry, the unit-cell transfer matrix satisfies

$$\mathbf{TPF} = \mathbf{PFT}^{*}. \tag{4.39}$$

Assuming that there exist an eigenstate with eigenvalue λ_n and eigenvector $\mathbf{\Psi}_n$ such that

$$\mathbf{T}\mathbf{\Psi}_n = \lambda_n \mathbf{\Psi}_n, \tag{4.40}$$

one can find that there exist another eigenstate with eigenvalue λ_n^* and eigenvector $\mathcal{PT}(\mathbf{\Psi}_n)$

when the structure is PT symmetric. To prove this, we apply the complex conjugate to (4.40) and then, after left multiplying by $\mathbf{PF}$, we get $\mathbf{PFT}^{*}\mathbf{\Psi}_n^{*} = \lambda_n^{*}\mathbf{PF}\mathbf{\Psi}_n^{*}$ which is yet simplified using (4.39) to

$$\mathbf{T}\mathcal{PT}\left(\mathbf{\Psi}_n\right) = \lambda_n^{*}\mathcal{PT}\left(\mathbf{\Psi}_n\right). \tag{4.41}$$

Therefore, the four eigenvectors for a PT-symmetric structure made of two CTLs is cast in the form

$$\begin{aligned}
\mathbf{\Psi}_1 &= \begin{bmatrix} \mathbf{\Psi}_{\mathrm{U1}} \\ \mathbf{\Psi}_{\mathrm{L1}} \end{bmatrix}, \ \mathbf{\Psi}_3 = \mathcal{PT}\left(\mathbf{\Psi}_1\right) = \begin{bmatrix} \mathbf{f}\mathbf{\Psi}_{\mathrm{L1}}^{*} \\ \mathbf{f}\mathbf{\Psi}_{\mathrm{U1}}^{*} \end{bmatrix}, \\
\mathbf{\Psi}_2 &= \begin{bmatrix} \mathbf{\Psi}_{\mathrm{U2}} \\ \mathbf{\Psi}_{\mathrm{L2}} \end{bmatrix}, \ \mathbf{\Psi}_4 = \mathcal{PT}\left(\mathbf{\Psi}_2\right) = \begin{bmatrix} \mathbf{f}\mathbf{\Psi}_{\mathrm{L2}}^{*} \\ \mathbf{f}\mathbf{\Psi}_{\mathrm{U2}}^{*} \end{bmatrix}.
\end{aligned} \tag{4.42}$$

From (4.42) on finds that the necessary and sufficient conditions that are required such that the four eigenvectors coalesce, i.e, an EPD of fourth order is formed, are

$$\begin{aligned}
&\mathbf{\Psi}_{\mathrm{U1}} = \mathbf{\Psi}_{\mathrm{U2}}, \quad \mathbf{\Psi}_{\mathrm{L1}} = \mathbf{\Psi}_{\mathrm{L2}}, \\
&\mathbf{\Psi}_{\mathrm{U1}} = \mathbf{f}\mathbf{\Psi}_{\mathrm{L1}}^{*}, \quad \Psi_{\mathrm{U2}} = \mathbf{f}\mathbf{\Psi}_{\mathrm{L2}}^{*}.
\end{aligned} \tag{4.43}$$

Therefore, we conclude that there is nothing that prohibits the existence of full-order EPD (i.e., an EPD or order 4) in a PT-symmetric structure made by two coupled waveguides. Indeed, we will show numerically a case of a forth order EPD in a two coupled TLs with PT symmetry.

We now find the constraints on the transfer matrix for two CTLs that are PT symmetric. The commutative property $\mathbf{TPT} = \mathbf{PFT}^*$ implies that the transfer matrix is represented using a reduced set of parameters as

$$\mathbf{T} = \begin{bmatrix} T_{11} & T_{12} & T_{13} & T_{14} \\ T_{21} & T_{22} & T_{23} & T_{24} \\ T_{13}^* & -T_{14}^* & T_{11} & -T_{21}^* \\ -T_{23}^* & T_{24}^* & -T_{21}^* & T_{22}^* \end{bmatrix}. \tag{4.44}$$

The eigenvalues are found by solving $P(\lambda) = \det(\mathbf{T} - \lambda\mathbf{I}) = 0$ which is a polynomial equation of order 4. A fourth order EPD conditions at a given angular frequncy ω is found by enforcing that the polynomial is equal either to $P(\lambda) = (\lambda - 1)^4$ or to $P(\lambda) = (\lambda + 1)^4$, depending on the degenerate eigenvalue that is either $\lambda = \exp(-jkd) = 1$ or $\lambda = \exp(-jkd) = -1$ (this two conditions lead to a wavenumber either at $k = 0$ or at $k = \pi/d$ in the first Brillouin zone). As a result, the necessary conditions that a fourth order EPD occurrs at a given angular frequncy ω, are

$$\begin{aligned} \mathrm{Re}\,(T_{11} + T_{22}) &= \pm 2, \\ |T_{11} + T_{22}|^2 + 2\mathrm{Re}\,(T_{14}T_{23}^*) - |T_{13}|^2 - |T_{24}|^2 &= 4. \end{aligned} \tag{4.45}$$

There are a lot of degrees of freedom to realize a fourth order EPD, where 6 parameters should be selected just to satisfy the 2 conditions in (4.45). In the next section, we present one example to demonstrate that indeed PT symmetry does not prohibit full order degeneracy.

4.4 Results and Discussion

In the following examples, waveguides are made of microstrip lines over a grounded dielectric substrate with a dielectric constant $\varepsilon_r = 2.2$ and height $H = 1.575$ mm. All metals are assumed to be perfect conductors. The width of each microstrip line is chosen to be $w = 5$ mm, which corresponds to a 50 Ohm characteristic impedance for each TL (when uncoupled). For simplicity, the TLs are assumed to have a fixed gap of $s = 0.5$ mm in the coupled sections in all the following examples. All the periodic structures under study have a period $d = 40$ mm, and the rest of the dimensions are left for optimization and investigation. The microstrip lines are made of cascaded coupled and uncoupled sections. We build the transfer matrix of a unit cell by cascading the transfer matrices of different uniform sections of coupled and uncoupled microstrip TLs using parameters (characteristic impedances and phase velocities) that are calculated using the analytic formulas in [84, 85], based on quasistatic models.

We consider two cases: CTLs with $N = 2$ (even) and $N = 3$ (odd). In the examples, P symmetry is broken by changing one dimension in the TLs that exist at $x < 0$ with respect to the ones at $x > 0$ as we will show later for the case of two CTL ($N = 2$) and three CTL ($N = 3$). The P symmetry is also broken by adding time symmetry when losses and gain are present, as we will show later on for the case of two CTL ($N = 2$).

To assess the presence of an EPD, we use the concept of coalescence parameter, that represents the "distance" between vectors in a multidimensional space. We calculate the angle between two eigenvectors $\mathbf{\Psi}_n$ and $\mathbf{\Psi}_m$ as

$$\cos\left(\theta_{mn}\right) = \frac{\left|\langle \mathbf{\Psi}_n, \mathbf{\Psi}_m \rangle\right|}{\|\mathbf{\Psi}_n\| \, \|\mathbf{\Psi}_m\|} \ , \tag{4.46}$$

where the inner product is defined as $\langle \mathbf{\Psi}_n, \mathbf{\Psi}_m \rangle = \mathbf{\Psi}_n^{\dagger} \mathbf{\Psi}_m$, with the dagger symbol † repre-

senting the complex conjugate transpose operation, and $\|\mathbf{\Psi}_n\|$ and $\|\mathbf{\Psi}_m\|$ denote the norms of the vectors.

In the even $N = 2$ case, to observe the occurrence of a DBE (degeneracy of order 4), the coalescence parameter is defined to assess the coalescence of all of the system four eigenvectors as

$$C_{\text{DBE}} = \frac{1}{6} \sum_{\substack{m=1,n=2 \\ n>m}}^{4} \left|\sin\left(\theta_{mn}\right)\right|. \tag{4.47}$$

In the odd $N = 3$ case, to observe the occurrence of an SIP (degeneracy of order 3) the coalescence parameters is defined to assess the coalescence of the three eigenvectors with positive wavenumber as

$$C_{\text{SIP}} = \frac{1}{3} \sum_{\substack{m=1,n=2 \\ n>m}}^{3} \left|\sin\left(\theta_{mn}\right)\right|, \tag{4.48}$$

.

Still for the odd $N = 3$ case, to observe the occurrence a 6DBE (degeneracy of order 6), the coalescence parameters is defined to assess the coalescence of all the eigenvectors as

$$C_{\text{6DBE}} = \frac{1}{15} \sum_{\substack{m=1,n=2 \\ n>m}}^{6} \left|\sin\left(\theta_{mn}\right)\right| \tag{4.49}$$

In the following, we demonstrate using numerical examples that P symmetry should be

broken for CTLs with $N = 2$ to enable the existence of full-order degeneracy (i.e., a fourth order one) which is called DBE, when waveguides are lossless and gainless. For CTLs with $N = 3$, we show that SIP and 6DBE (full-order degeneracy) are both possible for the cases where P symmetry is broken.

4.4.1 Two Periodically Coupled TLs Exhibiting 4th Order EPD

Breaking Parity Symmetry Leads to a DBE

We study here CTLs transmission lines consisting of periodically coupled and uncoupled sections as shown in Fig. 4.3a. The upper and lower TLs are identical except for the heights of the vertical TLs. P symmetry can be introduced to the structure by enforcing the same heights of the vertical TLs $h_1 = h_2$. For every combination of $h_1$and h_2 we optimize the frequency to get the best point that is close to a DBE (i.e., full-order degeneracy for $N = 2$) by checking the coalescence parameter C_{DBE} of 4 eigenvectors. This concept was developed in [41] for a fourth order degeneracy (DBE) and was used also in [55] for a third order degeneracy (SIP). The coalescence parameter is a figure of merit to measure how close a system is to an ideal degeneracy condition, where small values indicates how well the eigenvectors of the structure are close to each other, with $C_{\text{DBE}} = 0$ being the exact coalescence. Figure 4.3b depicts the minimum coalescence parameter that could be obtained by sweeping the frequency through every combination of h_1 and h_2. The figure shows that a coalescence parameter of $C_{\text{DBE}} = 0$ is observed when the relation between $h_1$and h_2 is the following $|h_1 - h_2| \approx 2$ mm. Therefore, it is clear that for this particular case, breaking the P symmetry is crucial to having high-order EPD which is DBE for this case. Also, the figure shows that the P symmetry situation represented by the line $h_1 = h_2$ (denoted by the dashed red line in Fig. 4.3b) never satisfy the condition to have a vanishing coalescence parameter C_{DBE} for a DBE to occur.

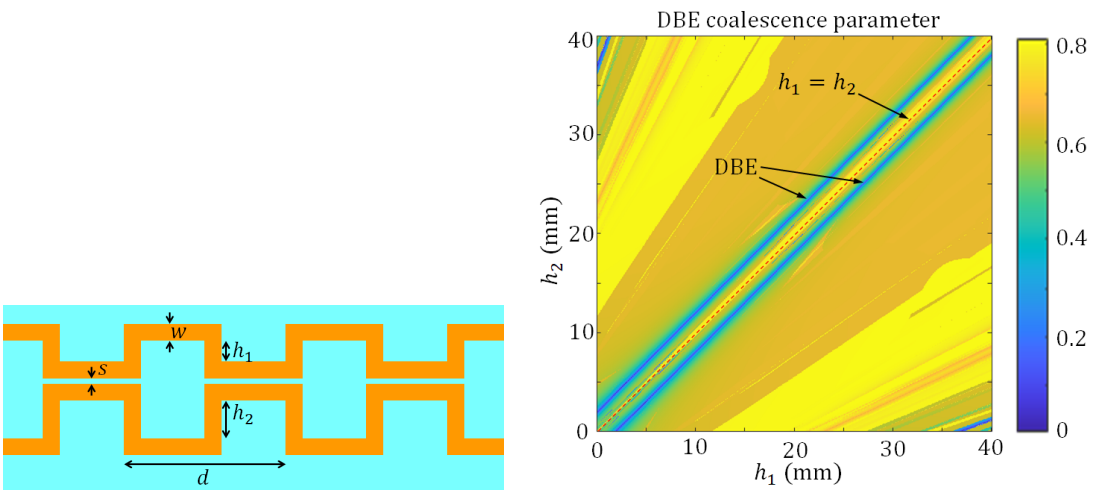

(a) (b)

Figure 4.3: (a) Two periodically coupled TLs (i.e., $N = 2$) without gain and loss where P symmetry and its breaking are controlled by the two dimensions h_1 and h_2. The structure has P symmetry when $h_1 = h_2$. (b) Colored map showing coalescence parameter C_{DBE} versus dimensions h_1 and h_2. The DBE occurs when $C_{\text{DBE}} = 0$. The dark blue zones show the relation between h_1 and h_2 that results in a DBE in the dispersion relation of the structure.

Figure 4.4 shows the dispersion diagrams for three different combinations of h_1 and h_2. Figure 4.4b depicts how the dispersion diagram would look for P-symmetric structure that does not exhibit high-order EPD, whereas, breaking the P symmetry is necessary to have DBE as shown in Fig. 4.4a and Fig.4.4c. Note that the frequency where there is a DBE for the P-symmetry broken cases is not fixed.

Fourth Order EPD in Waveguides with PT-Symmetry

We study here PT-symmetric CTLs transmission lines consisting of uncoupled TL sections (assumed to be very far away form each other) and the coupling is introduced using discrete capacitors with $C = 5$ pF that are periodically connected between the two TLs as shown in

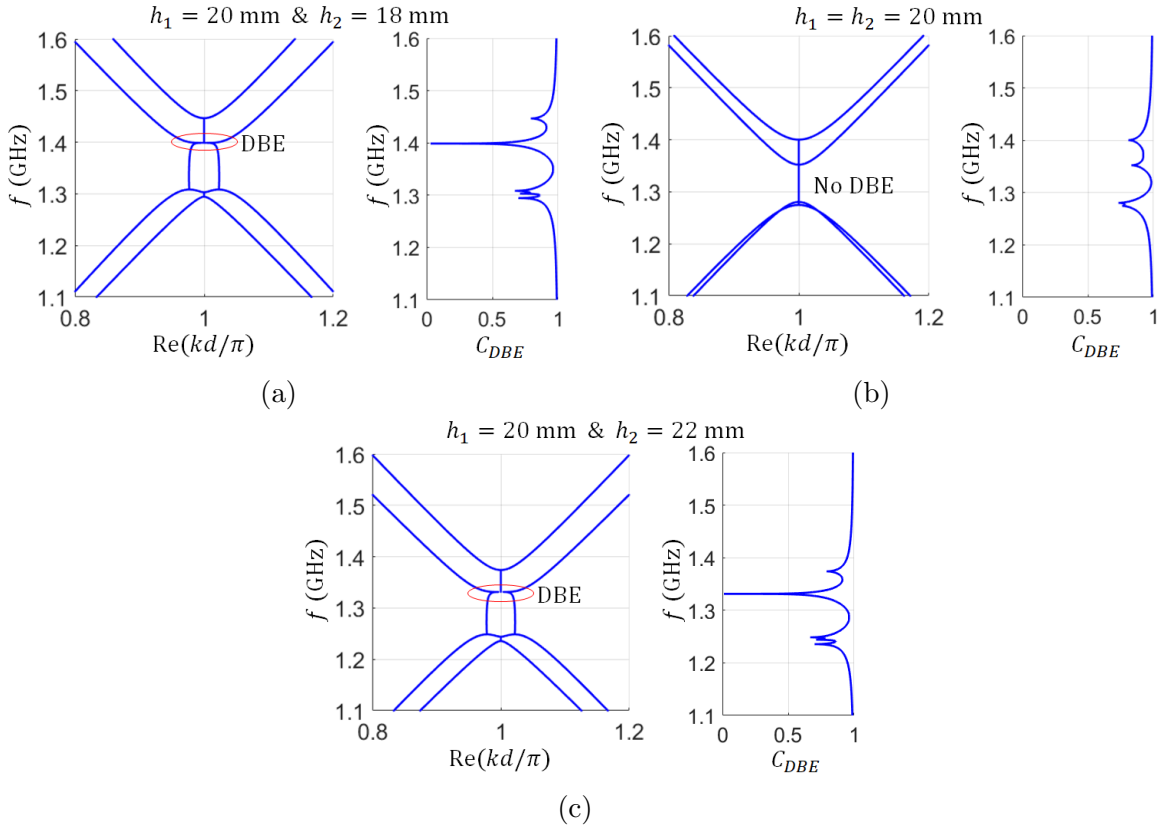

Figure 4.4: Results for two periodically coupled TLs (i.e., $N = 2$) without gain and loss. Dispersion relation showing the real part of wavenumber and coalescence parameter versus frequency when: (a) and (c) P symmetry is broken and EPD condition is satisfied and (b) when the structure has P symmetry where the condition of high-order EPD can never be satisfied.

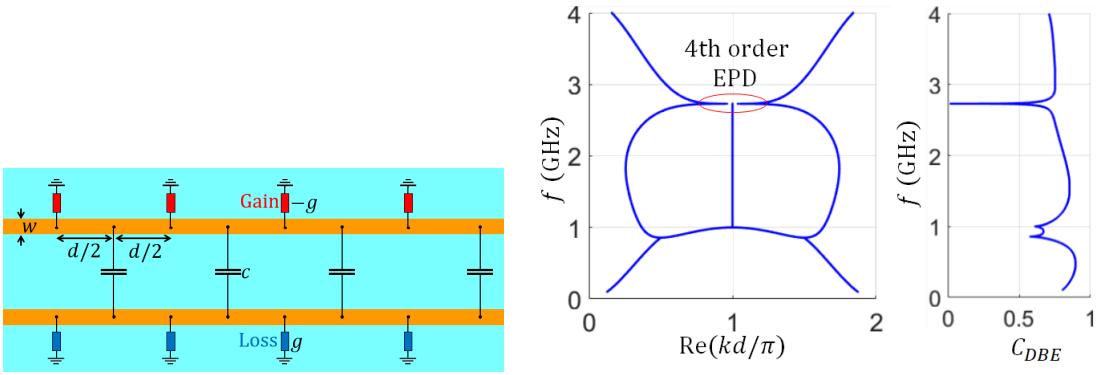

(a) (b)

Figure 4.5: (a) Two periodically coupled TLs (i.e., $N = 2$) with loss and gain that are PT symmetric. (b) Modal dispersion showing the real part of the four wavenumbers and the coalescence parameter (4.47) versus frequency. The figure shows that PT symmetry does not prohibit full order degeneracy (that is of order 4 here), contrarily to P symmetry alone that prohibits the occurrence of a fourth order EPDes.

Fig. 4.5a. The TLs are periodically loaded with gain and loss elements having g =0.05 S. We show in Fig. 4.5b shows the dispersion diagram when the frequency is swept. It is clear form the figure that the structure exhibits 4th order EPD which is a verification that PT symmetry does not prohibit full order degeneracy. Fourth order EPD that occurs in lossless and gainless waveguides is often referred to as DBE. In the example we present in Fig. 4.5a, because the waveguide has gain and loss, we do not refer to the EPD that occurs, shown in 4.5b, as DBE.

4.4.2 Three Periodically Coupled TLs Exhibiting an SIP and a 6DBE

In this subsection, we address the three periodically coupled TLs (i.e., odd case with $N = 3$) using an analogous approach to the two periodically coupled TLs investigated in a previous subsection. We demonstrate that breaking P symmetries in structures with an odd number

(especially three) of coupled waveguides or coupled TLs allows some EPD orders that cannot be obtained in the P-symmetric structures. For instance, breaking the P symmetry in the three coupled TLs shown in Fig. 4.6a where the upper and lower TLs' vertical heights $h_1 = 28.11$ mm and $h_2 = 32.1$ mm, respectively, allows the structure to exhibit a third-order EPD, i.e., a stationary inflection point (SIP) as shown in Fig. 4.6b. Moreover, the broken P symmetry also facilitates to have sixth-order EPD (6DBE) (i.e., full-order degeneracy of order $2N = 6$) as shown in Fig. 4.6c for the case where $h_1 = 1.22$ mm and $h_2 = 57.56$ mm. The third-order and sixth-order EPDs are displayed in the corresponding dispersion diagrams and confirmed by the coalescence parameter C_{SIP} and C_{6DBE} in Fig. 4.6b and 4.6c, respectively.

Parity symmetry in this subsection is broken by changing one dimension for the TL that exist at $x < 0$ with respect to the one for TLs at $x > 0$. An alternative way to break the P symmetry is by introducing glide symmetry in the structure [86, 87, 88, 89, 90, 91, 92]. An example of a structure that looks similar to the one in Fig. 4.6a but with introduced glide symmetry to obtain the SIP is provided in [55].

4.5 Conclusion

Symmetry plays an important role in the existence of higher order EPDs. P symmetry prohibits the existence of a degenerate band edge (DBE) in two coupled periodic waveguides. P symmetry must be broken for two coupled waveguides to support a DBE. P symmetry also prohibits the existence of an SIP and a 6DBE in three coupled periodic waveguides and it has to be broken to obtain these two degenercies. Analogous conclusions have been obtained for wavegudies made of N arbitrary ways (each way corresponds to a TL and supports two

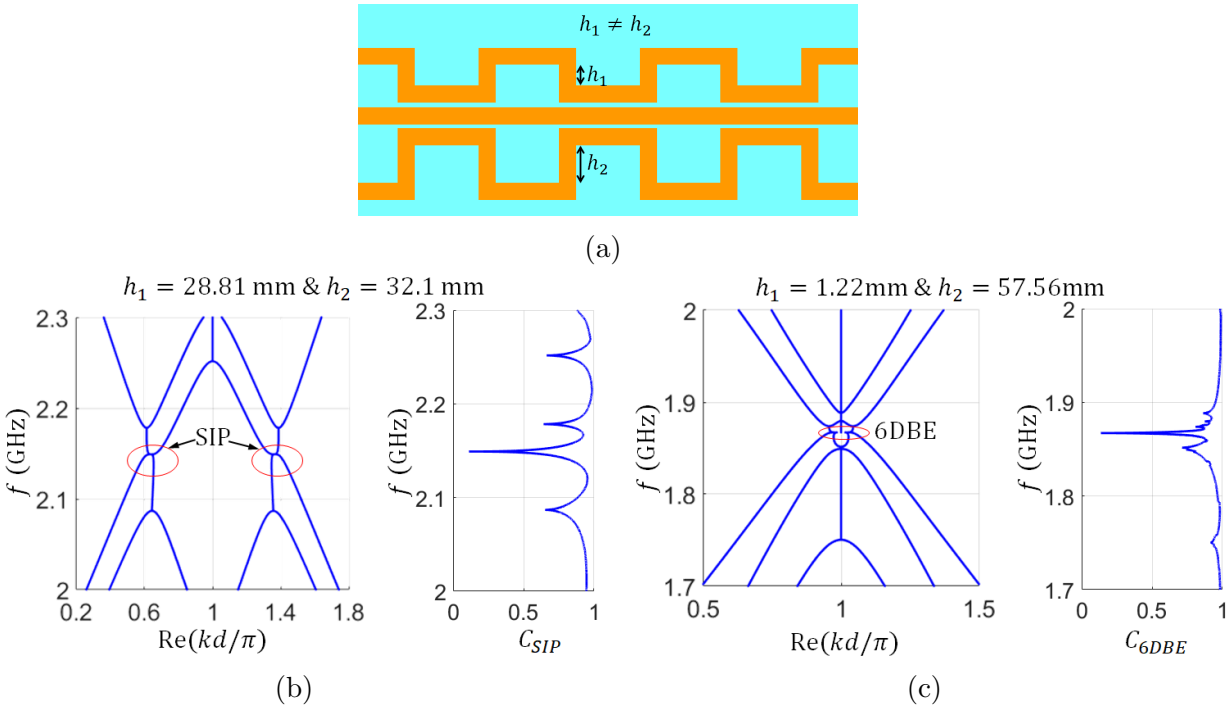

Figure 4.6: Three periodically coupled TLs (i.e., $N = 3$) without gain and loss. In (b) and (c) we show examples where broken P symmetry leads to a 3rd order EPD (i.e., the SIP) and a 6th order EPD (i.e, the 6DBE), respectively.

modes, one in each direction). Moreover, PT symmetry does not prohibit the existence of a fourth order EPD in two coupled periodic waveguides. To derive these properties we have assumed that the waveguide satisfies reciprocity.

Chapter 5

Degenerate Distributed Feedback Photonic Structure with Double Grating Exhibiting Degenerate Band Edge

We propose a degenerate version of the Bragg condition, associated to a degenerate band edge (DBE) [93]. A standard Bragg condition can be implemented using a periodic grating that operates at the regular band edge. The structure we propose to realize a DBE is made of two stacked identical gratings that form two coupled periodic waveguides with broken mirror symmetry. The occurrence of the DBE is verified by using both an eigenmode solver and the calculations of scattering parameters, using full-wave simulations. The proposed structure is a good candidate to conceive a degenerate distributed feedback lasers operating at the DBE.

5.1 Motivation and State of the Art

We present a degenerate version of the Bragg condition in a double grating, leading to a 4th order degeneracy, namely a degenerate band edge (DBE), where four eigenmodes coalesce forming a single degenerate eigenmode. Compared to previous studies [43, 37, 94, 95, 46, 96, 62] devoted to the fundamental aspects of the DBE, here we build on those concepts and specifically show a realistic structure that supports a DBE, based on two coupled dielectric layers with periodic gratings, shown in Fig. 5.1a. The standard Bragg condition $kd = m\pi$ for a periodic waveguide, where k is the Bloch wavenumber, d is the waveguide period, and m is an integer, is associated with the regular band edge (RBE) [97, 98]. A Bragg condition implies that two modes with power flux in opposite directions merge at a band edge to form a degenerate mode with vanishing group velocity. The Bragg condition is used in distributed feedback (DFB) lasers so that light is reflected in a distributed fashion within a cavity rather than only at the end mirrors [97, 99, 100, 98]. The Bragg condition is implemented through a periodic grating that acts as a dielectric waveguide. DFB lasers require the presence of an active medium in addition to satisfying the Bragg condition $kd = m\pi$ to form a self sustained resonant mode that keeps oscillating [98]. The "degenerate DFB" concept presented here could improve laser properties.

The DBE is a particular kind of exceptional point of degeneracy (EPD) of order 4 in a waveguide without loss and gain, where 4 eigenmodes coalesce in their wavenumbers and polarization states. The concept of degeneracy of the eigenvalues and eigenvectors and their perturbation was discussed in [12, 13, 15, 14], and more recently also in [43, 37, 101, 62, 41, 49]. Here, we use those concepts to show that the double grating in Fig. 5.1a exhibits a DBE (i.e., an EPD of order four) by engineering the structure's geometrical dimensions. At a DBE the dispersion diagram is locally represented as $\omega_d - \omega = h\,(k - k_d)^4$, where ω_d and k_d are the DBE angular frequency and wavenumber, respectively, and the parameter h describes the flatness of the dispersion curve. Therefore, because of the very flat dispersion,

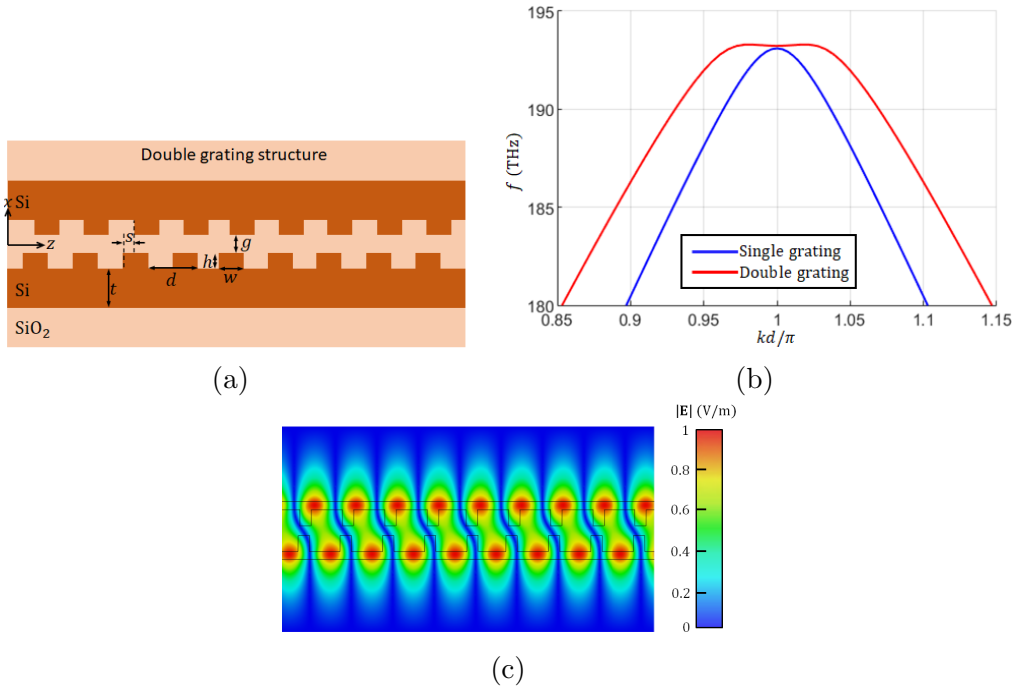

Figure 5.1: (a) Degenerate distributed feedback photonic cavity with double grating, based on a DBE, obtained by breaking mirror symmetry. (b) Dispersion diagram of the eigenmodes in the double grating (a) when the geometry is optimized to exhibit a DBE (red curve). We also show the dispersion of modes in a single grating (blue curve). Note the much flatter dispersion of the mode in the double graing (red curve). (c) Electric field distribution of the DBE mode calculated at $kd = \pi$.

not only the degenerate mode has a vanishing group velocity $v_g = 0$, but also its second and third derivatives vanish. Photonic devices operating at the DBE have the potential to exhibit better performance than those operating at the RBE [94, 95, 46, 96, 11, 62, 2, 3].

5.2 Double Grating Structure

The waveguide with double grating in Fig. 5.1a consists of a standard grating over a dielectric layer, coupled to another grating obtained by a mirror operation in the x direction, followed by a translation s along z. The shift s breaks mirror symmetry [93], because mirror symmetry

prohibits the existence of a DBE (as dicussed in Ch. 4) in two coupled waveguides due to the existence of even and odd modes that are always decoupled from each other. The double grating in Fig. 5.1a is made of two silicon on insulator (SOI) waveguides with silicon refractive index $n_{\mathrm{Si}} = 3.45$, and with a cladding material of silicon dioxide with refractive index $n_{\mathrm{SiO2}} = 1.97$.

The modal dispersion relation in Fig. 5.2 is obtained using the full-wave eigenmode solver implemented in CST Studio Suite. We used periodic boundaries at two virtual cross sections at a distance of a period d. We look for modes polarized along y, hence we use perfect electric conductor (PEC) walls at planes with constant y to account for field invariance in the y direction. The computational domain is truncated by PEC also at $x = \pm 12t$, where t is the dielectric layer thickness as illustrated in Fig. 5.1a, and it is sufficiently large not to affect the field in the grating area, to ensure that the studied modes decay away from the waveguide in the positive and negative x directions.

The dielectric waveguide has thickness $t = 67$ nm, the gratings has period $d =$335 nm, width $w = 87$ nm, and height $h = 121$ nm. The rest of parameters, the coupling gap g and the shift between the waveguides s, are left to be optimized to achieve a DBE. An optimization procedure based on having a DBE in the dispersion relation leads to $g = 100$ nm and $s = 20$ nm. The dispersion relation obtained from the eignmode solver for the optimized unit cell in the Fig. 5.1b shows a DBE at around 193 THz (red curve). The flatness of the DBE is compared to that of the the dispersion of modes in the single grating structure (blue curve) with the same waveguide and grating parameters except for the grating height that is now 42 nm in order to have a regular band edge more or less at the DBE frequency of 193 THz. It is clear from the figure that the dispersion relation for the double grating structure (red curve) is flatter than that of single grating structure (blue curve). The field distribution of the DBE mode at $k = \pi/d$ is shown in Fig. 5.1c.

Figure 5.2 shows the dispersion relation of three distinct designs of the double grating struc-

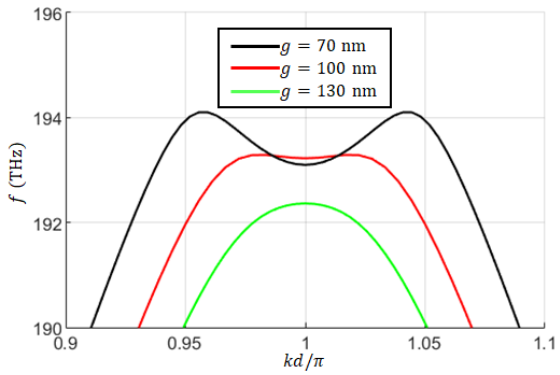

Figure 5.2: Dispersion diagram of modes in the double grating in Fig. 5.1a for three distinct gap values. The change of the dispersion curve from a split band edge ($g = 70$ nm) to regular band edge ($g = 130$ nm) implies the existence of DBE using a value of g between 70 nm and 130 nm. Indeed, the figure shows that the DBE occurs when $g = 100$ nm (red curve).

ture in Fig. 5.1a based on three distinct values of the coupling gap g, the rest of the dimensions are the same as the ones mentioned for the case above. Note that for $g = 70$ nm the dispersion shows a split band edge [73], with four modes around $f = 193$ THz (black curve), which coalesce when using $g = 100$ nm. For larger values of g, the green curve shows a RBE. Indeed, when a parameter is swept (e.g., g) and one finds both a RBE and a split band edge, there is a proper intermediate value (here, $g = 100$ nm) that leads to a DBE [73].

We also verify the existence of the DBE in the proposed double grating structure by finding the scattering matrix using frequency-domain full-wave simulations. Open (radiation) boundaries are used in this simulation and we use waveports as shown in Fig. 5.3a where two modes (even and odd) are excitable on each port. Note that simulating one unit cell would not lead to an accurate transfer matrix because it would not fully account for the structure periodicity since a waveport supports a waveguide mode and not a Bloch mode. Therefore, in the simulation we include two segments, on the left and right sides of the unit cell, that act as adiabatic transitions between the dielectric waveguide mode and the grating, as shown in Fig. 5.3a. The transition is a chirped grating with height steps of 30 nm, until

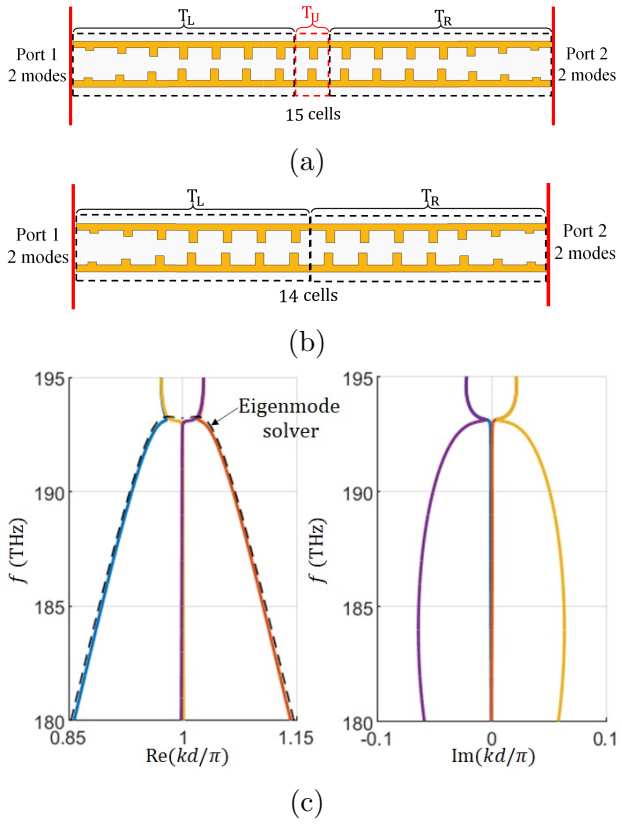

Figure 5.3: (a) Finite-length structure used to estimate the transfer matrix $\underline{\mathbf{T}}_{\mathrm{U}}$ of one unit cell in the middle. (b) Structure used to de-embed the effect of the two transition regions connected to the left and right sides of the unit cell in (a). (c) Dispersion diagram showing four complex-valued wavenumber versus frequency illustrating the coalescence of four wavenumbers at the DBE point $k_d d = \pi$, which is the degenerate Bragg condition. The dispersion is obtained based on the transfer matrix $\underline{\mathbf{T}}_{\mathrm{U}}$ found by dembedding the structure in (b) from (a). The black-dashed curve shows the dispersion of the purely real branch obtained from the eigenmode solver, already plotted in Fig. Fig. 5.1b, for validation.

we reach the whole grating height $h = 120$ nm. However our goal is to find the transfer matrix $\underline{\mathbf{T}}_{\mathrm{U}}$ only. Therefore, we also simulated another structure with two chirped gratings as shown in Fig. 5.3b, which is the same structure as in Fig. 5.3a but without the unit cell at the center. The structure in Fig. 5.3b is used to deembed the effect of the two transition segments from the results relative to Fig. 5.3a, similarly to what was done in [77, 55].

Using even and odd modes in the ports shown in Fig. 5.3a and 5.3b, and defining their associated incident and reflected waves

$$\begin{aligned} \mathbf{b} &= \begin{bmatrix} b_{\mathrm{e}1}, & b_{\mathrm{o}1}, & b_{\mathrm{e}2}, & b_{\mathrm{o}2} \end{bmatrix}^T, \\ \mathbf{a} &= \begin{bmatrix} a_{\mathrm{e}1}, & a_{\mathrm{o}1}, & a_{\mathrm{e}2}, & a_{\mathrm{o}2} \end{bmatrix}^T. \end{aligned} \tag{5.1}$$

such that $\mathbf{b} = \underline{\mathbf{S}}\mathbf{a}$. Using full-wave simulations, we find the 4×4 scattering matrix expressed as

$$\underline{\mathbf{S}} = \begin{bmatrix} \mathbf{S}_{11} & \mathbf{S}_{12} \\ \mathbf{S}_{21} & \mathbf{S}_{22} \end{bmatrix}. \tag{5.2}$$

It is convenient to define the state vectors $\mathbf{\Psi}_1 = \begin{bmatrix} a_{\mathrm{e}1}, & a_{\mathrm{o}1}, & b_{\mathrm{e}1}, & b_{\mathrm{o}1} \end{bmatrix}^T$ and $\mathbf{\Psi}_2 = \begin{bmatrix} b_{\mathrm{e}2}, & b_{\mathrm{o}2}, & a_{\mathrm{e}1}, & a_{\mathrm{o}1} \end{bmatrix}^T$, relative to port 1 and port 2, respectively. They are defined in way that the first two elements represent the amplitudes of waves propagating in the positive z direction, whereas the second two elements represent the amplitudes of waves propagating in the negative z direction. As a consequence, the transfer matrix $\underline{\mathbf{T}}$ relating them, $\mathbf{\Psi}_2 = \underline{\mathbf{T}}\mathbf{\Psi}_1$, is found as [47]

$$\underline{\mathbf{T}} = \begin{bmatrix} \mathbf{S}_{21} - \mathbf{S}_{22}\mathbf{S}_{12}^{-1}\mathbf{S}_{11} & \mathbf{S}_{22}\mathbf{S}_{12}^{-1} \\ -\mathbf{S}_{12}^{-1}\mathbf{S}_{11} & \mathbf{S}_{12}^{-1} \end{bmatrix}. \tag{5.3}$$

The T-matrices of the two structures shown in Figs. 5.3a and 5.3b are $\underline{\mathbf{T}}_{15} = \underline{\mathbf{T}}_{\mathrm{R}}\underline{\mathbf{T}}_{\mathrm{U}}\underline{\mathbf{T}}_{\mathrm{L}}$ and $\underline{\mathbf{T}}_{14} = \underline{\mathbf{T}}_{\mathrm{R}}\underline{\mathbf{T}}_{\mathrm{L}}$, respectively, where $\underline{\mathbf{T}}_{\mathrm{R}}$ and $\underline{\mathbf{T}}_{\mathrm{L}}$ are the T-matrices of the two chirped grating structures. The chirped structure represented by $\underline{\mathbf{T}}_{\mathrm{R}}$ is a flipped version, in the z direction, of the other one represented by $\underline{\mathbf{T}}_{\mathrm{L}}$, and therefore they satisfy $\underline{\mathbf{T}}_{\mathrm{R}} = \mathbf{F}\underline{\mathbf{T}}_{\mathrm{L}}^{-1}\mathbf{F}^{-1}$, if $\underline{\mathbf{T}}_{L}$ is not singular, where $\mathbf{F}$ is a transformation matrix that flips the direction of wave propagation, made by two $\mathbf{0}$ in the diagonal blocks and two identity matrices in the codiagonal blocks.

Hence, we calculate the new T-matrix $\underline{\mathbf{T}}_{\mathrm{n}} = \underline{\mathbf{T}}_{15}\underline{\mathbf{T}}_{14}^{-1} = \underline{\mathbf{T}}_{\mathrm{R}}\underline{\mathbf{T}}_{\mathrm{U}}\underline{\mathbf{T}}_{\mathrm{R}}^{-1}$ whose eigenvalues are the same of those of the unit-cell T-matrix $\underline{\mathbf{T}}_{\mathrm{U}}$, similarly to what is done in [77, 55]. The T-matrices $\underline{\mathbf{T}}_{15}$ and $\underline{\mathbf{T}}_{14}$ are obtained by transformation of the scattering matrices associated to the 4-port structures in Figs. 5.3a and Fig. 5.3b based on5.3.

According to Floquet-Bloch theory, we look for periodic solutions of the state vector as e^{-jkd} where k is the Floquet-Bloch complex wavenumber, that satisfy $\mathbf{\Psi}' = \lambda\mathbf{\Psi}$, with $\lambda \equiv e^{-jkd}$, where $\mathbf{\Psi}$ and $\mathbf{\Psi}' = \underline{\mathbf{T}}_{\mathrm{U}}\mathbf{\Psi}$ are the state vectors at the input and output of a unit cell. The eigenvalue problem is then formulated as

$$\underline{\mathbf{T}}_{\mathrm{U}}\mathbf{\Psi} = \lambda\mathbf{\Psi}, \tag{5.4}$$

where the eigenvalues $\lambda_n \equiv e^{-jk_nd}$, with $n = 1, 2, 3, 4$, are obtained by solving the dispersion characteristic equation $D(k, \omega) \equiv \det(\underline{\mathbf{T}}_{\mathrm{U}} - \lambda\underline{\mathbf{1}})$, with $\underline{\mathbf{1}}$ being the 4×4 identity matrix.

We show in Fig. 5.3c the Floquet-Bloch complex-valued wavenumber dispersion diagram

of the four eigenmodes of the structure in Fig. 5.1a. The dispersion diagram confirms the existence of the DBE at a frequency $f \approx 193$ THz, where four branches coalesce. The black-dashed curve is the dispersion diagram with a purely real wavenumber obtained via the eigenmode solver using phase-shift boundary conditions, shown here for comparison purposes. Indeed, a good matching is found for the curve with purely real wavenumber, which validates the method described above based in the dembedding procedure, that confirms the existence of the DBE.

5.3 Conclusion

We have proposed a photonic structure with double grating that exhibits a DBE in its dispersion diagram where a degenerate Bragg condition occurs at $kd = \pi$. We have demonstrated the occurrence of the DBE using two methods: (i) by finding the dispersion relation of modes with purely real wavenumbers using an eigenmode solver and observing the very flat dispersion, and (ii) by finding the four complex-valued wavenumbers from the scattering parameters by using full-wave simulations. The degenerate Bragg condition we have found in the double grating structure can be used to conceive a "degenerate distributed feedback laser", that may lead to interesting properties, even augmented when compared to a DFB laser. The first DBE laser analysis was carried out in [11] using a transmission line method for an ideal structure. Interesting properties were found in that ideal DBE structure like stability of the lasing oscillation frequency when varying the load, and lower threshold than the one in the RBE laser, even in the case when the RBE cavity has the same quality factor of the DBE cavity. Future studies shall be devoted to study the cavity effect and the lasing properties of the double grating with degenerate Bragg condition presented in this chapter.

Chapter 6

Theory of Exceptional Point of Degeneracy in Backward-Wave Oscillator with Distributed Power Extraction

We show how an exceptional point of degeneracy (EPD) is formed in a system composed of an electron beam interacting with an electromagnetic mode guided in a slow wave structure (SWS) with distributed power extraction from the interaction zone [102]. Based on this kind of EPD, a regime of operation is devised for backward wave oscillators (BWOs) as a synchronous and degenerate regime between a backward electromagnetic mode and the charge wave modulating the electron beam. Degenerate synchronization under this EPD condition means that two complex modes of the interactive system do not share just the wavenumber, but they rather coalesce in both their wavenumbers and eigenvectors (polarization states) [102]. In principle this condition guarantees full synchronization between the electromagnetic wave and the beam's charge wave for any amount of output power extracted from the

beam, setting the threshold of this EPD-BWO to any arbitrary, desired, value. Indeed, we show that the presence of distributed radiation in the SWS results in having high-threshold electron-beam current to start oscillations which implies higher power generation. These findings have the potential to lead to highly efficient BWOs with very high output power and excellent spectral purity.

6.1 Motivation and State of the Art

Exceptional points of degeneracy (EPDs) are points in parameter space of a system at which two or more eigenmodes coalesce in their eigenvalues (wavenumbers) and eigenvectors (polarization states). Since the characterizing feature of an exceptional point is the strong degeneracy of at least two eigenmodes, as implied in [16], we stress the importance to referring to it as a degeneracy. Despite most of the published work on EPDs is related to PT symmetry [17, 103, 22, 23, 104] the occurrence of an EPD actually does not require a system to satisfy PT symmetry. Indeed, EPDs have been recently found also in single resonators by just adopting time variation of one of its components [63]. EPDs are also found in uniform waveguides at their cutoff frequencies [70] and in periodic waveguides at the regular band edge (RBE) and at the degenerate band edge (DBE). However, these RBE and DBE are EPDs realized in lossless structures [42, 43, 44, 48, 47, 68]. Here, we investigate an EPD that requires both distributed power extraction and gain being simultaneously present in a waveguide called here as "slow wave structure" (SWS) since its mode is used to interact with an electron beam. Note that the passivity of the waveguide here is not dominated by dissipative losses but rather from power that is extracted in a continuous fashion from the SWS. Therefore, modes that propagate in such a waveguide experience exponential decay while they propagate, as if the waveguide was lossy. A particular and well studied case of simultaneous existence of symmetric gain and loss is based on Parity-time (PT)-symmetry,

which is a special condition that leads to the occurrence of an EPD [17, 103, 22, 23, 104], that however requires a spatial symmetry in gain and loss. The EPD considered here is far from that condition, involving two completely different media that support waves, a plasma and a waveguide for electromagnetic waves, but still require their interaction and the simultaneous presence of gain and "loss". We stress that in this chapter the term "loss" is not associated to the damping of energy, but it is rather referred to a waveguide perspective where energy exits the waveguide in a distributed fashion, a mechanism referred to as distributed power extraction (e.g., distributed radiation) from the interaction zone, for example by realizing a distributed long slot along the SWS or a set of periodically spaced holes as in Fig. 6.1.

In this chapter the linear electron beam is modeled using the description presented in[105]. Then we use a generalization of the well established Pierce model [106] to account for the interaction of the electromagnetic (EM) wave in the SWS and the electron beam, assuming small signal modulation of the beam. The Pierce model consists of an equivalent transmission line (TL) governed by telegrapher's equations, coupled to a plasma-like medium (the linear electron beam) governed by the equations that describe the electron beam dynamics. Here we add a distributed load in the Pierce model TL equations that represents the distributed power extraction. Indeed, the distributed radiation coming out of a SWS is conventionally represented by a distributed equivalent "radiation resistance" in a TL, following the well established terminology used in Antenna Theory [107, 108, 109]. Recently, two coupled transmission lines with balanced gain and loss (balanced refers to the combination that generates an EPD) were shown to support EPDs without the need of PT-symmetry [40, 41]. Even farther from the usual PT-symmetry condition, in this chapter the EPD is generated by a TL supporting backward EM wave propagation that interacts with a linear electron beam which is a plasma medium that supports two non-reciprocal waves. We show how this EPD condition can be used in high power electron beam devices. Backward-wave oscillators (BWOs) are widely used as high power sources in radars, satellite communications, and various other applications. A BWO is composed of a SWS that guides EM backward waves,

where their phase and group velocities have opposite directions. The interaction between the electron beam and a backward EM mode constitutes a distributed feedback mechanism that makes the whole system unstable at certain frequencies [110, 111]. One of the most challenging issues in BWOs is the limitation in power generation level, i.e., the extracted power from the electron beam relative to its total power. Indeed conventional BWOs exhibit small starting beam current (to induce sustained oscillations) and limited power efficiency, without reaching very high output power levels. The extracted power in a conventional BWO is taken from one of the SWS waveguide ends. In this chapter, we investigate the physics of EPD resulting from the interaction between an electron beam and an EM mode, moreover, we propose to use such EPD to conceive high power sources, and this technique can be used from microwaves to terahertz frequencies. The proposed "degenerate synchronization regime" of operation in a BWO is based on the EPD generated by the simultaneous presence of gain (coming from the electron beam) and continuous distributed power extraction from the EM guided wave (rather than power extraction from the waveguide end). Therefore we stress that the term "loss" does not refer to material loss but rather to a distributed power extraction mechanism (Fig. 6.1) that in antennas terminology is referred to as "radiation loss", while the gain is provided by the electron beam interacting with the SWS. The distributed power extraction from the interaction zone occurs either via a distributed set of radiating slots along the SWS (Fig. 6.1), or alternatively by collecting the distributed extracted power via an adjacent coupled waveguide.

Recently, SWSs exhibiting a degenerate band edge (DBE), which is an EPD of order four in a *lossless* periodic waveguide, were proposed to enhance the performance of high power devices [4, 112, 5, 57]. It is important to point out that the DBE discussed in these previously mentioned works were obtained in the cold SWS by exploiting periodicity, and the benefit of such DBE would gracefully vanish while increasing the electron beam power. In this chapter, instead, we propose an interaction regime where the EPD is maintained in the hot SWS, i.e., in presence of the interacting electron beam, that is a very large source of distributed gain.

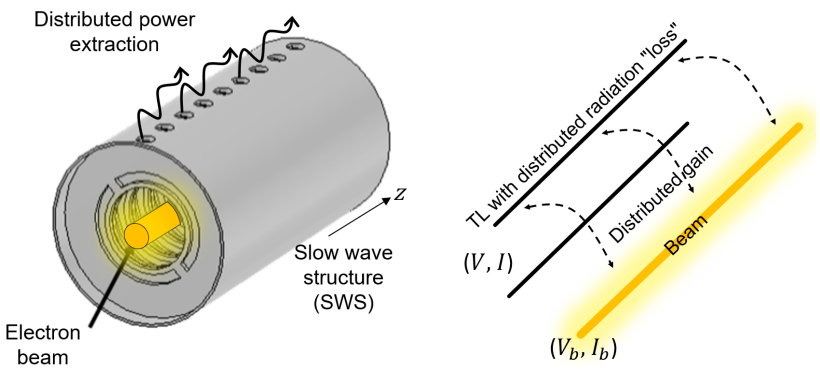

(a) (b)

Figure 6.1: (a) An example of SWS with distributed radiating slots that extract power from the guided modes interacting with the electron beam. (b) Pierce-based equivalent transmission line model of the SWS with distributed "loss" (i.e., radiation) coupled to the charge wave modulating the electron beam. From the transmission line point of view, the interaction with the beam is seen as distributed gain.

The degenerate synchronization between the charge wave induced on the electron beam and the EM slow wave occurs at the EPD, making this degenerate synchronization regime a very special condition not explored previously.

6.2 System Model

Consider the SWS shown in Fig. 6.1a supporting a Floquet-Bloch mode whose slow wave spatial harmonic interacts with an electron beam, and radiates via a distributed set of slots (radiation occurs via a fast wave spatial harmonic, usually the so called "-1" harmonic). The configuration in Fig. 6.1a is given as a possible realization, though another one may consist in collecting the power exiting the interaction zone in a distributed fashion by an adjacent waveguide. We assume that the interaction between the SWS mode and the electron beam is modeled via the Pierce small-signal theory of traveling-wave tubes [105, 113, 114, 115, 106, 116, 117] that describes the evolution of the EM fields and electron beam dynamics

assuming small signal modulation in the beam's electron velocity and charge density. The beam electrons have average velocity and linear charge density u_0 and ρ_0, respectively. The electron beam has an average (dc) current $I_0 = -\rho_0 u_0$ and a dc (time-average) equivalent kinetic dc voltage $V_0 = \frac{1}{2}u_0^2/\eta$ [111], [118], and $\eta = e/m = 1.758820\times10^{11}$ C/Kg is the charge-to-mass ratio of the electron with charge equal to $-e$ and m is its rest mass and ρ_0 is negative. The small signal modulation in electron beam velocity and charge density u_b and ρ_b, respectively, form the so called "charge wave". The linearized basic equations governing charge motion and continuity are written in their simplest form as [106]

$$\begin{aligned} \partial_t u_b + u_0 \partial_z u_b &= -\eta e_z, \\ \partial_t \rho_b &= -\rho_0 \partial_z u_b - u_0 \partial_z \rho_b, \end{aligned} \tag{6.1}$$

where e_z is the electric field component in the z-direction of the EM mode in the SWS interacting with the electron beam, and the operator ∂_σ indicates differentiation with respect to the variable σ. For convenience, we define the equivalent kinetic beam voltage and current as $v_b = u_b u_0/\eta$ and $i_b = u_b\rho_0 + u_0\rho_b$. Assuming an $e^{i\omega t}$ time dependence for monochromatic fields, the two equations in (6.1) are written in terms of the beam equivalent voltage and current in phasor domain as

$$\begin{aligned} \partial_z V_b &= -i\beta_0 V_b - E_z, \\ \partial_z I_b &= -igV_b - i\beta_0 I_b, \end{aligned} \tag{6.2}$$

where $\beta_0 = \omega/u_0$ is the beam's equivalent propagation constant and $g = \frac{1}{2}I_0\beta_0/V_0$. Small fonts are used for the time-domain representation while capital ones are used for the phasor-domain representation.

The EM mode propagating in the SWS is described by the equivalent transmission line in Fig. 6.1b, with distributed per-unit-length series impedance Z and shunt admittance Y, and equivalent voltage $V(z)$ and current $I(z)$ phasors that satisfy the telegrapher's equations

$$\begin{aligned} \partial_z V &= -ZI, \\ \partial_z I &= -YV + I_s. \end{aligned} \tag{6.3}$$

The term I_s in (6.3) accounts for the electron stream flowing in the SWS that loads the TL as a shunt displacement current according to [106, 114, 117] and whose expression is given by $I_s = -\partial_z I_b$. For the non-interactive EM system (i.e., when I_s=0), the propagation constant and the characteristic impedance of the electromagnetic mode are given by $\beta_p = \sqrt{-ZY}$ and $Z_c = \sqrt{Z/Y}$, respectively. The two root solutions represent waves that propagate in opposite directions, i.e., both β_p and $-\beta_p$ are valid solutions because of reciprocity. In this chapter we consider that the SWS supports either a "forward" or a "backward" mode. The modal propagation constant is a complex number, $\beta_p = \beta_{pr} + i\beta_{pi}$,where $\beta_r\beta_i < 0$ for forward modes and $\beta_r\beta_i > 0$ for backward modes. For example, when the the TL is supporting forward wave propagation both roots in β_p and Z_c must be taken as the principal square roots, so that their real part is positive. In this case β_p turns out to be in in the fourth complex quadrant [119]. However, for TL supporting backward wave propagation the root of $\beta_p = \sqrt{-ZY}$ is taken as the principle square root (resulting in a positive real part) while the root of $Z_c = \sqrt{Z/Y}$ is taken as the secondary square root (resulting in a negative real part). In this case β_p turns out to be in in the first complex quadrant[119].

Based on the Pierce's model [106], the EM wave couples to the electron beam with its longitudinal electric field given by $E_z = -\partial_z V$. For convenience, we define a state vector $\mathbf{\Psi}(z) = [\ V(z),\ \ I(z),\ \ V_b(z),\ \ I_b(z)\ ]^T$ that describes the system evolution with coordinate z. Thus, the interacting EM mode and electron-beam charge wave are described as [117]

$$\partial_z \mathbf{\Psi}(z) = -i\underline{\mathbf{M}}\mathbf{\Psi}(z), \tag{6.4}$$

where $\underline{\mathbf{M}}$ is the 4×4 system matrix

$$\underline{\mathbf{M}} = \begin{bmatrix} 0 & -iZ & 0 & 0 \\ -iY & 0 & -g & -\beta_0 \\ 0 & -iZ & \beta_0 & 0 \\ 0 & 0 & g & \beta_0 \end{bmatrix}. \tag{6.5}$$

This description in terms of a multidimensional first order differential equation in (6.4) is ideal for exploring the occurrence of EPDs in the system since an EPD is a degeneracy associated to two or more coalescing eigenmodes, hence it occurs when the system matrix $\underline{\mathbf{M}}$ is similar to a matrix that contains a non-trivial Jordan block. In general there are four independent eigenmodes, and each eigenmode is described by an eigenvector $\mathbf{\Psi}(z)$, hence it includes both the EM and the charge wave. At the EPD investigated in this chapter two of these four eigenvectors coalesce.

6.3 Second order EPD in an Interacting Electromagnetic Wave and an Electron Beam's Charge Wave

Assuming a state vector z-dependence of the form $\mathbf{\Psi}(z) \propto e^{-ikz}$, where k is the wavenumber of a mode in the interacting system, i.e., in the hot SWS, the eigenmodes are obtained by solving the eigenvalue problem $k\mathbf{\Psi}(z) = \underline{\mathbf{M}}\mathbf{\Psi}(z)$, and the modal dispersion relation is given by

$$
\begin{aligned}
D(\omega, k) &= \det\left(\underline{\mathbf{M}} - k\underline{\mathbf{I}}\right) \\
&= k^4 - 2\beta_0 k^3 + \left(\beta_0^2 + ZY - iZg\right)k^2 \\
&\qquad -2\beta_0 ZYk + \beta_0^2 ZY = 0.
\end{aligned} \tag{6.6}
$$

The solution of this equation leads to four modal complex wavenumbers that describe the four modes in the EM-electron beam interactive system. A second order EPD occurs when two of these eigenmodes coalesce in their eigenvalues and eigenvectors, which means that the matrix $\underline{\mathbf{M}}$ is similar to a matrix that contains a Jordan block of order two [40, 41]. Following the theory in [33], the algebraic formulation that is often used to determine EPDs is equivalent to a bifurcation theory that is here applied. Indeed the EPD radian frequency and wavenumber are simply obtained by setting $D(\omega_e, k_e) = 0$ and $\partial_k D(\omega_e, k)\big|_{k_e} = 0$ as in [33], where the EPD is designated with the subscript e. Based on the derivation presented in [102], these two conditions show that the EPD occurs when the transmission line per-unit-length series impedance and shunt admittance are $Z = Z_e$ and $Y = Y_e$, where

$$
Z_e = \frac{i\beta_{0e}^2\delta_e^3}{g_e}, \qquad Y_e = \frac{ig_e(\delta_e + 1)^3}{\delta_e^3}, \tag{6.7}
$$

and $\delta_e = (k_e - \beta_{0e})/\beta_{0e}$ represents the relative deviation of degenerate modal wavenumber k_e (of the interactive system) from the beam equivalent propagation constant $\beta_{0e} = \omega_e/u_0$.

Using (6.7), we constrain δ_e to provide Z_e and Y_e with positive real part, that means we assume that the TL is passive because of SWS losses and especially because of the distributed power extraction mechanism. Figure 6.2 shows the two sectoral regions of δ_e that allow EPDs for transmission line that support either forward or backward propagation. These two regions satisfy the passivity condition of the TL, $\mathrm{Re}(Z) \geq 0$ and $\mathrm{Re}(Y) \geq 0$, where the real part of Z and Y represents mainly distributed power extraction (i.e., radiation losses

using a terminology in the antennas community). It is important to point out that dark blue regions in Fig. 6.2 correspond to complex values of δ_e where EPD is obtained for TL that has also gain (independently of the electron beam). The two light blue and red narrow sectoral regions in Fig. 6.2 also correspond to an electron beam that delivers energy to the TL [102]. In the rest of this chapter we focus on the light blue region that represents complex values of δ_e associated to EPDs resulting from the interaction of a backward propagating electromagnetic wave and the charge wave modulating the electron beam. We stress that distributed radiated power is represented by series and/or parallel "losses" in the passive TL.

We now simplify the two equations given in (6.7) to get rid of δ_e as follows: from the first equation in (6.7) we find that $\delta_e = \sqrt[3]{-ig_eZ_e/\beta_{0e}^2}$, where the proper choice of root, based on chart in Fig. 6.2, is the one that guarantees the passivity of the TL and that there is power delivered from the beam to the TL [102]. For example, the root of $\sqrt[3]{-ig_eZ_e/\beta_{0e}^2}$ should lie in the light blue region in the chart to have an EPD with passive TL that support backward wave. Roots of $\sqrt[3]{-ig_eZ_e/\beta_{0e}^2}$ that lie in the dark blue region are ignored because they would result in an EPD that requires an active TL, while here we consider only passive TLs because of power extraction. The EPD conditions in (6.7) are simplified by substituting the previous expression of δ_e in the second equation of (6.7), leading to an interesting equation that constrains the TL parameters and the electron beam parameter g_e:

$$-Z_eY_e/\beta_{0e}^2 = \left(\sqrt[3]{-ig_eZ_e/\beta_{0e}^2} + 1\right)^3. \tag{6.8}$$

The above equation constrains all the system parameters to have an EPD, hence it says that for an EPD to occur, a specific choice of the electron beam current $I_0 = I_{0e}$ and angular frequency $\omega = \omega_e$ must be selected. This is in good agreement with the general

theory presented in [120] that indicates that a two-parameter family of complex matrices accounting for a strong coupling between eigenvalues possesses a double eigenvalue with the Jordan block, which defines the EPD. In other words it says that for a given electron beam described by β_{0e}, and g_e, the cold TL parameters Z_e and Y_e must be chosen accordingly. The condition in (6.8 can also be rewritten in term of the propagation constant β_{pe} and the characteristic impedance Z_{ce} of the cold TL as $(\beta_{pe}/\beta_{0e})^2 = \left(\sqrt[3]{g_e Z_{ce}\beta_{pe}/\beta_{0e}^2} + 1\right)^3$.

In general, the interaction between the charge wave and the EM wave occurs when they are synchronized, i.e., by matching the EM wave phase velocity ω/β_p to the average velocity of the electrons $u_0 = \omega/\beta_0$, a condition that is specifically called "synchronization". Note that this is just an initial criterion, because the phase velocity of the modes in the *interactive* systems are different from ω/β_p and u_0. When the system parameters are such that equation (6.8) is satisfied and hence an EPD occurs, there are two modes (in the interactive system) that have exactly the same phase velocity $\omega/\mathrm{Re}(k_e)$. Since this synchronization condition corresponds to an EPD, the two modes in the interactive system are actually identical also in their eigenvectors $\mathbf{\Psi}$. Note that the spatial z-evolution of the interacting EM and electron charge wave is described by four modes that are solutions of (6.4), three of which have a positive real part of k [102]. At the EPD two of these four modes coalesce, i.e., they become identical, that is why we refer to this condition as "degenerate synchronization". In this chapter we explore and enforce this very special kind of synchronization based on an EPD. In particular we enforce two of the resulting eigenmodes to fully coalesce in both their wavenumber and system state variable $\mathbf{\Psi}(z)$. This condition is a different kind of EPD found in physical systems that does not satisfy PT-symmetry since it involves the coupling between two different media of propagation, and may be very promising for achieving regimes of operation in electron beam devices, with advantages not obtainable in conventional regimes.

The EPD condition obtained in (6.8) guarantees that the system has two repeated eigenvalues and two coalesced eigenvectors [102]

$$k_e = \sqrt[3]{\beta_{0e}\beta_{pe}^2},$$
$$\boldsymbol{\Psi}_e = [\ 1,\ \ ik_e/Z,\ \ 1/\delta_e,\ \ g_e/(\beta_{0e}\delta_e^2)\ ]^T, \tag{6.9}$$

that form the "degenerate synchronization". For the interacting system of EM and charge wave, the EPD represents a point in parameter space at which the system matrix $\mathbf{M}$ in (6.5) is not diagonalizable and it is indeed similar to a matrix that contains a 2×2 Jordan block. This implies that the solution of (6.4) includes an algebraic linear growth factor resulting in unusual wave propagation characteristics as discussed next.

Solution of (6.6) leads to four eigenmode wavenumbers and due to the highly non-reciprocal physical nature of the electron beam, three have positive real part (i.e., $\mathrm{Re}(k) > 0$) and one has it negative. According to the traveling-wave tube theory in [113], [106], conventionally applied to BWOs [110], these three distinct wavenumbers with $\mathrm{Re}(k) > 0$ participate to the synchronization mechanism, and the electric field in the SWS is generally represented as

$$V(z) = V_1 e^{-ik_1 z} + V_2 e^{-ik_2 z} + V_3 e^{-ik_3 z}. \tag{6.10}$$

Remarkably, at the EPD the interactive system has two modes with the same degenerate wavenumber k_e, resulting in a guided electric field with linear growth factor as

$$V(z) = zV_1 e^{-ik_e z} + V_2 e^{-ik_e z} + V_3 e^{-ik_3 z}, \tag{6.11}$$

which is completely different from any other regime of operation. A degenerate mode de-

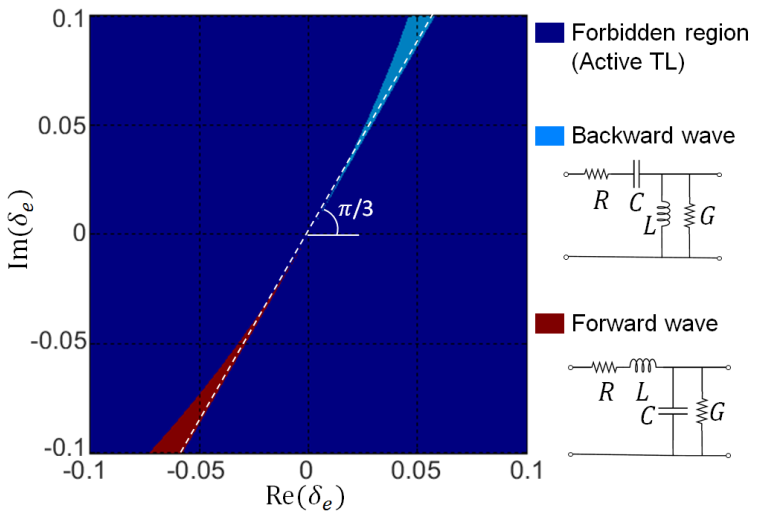

Figure 6.2: The two sectoral regions represent complex values of δ_e, associated to EPDs resulting from the interaction of backward or forward electromagnetic waves (radiation is represented in TL by series or/and parallel losses) and the charge wave of electron beam. The value $\delta_e = (k_e - \beta_0)/\beta_0$ represents the wavenumber deviation of the EPD complex wavenumber k_e (of the interactive system) from the equivalent electron beam wavenumber β_0, that satisfies (6.7), assuming SWS realizations based on passive equivalent TLs. There are two regions of possible realizations (red and light blue), associated to the two distributed per-unit-length TL circuits on the right panel, that represent SWSs supporting either forward or backward wave propagation. In this chapter we focus on EPDs obtained from backward electromagnetic waves interacting with an electron beam, i.e., those leading to $\mathrm{Re}(\delta_e) > 0$ and $\mathrm{Im}(\delta_e) > 0$.

scribed by $\mathbf{\Psi}_e$ is composed also of the charge wave, which implies that also the charge wave propagation is described as in (6.11), with two terms having the same degenerate wavenumber k_e, and one of them exhibiting the algebraic linear growth besides the exponential behavior.

In the following we show an example of degenerate synchronization based on an electron beam with dc voltage of $V_0 = 23$ kV and dc current of $I_0 = 0.1$ A. We derive the system parameters assuming that the EPD electron beam current $I_0 = I_{0e} = 0.1$ A (hence the choice of the TL parameters are chosen accordingly) and assume the operational frequency at which the EPD occurs is 1 GHz. We require (as an example) a relative degenerate wavenumber deviation of $\delta_e = 0.01 + i0.017$ that is lying exactly on the white dashed line shown in Fig. 6.2, with $\angle\delta_e = \pi/3$ (the phase of δ_e). The corresponding wavenumber of two coalescing modes in the interactive system is $k_e = (1 + \delta_e)\,\beta_{0e}$ which is $k_e = (1.01 + i0.017)\,\beta_{0e} = 70.55 + i1.21$ m^{-1}.

By imposing the beam parameters and the chosen δ_e in the EPD conditions in (6.7) we obtain the distributed per-unit-length TL impedance and admittance of SWS to be $Z_e = -i257.1$ Ohm m^{-1} (i.e., capacitive) and $Y_e = 1 - i19.54$ siemens m^{-1} (i.e., inductive with losses), representing a backward wave in the SWS. Losses here are not modeling energy damping but rather energy extraction (e.g., radiation) from the TL, per unit length, like in a backward leaky wave antenna [121]. To obtain these values, we have chosen the per-unit-length TL parameters for backward wave propagation as $C = 0.62$ pFm, $L = 8.14$ pHm, $R = 0$ Ohm m^{-1} and $G = 1$ siemens m^{-1}. Figure 6.3 shows the dispersion relation of three complex modes in the "hot" SWS, i.e., in the interactive EM wave-electron beam system, obtained using the Pierce-based model as explained in [117]. (The fourth mode with $\mathrm{Re}(k_e) < 0$ is not shown since it does not have a significant role in the synchronism). We show in Fig. 6.3 the real and imaginary parts of wavenumbers of three eigenmodes in the hot SWS versus normalized frequency (red curves), together with the dispersion of the beam alone (i.e., the beam "line" in green that actually represents two curves since we are neglecting the effect of the beam plasma frequency here) and of the backward wave in the cold SWS (blue curve, with negative slope). It is obvious from the figure that two eigenmodes of the interactive system coalesce at the EPD frequency f_e, forming an EPD of order two. Each of these two eigenmode has an EM wave and a charge wave counterpart, though far from the EPD frequency they tend to recover the beam line (green line) and the EM mode in the cold SWS (blue line).

We recall that the SWS is a periodic structure, and it is the slow wave harmonic of a mode that interacts with the electron beam charge wave. Though slow waves do not radiate, a spatial Floquet-Bloch harmonic of the mode is fast and able to radiate through the slots [121], justifying the presence of the conductance $G = 1$ siemens m^{-1}, real part of $Y_e = 1 - i19.54$ siemens m^{-1}, in the TL model.

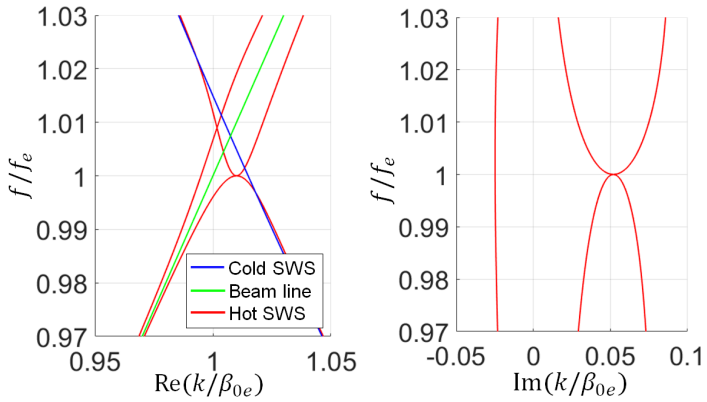

(a) (b)

Figure 6.3: Dispersion diagram for three of the four complex modes in the "hot" SWS (the modes in the SWS interacting with the electron beam), in red, showing the existence of a second order EPD, where two modes coalesce in their wavenumbers and eigenvectors: (a) Real part of the wavenumber of the modes phase-propagating in the positive z direction ($\mathrm{Re}(k_e) > 0$). The blue line represents the dispersion of the EM mode in the cold SWS supporting a backward propagation, whereas the green line is the electron beam's charge wave dispersion, without accounting for their interaction. (b) Imaginary part of the wavenumber of the three modes with $\mathrm{Re}(k_e) > 0$ resulting from the interaction. The EPD wavenumber at $f = f_e$ represents two fully degenerate and synchronous modes with exponential growth in z.

6.4 EPD-BWO Threshold Current

The EPD is here employed to conceive a regime of operation for BWOs based on "degenerate synchronization" between an EM wave and the electron beam. To explain this concept we refer to the setup in Fig. 6.4a for a BWO that has "balanced gain and radiation-loss" per unit length, where distributed loss is actually representing distributed radiation (per unit length) via a shunt conductance G (see Fig. 6.4). The description is following the steps in [106] and [110] outlined for BWOs, where the TL is represented by a distributed circuit model shown in Fig. 6.4b that supports backward waves. An important difference from a standard BWO is that here the TL has shunt distributed "losses" that actually model the distributed radiation and whose presence is necessary to satisfy the EPD condition (6.8). We assume to have an unmodulated space charge at the beginning of the electron beam, i.e., $V_b(z = 0) = 0$ and $I_b(z = 0) = 0$ and we assume that the SWS waveguide length is

$\ell = N\lambda_e$, where $\lambda_e = 2\pi/\beta_{0e}$ is the guided wavelength calculated at the EPD frequency and N is the normalized SWS length. We also assume that the SWS waveguide is terminated by a load at $z = 0$ matched to the characteristic impedance of the TL (without loss and gain) $R_o = \sqrt{L/C}$ and by a short circuit at $z = \ell$. We follow the same procedure used in [110] to obtain the *starting oscillation condition* which is based on imposing infinite voltage gain $A_v = V(0)/V(\ell) \to \infty$. After simplification, and using the three-wave traveling-wave theory [106, 110], the voltage gain is written in terms of the three modes concurring to the synchronization (those with $\mathrm{Re}(k) > 0$) as

$$A_v^{-1} e^{i\beta_0 \ell} = \frac{e^{-i\beta_0 \delta_1 \ell} \delta_1^2}{(\delta_1 - \delta_2)(\delta_1 - \delta_3)} + \frac{e^{-i\beta \delta_2 \ell} \delta_2^2}{(\delta_2 - \delta_3)(\delta_2 - \delta_1)} + \frac{e^{-i\beta_0 \delta_3 \ell} \delta_3^2}{(\delta_3 - \delta_1)(\delta_3 - \delta_2)} = 0, \tag{6.12}$$

where $\delta_n = (k_n - \beta_0)/\beta_0$ and k_1, k_2 and k_3 are the three wavenumbers of the interactive EM-beam system with positive real part that are solutions of (6.6). In close proximity of the EPD there are two modes coalescing, with $\delta_1 = \delta_a + \Delta/2$ and $\delta_2 = \delta_a - \Delta/2$ where $\delta_a = (\delta_1 + \delta_2)/2$ is the average, and $|\Delta| \ll |\delta_a|$ is a very small quantity that vanishes at the EPD. By observing that $|e^{-i\beta_0 \delta_3 \ell}| \ll 1$ for very large ℓ because $\mathrm{Im}(k_3)<0$, the gain expression in (6.12) reduces to

$$A_{ve}^{-1} e^{i\beta_0 \ell} \approx \frac{e^{-i\beta_0 \delta_a \ell} \delta_a^2}{(\delta_a - \delta_3)} \frac{\sin(\Delta\beta_0 \ell/2)}{\Delta/2} = 0 \ . \tag{6.13}$$

From the above condition, assuming very large ℓ, the first oscillation frequency occurs when $\Delta\beta_0 \ell = 2\pi$. This happens when the constraint on the wavenumbers $k_1 - k_2 = 2\pi/\ell$ is

satisfied. This shows a very important fact, that for infinitely long structure $\ell \to \infty$ the starting oscillation condition is $k_1 = k_2 = k_e$, which corresponds to the EPD condition. This implies that the EPD is the exact condition for synchronization between the charge wave and EM wave, accounting for the interaction in infinitely long SWSs, that guarantees the generation of oscillations at the EPD frequency $f_e = \omega_e/(2\pi)$.

For finite length SWS, oscillations occurs when $k_1 - k_2 = 2\pi/\ell$ is satisfied, assuming very large ℓ, and since $|\Delta| \ll |\delta_a|$, we have both k_1 and k_2 very close to k_e, which implies that the systems is close to the EPD and hence the threshold beam current I_{th} that starts oscillations is slightly different from I_{0e}. A beam current slightly away from the EPD one causes the wavenumbers to bifurcate from the degenerate one k_e, following the Puiseux series approximation [122] (also called fractional power expansion) as

$$k_n - k_e \approx (-1)^n \alpha \sqrt{I_0 - I_{0e}}, \tag{6.14}$$

with $n = 1, 2$, and α is a constant. This implies that $k_1 - k_2 \approx -2\alpha\sqrt{I_0 - I_{0e}}$, and by comparing this with the $k_1 - k_2$ difference associated to the threshold beam current in a finite length SWS we infer that the threshold beam current I_{th} that makes the EPD-BWO of finite length ℓ oscillate, asymptotically scales as

$$I_{th} \sim I_{0e} + \left(\frac{\pi/\alpha}{\ell}\right)^2. \tag{6.15}$$

In a conventional BWO, that has no distributed power extraction and the power is delivered only to the load R_0, the threshold current scaling decrease with the SWS length asymptotically as $I_{th} \sim \zeta/\ell^3$ [123, 110], where ζ is a constant. Instead, the EPD-BWO has a

threshold current in (6.15) always larger than the EPD beam current I_{0e}, which represents the current that keeps the oscillation going and simultaneously balance the distributed radiated power. Importantly, the EPD beam current I_{0e} can be engineered to any desired (high) value depending on how much power one wants to extract from the electron beam.

The above derivation was based on assuming $\ell \to \infty$, and a rigorous derivation for any length of the EPD-BWO SWS as done in [102] that leads to the determination of the threshold current and oscillation frequency. This Pierce-based formulation for the beam current threshold is used to compute the results shown in Fig. 6.4 for varying the EPD-BWO length and the shunt conductance G that represents the distributed radiation.

Figure 6.4e shows the scaling of the threshold current versus SWS length for a system with the same parameters used in the previous example. The scaling shows that for infinitely long SWSs the oscillation starting current is equal to the EPD beam current I_{0e} which is consistent with the asymptotic relation in (6.15). Figure 6.4d also shows a comparison between the threshold current of the conventional BWO (that does not have distributed power extraction, i.e., $G = 0$) and that of the EPD-BWO (with distributed power extraction, represented by $G = 1$ siemens m^{-1}) by showing their current scaling with the SWS length. The threshold beam current I_{th} of the conventional BWO vanishes when the SWS length increases, whereas the threshold beam current I_{th} of the EPD-BWO tends to the value of $I_{0e} = 0.1$ A. Figure 6.4e shows the threshold beam current $I_0 = I_{0e}$ (blue curve) that leads to the EPDs as a function of the radiation "loss" per unit length G . We also show the required starting beam current (i.e. the threshold) for oscillations (red curve) for a finite length "hot" SWS working at the EPD; we assume the SWS length normalized to the wavelength at the EPD frequency of $N = 70$. It is important to point out that the radiated power per-unit-length of the SWS is determined using $p_{rad}(z) = \frac{1}{2}G|V(z)|^2$, thus it is linearly proportional to the parameter G , i.e., higher values of G imply higher radiated power per-unit-length and therefore higher level of energy extraction from the SWS.

We have shown two very important facts here: first, the threshold beam current is very close to the EPD beam current for any desired value of power extracted. This indicates that the EPD condition for hot SWSs with finite length is the condition that basically guarantees full synchronization between the EM guided mode and the beam's charge wave. Secondly, the threshold current increases monotonically when increasing the required radiated power per unit length which implies a tight synchronization regime guaranteed for any high power generation. Therefore, in principle according to a Pierce-based model, the synchronism is maintained for any desired power output, and this trend is not observed in conventional BWOs where the load is at the beginning or end of the SWS.

6.5 Conclusion

We have conceptually demonstrated the occurrence of an EPD in an interactive system made of a linear electron beam and a guided electromagnetic wave. This EPD condition leads to a regime of operation for BWOs where the EPD guarantees a synchronism between a backward wave and a beam's charge wave through enforcing the coalescence of two modes in both their wavenumber and state vector, a regime we named "degenerate synchronization". A remarkable aspect of this EPD-BWO regime is that the "gain and distributed-power-extraction balance" condition leads to a perfect degenerate synchronization between the charge wave and EM wave for any amount of designed distributed power extraction. This distributed power extraction can be in the form of distributed radiation from the interaction zone or of distributed transfer of power from the hot SWS to an adjacent coupled waveguide. Under this EPD-BWO regime, in principle it is possible to extract large amounts of power from the electron beam and therefore the EPD-BWO exhibits high starting beam current. In theory the starting-oscillation beam current (i.e, the threshold) could be set to arbitrary

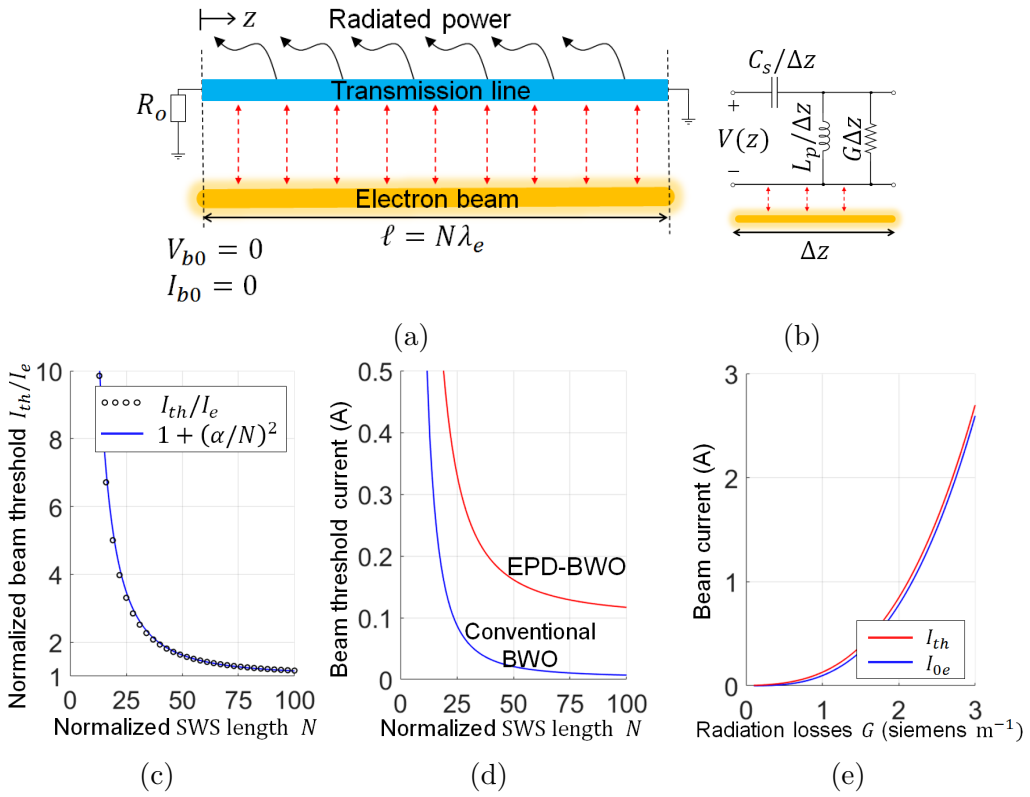

Figure 6.4: (a) Schematic setup for BWOs with "balanced gain and radiation-loss". (b) Equivalent transmission line model of the SWS with distributed (per-unit-length) series capacitance and shunt inductance for a SWS that supports backward waves. The distributed shunt conductance G represents distributed power extraction, that is indeed given by $p_{rad}(z) = G|V(z)|^2/2$. (c) Scaling of the oscillation-threshold beam current I_{th} versus SWS length normalized to the wavelength $N = \ell/\lambda_e$, where $\lambda_e = 2\pi/\beta_{0e}$ is the guided wavelength calculated at the EPD frequency. It is obvious that for infinite long SWS where $N \to \infty$ we have $I_{th} \to I_{0e}$ which implies that the EPD synchronization condition is also the threshold for infinitely long SWSs. (d) Comparison of the threshold current for an EPD-BWO and a standard BWO for increasing SWS length. Note that the threshold of the EPD-BWO does not decreases to zero for longer SWSs, a characteristic that is fundamentally different from that of a standard BWO. (e) Scaling of the EPD beam current $I_0 = I_{0e}$ (blue curve) versus radiation losses G. We also show the scaling of the threshold beam current (red curve) for a finite-length SWS with $N = 70$. Note that the threshold beam current is very close to the EPD current for any amount of required distributed extracted power which indicates that in principle the synchronism is achieved for any output power level.

large values, in contrast to what happens in conventional BWOs where the beam's starting current tends to vanish when the SWS lengths increases. Remarkably, in the EPD-BWO regime the starting oscillation current is always larger than the EPD's beam current that, in principle, can be set to large values by increasing the amount of power extracted per unit length. Therefore we have shown the fundamental principle that the amount of power generated under the EPD-BWO regime has no upper limit (the actual limit would be imposed only by the constraints encountered in the practical realizability), contrarily to conventional knowledge of BWOs.

Note that the degenerate synchronization regime discussed in this chapter is very different from the ones discussed in [4, 112, 5, 57]. There, it was the "cold" SWS that exhibited a degeneracy condition, like the degenerate band edge (DBE), which is an EPD of order four, or the stationary inflection point (SIP), which is an EPD of order three, that were proposed to enhance the performance of high power devices. Those DBE and SIP EPD conditions were obtained in cold SWSs based on periodicity, and indeed the interaction of the EM modes with the electron beam would perturb those degeneracy conditions, and even destroy them for increasingly large values of electron beam currents. Here, instead, we have proposed a fully synchronous degenerate regime based on the concept of "distributed radiation and gain balance", where the EPD occurs in the hot structure, i.e., in presence of the interacting electron beam with any amount of current and hence, in principle, for any large amount of power.

Chapter 7

High Power X-band Relativistic BWO with Degenerate Synchronous Regime Operating at an Exceptional Point

An exceptional point of degeneracy (EPD) is induced in a system made of a linear electron beam interacting with an electromagnetic (EM) guided mode in a vacuum tube made of a corrugated circular metallic waveguide with distributed output ports [102, 124]. This scheme enables a degenerate synchronous regime in backward wave oscillators (BWOs) where the electron beam provides distributed gain to the EM mode with distributed power extraction. Particle-in-cell simulation (PIC) results demonstrate that the proposed EPD-BWO has a starting-oscillation current that scales quadratically with BWO length to a non-vanishing value, which does not occur in standard BWOs and demonstrates the occurrence of the EPD and hence the degenerate synchronism operational regime [124]. The degeneracy of two interactive hybrid modes is also verified by observing the coalescence of their complex-valued wavenumbers at the EPD frequency. Observations on the kinetic energy distribution of the electrons along the BWO demonstrate that the proposed EPD-BWO regime is capable

of achieving higher power conversion efficiency at higher levels of power generation due to its ability of maintaining the synchronism for longer BWO lengths compared to the standard BWO regime of operation [102, 124].

7.1 Motivation and State of the Art

An exceptional point of degeneracy (EPD) is here demonstrated in a system made of an electron beam interacting with an electromagnetic (EM) guided mode. The characterizing feature of an exceptional point is the spectral singularity resulting from the degeneracy of at least two eigenstates. We stress the importance to refer to it as "degeneracy" as implied in [16]. Despite most of the published work on EPDs are related to parity time (PT) symmetry [17, 38], the occurrence of EPDs does not necessarily require a system to satisfy the PT symmetry condition, however, in several case it involves a system to simultaneously have gain and loss [125]. The system we consider in this chapter involves two complete different media that support waves: an electron beam (e-beam) that supportsspace charge waves and a waveguide that supports EM waves. Exchange of energy occurs when an EM waves in a slow wave structure (SWS) interacts with the e-beam. In this chapter the degeneracy condition is enabled by the distributed power extraction (DPE) from the SWS waveguide as shown in Fig. 7.1. The energy that is extracted from the e-beam and delivered to the guided EM mode is considered as a distributed gain from the SWS perspective, whereas the DPE represents extraction "losses" and not mere dissipation [102, 126].

Backward-wave oscillators (BWOs) are high power sources where the power is transferred from a very energetic e-beam to a synchronized EM mode [127]. The extracted power in a conventional BWO is usually taken at one end of the SWS [128, 110] as shown in Fig. 7.1a. One challenging issue in BWOs is the limitation in power generation level. Indeed conventional BWOs exhibit small starting beam current (to induce sustained oscillations)

and limited power efficiency without reaching very high output power levels [129]. Several techniques were proposed in literature to enhance the power conversion efficiency of BWOs by optimizing the SWS and its termination. For example, non-uniform SWSs were proposed to enhance efficiency of BWOs in [130], in [131] a resonant reflector was used to enhance efficiency to about 30%, and a two-sectional SWS was also proposed to enhance the power efficiency in [132]. These were optimization techniques. Here, instead, we demonstrate the effectiveness of a regime of operation of a BWO based on an EPD , i.e., exploiting the properties pertaining to the physics of an EPD realized using a DPE scheme as depicted in Fig. 7.1b. We refer to a BWO that is operating at an EPD, like the one in Fig. 7.1b, as an EPD-BWO. In this chapter we show the physical mechanism of an EPD arising from the interaction of an e-beam and and EM wave in a SWS and we show how this finding can be used as a regime of operation in what we call an EPD-BWO to produce very high power with high efficiency.

In our previous work in [102] a theoretical and idealistic analysis of EPD-BWOs based on a generalized Pierce model [106] was presented. Here, the demonstration of the EPD-BWO physical mechanism, is provided in a realistic system as the one in Fig. 7.1b using particle-in-cell (PIC) simulations. PIC simulations provide some of the most accurate results available from the state of the art modeling techniques of realistic vacuum electronics devices and by many are regarded as an essential step toward the experimental demonstration of a prototype. A realistic interaction between an electromagnetic wave and an electron beam is investigated in a cylindrical metallic SWS with various extraction ports as shown in Fig. 7.1b. This chapter proves the existence of the EPD in such a system by first demonstrating the asymptotic trend of the *starting* e-beam current that decreases quadratically with SWS length to a non-vanishing value, which is predicted theoretically in [102] and here demonstrated using accurate PIC simulations. In this chapter, we also derive an important formula that estimates the value of the e-beam current that generates the EPD (it was not provided in [102]). Besides the observed unconventional trend of the starting current peculiar of the

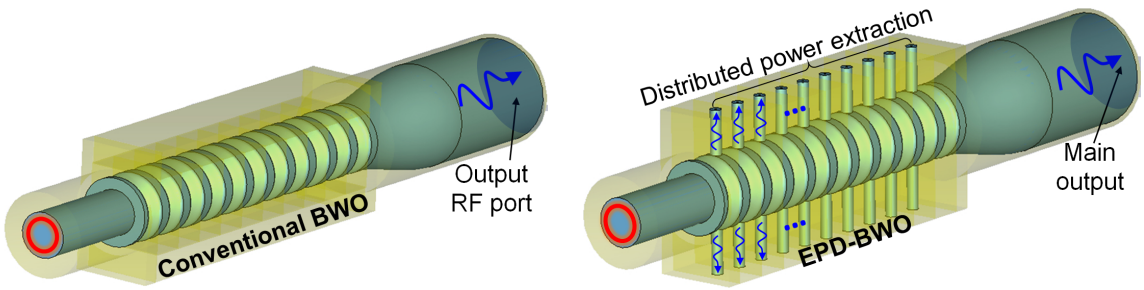

(a) (b)

Figure 7.1: (a) Conventional BWO where the power is extracted from the waveguide end; (b) EPD-BWO where the power is extracted in a distributed fashion to satisfy the EPD condition. The power is extracted using distributed wire loops (as an example) that are connected to coaxial waveguides.

occurrence of an EPD, using PIC simulation, we also show the degeneracy of the complex-valued wavenumbers of two hybrid modes (EM waves interacting with the electron beam) in the realistic waveguide system when the beam dc current is set to specific value at a specific frequency. We provide the performance of the EPD-BWO in terms of output power and power efficiency: they greatly exceed those provided by a comparable conventional design of a BWO Fig. 7.1a. We show the main physical reason behind the high power conversion efficiency associated with the proposed EPD-BWO regime by observing the electrons kinetic energy distribution along the SWS using PIC simulations. We observe that the EPD-BWO better maintains the synchronism and electron coherence over the SWS length as compared to standard BWOs and therefore allows higher level of power conversion. Therefore this chapter not only demonstrates the physical existence of an EPD in a vacuum tube with distributed power extraction, by means of accurate PIC simulations, it also shows a design of an EPD-BWO and its great potentials in terms of very high power generation and efficiency.

7.2 Fundamental Concepts: EPD in theoretical Pierce-Based Model

The interaction between the e-beam charge wave and the EM wave in the SWS occurs when they are synchronized, i.e., when the EM wave phase velocity $v_{ph} = \omega/\beta_p$ is matched to the average velocity of the electrons u_0, where β_p is the phase propagation constants of the "cold" EM wave, i.e., when it is not interacting with the e-beam. The synchronization condition provides an estimate of the oscillation frequency of BWO ($\omega \approx u_0\beta_p$) and is considered as an initial criterion, because the phase velocity of the "hot" modes, i.e., in the *interactive* system, are different from v_{ph} and u_0 due to the interaction [106, 133].

The interaction between the e-beam and the EM wave in vacuum tube devices was theoretically studied by Pierce in [106]. Assuming a wave eigenfunctions of the interactive system of infinite length in the form of $\phi(z,t) \propto e^{i\omega t - ikz}$, Pierce showed that the solutions of the linearized differential equations that govern the electron beam charges' motion and continuity in presence of the SWS EM field yield four eigenmodes whose dispersion relation is given by the following characteristic equation [106, 133]

$$D(\omega,k) = k^4 - 2\beta_0 k^3 + \left(\beta_0^2 - \beta_p^2 + \frac{I_0 Z_c \beta_p \beta_0}{2V_0}\right) k^2 + 2\beta_0\beta_p^2 k - \beta_0^2\beta_p^2 = 0, \tag{7.1}$$

where $\beta_0 = \omega/u_0$ is the unmodulated beam wavenumber, V_0 and I_0 are the e-beam equivalent dc voltage and dc current, respectively, and Z_c is characteristic impedance of the cold EM mode. The Pierce model has been extended in Ref.[102, 126] to the case of a SWS with DPE, where the propagation constant and characteristic impedance of the cold EM mode

are complex: $\beta_p = \beta_{pr} + i\beta_{pi}$ and $Z_c = Z_{cr} + iZ_{ci}$.

A second order EPD occurs in the interactive system when two solutions of (7.1) are identical, $k_1 = k_2 = k_e$, where k_e is the degenerate wavenumber, at a given angular frequency ω_e. This yields that *two* hot modes have exactly the same phase velocity $\omega/\mathrm{Re}(k_e)$ which means that synchronization is achieved in the interactive system and not in the cold system. The conditions that lead to having two degenerate wavenumbers of hot modes are $D(\omega_e, k_e) = 0$ and $\partial_k D(\omega_e, k)\big|_{k_e} = 0$ [33], which yet is simplified by getting rid of k_e to [102]

$$\left(\frac{\beta_p}{\beta_0}\right)^2 = \left(\sqrt[3]{\frac{I_0 Z_c \beta_p}{2V_0\beta_0}} + 1\right)^3 . \tag{7.2}$$

The above condition represents a constraint involving the operational frequency ω, e-beam dc voltage V_0 and current I_0, and cold SWS circuit wavenumber β_p and characteristic impedance Z_c to have an EPD.

When DPE occurs in the SWS, the propagation constant and characteristic impedance of the "cold" EM mode (i.e., without coupling to the electron beam) are complex: $\beta_p = \beta_{pr} + i\beta_{pi}$ and $Z_c = Z_{cr} + iZ_{ci}$. The cold propagation constant imaginary part β_{pi} accounts for power attenuation along the SWS due to the leakage of power out of the SWS. Note that $\beta_{pr}\beta_{pi} > 0$ for a "backward" EM wave that is traveling in the cold SWS (we are using the $\exp(i\omega t)$ time dependency which implies that the EM modes propagates as $\exp(-i\beta_p z)$). Since the phase propagation constant β_{pr} is positive, because it has to match the electron beam effective wavenumber $\beta_0 = \omega/u_0$, one has $\beta_{pi} > 0$. Furthermore, for a backward wave with $\beta_{pr} > 0$, one has $Z_{cr} < 0$ since power travels along the $-z$ direction in the cold SWS. Therefore in the above formulas we have that $Z_c\beta_p = (Z_{cr}\beta_{pr} - Z_{ci}\beta_{pi}) + i\,(Z_{ci}\beta_{pr} + Z_{cr}\beta_{pi})$ is complex.

Note that an EPD requires the coalescence of the two eigenvectors associated to the two

degenerate eigenvalues as well. This has been proven in Ref. [102] by analytically determining the two eigenvectors and by showing their analytical convergence. Here we want to add another perspective to ensure the system has an EPD, by showing that this strong degenerate condition is related to the description of the two degenerate eigenvelues' perturbation in terms of the Puiseux fractional power expansion [122] that, truncated to its first term, implies $(k_n - k_e) \approx (-1)^n \alpha_1 \sqrt{\omega - \omega_e}$ where k_n, with $n = 1, 2$, are the two perturbed wavenumbers in the neighborhood of (ω_e, k_e). The enabling factor for this characterizing fractional power expansion is the fact that at the point (ω_e, k_e) we have $\partial_\omega D(\omega, k_e)\big|_{\omega_e} \neq 0$ and therefore (7.2) will yield a branch point $(k - k_e) \approx \alpha_1 \sqrt{\omega - \omega_e}$ in the dispersion diagram, where $\alpha_1 = \sqrt{-2\partial_\omega D / \partial_k^2 D}\big|_{(\omega_e, k_e)}$ as shown in Ref. [122]. The existence of the Puiseux series results in having a Jordan block in the system matrix which is one of the characterizing features of EPDs, as it was shown in [102] in details, in terms of the two coalescing eigenvectors.

The cold propagation constant imaginary part β_{pi} accounts for power attenuation along the SWS due to the leakage of power out of the SWS as shown in Fig. 7.1b. Under the assumption that $|\beta_{pi}| \ll |\beta_{pr}|$ the complex EPD condition in (7.2) is simplified to

$$I_0 = I_{0e} \approx \frac{128}{81\sqrt{3}} \frac{V_0}{-Z_{cr}} \frac{\beta_{pi}^3}{\beta_0^3}\bigg|_{\beta_{pr}=\beta_0}. \tag{7.3}$$

A detailed formulation of the derivation and the assumptions used to derive (7.3) is presented in [124]. From a theoretical perspective, the EPD condition is satisfied just by tuning the e-beam dc current I_0 to a specific value which we call EPD current I_{0e} [120]. The EPD condition in (7.3) shows that the required e-beam dc current I_{0e} increases cubically when increasing the amount of distributed extracted power, which is represented in terms of the imaginary part β_{pi} of the cold SWS's EM mode. The fact that an EPD e-beam current I_{0e} is found for any amount of distributed power extraction, implies a tight (degenerate)

synchronization regime is guaranteed for any high power generation. Therefore, in principle the synchronism is maintained for any desired distributed power output, according to the Pierce-based model. Note that this trend is definitely not observed in standard BWOs where interactive modes are non-degenerate and the load is at one end of the SWS (i.e., $\beta_{pi} \approx 0$ in SWSs made of copper without DPE).

The starting current for oscillation in a conventional BWO, where the supported modes are non-degenerate, was theoretically studied in [110]. The *starting oscillation condition* is determined by imposing infinite gain $A_v \to \infty$, where the gain A_v is defined as the field amplitude ratio at the begin and end of the SWS [110]. Accordingly , the starting current of oscillation in a conventional BWO scales with the SWS length ℓ as $I_{st} = \zeta/\ell^3$ [123, 110] , where ζ is a constant. When a BWO with DPE operates in close proximity of the EPD, i.e., when the beam dc current I_0 is close to the EPD current I_{0e}, there are two coalescing modes out of the three interacting modes with positive Re(k) and they are denoted by $k_1 = k_e + \alpha\sqrt{I_0 - I_{0e}}$ and $k_2 = k_e - \alpha\sqrt{I_0 - I_{0e}}$ [122], where $\alpha = \sqrt{-2\partial_I D/\partial_k^2 D}\big|_{(\omega_e, k_e)}$ is constant. By imposing infinite gain $A_v \to \infty$ for this case, it has been shown in [102] that the starting current of oscillation is determined in term of the EPD current and the SWS length as

$$I_{st}|_{EDP-BWO} = I_{0e} + \left(\frac{\pi}{\alpha\ell}\right)^2. \tag{7.4}$$

This remarkable result shows that the starting current decreases to the EPD beam current for increasing length of the SWS, in contrast to the starting current in conventional BWOs that vanishes for increasing length of the SWS. The demonstration of these two scaling laws varying the SWS length of a realistic structure as in Fig. 7.1 is carried out in the next section using PIC simulations.

7.3 Particle-In-Cell Simulations of Degenerate Synchronous Regime in BWO

We demonstrate the EPD-BWO regime by taking a conventional BWO design operating at X-band shown in Fig. 7.1a. The proposed EPD-BWO is shown is Fig. 7.1b where DPE is introduced using distributed wire loops that are connected to coaxial waveguides. The original SWS geometry shown in Fig. 7.2a, is a circular copper waveguide with azimuthal symmetry and with inner and outer radii of $R_i = 11.5$ mm and $R_o = 16.5$ mm, respectively, and period $d = 15$ mm. The surface corrugation of SWS in one period is described by a flat surface $R(z) = R_o$ for $0 \leq z < w$, where $w = 5$ mm, and a sinusoidal corrugated surfaces for the rest of the period described as $R(z) = (R_o + R_i)/2 + ((R_o - R_i)/2)\cos(2\pi(z-w)/(d-w))$ for $w \leq z < d$. The whole body of the BWO is made of copper with vacuum inside. The DPE is introduced by adding two wire loops in each unit cell, above and below as shown in Fig. 7.2b, that couple to the azimuthal magnetic field (shown in Fig. 7.3b), and by Farady's Law an electromotive force is generated that excites each coaxial waveguide, similarly to the way power is extracted from magnetrons (Ch. 10 in Ref. [127]). The coaxial cables have outer and inner radii equal to 2.57 mm and 0.5 mm, respectively, leading to a 98 ohm characteristic impedance.

7.3.1 EM modes in Cold SWS

We first analyze the EM modes supported by the two cold SWSs in Fig.7.2a and in Fig. 7.2b (we refer to a "cold" SWS when we do not consider the interaction with the e-beam). Therefore, Fig. 7.2c shows a comparison between the dispersion relation of the EM modes in the two "cold" SWSs: one used in the conventional BWO in Fig. 7.2a, and the other

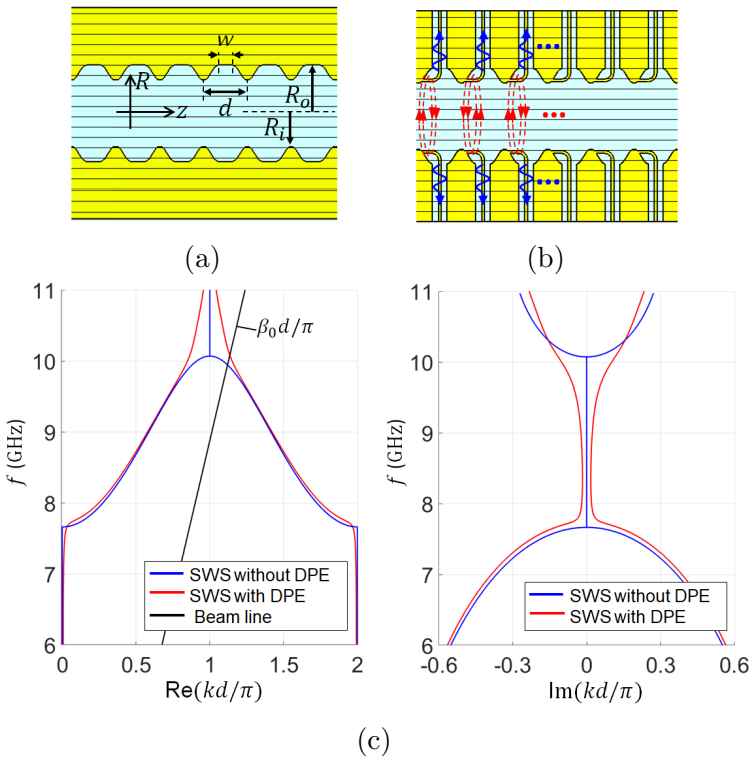

Figure 7.2: Details of the longitudinal cross-sections of a SWS without (a) and with DPE (b). (c) Dispersion of EM guided modes in the "cold" SWSs in (a) and (b), without (blue curve) and with (red curve) distributed power extraction (DPE), respectively. The dispersion shows the real and imaginary parts of the complex wavenumber. The non-zero imaginary part of wavenumber (red line) shows that the SWS in (b) exhibits distributed power extraction. The black line is the "beam line" described by $\beta_0 = \omega/u_0$, and the intersection point with the curve of $\beta_{pr} = \mathrm{Re}(\beta_{pr})$ represents the approximative synchronization point.

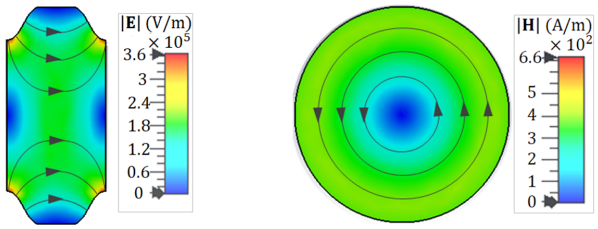

(a) (b)

Figure 7.3: Field distribution for the TM-like mode supported by the SWS in Fig. 7.2a: (a) electric field in a unit cell of the longitudinal cross-section of 7.2a, and (b) magnetic field on the transverse cross-section at the largest radius of the corrugated circular waveguide. Fields are found with the mode solver of CST Studio Suite.

one used in the BWO with DPE in Fig. 7.2b. The dispersion diagram shows only the EM mode that is TM-like, i.e., the one with an axial (longitudinal) electric field component, with electric and magnetic field distributions shown in Fig. 7.3. The dispersion curves in Fig 7.2c show that the EM mode in the cold SWS with DPE is a backward wave that has a propagation constant with non-zero imaginary part β_{pi} at the frequency where the interaction with the e-beam would occur, i.e., at the point where the EM wave phase velocity ω/β_{pr} is synchronized to the relativistic velocity of electrons $u_0 = 0.88c$, where c is the speed of light in vacuum. This means that the cold SWS in Fig. 7.2b is suitable for our design of a BWO with an EPD [126, 102]. The complex wavenumber dispersion relation in presence of DPE, shown in Fig 7.2c, is obtained by using two multi-mode ports at the begin and end of a SWS unit-cell where each port has 30 circular-waveguide modes (almost all evanescent) that sufficiently represent the first TM-like Floquet mode in the periodic SWS, while all the coaxial waveguides are matched to their characteristic impedance to absorb all the outgoing power. This is done using the Finite Element Frequency Domain solver implemented in CST Studio Suite by DS SIMULIA that calculates the scattering parameters of the unit cell, that have then been converted to a transfer matrix to get the SWS complex Floquet-Bloch modes following the same method in [57].

7.3.2 Existence of EPD-BWO Regime

We demonstrate the EPD-BWO regime by considering a conventional BWO operating at X-band whose SWS is shown in Fig. 7.2a, with added DPE ports as in Fig. 7.2b. An example of the dispersion of the complex-wavenumber modes in the interactive ("hot") EM e-beam system with DPE has been shown in [126, 102] using the Pierce-based model revealing the occurrence of an EPD in an idealize system made of transmission lines. Here instead we provide a concrete demonstration of the EPD-BWO regime in the SWS in Fig. 7.1b using PIC simulations, and resorting to some unique features of the EPD in the e-beam - EM wave interactive system, that supports two degenerate modes in the hot SWS. Simulations based on the PIC solver, implemented in CST Studio Suite, use a relativistic annular e-beam with dc voltage of $V_0 = 600$ kV, inner and outer radii of $R_{ib} = 9$ mm and $R_{ob} = 10.3$ mm, respectively, and with dc axial magnetic field of 2.6 T to confine the electron beam. The cathode is modeled using the dc emission model with 528 uniform emission points. The full-wave simulation uses around 1.3M Hexahedral mesh cells to model the SWS.

The output signals and their corresponding spectra for both BWOs, with and without DPE, are shown in Fig. 7.4 where a self-standing oscillation frequency of 9.7 GHz is observed when the used beam dc current is $I_0 = 1740$ A for both cases.

We study the starting e-beam current for oscillation in both types of BWO (the conventional one, and the EPD-BWO in Fig. 7.1) by sweeping the e-beam current I_0 and monitoring the RF power and its spectrum of the waveguide output signal at the right end of the cylindrical waveguide. Using a SWS with 11 unit-cells we show in Fig. 7.5 the output power at the main port at the right end of the SWS when the e-beam current is just below and just above the threshold current. A self-standing oscillation frequency of 9.7 GHz is observed when the

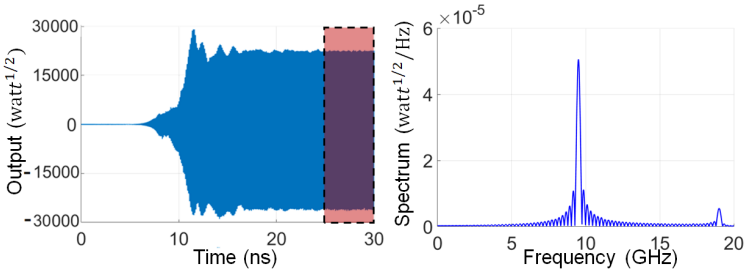

(a)

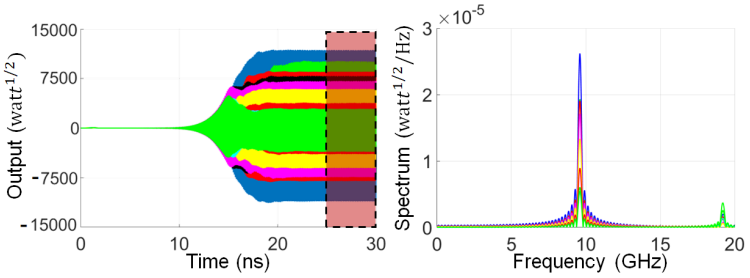

(b)

Figure 7.4: Output signals and their corresponding spectra for: (a) Conventional BWO where the output power is only extracted from one port as shown in Fig. 7.1a. (b) EPD-BWO where power is extracted from multiple ports as shown in Fig. 7.1b, they all have the same frequency of oscillations. In both cases, the time-window used for the Fourier transforms is depicted by a rectangle.

e-beam dc current I_0 for the conventional BWO is at or larger than than 250A, while for the EPD-BWO, self-standing oscillations is observed for an e-beam current I_0 equal or greater than 1230A. Such oscillations are not observed for smaller e-beam current, as for example 225A for the conventional BWO and 1170A for the EPD-BWO. Therefore we conclude that the the starting current of oscillation is approximately 250A for the conventional BWO, and 1230A for the EPD-BWO, when the SWS length is 11 periods. We show performance summary in Table 7.1

To assess the occurrence of an EPD we verify the unique scaling trend of the starting current in (7.4) by repeating the previous study for different SWS lengths. Fig. 7.6 shows the starting current scaling trends for both conventional BWO and EPD-BWO based on PIC simulation

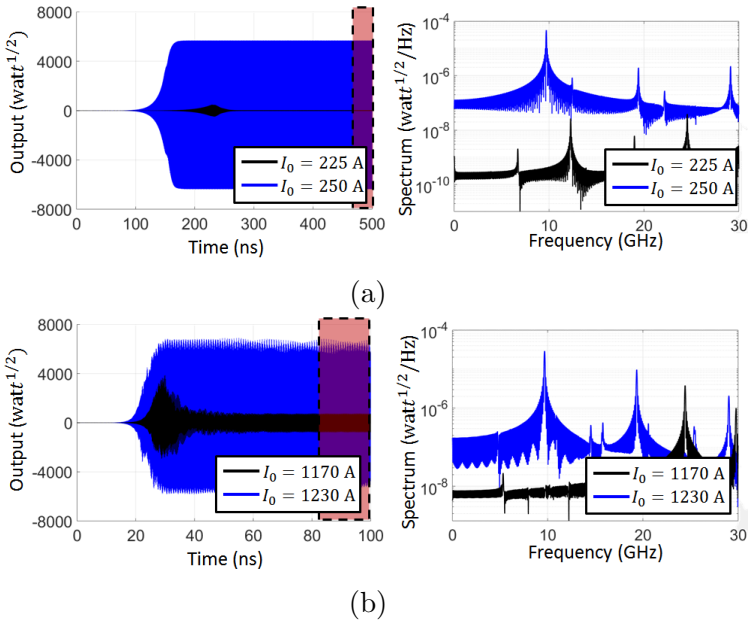

Figure 7.5: Output signal at the right-end waveguide port and its corresponding spectrum when the SWS has 11 unit-cells, at (blue) and below (black) the e-beam starting current for: (a) Conventional BWO, and (b) EPD-BWO. The frequency spectrum shows that there is not self-standing oscillation at 9.7 GHz when the e-beam dc current is below the oscillation threshold, i.e., when the current is below 250A for the conventional BWO, and below 1230A for the EPD-BWO, but self-standing oscillation occurs at these two e-beam current values, hence they represent the starting currents for the two types of BWOs. It is important to stress that the figure shows only the output power at the right-end port of the EPD-BWO, and that the output value of the EPD-BWO from only the right-end waveguide port is comparable to the one coming out of the conventional BWO.

	Conventional BWO	EDP-BWO
Starting current	250 A	1230 A
Oscillation frequency	9.7 GHz	9.7 GHz
Output power ($I = I_{st}$)	0.8 GWatt	0.28 GWatt
Efficiency ($I = I_{st}$)	15 %	35 %

Table 7.1: Performance summary for conventional BWO and EPD-BWO operating at X-band frequency when the SWS has 11 unit-cells

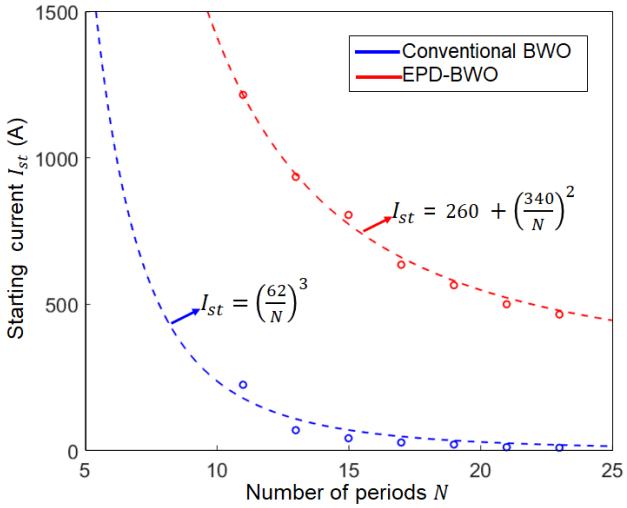

Figure 7.6: Scaling of starting e-beam current for oscillation in conventional BWO and EPD-BWO. Dashed lines represent fitting curves. The EPD-BWO shows a starting current trend that does not vanish for long SWS.

results, varying the number of periods of the SWS. The dashed lines represent fitting curves and the case of EPD-BWO shows very good fitting with 99% R-square. In comparison to a conventional BWO, the EPD-BWO is characterized by a starting current (threshold) that does not tend to zero as the SWS length increases, and a scaling that is a quadratic function of the inverse of the SWS length.

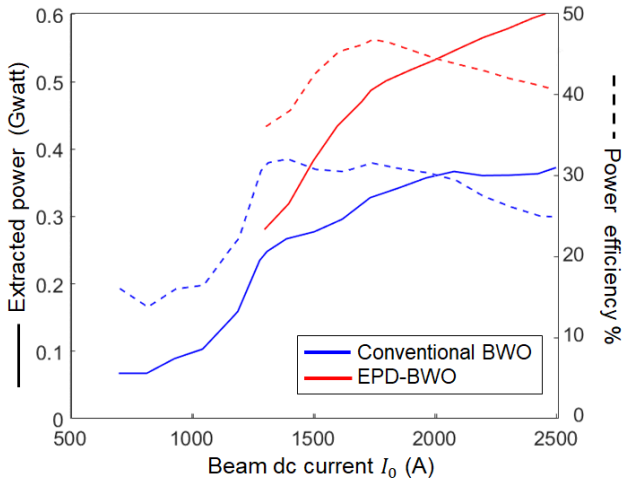

Figure 7.7: Comparison between the efficiency of a conventional BWO and an EPD-BWO using $N = 11$. The EPD-BWO shows improved efficiency at higher level of power generation compared to the conventional BWO.

7.3.3 Power Performance: EPD-BWO Compared to a Conventional BWO

We compare the RF conversion power efficiency (RF output power over dc e-beam power) of the conventional BWO with that of the EPD-BWO in Fig. 7.7 for e-beam dc currents that exceed the starting current, assuming the SWS has 11 unit-cells. The figure shows that the EPD-BWO has higher efficiency and also higher level of output power compared to a conventional BWO with same dimensions. The results show that the EPD-BWO has a maximum efficiency of about 47% at about 0.5 GW output power (the sum of the power from each output in Fig. 7.1b). Instead, the conventional BWO has a maximum efficiency of about 33% at an output power level of about 0.27 GW. It is important to point out that the EPD-BWO has a higher threshold beam current to start oscillations compared to the conventional one which is in consistent with the theoretical results in [102] and with the requirement of generating higher power levels.

Figure 7.8 shows the electric field distribution for the conventional BWO and the EPD-BWO when the e-beam dc current I_0 is 1750 A, in both cases, for a SWS of 11 unit cells. The

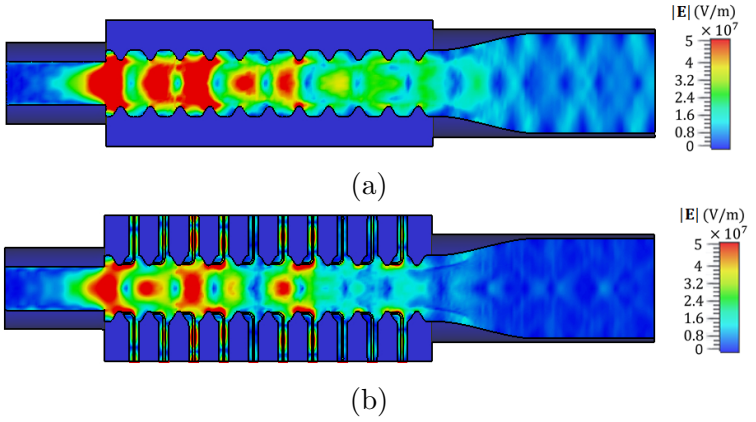

Figure 7.8: Electric field distribution in the SWS for: (a) conventional BWO and (b) EPD-BWO. The figure in (b) shows power extraction in distributed fashion from the coaxial waveguides at the top and bottom of the circular waveguide.

figure shows that for the conventional BWO the power is extracted only from the main port at the right end, whereas for EPD-BWO most of the power is extracted in a distributed fashion from the top and bottom coaxial waveguides, resulting in much high power and high efficiency as demonstrated in Fig. 7.8.

7.4 Maintaining Synchronism at High Power Levels

The interaction between the electron beam and the guided EM field requires synchronism. Synchronism is achieved when the electrons average velocity and phase velocity of the EM wave supported by the SWS are matched. The power delivered to the EM field in the BWOs is provided by the electrons's kinetic energy. Therefore, extracting more energy from the electron beam would result in further decreasing the average speed of electrons, which in turns leads the system out of synchronism. Consequently, the level of power extraction and the power conversion efficiency would be limited because synchronism is maintained only for finite SWS lengths. The advantage of using the EPD concept in BWOs through introducing

DPE is that the synchronism is maintained for higher levels of power extraction as compared to conventional BWOs. To show that, we compare the synchronism in the EPD-BWO regime and in the conventional BWO by performing PIC simulations and monitoring the electrons kinetic energy along the BWO as shown in Fig. 7.9. PIC simulations are performed for structures with a number of unit-cells $N = 20$ to be able to see the electrons behavior over a large length. The plots in Fig. 7.9 presents the phase plots of electrons

showing the space bunching of electrons . PIC simulator used about 6×10^6 particle charges to model the electron beam, where each particle has a macro-charge of about $q_p = -7 \times 10^6 e$ ($e = 1.602 \times 10^{-19}$ C) that represents a cloud of electrons, where e is the charge of one electron. Each plot in Fig. 7.9 shows the kinetic energy of the electrons along the structure , i.e., each dot in the plot corresponds to the kinetic energy of every electron belonging to a given particle charge at position z. We show first the conventional BWO case when the beam dc current $I_0 = 30$ A is just above the estimated starting current $I_{st} = 29.8$ A. For this case the EM mode-charge wave synchronization is maintained for almost all the SWS length as shown in Fig. 7.9a. The electrons energy distribution along the SWS, at a given time instant after reaching the steady state regime, becomes more irregular when we increase the beam dc current as shown in Fig. 7.9b and Fig. 7.9c. These figures show that length over which the synchronization and coherence of electron is satisfied, decreases when trying to extract more power by increasing the beam dc current. We now compare the EPD regime with the one of the conventional BWO using the same beam dc current, which is approximately 18 times the starting current of conventional BWO case and approximately equal to the starting current of the EPD-BWO case (I_0 =550 A). The phase space plot of the electrons at a given time instant after reaching the steady state regime in Fig. 7.9c and Fig. 7.9d shows that the EPD-BWO better maintains the synchronism and electron coherence over the whole SWS length as compared to the conventional BWO, at higher power levels. These observations contribute to the explanation of why the EPD-BWO regime leads to higher output power levels and higher power conversion efficiency than those of a conventional BWO. The dashed

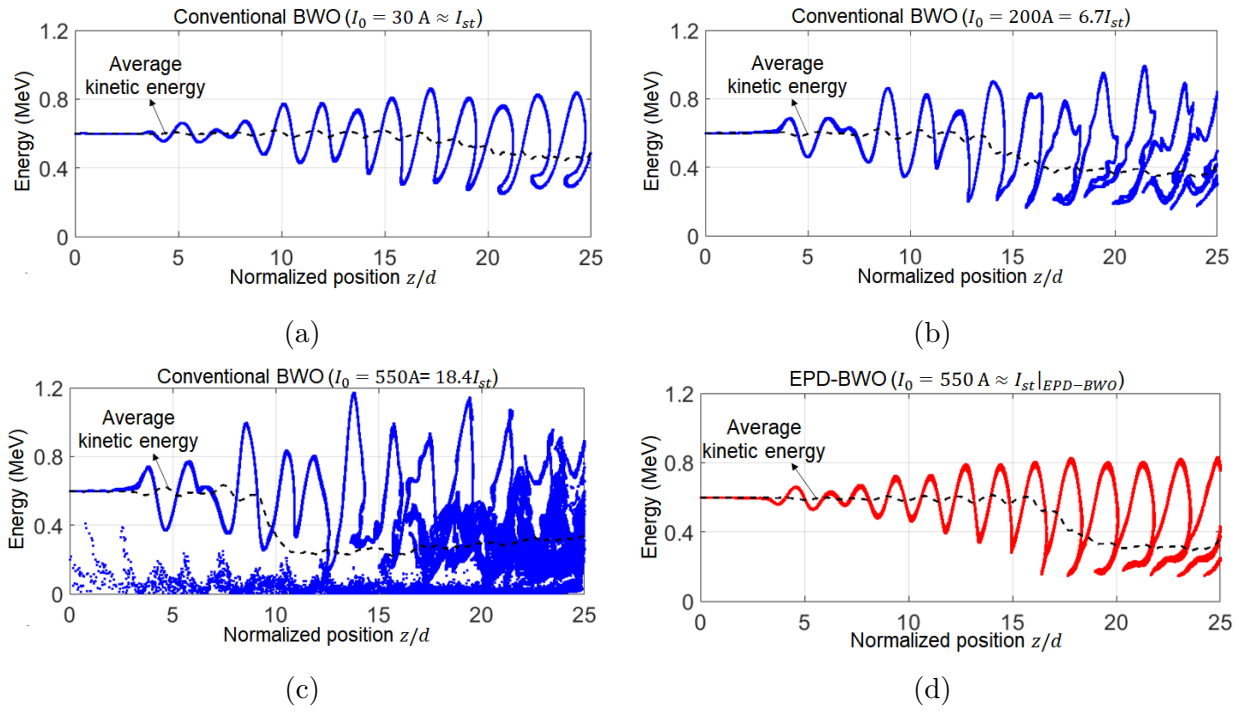

Figure 7.9: Phase space plot of electrons showing the electrons' kinetic energy distribution at a time instant after reaching the steady regime. (a), (b) and (c): conventional BWO when the beam dc current is 30 A, 200 A and 550 A. (d): EPD-BWO when the beam dc current is just above the starting current for oscillation 550 A. (a), (b) and (c) show that synchronism is lost when attempt to increase power extraction level by increasing the beam dc current, whereas for DPE case in (d), synchronism is maintained for a longer SWS length when compared to the conventional BWO in (c), assuming that they use the same beam dc current. The dashed black lines in the figures represent the time-averaged kinetic energy which decreases with growing z-location because of the energy transfer from electron beam to the SWS.

black line in each figure represents the time-averaged kinetic energy of the electrons at each z-location calculated as $E_{k,avg}(z) = \frac{1}{T}\int_{t=t_{ref}}^{t=t_{ref}+T} E_k(z,t)$, where t_{ref} is any time instant after steady state regime is reached, $T = 1/f$ and f is the oscillation frequency, and $E_k(z,t)$ is equivalent electrons kinetic energy calculated as the mean of electrons energy existing in small proximity of 1 mm window along the coordinate z at time instant t. Comparing Fig. 7.9c and Fig. 7.9d, the electrons kinetic energy, and hence the electrons average velocity, is maintained for longer lengths as compared to the BWO with standard regime, and therefore would result in a higher energy transfer and higher power conversion efficiency.

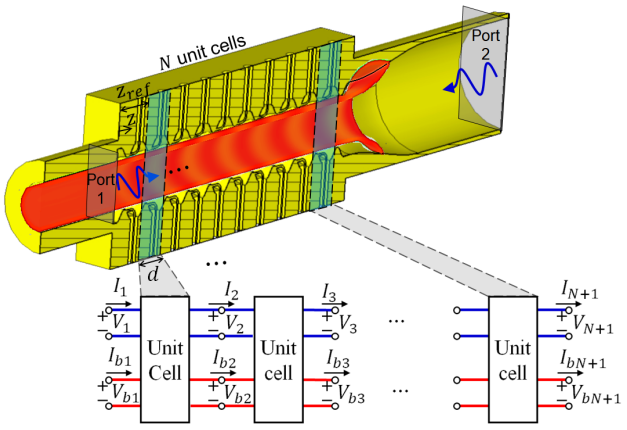

Figure 7.10: Setup used to determine the complex wavenumber versus frequency dispersion relation of hybrid modes in hot SWSs based on PIC simulations. Each unit cell in the hot SWS is modeled as a multi-port network circuit with *equivalent* voltages and currents representing EM waves (V_n, I_n) and space-charge waves(V_{bn}, I_{bn}) dynamics.

7.5 Demonstration of Degenerate Dispersion of Hybrid Hot Modes Using PIC Simulations

The goal is to verify the degeneracy of the wavenumbers of the modes of the interactive system (i.e, the hybrid modes) in the hot SWS using PIC simulations. Previously, the degenerate dispersion has been shown using the approximate analytical method based on the Pierce model [102]. Here we adopt the general procedure described in [134] to estimate the complex-valued wavenumbers of the interactive (hybrid) modes, and show the hybrid mode degeneracy using data extracted from PIC simulations. The procedure is based on exciting the SWS from both sides by EM waves having monochromatic signal as illustrated in Fig. 7.10, and then calculating the hybrid-system state vectors that describe the EM field and the electron beam dynamics at discrete periodic locations along the SWS. The time domain data extracted from PIC simulations are transformed into phasors after reaching a steady regime. We then find the transfer matrix of the unit-cell of the "hot" SWS that

best relates the calculated state vectors. Once the estimate of the unit-cell transfer matrix is obtained, we find the complex values of the wavenumbers of the hybrid eigenmodes in a hot SWS using Floquet theory. The details of the steps used to generate the hybrid-modes dispersion relation in the hot SWS are provided in [124, 134].

The wavenumber-frequency dispersion describing the complex-valued wavenumber of the hybrid eigenmodes in the hot SWS is determined by running multiple PIC simulations of a SWS with 11 unit-cells at different frequencies and then determining the transfer matrix of the unit-cell at each frequency. Calculations are based on using a beam dc current of $I_0 = 260$A, which is the value of EPD beam current (pertaining to the infinitely long SWS) according to the fitting shown in Fig. 7.6; the use of this current value of current should guarantee the coalescence of two interactive modes. It is worth mentioning that the used beam current in this case is below the starting current of oscillation of the hot SWS of 11 uni cells, which is estimated to be 1215 A, therefore, one can model each unit cell in the structure using a transfer matrix as discussed in [124, 134]. The dispersion diagram of the four modes in the hot EM-electron beam system is shown in Fig. 7.11a (solid curves) using 27 frequency points (27 PIC simulations). The dashed red line represents the space-charge wave (i.e., the beam line) of the isolated electron beam. The figure show a degeneracy of both the real and imaginary parts of the wavenumbers of two hybrid modes (the red and blue curves) at a frequency near $f = 9.87$ GHz which is very close to the oscillation frequency. As a further proof, we also verify that the EPD is obtained when the beam dc current is set to a specific value, by observing the wavenumber-beam current dispersion describing the hybrid eigenmodes at $f = 9.87$ GHz, which is the frequency at which we expect to find the EPD. This is shown in Fig. 7.11b where two dispersion curves of the four interactive modes intersect (in their real and imaginary parts) when sweeping the beam current (the red and blue curves). The figure show that the EPD occurs when the beam current is close to 260 A, which is consistent with result in Fig. 7.6.

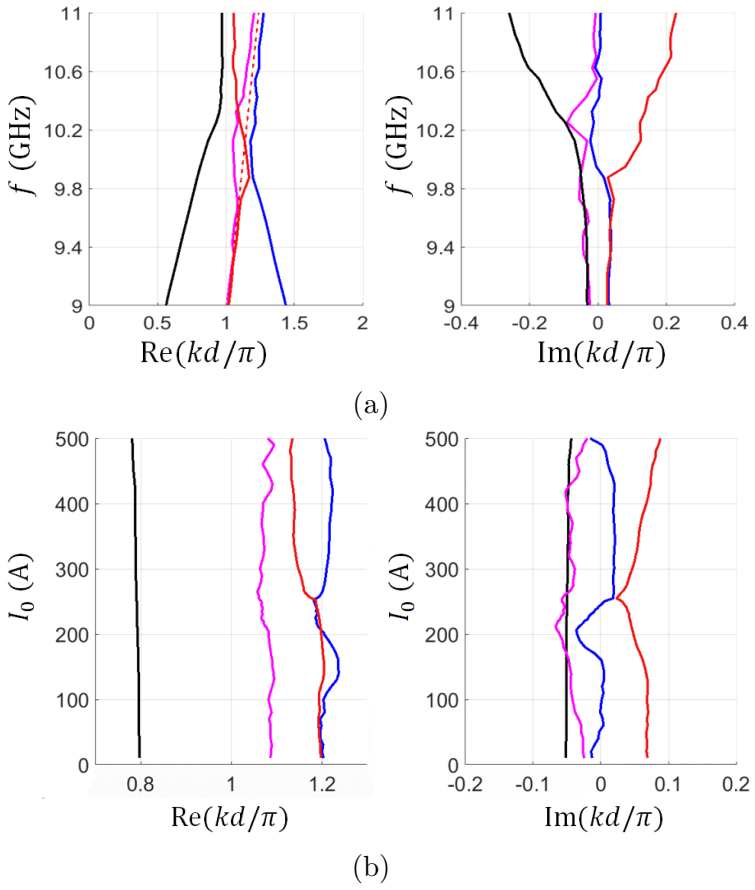

Figure 7.11: Dispersion of complex-valued wavenumbers of the four hybrid modes in the hot SWS of 11 unit-cells, estimated from data extracted from PIC simulation : (a) varying frequency when the electron beam dc current is $I_0 = 260$A and (b) varying the beam dc current, at $f = 9.87$ GHz. All the considered beam dc currents used to generate the results in (a) and (b) are lower than the starting current of oscillation, estimated to be 1215 A. The plots show a modal degeneracy (in the real and imaginary parts) when the the beam dc current is $I_0 = 260$A and the operating frequency is $f = 9.87$ GHz

7.6 Conclusion

The physical mechanism of an EPD in a hybrid system where a linear electron beam interacts with an EM mode has been demonstrated in a BWO made of a circular corrugated waveguide with distributed power extraction. The EPD demonstration is based on using PIC simulations modeling realistic interactions between an electron beam and the EM modes in the waveguide; therefore this chapter expands the previous EPD observation in [102] that was made using an approximate analytical method based on the simplistic Pierce model. The manifestation of such EPD is useful to conceive a degenerate synchronous regime for BWOs that have a starting-oscillation current law that decreases quadratically to a given fixed value for long waveguide interaction lengths; as a consequence PIC simulations show higher efficiency and much higher output power than a standard BWO. The unique quadratic threshold scaling law for long waveguide interaction lengths observed in the realistic EPD-BWO setting studied here demonstrates the EPD-based synchronization phenomenon, compared to that in a standard BWO that has a starting-oscillation current law that vanishes cubically. As a further confirmation, we have also shown the complex-valued wavenumber degeneracy in the realistic hot SWS with distributed power extraction, elaborating data extracted from PIC simulations. The distributed power extraction concept is useful to generate the EPD and we have shown that the propose degenerate BWO regime leads to higher power extraction and higher power efficiency when compared to a standard BWO. The physical mechanism of why more power can be extracted is also explained in terms of observations made on the distribution of the electrons kinetic energy revealing that the synchronous behavior of the EPD-BWO is mantained for longer SWS lengths and at higher power levels than what observed in a standard BWO

Chapter 8

High Power Backward Wave Oscillator using Folded Waveguide with Distributed Power Extraction Operating at an Exceptional Point

The concept of exceptional point of degeneracy (EPD) is used to conceive an exceptional synchronization regime that is able to enhance the level of output power and power conversion efficiency for backward wave oscillators (BWOs) operating at millimeter-wave and Terahertz frequencies [135]. Standard BWOs operating at such high frequency ranges typically generate output power not exceeding tens of watts with very poor power conversion efficiency in the order of 1%. The novel concept of exceptional synchronization for the BWO based on a folded waveguide is implemented by engineering distributed gain and power extraction along the slow-wave waveguide [135]. The distributed power extraction along the folded waveguide is useful to satisfy the necessary conditions to have an EPD at the synchronization point [102, 124, 135]. Particle-in-cell (PIC) simulation results shows that BWO operating at

an EPD regime is capable of generating output power exceeding 3 kwatts with conversion efficiency of exceeding 20% at frequency of 88.5 GHz [135].

8.1 Motivation and State of the Art

The capability to generate significant power at millimeter-wave and terahertz (THz) frequencies using vacuum electronics sources has motivated many investigations due to the their high demand on applications such as imaging, spectroscopy and communications [136, 137, 138, 139, 140, 141]. Vacuum electronic devices operating at millimeter-wave and THz frequencies often use folded waveguides (serpentine-shaped waveguide) as shown in Fig. 8.1a. The advancement of fabrication technologies such as LIGA (LIthographie, Galvanoformung, Abformung) have made it easy to fabricate and develop vacuum electronic devices operating at these high frequencies [142, 143, 144, 145, 146, 139].

Exceptional points of degeneracy (EPD) are points in parameter space of a system at which two or more eigenmodes coalesce. Despite most of the published work on EPDs are related to parity time (PT) symmetry [17, 38], the occurrence of EPDs does not necessarily require a system to exactly satisfy the PT symmetry condition. In general, but not always [48, 41, 49] , the occurrence of EPD in waveguides requires simultaneous presence of gain and loss [40, 41]. Instead of using losses, the EPD in this work is enabled by the distributed power extraction (DPE) from the folded waveguide as shown in Fig. 8.1b. The ideal concept of simultaneous radiation losses and distributed gain in two coupled waveguides leading to an EPD was already discussed in [40] in a theoretical setting. In this chapter the concept is achieved using a single serpentine waveguide coupled to an electron beam (e-beam). The energy extracted from the e-beam and delivered to the guided electromagnetic (EM) mode is considered as a distributed gain from the waveguide perspective, whereas DPE represents extraction "losses" and not mere dissipation [126, 102, 124]. The distributed extracted power

from the discrete waveguide ports along the serpentine (Fig. 8.1) could be directed toward an array antenna and hence radiated generating a collimated EM beam or could be collected in an external waveguide after proper optimization for power combining.

In [102], we have studied the theoretical and idealistic analysis of a BWO with exceptional synchronization operating at an EPD (we named it EPD-BWO) using a generalized Pierce model [106] that accounts for waveguide with distributed power extraction modeled as losses. Here we show analytically and numerically using particle-in-cell (PIC) simulations that an EPD-BWO is characterized by the asymptotic trend of the *starting* e-beam dc current that decreases quadratically with slow wave structure (SWS) length to a non-vanishing value that can be properly designed based on the required output power. In this chapter, we focus on the realization and implementation of the exceptional synchronization of the EPD-BWO at millimeter-waves since it is very challenging to generate significant power levels at such high frequencies. Though we do not show it here, the concept of exceptional synchronization is expected to be advantageous also at THz frequencies. The use of EPD enables to have higher starting current for oscillation which indicates higher level of power extraction from the e-beam kinetic energy.

Works on BWOs operating at millimeter-wave and THz have reported a generated output power not exceeding tens of watts with power conversion efficiency around 1% [147, 148, 145, 149, 150, 151, 152, 141]. In this chapter we employ the concept of EPD to enhance such poor efficiency and to increase the level of output power. We asses the advancements in the performance of BWO operating at an EPD (EPD-BWO) over a standard BWO (STD-BWO) using particle-in-cell (PIC) simulations.

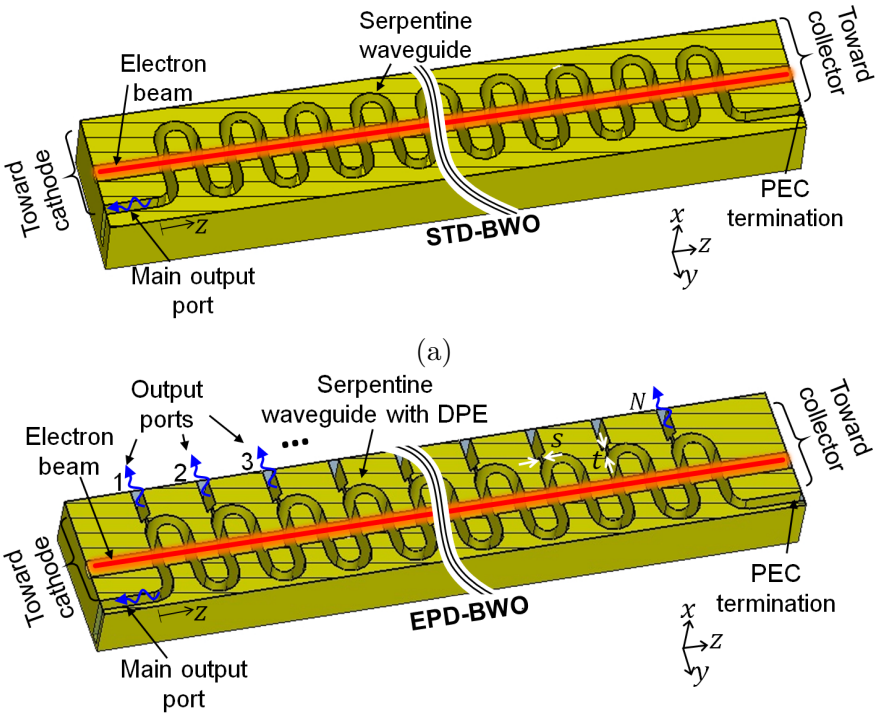

Figure 8.1: BWO with folded waveguide operating at millimeter waves: (a) standard (STD)-BWO where the power is extracted from a waveguide end; (b) EPD-BWO where the power is extracted in a distributed fashion to enable the occurrence of the exceptional synchronization regime when working at an EPD. The distributed power is extracted by introducing a small slot in each folded waveguide period that couples portion of the power in the folded waveguide to the outgoing rectangular waveguides.

8.2 Implementation of Exceptional Synchronism Regime Based on EPD in a Folded Waveguide

A simple model for the interaction between the e-beam and the EM wave in vacuum tube devices was provided by Pierce in [106]. Augmenting the Pierce model to include SWSs with distributed loads, we have shown in [126, 102, 124] that a second order EPD is found as a special degeneracy of the interactive (i.e., hot) electron beam-EM modes when DPE along the waveguide is added and when the beam dc current is set to specific value $I_0 = I_{0e}$, i.e., using

this e-beam dc current guarantees that two modes in the interactive system are synchronized. The e-beam dc current I_{0e} is the specific value that guarantees the degeneracy of two modes, which can be set to a desired value by properly designing the interactive SWS system. The cold SWS with DPE has a complex propagation constant $\beta_c = \beta_{cr} + i\beta_{ci}$ around the synchronization point, where the imaginary part β_{ci} accounts for the DPE along the SWS and the subscript c denotes circuit that is representing the cold SWS. We have shown in [126, 102, 124] that the EPD e-beam dc current has a proportionality $I_{0e} \propto \beta_{ci}^2$, where the parameter β_{ci} represents the DPE introduced in the SWS and is determined by engineering the DPE from the SWS. The fact that an EPD e-beam current I_{0e} is found for any amount of desired distributed power extraction implies that this so called "exceptional synchronization" regime is guaranteed for any desired high power generation. Therefore, in principle, the synchronism is maintained for any desired distributed power output, according to the augmented Pierce-based model presented in [126, 102]. Note that this trend is definitely not observed in standard BWOs where interactive modes are non-degenerate and the load is at one end of the SWS. Furthermore in a STD-BWO the starting (i.e., threshold) current vanishes with increasing SWS length, whereas in an EPD-BWO it decreases quadratically to a fixed, desired, value [126, 102, 124], that coincides with $I_{0e} \propto \beta_{ci}^2$, hence this value is related to the amount of DPE. Therefore, the exceptional synchronization regime enables a large transfer of power from the e-beam to the waveguide EM mode as compared to a standard regime.

Here, we show how to implement the EPD regime in a BWO that uses a folded waveguide and operating at millimeter wave and THz frequency through introducing DPE along the waveguide as illustrated in Fig. 8.1b. In particular, we consider a folded waveguide made of copper with rectangular cross-section of dimension $a = 1.9$ mm and $b = 0.2$ mm. The folded waveguide has a bending radius of $R_s = 0.3$ mm and the straight sections have length of $h = 1$ mm. The beam tunnel radius is $R_t = 0.175$ mm, with a filling factor of about 58%, i.e., the e-beam has radius of $R_b = 0.13$ mm. The DPE is conceived in the waveguide by making a small rectangular slot of dimensions $a \times s$, with $s = 0.05$ mm, in the wide side of

the rectangular cross section, and length $t = 0.1$ mm, in each period of the waveguide (as shown in Fig. 8.1b). The slots couples portion of the main power in the SWS to an outgoing rectangular waveguide with dimensions $a \times b$, as shown in Fig. 8.2b.

Figure 8.2c shows a comparison between the dispersion relation of EM modes in two "cold" SWSs: one used in a STD-BWO in Fig. 8.2a, and one used in the BWO with DPE in Fig. 8.2b. The dispersion curves show only the dominant EM mode TE_{10} which exhibits an axial (longitudinal, along the folded waveguide) electric field component able to interact with the e-beam. The dispersion curves in Fig 8.2c show that the cold SWS with DPE supports backward waves that have a propagation constant with non-zero imaginary part β_{ci} at the frequencies where the interaction with the e-beam may occur. The imaginary part of a mode propagating in the folded waveguide without DPE is almost equal to zero at the interaction points ($\omega/\beta_{cr} \approx u_0$, where u_0 is the electrons average speed and ω is the angular frequency). The complex wavenumber dispersion relation in presence of DPE, shown in Fig 8.2c, is obtained by simulating a single unit-cell that is connected to two ports at its beginning and end, while the power extraction waveguide is connected to a matched port, and the beam tunnel ends are terminated by prefect electric conductor (PEC) since the TE_{10} mode is below cutoff of such a tunnel (we have checked that varying the beam tunnel length and terminations does not affect the result). The interaction between the EM mode in the SWS and the e-beam occurs at the 2^{nd} Brillouin zone defined here as $\mathrm{Re}(kd/\pi) \in [4, 6]$. The dispersion relations we show in Fig 8.2c are plotted in the fundamental Brillouin zone defined here as $\mathrm{Re}(kd/\pi) \in [0, 2]$, for the sake of clarity. The Finite Element Frequency Domain solver implemented in CST Studio Suite by DS SIMULIA is used to calculate the two-port scattering parameters which are converted into a two-port transfer matrix representing one unit-cell. The complex Floquet-Bloch modes wavenumbers are then obtained by enforcing periodic boundaries for the obtained transfer matrix, following the method discussed in [57].

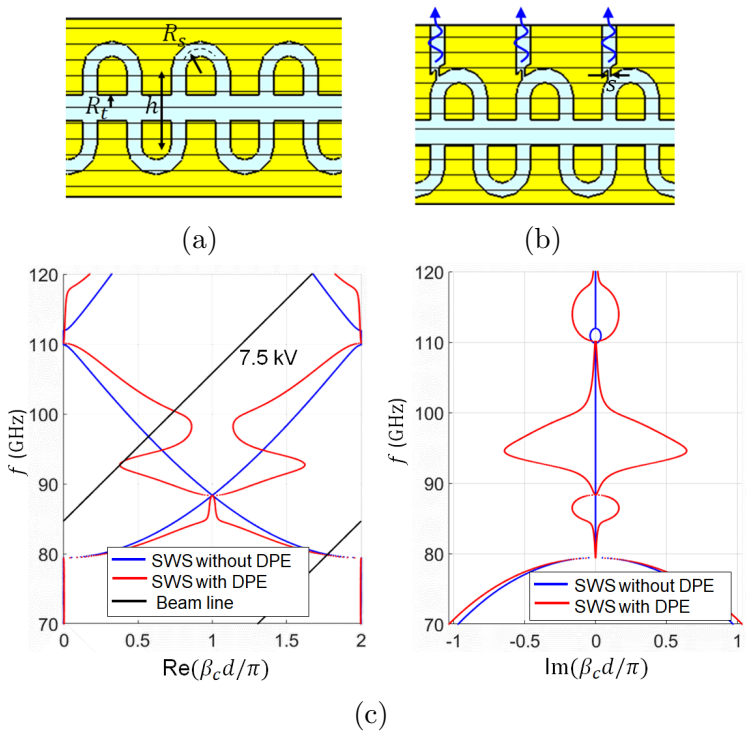

Figure 8.2: Details of the longitudinal cross-sections of a SWS without (a) and with DPE (b). (c) Dispersion of EM guided modes in the "cold" SWSs in (a) and (b), without (blue curve) and with (red curve) distributed power extraction (DPE), respectively. The dispersion shows the real and imaginary parts of the complex wavenumber. The non-zero imaginary part of wavenumber (red line) shows that the SWS in (b) exhibits distributed power extraction. The black line is the "beam line" described by $\beta_0 = \omega/u_0$, and the intersection point with the curve of $\beta_{pr} = \mathrm{Re}(\beta_{pr})$ represents the approximative synchronization point.

8.3 Particle-In-Cell Simulations of Exceptional Synchronous Regime in BWO

We perform PIC simulations to assess the performance and features of the proposed EPD-BWO using a folded waveguide and operating at millimeter wave frequency. The PIC simulations uses a pencil e-beam with dc voltage $V_0 = 7.5$ kV. An axial dc magnetic field of 2 T is used to ensure the confinement of the e-beam in all the cases considered in the chapter (i.e. EPD-BWOs and STD-BWOs). We verified using PIC simulations that the e-beam time-averaged current calculated at the end of the SWS ($z = Nd$) is the same as the e-beam dc current I_0, hence electrons do not hit the copper walls.

8.3.1 Starting Current

We start first by studying the starting (threshold) current of oscillation to see how much increase in starting current we obtain with the EPD-BWO with respect to a STD-BWO without DPE. Results show that the EPD-BWO exhibits a much higher starting current of oscillation with respect to a STD-BWO without DPE. Indeed the increase in starting current is an advantage here because it enables to push up the saturation power level of the BWO to much higher levels and therefore leads to a high level of power extraction. The output power for a STD-BWO is extracted from the Main port at the left end of the waveguide, whereas the output power of the EPD-BWO is extracted from the left waveguide port in addition to all DPE waveguide ports as shown in Fig. 8.1b. Fig. 8.3 shows the output ports signals, obtained from PIC simulations, for both BWOs with 13 unit cells when the e-beam current is just below and above the starting currents of each BWO (the threshold currents have been found by repeating simulations with varying e-beam dc current values with steps of 0.1 A for the STD-BWO and 0.01 A for the EPD-BWO). A self-standing oscillation frequency of 93.1

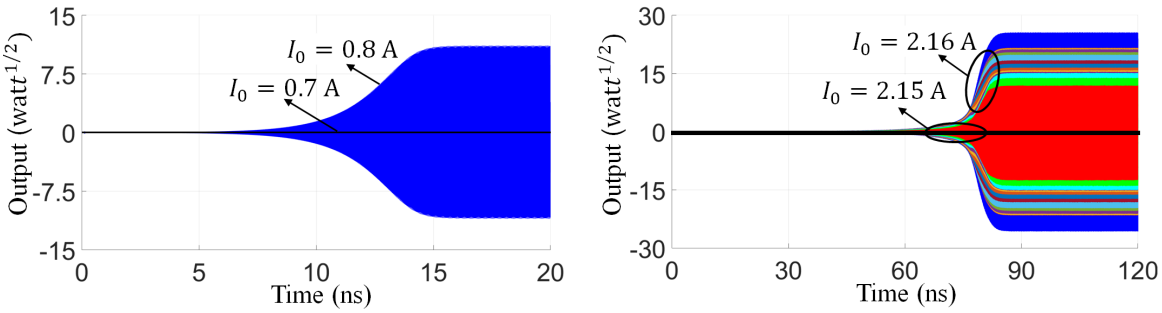

(a) (b)

Figure 8.3: Output signals for: (a) STD-BWO and (b) EPD-BWO, both having 13 unit-cells, when the e-beam dc current is just below and above the starting current of oscillation (I_{st}) for each BWO case. The output signal for the STD-BWO is extracted at the left-end port of the waveguide (a), whereas for the EPD-BWO the signals are extracted from the 13 distributed ports and from the left-end port, denoted by different colored curves (b).

GHz is observed when the beam dc current I_0 is at or larger than 0.8 A for the STD-BWO case, whereas a self-standing oscillation frequency of 88.2 GHz is observed when the beam dc current I_0 is at or larger than 2.16 A for the EPD-BWO case. The different colors in Fig. 8.3b represent the output signals from the 13 distributed ports and the left-end port (i.e., Main port) of EPD-BWO, they are arranged in descending order according to their maxima levels at steady state as: Main port, Port 2, Port 1, Port 3, Port 4, ..., Port 13, where the port numbering is illustrated in Fig. 8.1b. We estimate the starting current of the oscillation as the average of the two observed values of the e-beam currents where oscillation starts to occur and does not occur, respectively. Therefore,the starting currents I_{st} for STD-BWO and EPD-BWO are 0.75 A and 2.15 A, respectively. Considering larger and larger numbers of unit cells implies that $I_{st} \to 0$ for the STD-BWO case, and $I_{st} \to I_{0e}$ for the EPD-BWO case [102, 124]. We show performance summary in Table 8.1

To assess the occurrence of an EPD, we verify the unique scaling trend of the starting current in (8.1) by repeating the previous study for different SWS lengths. Such scaling trends for the starting current for both STD-BWO and EPD-BWO are shown using black dots in Fig.

	STD-BWO	EDP-BWO
Starting current	0.16 A	2.11 A
Oscillation frequency	93.1 GHz	88.2 GHz
Output power ($I = I_{st}$)	80 Watt	2640 Watt
Efficiency ($I = I_{st}$)	1.3 %	15 %

Table 8.1: Performance summary for standard BWO and EPD-BWO operating at millimeter wave frequency when the SWS has 20 unit-cells

8.4 based on PIC simulation results, varying the number of periods of the SWS. The dashed lines represent fitting curves; the case of EPD-BWO shows very good agreement with the fitting curve. The EPD-BWO is characterized by a starting current that does not tend to zero as the SWS length increases, in contrast to the starting current of a STD-BWO that vanishes for increasing SWS length. The observed scaling of the starting current of a EPD-BWO is a quadratic function of the inverse of the SWS length, which is the same trend observed theoretically in [102] using an augmented Pierce model. Indeed, we have shown in [102, 124] that the starting current of oscillation for EPD-BWO scales with the SWS length as

$$I_{st} = I_{0e} + \left(\frac{\alpha}{N}\right)^2, \tag{8.1}$$

where α is a constant. From the fitting shown in Fig. 8.4 we have found that $I_{st} = 2.09 + (3.2/N)^2$,therefore, following [102], the estimate of the EPD current is $I_{0e} = I_{st}|_{N\to\infty} = 2.09$ A. Later on in the next section, we show that the use of a current close to this value will lead to the degeneracy of two hot modes in the dispersion of the hot structure, using data extracted from PIC simulations. We refer to the modes of the system where the e-beam interacts with the EM wave of the SWS as "hot" modes, which are the modes that are composed of both EM and space-charge waves.

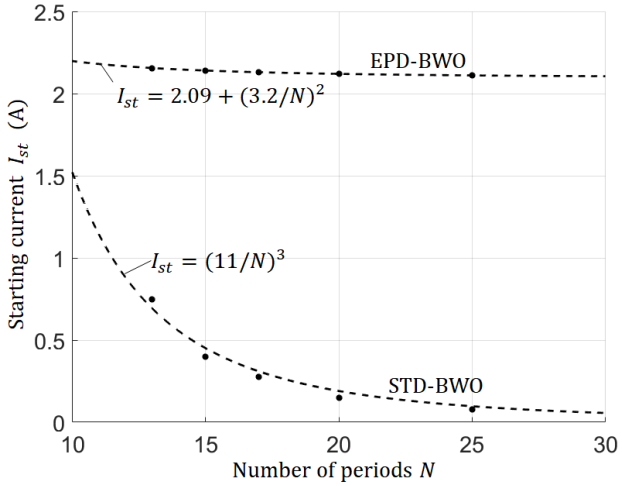

Figure 8.4: Scaling of starting e-beam dc current for STD-BWO and EPD-BWO with SWSs length (black dots). Dashed lines represent fitting curves. The EPD-BWO shows a starting current trend that does not vanish for long lengths, the quadratic decay is representative of a degeneracy condition.

8.3.2 Power Performance: EPD-BWO Compared to a STD-BWO

We calculate the output power for STD-BWO and EPD-BWO when the e-beam is 10% above the starting beam current for each case, i.e., $I_0 = 1.1I_{st}$, where the starting currents for both the EPD-BWO and STD-BWO are shown in Fig. 8.4. The output power P_{out} for the EPD-BWO case is calculated as the sum of the power delivered to the distributed ports and the main port. We show in Fig. 8.5a the output power and power conversion efficiency, defined as $\eta = P_{out}/(V_0 I_0)$, for both cases of EPD-BWO and STD-BWO when varying the number of periods (i.e., unit cells) of the folded waveguide . The figure shows that the EPD-BWO has always much higher output power level and power conversion efficiency as compared to the STD-BWO. We observe from the figure also that the output power and efficiency for the EPD-BWO increase as we increase the number of folded waveguide periods, unlike for the STD-BWO. The output power level starts to saturate as the number of periods approaches 27 for the EPD-BWO case.

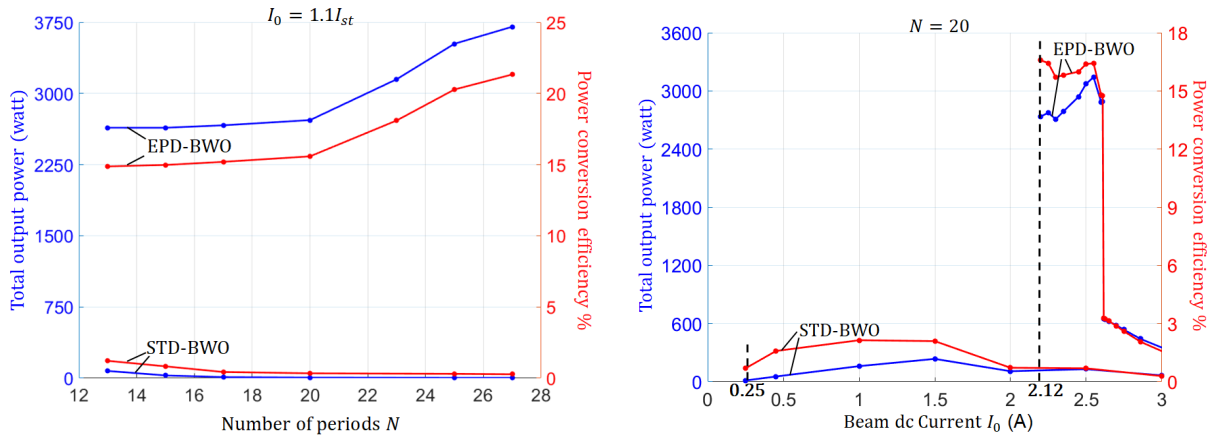

Figure 8.5: Comparison between the output power and power conversion efficiency of a STD-BWO and an EPD-BWO, both based on the same folded waveguide SWS, without and with DPE, respectively. In (a) we observe the power trends when varying the number of unit cells of the folded waveguide when the used beam dc current is 10% higher than the starting currents for the STD-BWO and EPD-BWO, and for each length. In (b) we observe the power trends when varying the the beam dc current, assuming the SWSs for the two BWOs are made of 20 unit cells. The figure shows that EPD-BWO has much higher efficiency at much higher level of power generation compared to the STD-BWO.

We then show in Fig. 8.5b the output power and power conversion efficiency for both cases of EPD-BWO and STD-BWO when changing the beam dc current, keeping the number of period equal to $N = 20$ for both kinds of BWOs. The figure shows that when the beam dc current is exceeding the starting current for each of the EPD-BWO and STD-BWO, the EPD-BWO is achieving much higher power conversion efficiency at much higher level of power extraction. Note that we sweep the current for a larger range for the STD-BWO case to be able reach the level of currents that is used for EPD-BWO to be able to have a fair comparison. Maximum output power is achieved for EPD-BWO case when the used current is $I_0 = 2.6$ A which is about 22% higher than the starting current of oscillation and 24% higher than the EPD current I_{0e} estimated from Fig. 8.4. We expect that longer length of the folded waveguide we use, the closer we are to the EPD and higher efficiency and output power are obtained.

8.3.3 Electron Phase Space Plots

We compare the phase space plots for EPD-BWO and STD-BWO regimes in Fig. 8.6. PIC simulations are performed for structures with a number $N = 15$ of unit-cells. The plots in Fig. 8.6 present the kinetic energy of the electrons showing their space bunching at a given time instant after reaching the steady-state regime. PIC simulator used about 2×10^6 charged particles to model the electron beam. The dashed black line in each figure represents the time-averaged kinetic energy of the electrons at each z-location calculated as $E_{k,avg}(z) = \frac{1}{T}\int_{t=t_{ref}}^{t=t_{ref}+T} E_k(z,t)$, where t_{ref} is any time instant after steady-state regime is reached, $T = 1/f$ and f is the oscillation frequency, and $E_k(z,t)$ is calculated as the mean of electrons' energy existing at time instant t in a small space window that start from $z - \Delta/2$ to $z + \Delta/2$ where Δ =0.025 mm . This space window is chosen to be with width $\sim \lambda_{0b}/20$, where $\lambda_{0b} = u_0/f$.

The STD-BWO case in Fig. 8.6a and Fig. 8.6b have a beam with dc current of $I_0 = 0.44$ A ($I_0 = 1.1I_{st}$) and $I_0 = 2.35$ A ($I_0 = 5.9I_{st}$), respectively; it is shown that the e-beam average kinetic energy (denoted by the dashed line) is almost constant (slightly decreased) which means that the e-beam exits the interaction region with almost the same kinetic energy and therefore it indicates that the energy transferred from the e-beam to the EM wave in the SWS is low and it yields a low level of output power. The EPD-BWO case is shown in Fig. 8.6c for a beam with dc current $I_0 = 2.35$ A ($I_0 = 1.1I_{st}$). The comparison between the plots shows that the EPD-BWO has a bit stronger bunching at the end of the SWS compared to STD-BWO even when using the same dc current. More importantly, the figure shows that the e-beam average kinetic energy (denoted by black dashed line) has a significant decrease along the z-direction which indicates a higher level of energy transfer from the e-beam to the EM wave in the SWS, hence a higher level of distributed power extraction. Since the total e-beam dc power is the same as for the case in Fig. 8.6b, higher power extraction also implies higher electronic conversion efficiency.

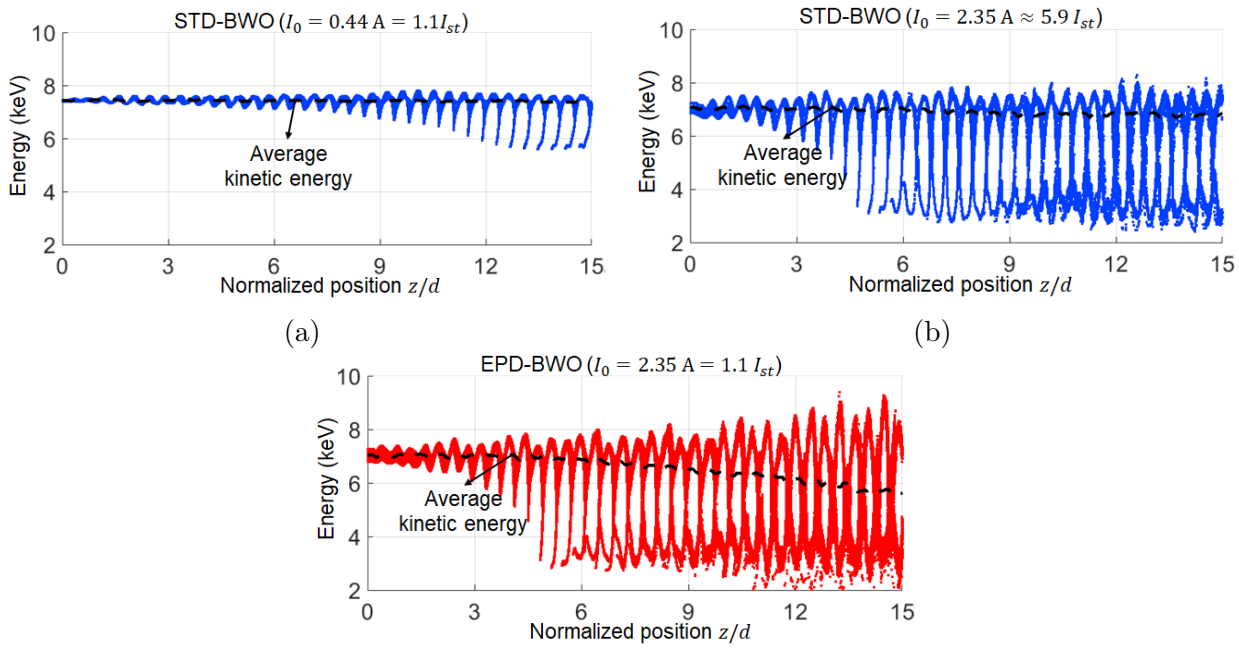

Figure 8.6: Phase space plot of electrons showing the electrons' kinetic energy distribution at a time instant after reaching the steady regime. (a) and (b): STD-BWO when the beam dc current is 0.44 A and 2.35 A. (c): EPD-BWO when the beam dc current is just above the starting current for oscillation 2.35 A. The dashed black lines represent the time-averaged kinetic energy of the electrons moving along the z-direction. (a) and (b) show that the e-beam average kinetic energy is almost constant (slightly decreases for increasing z) for the case of the STD-BWO, which indicates low level of power extraction. (c) shows that the e-beam average kinetic energy remarkably decreases along the z-direction which indicates a higher level of power extraction and higher efficiency as compared to the STD-BWO with the same beam dc current.

8.4 Degenerate Dispersion Relation for the Hot Structure Based on PIC Simulation

The goal of this section is to show the degeneracy of the wavenumbers of the modes of the interactive system (i.e, the hot modes) using PIC simulations. Previously the degenerate dispersion has been shown only using the approximate analytical method based on the Pierce model in [102]. Using the idealized analytical method we also demonstrated the degeneracy of two eigenvectors at the EPD [102]. Here we adopt the general numerical procedure described in [134] to estimate the wavenumbers of the interactive (hot) modes, and show the hot mode degeneracy using data extracted from PIC simulations. The advantage is that PIC simulations predict the behavior of a realistic structure, while the model in [102] was just based on Pierce theory. The procedure is based on exciting the structure from both sides of the SWS by EM waves having monochromatic signal as illustrated in Fig. 8.7a, and then calculating the state vectors that describe the EM field and the e-beam dynamics at discrete periodic locations along the SWS. The time domain data extracted from PIC simulations are transformed into phasors after reaching a steady state regime as described in [134]. We then find the transfer matrix associated to a unit-cell of the "hot" SWS that best relates the calculated state vectors at both ends of each unit cell. Once the estimate of the unit-cell transfer matrix is obtained, we find the hot eigenmodes in a hot SWS using Floquet theory. We provide details about the steps we used to generate the dispersion relation for the hot SWS in [135, 134].

The wavenumber-frequency dispersion describing the complex-valued wavenumber of the hot

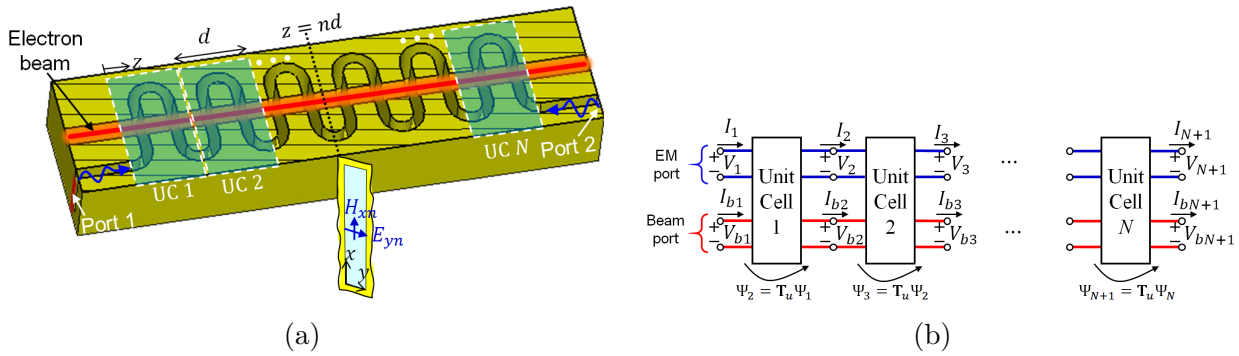

(a) (b)

Figure 8.7: (a) Setup used to determine the complex-valued wavenumber versus frequency dispersion relation of the hot modes in the hot SWS based on data extracted from PIC simulations. (b) Circuit model showing that each unit cell in the hot SWS is modeled as four-port network circuit with *equivalent* voltages and currents representing EM waves (V_n, I_n) and space-charge waves (V_{bn}, I_{bn}) dynamics.

eigenmodes in the hot SWS is determined by running multiple PIC simulations for a SWS made of 11 unit-cells, at different frequencies and at different beam dc currents, and then determining the transfer matrix of the unit-cell at each frequency and current combination. We sweep the e-beam dc current around the expected value of EPD beam current I_{0e}, which is the value of e-beam current pertaining to the infinitely long SWS according to the fitting shown in Fig. 8.4; the use a current that is close to this current value should guarantee the coalescence of two interactive beam-EM modes. It is important to mention that the used beam currents to generate the results in this section are below the starting current of oscillation which is estimated to be 2.175 A as shown in Fig. 8.4, in order to avoid strong saturation regimes proper of oscillators' dynamics. Therefore, by neglecting nonlinearities, one models each unit-cell of the hot SWS using a transfer matrix as discussed previously and in [135, 134]. Since the transfer matrix has dimension 4x4, there are four eigenvalues, i.e., for complex-valued wavenumbers associated to the four hot modes supported by the model shown in Fig. 8.7b. We plot only the three modes that have a wavenumber with a positive real part. The dispersion diagram of such three interactive modes in the hot EM-electron beam system is shown in Fig. 8.8 at different e-beam dc current. The figure shows a degeneracy of two hot modes (the red and blue curves) at a frequency near $f = 88.8$ GHz

which is very close to the oscillation frequency when the used e-beam dc current is around $I_0 = 2.055$A which is close to (and slightly lower) the value of EPD beam current value of $I_{0e} = I_{st}|_{N\to\infty} = 2.09$ obtained from the fitting shown in Fig. 8.4, calculated as a limit for an infinitely long SWS. All the e-beam currents I_0 considered show that two wavenumbers are either close to the degeneracy or degenerate. There is only a very small discrepancy between the estimate of EPD current I_{0e} obtained from the fitting of the starting currents varying length and from observing the degeneracy of two hot modes shown in Fig. 8.8. Such small discrepancy could be attributed to the use of finite precision in calculating the starting current of oscillation, or to the approximations implied in the retrieval method used to obtain the dispersion of hot structure, like possible nonlinearites that are not accounted for in our retrieval model.

8.5 Conclusion

We have conceived an exceptional synchronization regime to increase the output power and power conversion efficiency of BWOs operating at millimeter wave and THz frequencies. The exceptional synchronization regime is achieved through altering the folded waveguide by adding periodic power extraction ports. This allows the interactive system to work at an EPD which implies a maintained synchronism designed for any desired level of power extraction. PIC simulation results shows that a millimeter wave BWO operating at exceptional synchronization regime is capable of generating output power exceeding 3 kwatts with conversion efficiency of exceeding 20% at a frequency of 88.5 GHz. The unique quadratic starting current scaling law with waveguide interaction lengths observed from PIC simulations demonstrates the EPD-based synchronization phenomenon, compared to that in a STD-BWO that has a starting current law that vanishes cubically. The complex-valued

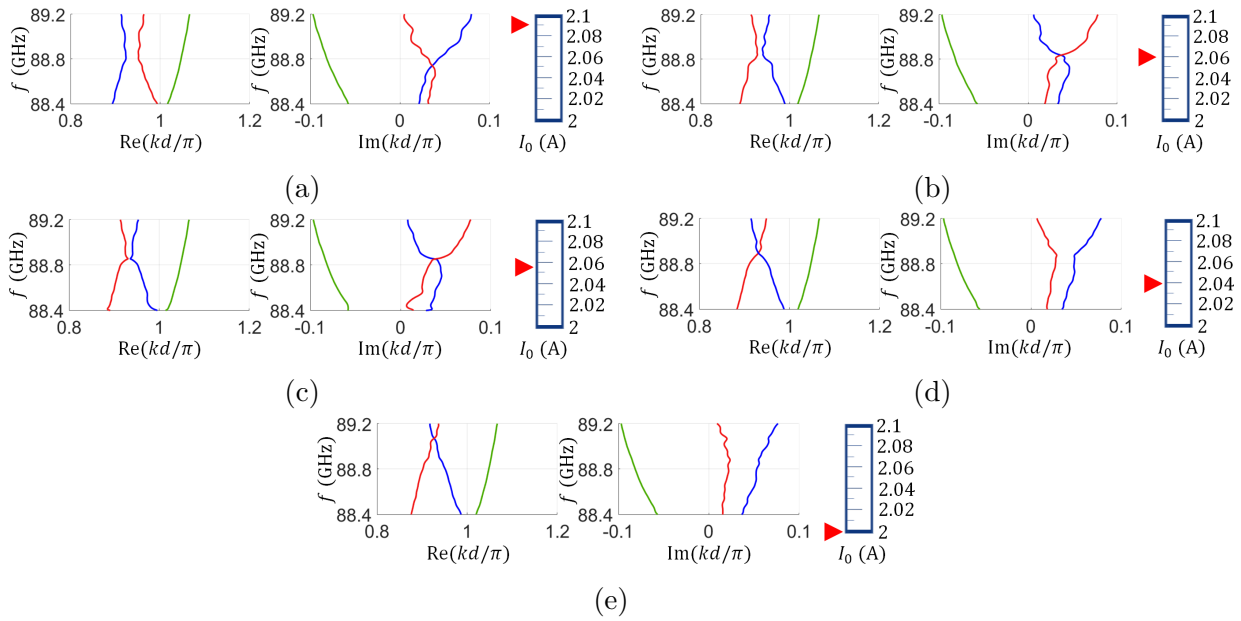

Figure 8.8: Dispersion of complex-valued wavenumbers in the fundamental Brillouin zone, of three hot modes showing the wavenumber degeneracy at about $I_0 = 2.055$A. The three modal wavenumbers with positive real part are retrieved from data obtained by PIC simulations relative to hot SWSs with 11 unit-cells, when using different e-beam dc current: (a)$I_0 = 2.09$A, (b)$I_0 = 2.06$A, (c)$I_0 = 2.055$A, (d)$I_0 = 2.04$ and (e)$I_0 = 2.00$A. All the considered beam dc currents to generate the results are lower than the starting current of oscillation which is estimated to be 2.175 A when using 11 unit cells. The plots show a modal degeneracy when the the beam dc current is about $I_0 = 2.055$A, which is very close to the EPD current value of $I_{0e} = 2.09$ estimated using the fitting in Fig. 8.4, and the operating frequency at which the degeneracy is observed is about $f = 88.8$ GHz, which is close to the oscillation frequency.

wavenumber degeneracy is confirmed by elaborating data extracted from PIC simulations which implies the existence of EPD in the interactive system. This new exceptional synchronization regime may pave the way to the realization of very high power sources at millimeter and submillimeter waves, with high power conversion efficiency.

Chapter 9

Traveling Wave Tube Eigenmode Solution for Beam-Loaded Slow Wave Structure Based on Particle-In-Cell Simulations

A scheme to characterize and model the dynamics of the electron beam-electromagnetic power exchange along a traveling wave tube (TWT) is proposed [134]. The method is based on defining a state vector at discrete periodic locations along the TWT and determining the transfer matrix of the unit cell of the "hot" (i.e., beam loaded) slow-wave structure (SWS) that takes into account the small-signal interaction between the electromagnetic guided field and the electron beam via three dimensional (3D) particle-in-cell (PIC) simulations [134]. Once the estimate of the unit-cell transfer matrix is obtained, we show how to find the hot guided eigenmodes in the interactive system made of an electromagnetic wave in the SWS coupled to an electron beam, by using Floquet theory. In particular, we show how to determine the complex-valued wavenumbers of the hot modes and the eigenvectors associated to

them. We focus on finding the hot modes supported by a TWT amplifier with a serpentine SWS operating at millimeter waves [134]. We show the dispersion relation of the modal complex-valued wavenumbers of the hot modes when varying frequency; near the synchronization point the results are in agreement with Pierce theory. Finally, we show how the proposed scheme is also useful to estimate the gain performance of a long TWT amplifier by cascading the transfer matrices estimated from PIC simulations of a shorter hot SWS. The results show that gain calculated based on the proposed model very well matches the one calculated from 3D PIC simulations of the whole structure [134]. The technique is general and can be applied to any SWS geometry where electromagnetic modes interact with an electron beam. The model we proposed can be a very powerful tool to understand the physics of TWTs and can be used for optimization purposes.

9.1 Motivation and State of the Art

Traveling wave tube (TWT) amplifiers are the devices of choice for several decades for radar and satellite communications applications when high power is required and also when reliability is important, like in satellite communications [153, 154]. TWTs are increasingly important to generate high power at millimeter wave and terahertz frequencies [136, 143, 137, 155, 140] where the current technology based on solid state devices struggles to generate even low power levels. An important mechanism for the energy transfer is the synchronization of the phase velocity v_c of the EM wave in the slow wave structure (SWS) with the average speed of the electrons u_0 [156, 157, 127, 158]. In linear beam devices like TWTs, the EM wave needs to have a longitudinal electric field component E_z to interact with the electron beam to form electron bunches. Therefore the electron beam is modulated in terms of electron's velocity and electron density forming a "space-charge wave" that is synchronized with the EM wave. The modes in the "hot" (i.e., beam loaded) SWS are hybrid physical phenomena

involving both the space-charge wave and EM field, i.e., each mode is made of these two components and may have a complex-valued wavenumber.

The study of the "cold" eigenmodes in the SWS, i.e., the EM modes that exist without considering the interaction with the electron beam, is important to establish the onset of the synchronization condition between the electron beam's space-charge wave and the EM wave in the SWS. Denoting with v_c the phase velocity of the EM mode in the cold SWS and with u_0 the average velocity of the electron beam, the initial synchronization condition is $v_c \approx u_0$. There are various EM solvers in commercial software packages that can be used to find the dispersion diagram of the EM modes in the cold SWS. Some of the most famous commercial eigenmode solvers are provided by finite element method-based packages by Ansys HFSS and DS SIMULIA (previously known as CST Microwave Studio). Often, eigenmode solvers work under the approximation of a lossless SWS.

The interaction of an EM wave with the electron beam results in what we call "hot" (EM+space-charge wave) modes whose phase velocity is different from the phase velocity of the cold EM eigenmode. Hence the "hot" eigenmodes, i.e., the eigenmodes in *interactive* system, have a dispersion diagram that is different from the one of the cold EM modes, especially in the frequency region where $v_c \approx u_0$ [159]. We use the term "hot SWS" to refer to the SWS where the EM wave interacts with the electron beam. In the literature, also other terms like "electron-wave" or "electronic-wave" have been used in [160, 161] to describe a hot mode in the interactive EM-electron beam system. Although the study of the EM eigenmodes in a cold SWS is very important, the main operation of TWTs depends mainly on the eigenmodes of the hot SWS. Note that the modes of the interactive system have complex-valued wavenumbers accounting for energy transfers from and to the electron beam and losses in the metallic waveguide.

The modeling and design of TWTs are carried out by either theoretical models or full-wave simulations. For about the past seventy years, Pierce's classical small signal theory has been

successfully used for the modeling and design of TWTs [113, 106, 156]. Pierce describes the dispersion relation for hot SWS as cubic polynomial [113]. Other studies have been provided in the literature to theoretically model TWTs as in [162, 160, 133, 163, 164, 165, 117, 57, 166, 167, 168, 169]. Although theoretical models are considered as good tools for the initial design of a TWT, they are inaccurate and the actual performance of TWTs is assessed by performing accurate particle-in-cell (PIC) simulations. Indeed, the accuracy of the Pierce model is significantly improved by including the accurate modal frequency dispersion of modes in the cold SWS and by calculating the Pierce interaction impedance versus frequency, both using full-wave numerical methods [134, 170, 171, 172]. The accuracy of Pierce model is further improved by the use of theoretical-based or empirical-based formulas to estimate the plasma frequency and its frequency dependent reduction factor [173, 174], as done in [134].

Advances in three dimensional (3D) electromagnetic simulation software make it possible to accurately model and simulate complex electromagnetic structures accounting for the interaction with an electron beam. Most of the simulation and design work of TWTs is carried out using PIC codes [175, 176]. Some commercial computational software provides solvers based on PIC code that allows to accurately simulate driven-source problems of TWTs taking into account all physical aspects of the problem. Although PIC solvers are currently the most accurate tools to model TWTs, they require a lot of simulation time and computer memory size, especially for TWTs with long lengths, therefore, sometimes running multiple PIC simulations may not be the most practical way to start the optimization process. Several methods were proposed in literature as an intermediate step between simple qualitative theoretical models and time-consuming accurate PIC simulations. Some of these methods are based on merging data extracted from a 3D cold SWS electromagnetic simulator with those of a particle solver. Methods like this and their developments are used in the well known codes as CHRISTINE [177, 164, 178], TESLA [179] and MUSE [180]. Other methods based on merging results from 3D EM simulations and particle solver simulations are also

proposed in [181, 182, 179, 183, 184, 185].

In this chapter, we present a method to model TWTs by finding the equivalent small-signal transfer matrix of a unit-cell based on accurate 3D PIC simulations of a SWS with a relatively small number of unit-cells, which is not very time consuming. The advantage of extracting the hot-SWS unit-cell transfer matrix is not only to infer the characteristics of the hot modes of the EM-beam interactive system (the main goal of this chapter) but also to predict the behavior of longer TWT structures without the need to simulate it using PIC. To date, no commercial software provides an eigenmode solver for hot SWSs taking into account the interaction with the electron beam and losses and the accurate geometry of the SWS.

The method shown in this chapter is based on finding the unit-cell transfer matrix through the interpretation of data extracted from PIC simulation for relatively short SWSs. We show that the method is used to calculate the complex wavenumbers of the hot modes supported in a interactive system made of an EM wave in the SWS coupled to an electron beam. The method also provides the contribution of the EM wave and space charge wave to each specific hot mode associated to each of the complex-valued modal wavenumbers. The proposed solver is based on accurate PIC simulations of finite length hot SWSs and takes account of the precise SWS geometry, materials' EM properties, electron beam cross-section area, confinement magnetic field and space charge effect. The advantage here is that the use of 3D PIC simulations allow to find a 4×4 matrix that fully accounts for all physical aspects of the problem (except nonlinearity, because we use a small signal model) without the need to rely on empirical parameters such as for example the interaction impedance or plasma frequency reduction factor that are used in other solvers. The proposed solver is based on monitoring both the EM fields and electron beam dynamics in each unit cell and then find the best transfer matrix that describe how the hot EM field-electron beam propagates along the TWT as shown in Fig. 9.1. In Subsection 9.2.1 we present all the simplifying assumptions used in our model. Notably, the method provides the dispersion

diagram of complex-valued wavenumbers versus frequency of all the hot modes supported in the interactive SWS. The method here provided could be generalized in the future to model nonlinearities through harmonic balance analysis.

9.2 Theoretical Framework

We demonstrate the performance of the proposed eigenmode solver by considering, as an illustrative example, the TWT amplifier made of a serpentine waveguide SWS with period d consisting of N unit-cells shown in Fig. 9.1a. The input and output radio frequency (RF) signals of the structure are defined as Port 1 and Port 2. However, in the following both will be used as inputs in order to find the complex-valued wavenumbers of the hot modes. It is important to point out that the following technique is general and can be applied to any kind of SWS, hence not only to serpentine waveguide SWSs. The PIC solver simulates the complex interaction between the guided EM wave and electron beam using a large number of charged particles and it follows their trajectories in self-consistent electromagnetic fields computed on a fixed mesh.

9.2.1 Assumptions

The goal is to estimate the wavenumbers and composition of the hot modes of the interactive system made of EM field and the electron beam in a TWT amplifier as the one in Fig. 9.1a. The method is based on finding the modes supported by the periodic distribution of equivalent networks shown in Fig. 9.1b. Each unit cell is modeled using a transfer matrix which is calculated, as explained in this section, based on the results of accurate

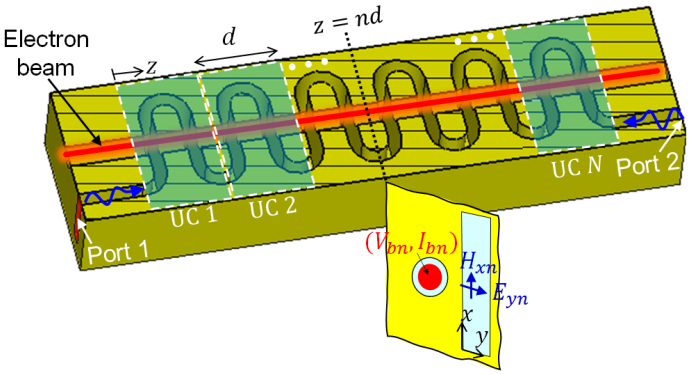

(a)

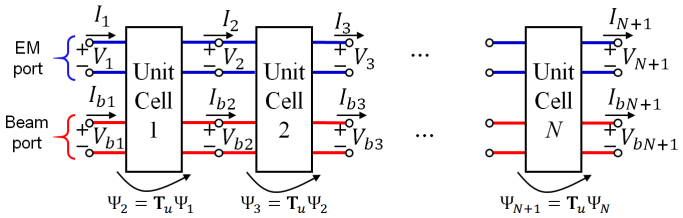

(b)

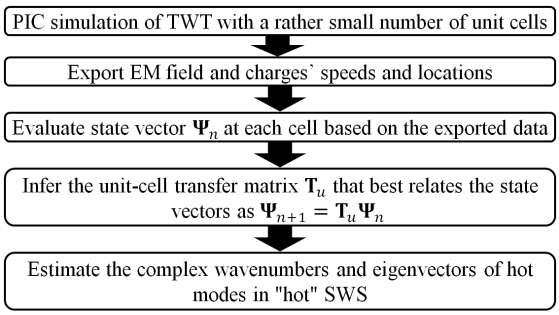

(c)

Figure 9.1: (a) General setup used to determine the complex-valued wavenumber versus frequency dispersion relation of hot modes in the interactive system made of an EM wave in the SWS coupled to an electron beam, based on 3D PIC simulations. In this figure we show a serpentine waveguide SWS, though the method is general and can be applied to several TWT structures. (b) Associated small-signal circuit model where each unit cell in the hot SWS is modeled as a four-port network circuit with *equivalent* voltages and currents representing EM waves (V_n, I_n) and space-charge waves (V_{bn}, I_{bn}) . Each unit cell has 4 ports, two for EM waves (with blue color) and two for space-charge waves (with red color), and describes the interaction between EM fields and the charge wave. The method in this chapter calculates the hot modes of the *infinitely-long* SWS made of cascaded 4-ports unit cells, where the transfer matrix $\mathbf{T}_u$ is estimated using 3D PIC simulations of the *finite-length* structure shown in (a). (c) Data flowchart used to extract the transfer matrix $\mathbf{T}_u$ of a unit cell and then determine the hot eigenmodes of the interactive SWS.

time domain PIC numerical simulations of the guided EM field interacting with the electron beam. The PIC method is based on charged particles motion equations and EM fields, discretized in space and time. Therefore, the EM field satisfies a discretized form of the time-domain Maxwell equations, and the PIC method accounts for the precise geometry and materials of the SWS and for the EM boundary conditions on the lateral walls of the periodic waveguide. Once time domain data are extracted from a PIC simulator, hot modes are found by imposing periodicity of fields/charge wave along the TWT longitudinal direction z in the phasor domain using the periodic distribution of equivalent unit cell networks in Fig. 9.1b, as discussed later on in this section. Therefore, the method estimates the complex wavenumbers of the hot modes that exist in an infinitely-long sequence of equivalent unit cell networks in Fig. 9.1b by elaborating the data provided by the 3D PIC method, simulating the EM field and electrons motion in a realistic TWT of finite length. In Fig. 9.1c we show the data flowchart used to accomplish this task: the time domain data extracted from 3D PIC simulations of relatively short SWSs are transformed into phasors and then used to find the unit-cell transfer matrix $\mathbf{T}_u$ of which we find the eigenvalues and eigenvectors as described in this section.

In using and elaborating the data provided by the PIC solver we make the following assumptions. In the study of linear beam devices like TWTs, a PIC solver calculates the speed of discrete charged particles, and we represent the longitudinal speed of all electron-beam charges as a one dimensional (1D) function $u_b^{tot}(z,t)$. This is achieved by averaging the speed of the charges at each z-cross section as described later on. Therefore, the electron-beam velocity and density are described by the functions $u_b^{tot}(z,t) = u_0 + u_b(z,t)$, and $\rho_b^{tot}(z,t) = \rho_0 + \rho_b(z,t)$, where u_0 and ρ_0 are the velocity and the density of the electrons in the unperturbed beam (i.e., the dc parts), and $u_b(z,t)$ and $\rho_b(z,t)$ represent their modulation functions. In what follows, the structure is excited by monochromatic EM signals, hence we assume that the beam modulations $u_b(z,t)$ and $\rho_b(z,t)$ are also monochromatic. We also assume that the ac modulation of the electron beam is small compared to the dc part, there-

fore the electron beam current is well approximated by the function $i_b^{tot}(z,t) = -I_0 + i_b(z,t)$, where I_0 is the dc value and $i_b(z,t)$ is its time harmonic modulation, hence we neglect non-linear effects. These assumptions are the same as in the Pierce model [113, 106], but the ac values are here calculated using averaging of results taken from time-domain accurate 3D PIC simulations. All the calculations are based on the steady state regime in a TWT, therefore the time domain signals calculated by PIC are transformed into phasors thanks to the assumption that every ac quantity is sinusoidal.

We assume that the EM fields in the *hot* (i.e., beam loaded) SWS of finite length are represented in phasor domain as superposition of modes of the infinitely-long hot SWS as

$$\begin{aligned} \mathbf{E}(x,y,z) &= \textstyle\sum_m \mathbf{E}^{\mathrm{Mode},m}(x,y,z), \\ \mathbf{H}(x,y,z) &= \textstyle\sum_m \mathbf{H}^{\mathrm{Mode},m}(x,y,z), \end{aligned} \tag{9.1}$$

where $\mathbf{E}^{\mathrm{Mode},m}$ and $\mathbf{H}^{\mathrm{Mode},m}$ are the electric and magnetic fields of the m^{th} hot mode in the infinitely-long interactive EM-beam SWS and they are assumed to be represented as a summation of Floquet spatial harmonics as

$$\begin{aligned} \mathbf{E}^{\mathrm{Mode},m} &= e^{-jk_m z} \textstyle\sum_q \mathbf{e}_q^{\mathrm{Mode},m}(x,y) e^{-j2\pi q z/d} \\ \mathbf{H}^{\mathrm{Mode},m} &= e^{-jk_m z} \textstyle\sum_q \mathbf{h}_q^{\mathrm{Mode},m}(x,y) e^{-j2\pi q z/d}. \end{aligned} \tag{9.2}$$

Fields are computed using 3D PIC simulations, and are sampled with a spatial period d along the SWS. Our goal is to find the complex-valued wavenumbers k_m and the eigenvectors of the hot beam-electromagnetic eigenmodes of the *infinitely-long* SWS using PIC simulations of the *finite-length* structure.

The discussion in the rest of the chapter is based on linearity of the system with respect to

the ac EM and space charge waves, i.e., assuming the EM is a small signal, and also on the assumption that the electron beam does not lose energy along its travel along the TWT, therefore during the retrieval method, the dc electron beam velocity u_0 is assumed to be constant along the TWT. This assumption is important because we assume that the transfer matrix describing each periodic cell is the same along the whole SWS length; however, it could be relaxed in future developments.

The physical quantities that represent the EM modes in the interacting SWS are the electric and magnetic fields $\boldsymbol{\mathcal{E}}(x, y, z, t)$ and $\boldsymbol{H}(x, y, z, t)$ which are represented in terms of equivalent voltages and currents $v_n(t)$ and $i_n(t)$ at discrete location of the periodic structure, where n is the unit cell index number. In the rest of the chapter, we assume that only one cold EM mode is able to propagate in each direction of the cold SWS, hence only a single pair (v_n,i_n) will be sufficient to describe the EM wave. Although these quantities cannot be uniquely defined in most kinds of waveguides, it is possible to define them and use them to model the space and temporal dynamics in a waveguide [186, 58, 187]. In case the SWS supports multiple modes that interact with the electron beam, one should use multiple pairs of voltage and current to describe the interaction with the electron beam (not studied here).

The space-charge wave is represented by equivalent ac kinetic voltages and beam currents $v_{bn}(t)$ and $i_{bn}(t)$, respectively, using the averaging method in Fig. 9.2 as described next.

We define a state vector that describes the EM and space-charge waves at locations $z = z_n = nd$ as

$$\boldsymbol{\psi}_n(t) = [\ v_n(t),\ \ i_n(t),\ \ v_{bn}(t),\ \ i_{bn}(t)\ ]^T. \tag{9.3}$$

In the following sections, we explain how this state vector is calculated using PIC calculations

at $z = nd$ locations along the SWS. Since we assume that at steady state all the quantities involved in the state vector are monochromatic, we define a state vector in phasor-domain as

$$\mathbf{\Psi}_n = [\ V_n,\ \ I_n,\ \ V_{bn},\ \ I_{bn}\ ]^T, \tag{9.4}$$

assuming an implicit $e^{j\omega t}$ time dependence. Lower case letters are used for the time-domain representation whereas capital letters are used for the phasor-domain representation.

In the phasor domain, we assume that the longitudinal propagation of the state vector satisfies the equation $\mathbf{\Psi}_{n+1} = \mathbf{T}_u \mathbf{\Psi}_n$, where $\mathbf{T}_u$ is the periodic unit cell 4×4 transfer matrix, which is unknown and assumed invariant along the periodic cells of the SWS. As explained next, the first goal is to provide a method to estimate the transfer matrix $\mathbf{T}_u$. Then, we assume that each of the hot EM-charge wave mode in (9.1)-(9.2) is described by a state vector variation as $\mathbf{\Psi}_n = \mathbf{\Psi}^{\text{Mode},m} e^{-jk_m nd}$, where k_m is the complex-valued wavenumber of such a mode. The main goal of this chapter is to find the complex wavenumbers k_m of all the hot modes in the interactive SWS and to find the EM and beam modal weights in (9.4) for each of the hot modes. This goal is achieved by solving the eigenvalue problem associated to the circuit in Fig. 9.1b,

$$\mathbf{T}_u \mathbf{\Psi}^{\text{Mode},m} = e^{-jk_m d} \mathbf{\Psi}^{\text{Mode},m}, \tag{9.5}$$

once the estimate of the transfer matrix $\mathbf{T}_u$ has been calculated as described in the next two sections.

In summary, the method we propose is a small-signal 1D model which is represented via

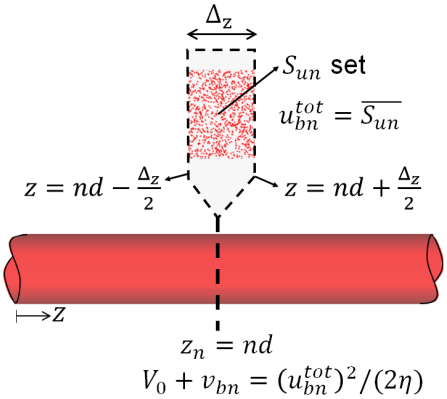

Figure 9.2: Illustration of how the speed of the space-charge wave u_{bn}^{tot} is calculated at the entrance of the n^{th} unit-cell (at $z = nd$) using PIC simulation data. The space-charge wave speed at $z = nd$ is calculated as the average of the speeds of the PIC-defined charges that are in the proximity of $z = z_n = nd$, i.e., in the small range defined as $z_n - \Delta_z/2 < z_c(t) < z_n + \Delta_z/2$, at time t. The subset of all the PIC-defined charges $S_u(t)$ in this spatial interval at time t is called $S_{un}(t)$ which represents the charges that exist at time t in the proximity of $z = z_n = nd$. Since the set of $S_{un}(t)$ is composed of many PIC-defined charges, we define their collection average $u_{bn}^{tot} = \overline{S_{un}}$, and the charge-wave equivalent kinetic voltage is $v_{bn}^{tot} = (u_{bn}^{tot})^2/(2\eta)$.

cascading a 4×4 transfer matrix that describes the state vector evolution along the z coordinate. The transfer matrix is obtained based on the data extracted from 3D PIC simulations of the interactive EM-beam system through processing of 3D PIC simulation data.

9.2.2 Determination of the System State-vector

Since the serpentine waveguide does not support a TEM mode, voltage and current cannot be uniquely defined. We use the equivalent representation in [186, 187, 58] that models the waveguide as a transmission line with equivalent voltage and current. Following the derivations in [186, 187, 58] for the TE_{10} mode in a straight rectangular metallic waveguide, and using the coordinates shown in the inset of Fig. 9.1a, the transverse fields are written in phasor domain as

$$
\begin{aligned}
E_y(x,z) &= V(z)\sqrt{\frac{2}{ab}}\sin\left(\frac{\pi x}{a}\right), \\
H_x(x,z) &= -I(z)\sqrt{\frac{2}{ab}}\sin\left(\frac{\pi x}{a}\right).
\end{aligned}
\tag{9.6}
$$

Using (9.6), the discrete voltages and the currents that represent the EM state in phasor domain at different rectangular cross-sections of the serpentine waveguide are defined as

$$
\begin{aligned}
V_n &= \sqrt{\frac{ab}{2}}E_{yn} \\
I_n &= -\sqrt{\frac{ab}{2}}H_{xn},
\end{aligned}
\tag{9.7}
$$

where E_{yn} and H_{xn} are the transverse electric and magnetic fields of the TE_{10} mode calculated at the center ($x = a/2$) of the rectangular waveguide cross section as shown in the inset in Fig. 9.1a and they are calculated at the unit cells boundaries shown in Fig. 9.1a. The transverse electric and magnetic field components E_{yn} and H_{xn} are calculated as phasors after the time domain data extracted from PIC simulations are integrated over a time period as explained later on. The proper normalization of voltages and currents in (9.7) provides the power carried by the TE_{10} mode in the SWS

$$
\begin{aligned}
P_n &= \tfrac{1}{2}\int_{x=0}^{a}\int_{y=0}^{b}\mathrm{Re}\left[-E_y(x,nd)H_x^*(x,nd)\right]dxdy \\
&= \tfrac{1}{2}\mathrm{Re}(V_nI_n^*).
\end{aligned}
\tag{9.8}
$$

Similar methods can be used to define voltage and current for other SWS geometries. For example, the voltage and current for a helix SWS could be defined as the voltage difference between the helix and host waveguide and the physical current in the helix, at specific z,

respectively, which can be calculated through the integration of electric and magnetic field.

A PIC solver provides the speeds and locations of all the charged particles used to model the electron beam at any time t. We define two dynamic sets that involve the speeds and coordinates z of all the charges in PIC simulation at any time instant t as $S_u(t) = \{u_1(t), u_2(t), ..., u_{Nq}(t)\}$ and $S_z(t) = \left\{z_1(t), z_2(t), ..., z_{N_q(t)}(t)\right\}$, respectively, where $N_q(t)$ is the total number of charged particles used by the PIC simulator to model the electron beam at time instant t. The space-charge wave modulating the electron beam is assumed to be represented using two physical quantities: the electrons' speed which is expressed in term of the beam equivalent kinetic voltage $v_b^{tot}(z,t)$, and the space-charge wave current modulation $i_b^{tot}(z,t)$, as also described in Refs. [111, 118, 106]. The beam total equivalent kinetic voltage at the entrance of the n^{th} unit-cell is defined as $v_{bn}^{tot}(t) = (u_{bn}^{tot}(t))^2/(2\eta)$, where $u_{bn}^{tot}(t) = \overline{S_{un}(t)}$ is the equivalent speed of the space-charge wave calculated as the average of the speeds of the set

$$S_{un}(t) = \left\{ \; S_u(t) \quad | \quad nd - \frac{\Delta_z}{2} < S_z(t) < nd + \frac{\Delta_z}{2} \; \right\}, \tag{9.9}$$

that is defined by all the charged particles that are in vicinity of the entry of the n^{th} unit-cell ($z = nd$), and within the small spatial interval Δ_z, as illustrated in Fig. 9.2. The length of the spatial interval Δ_z is chosen to be very small, i.e, $\Delta_z \leq \lambda_{0b}/20$, where $\lambda_{0b} = u_0/f$, and u_0 is the electron time-average speed and f is the frequency modulating the space-charge wave. Although Δ_z is chosen to be small, it should be also large enough to contain a very large set of charged particles, as illustrated in Fig. 9.2. The charge-wave current at the n^{th} unit-cell ($z = nd$) is defined as $i_{bn}^{tot}(t) = -\rho_{bn}^{tot}(t)u_{bn}^{tot}(t)$, where $\rho_{bn}^{tot}(t)$ is the electron beam charge density at the entry of the n^{th} unit-cell and is calculated as $\rho_{bn}^{tot}(t) = q_e N_{bn}(t)/\Delta_z$ where q_e is the macrocharge value of each PIC-defined particle and $N_{bn}(t)$ is the number

of such charged particles in the set $S_{un}(t)$. The ac modulated parts are then calculated as $v_{bn}(t) = v_{bn}^{tot}(t) - V_0$ and $i_{bn}(t) = i_{bn}^{tot}(t) + I_0$ which are used later on to construct the system's state vector. As described below, when we calculate the phasor I_{bn} associated to $i_{bn}(t)$ we will retain only the frequency component at radian frequency ω and not the higher order harmonics.

It is important to point out that in this illustrative example we assume that the SWS supports one cold EM mode that can propagate in each direction and that the electron beam is represented by a single state that describes the average behavior of the speed and density of the charged particles distribution. Describing the EM-charge wave state using the four-dimensional state vector (9.3) constitutes a good approximation in many cases where the SWS supports only one EM mode (in each direction) and the electron beam is modulated in a homogeneous way, i.e., the beam modulation does not change with radial and azimuthal angular directions. However, a more accurate model of the hot SWS could be obtained by using an equivalent multi-transmission line model to describes all the EM modes in the SWS, and an equivalent multi "beam transmission line" (or multi stream beam) to describe the electron beam. Indeed, since we know that in reality the momentum and charge density description of the electron beam dynamics usually looks like a multi-valued function, it may be convenient to decompose the electron beam using various areas in transverse cross section leading to a multi "beam transmission line" with multiple kinetic voltages and space-charge wave currents. For the sake of simplicity, in this chapter the electron beam dynamics is represented only with one "beam transmission line", i.e., with a single $(v_b(t), i_b(t))$ pair.

The interaction between the space-charge wave and the EM wave yields three eigenmodes that travel in the beam direction in addition to a mode (mainly made of only EM field) propagating opposite to the beam direction, indeed the latter has very little interaction with the electron beam [106]. The three hot modes with positive phase velocity are composed of both EM fields and space-charge wave modulations, and form the "three-wave" model used

in Refs. [113, 106, 156]. Under the assumption of using a single tone excitation of an EM wave from Port 1 and/or Port 2, all four hot EM-charge wave modes in the interacting system can be excited: an excitation from Port 1 mainly excites the three interacting hot modes, whereas the excitation from Port 2 excites mainly the EM mode propagating in opposite direction of the beam. Reflections may occur at the left and right ends in a realistic finite-length SWS, so in reality all four modes may be present, depending on the EM reflection coefficients at the two ends.

At steady state, the state vector at any fixed z location is represented in phasor-domain as in (9.4), assuming an implicit $e^{j\omega t}$ time dependence for all physical quantities. The phases of phasors are calculated with respect to a fixed time at steady state. The phasor-domain representation (9.4) of the state vector $\boldsymbol{\psi}_n(t)$ is calculated as

$$\boldsymbol{\Psi}_n = \frac{1}{T}\int_{t=0}^{T} \boldsymbol{\psi}_n(t+t_{ref})e^{-j\omega t}dt, \tag{9.10}$$

where $T = 2\pi/\omega$ and t_{ref} is a time reference used to calculate the phasors and it should be greater than the steady state time t_{ss}, i.e., $t_{ref} > t_{ss}$. It is important to mention that only the fundamental component at frequency ω is maintained after the Fourier transform is carried out to build the state vector in phasor domain $\boldsymbol{\Psi}_n$ in (9.4), hence all frequency harmonics in $\boldsymbol{\psi}_n(t)$ are neglected in the following. In the phasor-domain, we model each unit cell of the interacting SWS as a 4-port network circuit with voltages and currents representing both the EM waves and the electron beam dynamics, as shown in Fig. 9.1a. As described in the previous section, under the assumption of small signal modulation of the beam's electron velocity and charge density, the 4-port networks modeling the EM-charge wave interaction in each unit-cell of the hot SWS are assumed identical. Therefore, one can define a 4×4 transfer matrix $\mathbf{T}_u$ of the interaction unit-cell of a SWS using the relation between the input

and output state vector at each unit-cell as

$$\begin{aligned} \mathbf{\Psi}_2 &= \mathbf{T}_u \mathbf{\Psi}_1, \qquad (9.11.1) \\ \mathbf{\Psi}_3 &= \mathbf{T}_u \mathbf{\Psi}_2, \qquad (9.11.2) \\ &\vdots \\ \mathbf{\Psi}_{N+1} &= \mathbf{T}_u \mathbf{\Psi}_N, \qquad (9.11.N) \end{aligned} \tag{9.11}$$

where $\mathbf{\Psi}_{n+1}$ and $\mathbf{\Psi}_n$ are the output and input state vectors of the n^{th} unit-cell, respectively, where $n = 1, 2,..\ N$. The state vectors $\mathbf{\Psi}_n$ are calculated from ψ_n using PIC simulations; then an estimate of the transfer matrix $\mathbf{T}_u$ is inferred by the method described in the following section. Note that the unit-cell transfer matrix in (9.11) is assumed to be invariant along the SWS, which is an approximation, as discussed in the next subsection. In the following we calculate the unit cell transfer matrix based on two methods: (i) we find one $\mathbf{T}_u$ that best approximates all equations in (9.11) and (ii) we find all the individual $\mathbf{T}_u$ matrices in (9.11) and their eigenvalues. The average of the eigenvalues calculated using method (ii) is very close to the one obtained from method (i).

9.2.3 Finding the Transfer Matrix of a Unit Cell of the Interactive System

Approximate Best Fit Solution

The relations in (9.11) represent $4N$ linear equations in 16 unknowns which are the elements of the transfer matrix $\mathbf{T}_u$. Assuming $N > 4$, the system in (9.11) is mathematically referred to as overdetermined because the number of linear equations ($4N$ equations) is greater than the number of unknowns (16 unknowns). We rewrite (9.11) by clustering all the given

equations in matrix form as

$$[\mathbf{W}_2]_{4\times N} = [\mathbf{T}_u]_{4\times 4}\,[\mathbf{W}_1]_{4\times N}\,, \tag{9.12}$$

where

$$\mathbf{W}_1 = \left[\begin{array}{cccc} \boldsymbol{\Psi}_1, & \boldsymbol{\Psi}_2, & \ldots & \boldsymbol{\Psi}_N \end{array}\right], \tag{9.13}$$

is a $4 \times N$ matrix and its columns are the state vectors at input of each unit-cell, and

$$\mathbf{W}_2 = \left[\begin{array}{cccc} \boldsymbol{\Psi}_2, & \boldsymbol{\Psi}_3, & \ldots & \boldsymbol{\Psi}_{N+1} \end{array}\right], \tag{9.14}$$

is an analogous $4 \times N$ matrix but with a shifted set of the state vectors, i.e., its columns are the state vectors at the output of each unit-cell. Our first goal is to find the 16 elements of the transfer matrix $\mathbf{T}_u$.

An approximate solution that best satisfies all the given equations in Eq. (9.11), i.e., minimizes the sums of the squared residuals, $\sum_n ||\boldsymbol{\Psi}_{n+1} - \mathbf{T}_u \boldsymbol{\Psi}_n||^2$ is determined similarly as in [188, 189, 190] and is given by

$$\mathbf{T}_{u,best} = \Big([\mathbf{W}_2]_{4\times N}\,[\mathbf{W}_1]^T_{4\times N}\Big)\,\Big([\mathbf{W}_1]_{4\times N}\,[\mathbf{W}_1]^T_{4\times N}\Big)^{-1}. \tag{9.15}$$

It is important to point out that all the four modes of the interactive EM-charge wave system should be excited to be able to have four independent columns in the construction of the matrices $\mathbf{W}_1$ and $\mathbf{W}_2$ since we need apply the inverse operation in (9.15). This occurs when

there is sufficient amount of power incident on Port 1 and Port 2.

Distinct Determined Solutions

The transfer matrix $\mathbf{T}_u$ can also be determined directly by taking any four equations of Eq.(9.11). Assume we choose Eq. (9.11.q), Eq. (9.11.i), Eq. (9.11.j) and Eq. (9.11.k), and therefore yields

$$\mathbf{T}_{u,qijk} = [\mathbf{w}_{2,qijk}]_{4\times4}\,[\mathbf{w}_{1,qijk}]^{-1}_{4\times4}\,, \tag{9.16}$$

where

$$\mathbf{w}_{1,qijk} = \left[\begin{array}{cccc} \boldsymbol{\Psi}_q, & \boldsymbol{\Psi}_i, & \boldsymbol{\Psi}_j, & \boldsymbol{\Psi}_k \end{array}\right], \tag{9.17}$$

and

$$\mathbf{w}_{2,qijk} = \left[\begin{array}{cccc} \boldsymbol{\Psi}_{q+1}, & \boldsymbol{\Psi}_{i+1}, & \boldsymbol{\Psi}_{j+1}, & \boldsymbol{\Psi}_{k+1} \end{array}\right]. \tag{9.18}$$

Assuming the SWS has N unit cells, there will be C_4^N possible solutions for $\mathbf{T}_{u,qijk}$, where $C_4^N = N!/((N-4)!4!)$ is the number of the combinations to choose q, i, j and k out of N choices. Under the assumption that the transfer matrices of each unit-cell are identical, the sets of four eigenvalues resulting from the C_4^N solutions of $\mathbf{T}_{u,qijk}$ should be identical too. However, the electron beam nonlinearity and other factors may cause small discrepancy in

the eigenvalues resulting from the various eigenmode solutions of $\mathbf{T}_{u,qijk}$, as shown in the next section.

It is important to point out that some combinations may result in a underdetermined system where the rank of $\mathbf{w}_{1,qijk}$ could be less than 4, i.e., $\mathbf{w}_{1,qijk}$ could be singular (i.e., with a vanishing determinant). For example, when selecting unit cells toward the right end of the TWT (e.g., $q = N-3, i = N-2, j = N-1$ and $k = N$), the state vectors forming $\mathbf{w}_{1.qijk}$ are dominated by only one mode that has exponential growing in z direction, and therefore the matrix $\mathbf{w}_{1,qijk}$ tends to be singular. Therefore, one can neglect combinations that are close to be singular by checking the determinant of $\mathbf{w}_{1,qijk}$ for each combination. Following this method, multiple transfer matrices are found that lead to multiple wavenumbers that are clustered around four complex values.

9.2.4 Finding the Hot Eigenmodes of the Interactive System

Once the transfer matrix is estimated (either using the best-approximate solution $\mathbf{T}_{u,best}$ of the overdetermined system or determined solutions $\mathbf{T}_{u,qijk}$), the hot eigenmodes are determined by assuming a state vector to be in the form of $\mathbf{\Psi}_n \propto e^{-jknd}$, where k is the complex Bloch wavenumber that has to be determined and d is the SWS period. Inserting the assumed state vector z-dependency in (9.11) yields the eigenvalue problem in (9.5). Note that eigenvalues e^{-jkd} and eigenvectors $\mathbf{\Psi}_n$ of the eigenvalue problem in (9.5) depend only on the transfer matrix $\mathbf{T}_u$. The four eigenvalues,

$$e^{-jkd} = \mathrm{eig}(\mathbf{T}_u), \tag{9.19}$$

of the transfer matrix $\mathbf{T}_u$ lead to four Floquet-Bloch modes k_m, where $m = 1, 2, 3, 4$, with spatial harmonics $k_m + 2\pi q/d$, where q is an integer that defines the Floquet-Bloch harmonic index as in (9.2). Some examples are provided in the next sections. Note that Eq. (9.5) provides also the eigenvectors $\mathbf{\Psi}^{\text{Mode},m}$ and important information can be extracted from them. Each m^{th} eigenvector possesses the information of the respective weights of the EM field (V, I) and space-charge wave (V_b, I_b) in making that particular hot eigenmode solution. Furthermore, including the case when more EM modes are used in the SWS interaction zone or when two hot modes concur in the synchronization, an analysis of the eigenvectors can also show possible eigenvector degeneracy conditions. For example, in [126, 102, 124, 135], two hot modes are fully degenerate in wavenumbers and eigenvectors forming what was called a "degenerate synchronization" (degeneracy between two hot modes). Other important degeneracy conditions are those studied in [5], where three or four fully degenerate EM modes in the cold SWS are used in the synchronization with the electron beam, a condition refer to as "multimode synchronization" (degeneracy among cold EM modes).

In a finite length TWT, the total EM field (represented by V_n^{tot}, I_n^{tot}) and space-charge wave (represented by V_{bn}^{tot}, I_{bn}^{tot}) resulting from their interaction, calculated at each n^{th} location, are represented in terms of the four eigenmodes,

$$\mathbf{\Psi}_n^{\text{tot}} = \sum_{m=1}^{4} a_m \mathbf{\Psi}^{\text{Mode},m} e^{-jk_m nd}, \tag{9.20}$$

where a_m is the weight of the m^{th} mode, which depends on the mode excitation and boundary conditions, and $\mathbf{\Psi}^{\text{Mode},m}$ is the interactive system eigenvectors obtained from (9.5). Each Floquet-Bloch mode in the periodic hot SWS is represented as $\mathbf{\Psi}^{\text{Mode},m} e^{-jk_m nd}$.

In the next section we apply the proposed technique to find the complex-valued wavenumber k_m of each of the four hot eigenmodes $(m = 1, 2, 3, 4)$ for an illustrative serpentine TWT.

9.3 Application to Serpentine-Based TWT Amplifiers

Serpentine SWSs have recently gained a lot of interest due to the growing importance of millimeter wave and terahertz frequencies in modern applications and also due to the advancement of fabrication technologies such as LIGA (LIthographie, Galvanoformung, Abformung). As an illustrative example, we use the same geometry of serpentine SWS discussed in [145, 172], as shown in 9.1a. The serpentine waveguide is made of copper and has rectangular cross-section of dimensions $a = 1.9$ mm and $b = 0.325$ mm, bending radius of 0.325 mm (radius at half way between inner and outer radii), straight section length of 0.6 mm, period $d = 1.3$ mm, and beam tunneling radius of $R_t = 0.175$ mm. The simulated TWT comprises 15 unit-cells. An electron beam with dc voltage $V_0 = 20$ kV is used such that the synchronization occurs with a forward EM wave leading to amplification. With the given geometry, the cold SWS supports two cold EM modes, one in each diction, with Bloch wavenumbers β_c and $-\beta_c$. Because of the SWS periodicity, each EM mode is made of Floquet harmonics with wavenumbers $\beta_{c,l} = \beta_c + 2l\pi/d$, where l is an integer, and phase velocities $v_{c,l} = \omega/\beta_{c,l}$, where β_c is the wavenumber of the cold SWS in the fundamental Brillouin zone defined as $\beta_c d/\pi \in [0, 2]$. Note that β_c is defined here to be positive and therefore $k = \beta_c$ represents a forward wave, however, the cold SWS also supports a wave with wavenumber $k = -\beta_c$ together with all its Floquet harmonics. In Fig 9.3a we show the beam line $\beta_0 = \omega/u_0$ (red line) where $u_0 = \sqrt{2\eta V_0} = 0.28c$, and the dispersion diagram of EM modes in the *cold* SWS (black line) in the second Brillioun zone ($k = \beta_{c,1}$ and $k = -\beta_c + 4\pi/d$). The dispersion of the EM mode in the cold SWS (solid black) is found by the finite element method-based eigenmode solver implemented in CST Studio Suite by numerically simulating only one unit-cell of the cold serpentine SWS. Synchronization between the electron beam and the Floquet mode in the second Brillouin zone (defined as $\mathrm{Re}(kd/\pi) \in [2, 4]$) occurs when $v_{c,1} \approx u_0$ ($v_{c,1} = \omega/\beta_{c,1}$) at frequencies centered at $f = 88$ GHz and at $\mathrm{Re}(kd/\pi) \approx 2.8$.

All 3D PIC simulations in this chapter are performed using CST Particle Studio, a solver

where both EM fields and charged particle motion are modeled in 3D. The 3D segmentation performed by PIC simulations uses Hexahedral mesh with mesh size of about Δ=50 µm which is $\Delta \sim \lambda_{100\ \mathrm{GHz}}/60$,where $\lambda_{100\ \mathrm{GHz}} = 3$ mm corresponds to free space wavelength calculated at 100 GHz, i.e., close to the frequency of operation of the TWT. Figure 9.1a shows the setup used for PIC simulations. The time-domain simulations performed in this chapter use a time step of 70 fs which is about $T/143$ where $T = 1/f$ is the time period calculated at f =100 GHz. Simulations have been performed using a number of threads of 28 and the simulations have been accelerated using a GPU card (Kepler/Maxwell card). The run-time for a single PIC simulation for the structure with 15 unit cells was about 10 minutes.

We consider the electron beam to have a radius of R_b =0.13 mm, a dc current of 0.1 A and an axial confinement dc magnetic field of 0.6 T. Our goal is to obtain the dispersion of the hot serpentine SWS, i.e., the complex-valued wavenumber of the hot modes that account for the interaction between the electron beam and the EM wave. We excite the SWS from Port 1 with 2 W and from Port 2 with 1 W. An amplifier has the input at one port and the output at the other one, but here we want to excite all the supported eigenmodes sufficiently to be observed in the calculations. We start by studying the eigenmode wavenumbers in the interacting SWS system at constant frequency $f = 88$ GHz, which is very close to the synchronization point where $u_0 = v_{c,1}$. The four complex-valued wavenumbers of the hot modes are shown in Fig. 9.3b based on results from Eq. (9.15) leading to the four red crosses, and from Eq. (9.16) leading to various blue dots. The scattered blue dots represent 100 sets of four complex wavenumbers associated the largest 100 determinants of the matrix $\mathbf{w}_{1,qijk}$ out of the total 715 combinations. The inset in Fig. 9.3b shows that the wavenumbers of the three interacting hot modes lie on a circle as predicted by the original Pierce model [113, 106], though they do not form a perfect equilateral triangle.

The result show a good agreement between the red crosses that represent the four wavenum-

bers obtained from the eigenvalues of $\mathbf{T}_{u,best}$ where $\mathbf{T}_{u,best}$ is the best-approximate solution of the overdetermined system in Eq. (9.15) and the blue dots that represent the eigenmodes of various estimates of $\mathbf{T}_{u,qijk}$ obtained from solutions of (9.16) which are transfer matrices obtained based on different location along the SWS. The very small deviations between the wavenumbers obtained from different solutions is due to non-idealities resulting in having non-identical unit-cells along the structure which yields different transfer matrices. This may happen due to electron beam nonlinearity, the change of the beam dc kinetic voltage along the TWT, the slight change of the beam radius along the TWT, in addition to the errors due to finite mesh, which may be not periodic from cell to cell, and finite number of charged particles used to model the TWT dynamics. The mode with almost purely real wavenumber mode with $\mathrm{Re}(kd/\pi) > 3$, shown in Fig. 9.3b, represents the Floquet harmonic $k \approx -\beta_c + 4\pi/d$ of the hot mode, associated to the cold backward wave with negative wavenumber $-\beta_c$, not involved in the synchronism. The three modes with $2 < \mathrm{Re}(kd/\pi) < 3$ represent the three hot modes resulting from the EM-beam interaction, and the one with positive imaginary part of k is the mode responsible for signal amplification. The calculated three eigenmodes are in good agreement with the three-wave theory of the Pierce model [113, 106] around the synchronization point which indicates that the interaction yields three modes with $\mathrm{Re}(k)>0$: two of them are waves that are slower than the electron beam average speed u_0, and among these two, one wave is growing in the beam direction while the other one is decaying, the third mode is basically an unattenuated wave that travels faster than the beam-average speed u_0. In these calculations we did not consider the state vectors at the beginning and end of the structure (i.e., $\Psi_1$and Ψ_{16}) to generate our results because they may involve high order EM modes, besides the fundamental propagating eigenmodes in the SWS (higher order modes are excited when a discontinuity or a modification of the periodicity occurs).

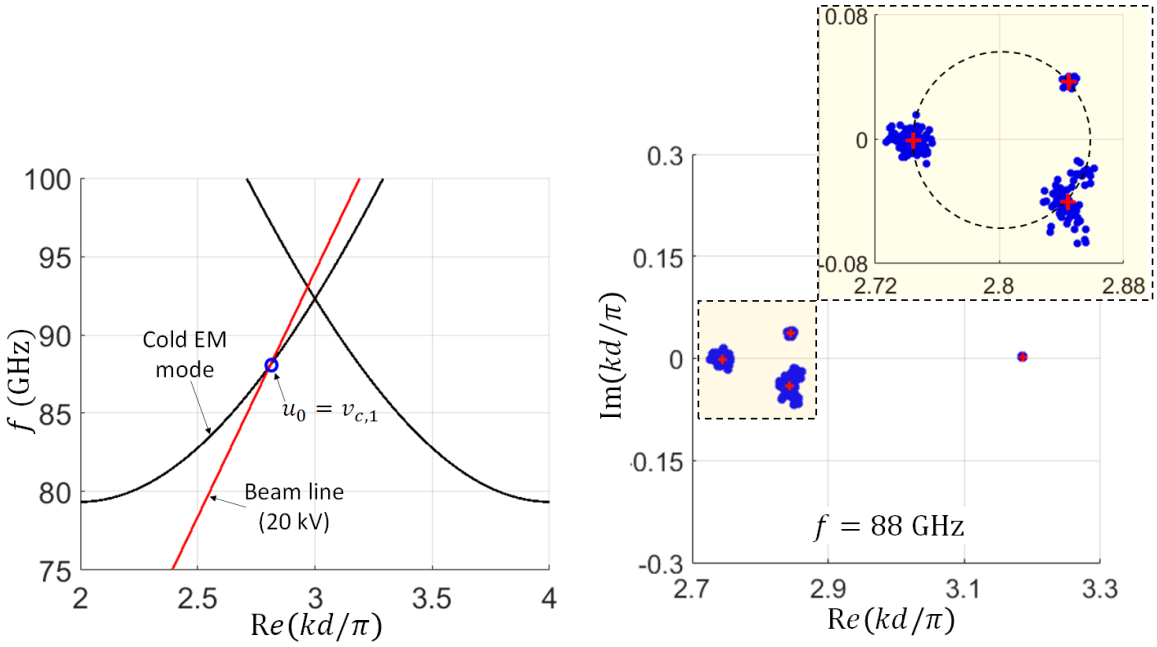

(a) (b)

Figure 9.3: (a) Dispersion relation showing the *cold* eigenmodes of the EM wave (black) and the beam line (red) in the second Brillouin zone defined here as $\mathrm{Re}(kd/\pi) \in [2, 4]$. The electron beam has a dc voltage of 20 kV and it interacts with a forward EM mode leading to TWT amplification. (b) Complex-valued wavenumbers of the eigenmodes in the interactive (hot) electron beam-EM mode in the serpentine SWS evaluated using PIC simulations, assuming a beam voltage of 20 kV and current of 0.1 A at $f = 88$ GHz. Red crosses represent the four wavenumbers obtained from the transfer matrix $\mathbf{T}_{u,best}$ obtained from Eq. (9.15). Blue dots represent different sets of four wavenumbers obtained from different sets of transfer matrices $\mathbf{T}_{u,qijk}$ obtained from (9.16) using different combinations of indices q, i, j and k. The figure inset shows that the three interacting modes' wavenumbers lie on a circle. Therefore, the distribution of the complex-valued wavenumbers is in agreement with what predicted by the Pierce model. The almost purely real wavenumber mode with $\mathrm{Re}(kd/\pi) > 3$ represents Floquet harmonic $k \approx -\beta_c + 4\pi/d$ of the hot mode with negative wavenumber not involved in the synchronism.

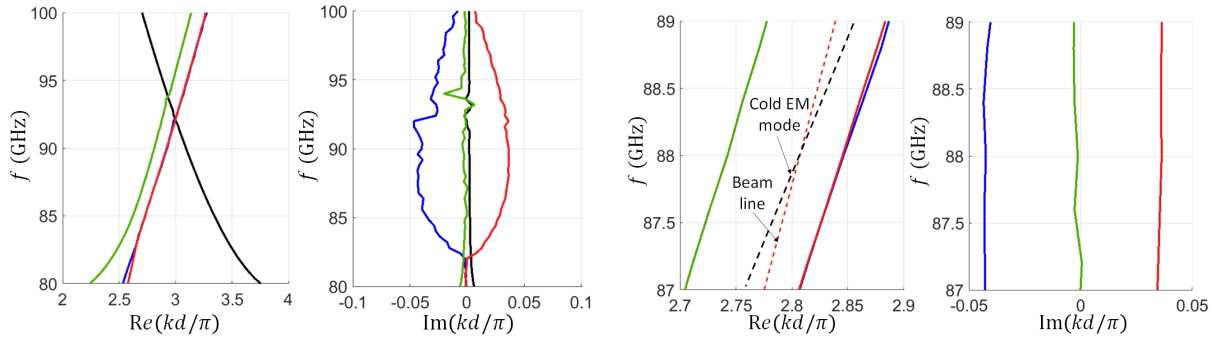

(a) (b)

Figure 9.4: (a) Wavenumber-frequency dispersion relation of the hot eigenmodes in the interactive serpentine SWS in Fig. 9.1a, evaluated using data extracted from PIC simulations, assuming a beam voltage of 20 kV and current of 0.1 A. (b) A zoomed in version that shows the three hot modes around the synchronization point. The dashed-red line is the wavenumber dispersion of the electron beam's space-charge wave described by $\beta_0 = \omega/u_0$, whereas the dashed-black line represents the wavenumber of the EM mode in the cold SWS, i.e., assuming no beam-EM interaction. The mode associated to the solid-red curve is responsible for amplification since Im(k)>0.

The wavenumber-frequency dispersion describing the eigenmodes in the hot SWS is determined by running multiple PIC simulations at different frequencies and then determining the transfer matrix of the unit-cell at each frequency using Eq. (9.15), i.e., the result shown by the red crosses. In other words we repeat the red-cross results shown in Fig. 9.3b at various frequencies. In Fig. 9.4a we show the modal dispersion relation (complex wavenumber versus frequency) of the four hot modes accounting for the EM-beam interaction in the serpentine SWS using 51 frequency points. The use of a single PIC simulation, instead of multiple PIC simulations, could also be investigated to find the dispersion relation when using a moderately wide-band gaussian pulse at the input ports, however it would require few extra steps in the post processing of the data to be able to decompose each tone behavior and it would not fully account for steady state regime resulting from the interaction with the electrons and further consideration to linearity issues should be given to be able to apply a Fourier transform (which involves superposition) to find the dispersion of the modes.

The hot dispersion diagrams are obtained using the best-approximate solution $\mathbf{T}_{u,best}$ of the overdetermined system in Eq. (9.15). The hot mode responsible for amplification is the one with wavenumber with positive imaginary part (solid red curve). The black solid line is the $+1$ Floquet harmonic of the hot mode propagating with $\mathrm{Re}(k) < 0$, i.e., in opposite direction of the beam flow, and basically no beam-EM interaction occurs, i.e., it is basically the EM mode in the cold SWS. We observe from Fig. 9.4a that the imaginary part of the growing mode (solid red) is maximum at frequency where the speed of the space-charge wave and that of the EM wave in the cold SWS are approximately matched as shown in Fig 9.3a, i.e., at $f \approx 88$ GHz.

We show in Fig. 9.4b a zoomed-in version of the same dispersion in Fig. 9.4a around the synchronization where $v_{c,1} \approx u_0$. The dashed lines represent the two uncoupled systems' modes: the beam line (dashed red) and the EM mode in the cold SWS (dashed black). The electron beam has a dc voltage of $V_0 = 20$ kV so the electron beam interacts with the forward EM wave resulting in an eigenmode with positive imaginary part leading to TWT amplification (solid red curve). Besides the wavenumber with positive imaginary part (solid red curve), which is responsible for amplification, the other two modes resulting from the interaction are decaying (solid blue) and unattenuated (solid green) modes, in agreement with the Pierce model [106].

The gain per unit-cell associated to the m^{th} mode is calculated as

$$G^{\mathrm{Mode},m} = \frac{P_{n+1}^{\mathrm{Mode},m}}{P_{n}^{\mathrm{Mode},m}} = e^{2\mathrm{Im}(k_m)d}, \tag{9.21}$$

which is equivalent to $20\log(e)\mathrm{Im}(k_m d)$ dB. The maximum imaginary part of the wavenumber of the amplification mode (solid red) is found at $f \approx 88$ GHz, at frequency where there is a synchronism, and it is $\mathrm{Im}(kd) \approx 0.036\pi$. Thus, the maximum gain per period resulting

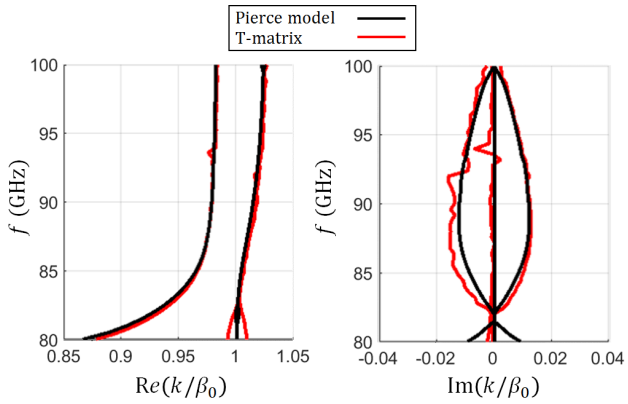

Figure 9.5: Comparison of wavenumber-frequency dispersion relation of the hot eigenmodes obtained based on the proposed model based on calculating theeigenvalues of the $\mathbf{T}_u$ matrix (red curves) and on the Pierce model (black curves) considering SWS loss and space charge effect including plasma frequency reduction factor

from the amplification mode (solid red) is $20\log(e)\times 0.036\pi$ =0.98 dB which is very close to the small-signal gain 1 dB reported in [172] that was obtained by simulating the serpentine TWT amplifier operating at 90 GHz.

We compare in Fig. 9.5 the dispersion diagram for the three interactive hot modes obtained based on our proposed model with that obtained based on an augmented Pierce model [134]. When using the Pierce model we consider a accurate wavenumber frequency dispersion of the cold modes as well as the Pierce interaction impedance, both calculated using full-wave simulations of the cold SWS. In the Pierce-based model we also account for SWS losses using scattering matrix full-wave simulations followed by the determination of the complex wavenumbers from the eigenvalues of the transfer matrix. We also account for the space-charge effect including the plasma frequency reduction factor. Details on how we obtained the dispersion and gain with the Pierce-based model [113, 106, 156, 157, 127] are shown in [134]. The comparison in Fig. 9.5 shows agreement between our method and the Pierce-based model. We believe that the dispersion diagram based on our model is more accurate because as we will show later in Sec. 9.4 our model very well predicts the gain behavior versus frequency when comparing it to 3D PIC results. It is expected that the accuracy using the proposed model is a general property since we use results from accurate 3D PIC

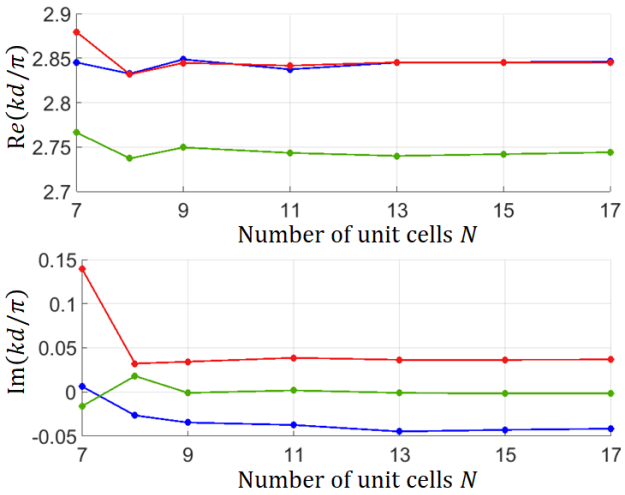

Figure 9.6: Convergence of complex-valued wavenumbers of the three interactive (hot) modes with $\mathrm{Re}(k) \approx \beta_0$ calculated at $f = 88$ GHz for SWSs with a swept number of unit cells used in PIC simulations. The shown wavenumbers are obtained from the best-approximate solution $\mathbf{T}_{u,best}$ of the overdetermined system Eq. (9.15). Convergence is obtained in the wavenumbers of the hot modes when the used number of unit cells exceeds 13, and it is already stable with 9 unit cells.

simulations of the actual geometry.

A convergence study is done by obtaining the wavenumbers of the hot SWS using different numbers of unit cells (all other parameters are kept the same). The purpose of this study to see the minimum required number of unit cells that gives good accuracy in obtaining the wavenumbers of hot modes. We show in Fig. 9.6 the complex-valued wavenumbers, calculated at $f = 88$ GHz where synchronization occurs, of the three interactive (hot) modes with $\mathrm{Re}(k) \approx \beta_0$, for SWSs with a swept number of unit cells in PIC simulations from 7 to 17. The figure shows that the wavenumbers converge when the number of unit cells exceed 13, and the result is already pretty stable after 9 unit cells. The convergence at frequencies close to the band edge (around 80 GHz) of the dispersion of the cold SWS may be slower and more prone to errors because of the weak interaction between the SWS and the electron beam (the modulation of the electron beam velocity and current is very small and it may be hard to capture).

A repeatability study is performed by obtaining the dispersion relation for the serpentine

hot SWS using two different numbers of unit cells (all other parameters are kept the same for the two TWT configurations as previously described). Indeed, the transfer matrix of the hot SWS unit-cell $\mathbf{T}_u$ should not be a function of the number of unit-cells used in the PIC simulations, therefore, the dispersion relation obtained using different numbers of unit cells should provide very similar results. In Fig. 9.7a we show the complex-valued wavenumbers of the hot modes calculated at 88 GHz from the unit-cell transfer matrix $\mathbf{T}_u$ estimated using data from PIC simulations of two SWSs with $N = 15$ (as in the previous example) and $N = 17$ unit cells. In each case, we plot 100 sets of four wavenumbers obtained from 100 estimated transfer matrices (distinct determined solutions): blue and green dots represent the cases with $N = 15$ and $N = 17$ unit cells, respectively. The plotted sets are the ones associated with the highest 100 determinants of the matrices $\mathbf{w}_{1,qijk}$ used to determine the unit-cell transfer matrices $\mathbf{T}_{u,qijk}$ out of the total 715 combinations for the case with $N = 15$ unit cells, and 1365 combinations for the case with $N = 17$ unit cells. The red and black crosses represent the wavenumbers obtained from the best-approximate solution of the overdetermined system for the cases with $N = 15$ and $N = 17$ unit cells, respectively. The clustering of wavenumbers in Fig. 9.7a shows a good agreement between the two cases based on $N = 15$ and $N = 17$ unit cells, where the relative error in the imaginary part of the wavenumber of the amplification mode (hot mode with positive imaginary part) is 0.6%. In Fig. 9.7b we compare the dispersion relations obtained based on the best-approximate solution of the overdetermined system (red and black crosses in Fig. 9.7a): solid and dotted curves represent the dispersion obtained from simulating the hot SWS with $N = 15$ and $N = 17$ unit cells, respectively. The figure shows an almost negligible discrepancy between the dispersion diagrams obtained using two SWS lengths.

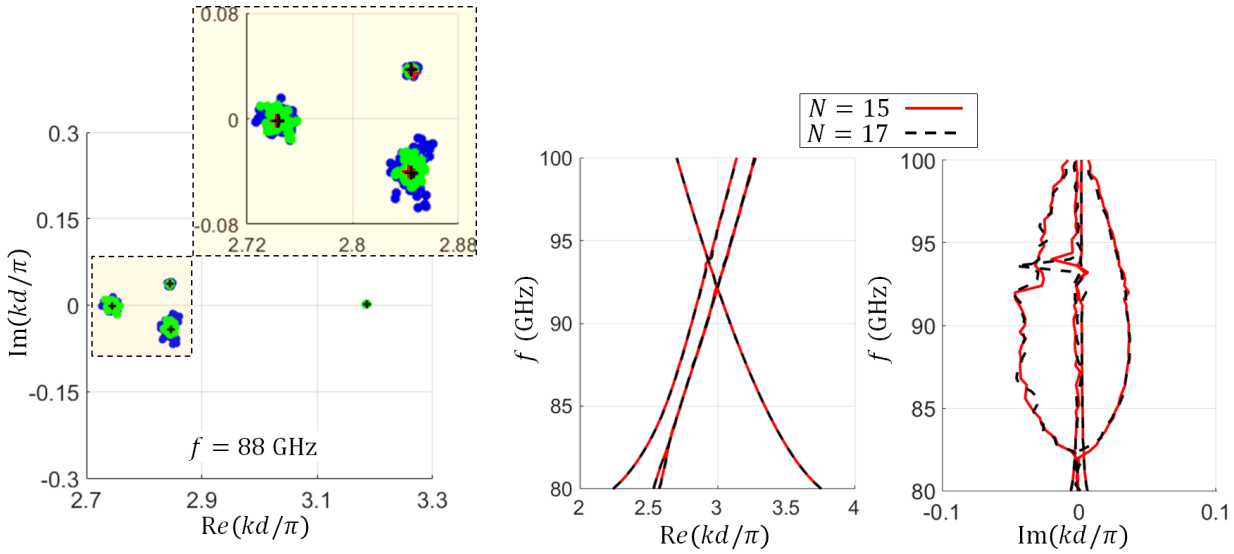

(a) (b)

Figure 9.7: Repeatability test for obtaining the complex-valued wavenumbers of the eigenmodes in the interactive (hot) electron beam-EM wave system in Fig. 9.1a, evaluated using data from PIC simulations of finite-length serpentine SWS structures with $N = 15$ and $N = 17$ unit cells. (a) Complex plane plot of the four complex wavenumbers in the second Brillouin zone, at $f = 88$ GHz. Blue and green dots represent the wavenumbers obtained from the distinct determined solutions using $N = 15$ and $N = 17$ unit cells, respectively. Whereas the red and black crosses represent the wavenumbers obtained from the best-approximate solution of the overdetermined system using $N = 15$ and $N = 17$ unit cells, respectively. (b) Wavenumber-frequency dispersion relations obtained from the best-approximate solution $\mathbf{T}_{u,best}$ of the overdetermined system Eq. (9.15) (red and black crosses in (a)). Solid red and dashed black curves represent the dispersion obtained from the simulation of the finite-length SWS with $N = 15$ and $N = 17$ unit cells, respectively, showing good agreement. Note that for each case we use the same color for all modes for sake of clarity of the figure.

9.4 Predicting the Gain of Finite Length TWT Amplifiers

In this section we show a powerful aspect of our proposed model which is the prediction of the gain behavior for relatively long SWSs based on the transfer matrix representing the system that is obtained based on PIC simulations of shorter SWSs, i.e., with significant fewer number of unit-cells. We demonstrate this concept by considering a TWT amplifier, shown in Fig. 9.8a, which is made of 35 periods of serpentine waveguide with the same unit-cell described in the previous section. We obtain the small signal gain of the structure using: (i) Pierce-based model, (ii) our method, and (iii) PIC simulations of the whole structure (i.e., the whole TWT with 35 unit cells). We assume the incident wave at the input is a monochromatic signal with power $P_{inc} = 50$ mW. Then, we calculate the gain as $G = P_{out}/P_{inc}$. When we calculate the gain based on our proposed model we use the equivalent transfer matrix of the whole structure as

$$\mathbf{\Psi}_{N+1} = \mathbf{T}_u^N \mathbf{\Psi}_1, \tag{9.22}$$

where $\mathbf{\Psi}_1$ and $\mathbf{\Psi}_{N+1}$ are the state vectors at the begin and the end of the structure and they are defined the same way as in Eq. 9.4, i.e., $\mathbf{\Psi}_1 = [\ V_1,\ \ I_1,\ \ V_{b1},\ \ I_{b1}\ ]^T$ and $\mathbf{\Psi}_{N+1} = [\ V_{N+1},\ \ I_{N+1},\ \ V_{b\ N+1},\ \ I_{b\ N+1}\ ]^T$. We find $\mathbf{\Psi}_1$ and $\mathbf{\Psi}_{N+1}$ by applying boundary conditions of the electron beam and the SWS. The electron beam is unmodulated at the structure entrance and therefore it has a boundary described by

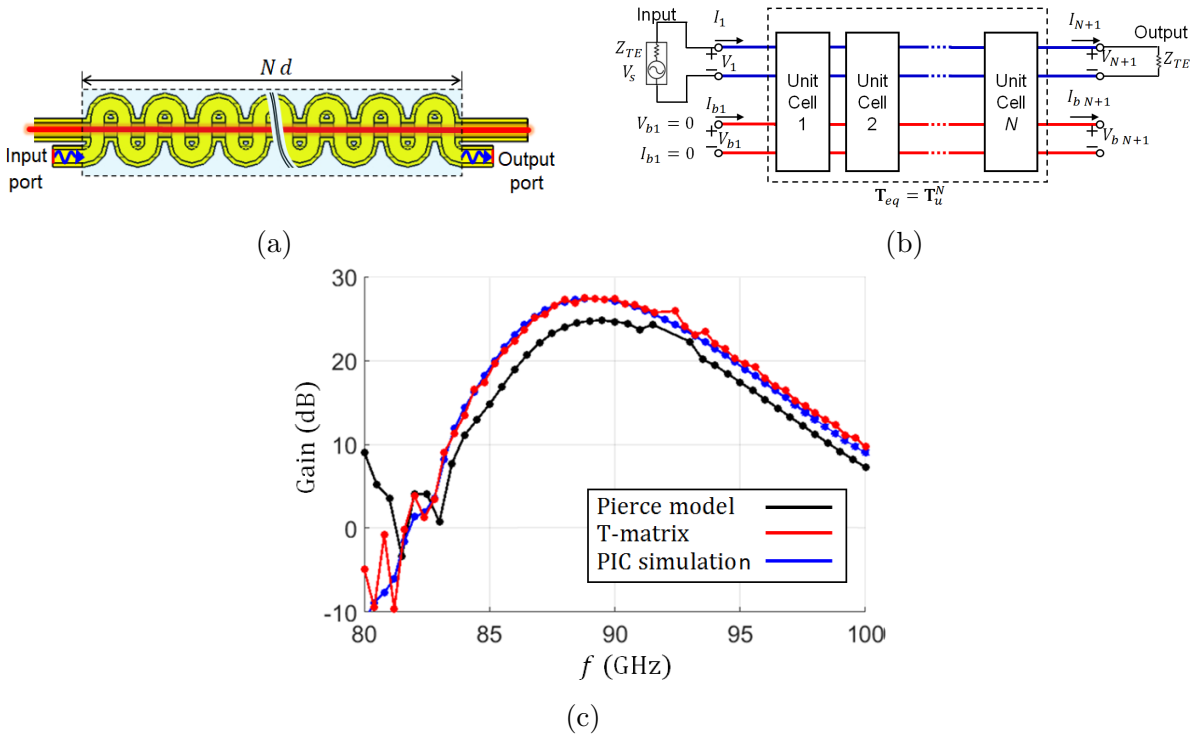

Figure 9.8: (a) TWT amplifier setup using a serpentine waveguide SWS with number of unit-cells of N. (b) Equivalent circuit model where each unit cell of the structure is modeled using 4-port network circuit with matrix $\mathbf{T}_u$ that is calculated based on PIC simulations with a fewer number of unit-cells as explained in the previous sections. The input and output ports of the amplifier are modeled using circuit ports with the same impedance of TE_{10} mode. The electron beam has boundary of $V_{b1} = 0$ and $I_{b1} = 0$ at the beginning of the structure because it is unmodulated when entering the SWS. (c) Comparison between the gain-frequency response of amplifier with number of unit-cells of $N = 35$. The blue curve is obtained based on 3D PIC simulations, performed using CST Particle Studio, of the whole structure in (a), the red curve is based on circuit model in (b) using the 4×4 matrix $\mathbf{T}_{u,best}$ obtained from PIC simulations following the method in 9.1 using only 15 unit-cells, and the black curve is based on the Pierce model. The Pierce-based model accounts for the modal frequency dispersion of the cold modes, Pierce interaction impedance as a function of frequency, and SWS losses, all obtained using full-wave simulations of the cold SWS. It also accounts for space charge effect, including the plasma frequency reduction factor.

$$
\begin{aligned}
V_{b1} &= 0, \\
I_{b1} &= 0.
\end{aligned}
\tag{9.23}
$$

The input is modeled as a generator in Fig. 9.8a composed by an ideal voltage source V_s and its internal impedance, that is the impedance of a TE_{10}mode, $Z_{TE} = \eta_0/\sqrt{1-(f_c/f)^2}$, where $\eta_0 = 120\pi$ Ohm and the cutoff frequency is $f_c = c/(2a) = 79.94$ GHz. The source voltage is related to the incident (available) power by $V_s = \sqrt{8P_{inc}Z_{TE}}$. The output port, where we extract power, is connected to a load with impedance Z_{TE}. Thus, the two boundaries of the SWS are described by

$$
\begin{aligned}
V_1 &= V_s - I_1 Z_{TE}, \\
V_{N+1} &= I_{N+1} Z_{TE}.
\end{aligned}
\tag{9.24}
$$

Solving the system of equations in 9.22-9.24, one finds $\mathbf{\Psi}_1$ and $\mathbf{\Psi}_{N+1}$. Consequently, the gain is calculated as $G = P_{out}/P_{inc}$, where the output power is calculated as

$$
P_{out} = \frac{1}{2}|I_{N+1}|^2 Z_{TE}. \tag{9.25}
$$

We show in Fig. 9.8c the comparison between the gain-frequency response that is obtained by three methods: the first is the method where 3D PIC simulations performed using CST Particle Studio and that are carried out for the setup in 9.8a with 35 unit-cell, the second method is based on circuit model shown in Fig. 9.8b using the 4×4 matrix $\mathbf{T}_{u,best}$ obtained from PIC simulations following the method in 9.1 using only 15 unit-cells, and the third

method is based on Pierce model [113, 106, 156, 157, 127]. The figure shows a very good agreement between our proposed model and full 3D PIC simulations of the 35 unit-cell structure where the error in the gain around the synchronization point is less than 0.5 dB. The small error in the gain between our proposed model and full 3D PIC simulations that occurs at low frequency (very close to the band edge of the dispersion of the cold SWS) might be caused by weak interaction between the SWS and the electron beam at these frequencies, and therefore the modulation of the electron beam velocity and current is very small may and it may be hard to capture (at those frequencies gain is 30 dB lower than the maximum gain). Fig. 9.8c shows that our model predicts gain more accurately than Pierce model which shows some rough approximation in the gain calculated around the synchronization point, being 2.8 dB off the PIC and our results. Therefore, our proposed model is rather powerful because it accurately models the system based only on a 4×4 transfer matrix that is easily found based on 3D PIC simulations of a short TWT. The T-matrix-based model of the hot SWS is accurate and predicts the performance of much longer TWTs without the need of performing extensive PIC simulations that would require long simulation time and large computer memory size.

9.5 Conclusion

A TWT eigenmode solver to determine the complex-valued wavenumbers of the hot eigenmodes in an interactive SWS (i.e., accounting for the interaction of the electron beam and the EM wave) has been demonstrated using a novel approximate technique based on data obtained from 3D PIC simulations. The technique is able to predict the growing mode's complex-valued wavenumber in a TWT made of a serpentine waveguide SWS for millimeter wave amplification. The method is general, and based on elaborating the data obtained from time domain 3D PIC simulations, hence accurately accounting for the precise waveg-

uide geometry, materials, losses, and beam space charge effects. We have also shown the effectiveness of our proposed model in predicting the gain versus frequency of relatively long TWT structures based on PIC simulations of much shorter SWS structures. In summary, the proposed technique is a useful tool for the understanding and the design of TWT amplifiers.

The determination of wavenumbers and eigenvectors of all the hot modes supported in a TWT amplifiers discussed here can also be useful to study hot-mode degeneracy conditions in hot SWSs as those investigated in [126, 102, 124, 135]. Furthermore, the proposed method could be applied to the study of electron beams in beam tunnels with complicated geometries, with the goal of estimating the reduced plasma frequency.

Chapter 10

Reduced Plasma Frequency Calculation Based on Particle-In-Cell Simulations

We propose a scheme to calculate the reduced plasma frequency of a cylindrical-shaped electron beam flowing inside of a cylindrical tunnel, based on results obtained from Particle-in-cell (PIC) simulations [191]. In PIC simulations, we modulate the electron beam using two parallel, non-intercepting, closely-spaced grids which are electrically connected together by a single-tone sinusoidal voltage source. The electron energy and the beam current distributions along the length of the tunnel are monitored after the system is operating at steady-state [134, 191]. We build a system matrix describing the beam's dynamics, estimated by fitting a 2×2 matrix that best agrees with the first order differential equations that govern the physics-based system. Results are compared with the theoretical Branch and Mihran model, which is typically used to compute the plasma frequency reduction factor in such systems [191]. Our method shows excellent agreement with the theoretical model, however, it is also general. Our method can be potentially utilized to determine the reduced plasma frequencies of

electron beams propagating in differently-shaped beam tunnels, where no theoretical model yet exists, such as the case of a cylindrical or elliptical electron beam propagating inside of a metallic beam tunnel of cylindrical, square, or elliptical cross-section. It can be applied also to electron beams composed of multiple streams.

10.1 Motivation and State of the Art

The plasma frequency concept originates from the fact that an infinite cloud of electrons with volumetric charge density ρ_v oscillates at a plasma frequency $\omega_p = \sqrt{\eta\rho_v/\varepsilon_0}$ when any electron in the cloud is perturbed from its equilibrium position, where η is the charge-to-mass ratio of an electron and ε_0 is the permittivity of free space [192]. Plasma oscillations in linear electron beams are induced by space-charge fields, as explained in Ch. 7 of [111] and Ch. 9 of [118], which result in repulsive longitudinal forces between charges. However, the calculation of the plasma frequency for a linear stream of charges with finite cross-section requires the consideration of the radial variation of the space-charge fields, electron velocities, and volume charge densities within the beam cross section. Such parameters will fringe, or decay, with radial distance away from the beam center due to the boundary between a beam of finite cross-section and surrounding vacuum, as well as the presence of the beam tunnel's conducting walls where the longitudinal electric field vanishes. The electronic wave theory for linear beam tubes was developed by Hahn [193] and refined by Ramo [114], utilizing the solutions of Maxwell's equations with corresponding boundary conditions to directly compute the reduced plasma frequency of an electron beam that has a finite cross section and is contained within a cylindrical metallic tunnel. Branch and Mihran further built upon Ramo's work and introduced the plasma frequency reduction factor term, R for cases of both solid and annular electron beams propagating within cylindrical metallic tunnels [173]. It was found that an electron beam with finite cross section will have a plasma frequency

that is reduced compared to that of an electron beam with infinite cross section and with the same volumetric charge density. Thus, the reduced plasma frequency is expressed as $\omega_q = R\omega_p$, where $0 < R < 1$. The reduced plasma frequency is one of the fundamental parameters that affects the dispersion characteristics of the so-called space-charge wave or electronic waves, as explained in [114], Ch. 7 of [111], Ch. 9 in [118], and Ch.9 in [157], which are the waves within the electron beam that possess both velocity and charge modulation in space and time. A linear stream of electrons with average speed u_0 supports multiple space-charge waves with wave function $e^{j\omega t - jkz}$. Typically, there are two dominant charge waves with approximate wavenumbers $k = (\omega \pm \omega_q)/u_0$ [114] and Ch. 7 of [111]. Further theoretical effort was done in works [174, 164], where the authors came up with closed-form formulas to find the plasma frequency reduction factor without numerically solving Branch and Mihran's transcendental equation for the parameter T within the electron beam.

The plasma frequency reduction factor R is one of the fundamental design parameter in electron beam devices since it affects synchronization. As a consequence, the value of R affects the frequency of peak gain in traveling wave tube amplifiers modeled by Pierce theory. Additionally, the choice of drift-tube length between cavities in klystrons for optimal extraction of energy from the modulated electron beam depends on accurate computation of the reduced plasma frequency [114]. The accurate calculation of R is necessary for the modeling and designing of TWTs . For instance, the famous classical theory developed by Pierce requires the calculation of the reduced plasma frequency in order to calculate the parameter $4QC^3 = \omega_q^2/\omega^2$ [156], Ch. 10 in [157], Ch. 12 in [118], which is necessary to accurately calculate the gain. However, the theoretical calculation of the reduced plasma frequency loses accuracy when the tunnel geometry is different from a circular cylinder or when the electron beam has a cross section that is not circular or annular. The reduced plasma frequency for beams in complex tunnel structures such as a cylindrical beam in folded or helical waveguide is approximated in many works by assuming that the tunnel is cylindrical, i.e., by neglecting the structure periodicity and deformations in the shape of the

cylindrical tunnel due to the slow wave structure geometry. Some authors have previously provided a formulation to determine the reduced plasma frequency of an electron beam propagating within a helix slow-wave structure approximated using the sheath helix model, as in [164]; this formulation has been used in TWT modeling software such as CHRISTINE and LMsuite [177, 180]. However, it is not trivial to compute R using the sheath helix model, and most authors studying linear beam tubes simply use the values for R from the Branch and Mihran model [194, 195, 196]. Furthermore, experimental work has also been performed in [197, 198] aiming at determining the reduced plasma frequency in linear beam tubes. To date, there is a lack of literature available to provide a robust method that can be easily used to verify or find the reduced plasma frequency in complex structures.

In this chapter, we present a method that is more general than the Branch and Mihran model (which only yields real-valued space charge wavenumbers) and is rather simple to use. We model the electron beam dynamics by finding the system matrix that describes the small-signal evolution of the electron beam with position and time. The method is the similar to the the one presented in [134] that was applied to traveling wave tubes. Here, the method is applied to find the eigenmodes of the space-charge waves in a beam tunnel, i.e., waves that do not interact with a propagating electromagnetic mode in a slow wave waveguide. The presented method is based on defining and then finding the system matrix through the interpretation of data extracted from particle-in-cell (PIC) simulations. After the system matrix is determined, we then calculated the two charge-wave wavenumbers. The reduced plasma frequency of the electron beam is inferred by finding the deviation of the two space charge wavenumbers from the average electronic phase constant $\beta_0 = \omega/u_0$.

The purpose of this chapter is to show how the proposed method based on three-dimensional PIC simulations is used to calculate the complex wavenumbers of the space-charge waves supported by an electron beam. Since this is the first time we apply the proposed method to the study of the reduced plasma frequency, we apply it to the case of a circular cylindrical

beam within a circular cylindrical tunnel, i.e., the case where the solution is known from a previously developed analytical method [114, 173, 174]. In other words, the scope of this chapter is to show that the proposed method works for a simple configuration; hence it is a good candidate to study even more complicated configurations where there is no known analytical solution for the plasma frequency reduction factor, such as the case of a two-stream electron beam propagating within a metallic structure that can exhibit growing space charge waves (complex space charge wavenumbers) due to the two-stream instability effect [199, 200, 201]. Motivated by previous work on two-stream instability amplifiers, Islam et al., [202, 203] have proposed a method to generate a two-stream electron beam with two different energies from a single-cathode potential. Our PIC-based model may be useful also to determine the complex space charge wavenumbers in such a configuration. Additionally, our PIC-based model may also be used to study the space-charge wavenumbers for electron beams which interact with lossy materials, such as the case of the resistive wall amplifier [204, 205, 206, 207].

10.2 PIC-Based Method

The electron beam has equivalent kinetic dc voltage and dc current V_0 and I_0, respectively, where the dc equivalent kinetic voltage in the non relativistic case is $V_0 = u_0^2/(2\eta)$ and u_0 is the electrons time-averaged speed, c is the free space speed of light, and $\eta = e/m$ is the charge to mass ratio and e is the electron charge represented as positive number. The magnetically-confined electron beam has a circular cross-section with radius R_b, and is flowing within a metallic cylindrical tunnel with radius R_t, as illustrated in Fig. 10.1a. We introduce modulation to the beam using two closely-spaced grids that are made of fictitious metal that is transparent to electrons, i.e., it allows electrons to pass through the grid without

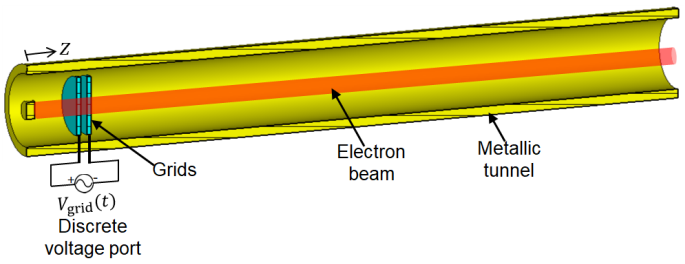

(a)

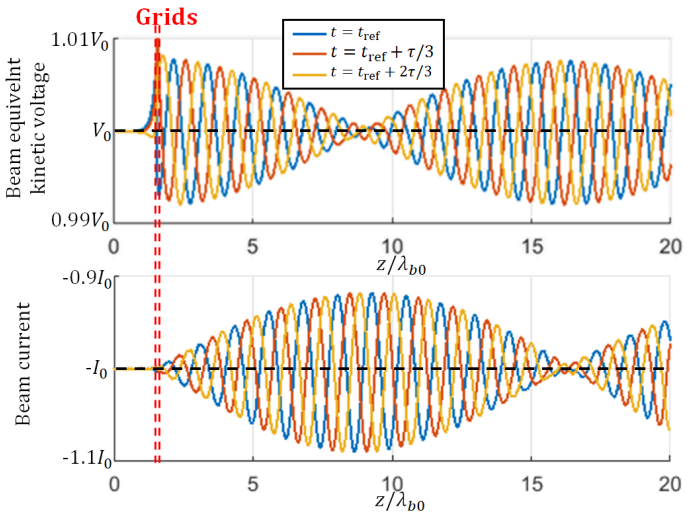

(b)

Figure 10.1: (a) Setup for PIC simulation used to determine the reduced plasma frequencies of the electron beam in a cylindrical tunnel. Modulating grids are simulated as perfect electric conductors which are transparent to particles. (b) An example of the distribution of the electron beam total (dc and ac) equivalent kinetic voltage, defined as $v_b^{tot}(z,t) = V_0 + v_b(z,t)$ with dc equivalent kinetic voltage V_0 and ac equivalent kinetic voltage $v_b(z,t)$ under the small-signal approximation, and current $i_b^{tot}(z,t) = -I_0 + i_b(z,t)$, calculated based on particles' data exported from PIC simulations at steady state, showing the space-time modulation in the beam voltage and current with respect to arbitrary reference time t_{ref}, where τ is the period of the sinusoidal excitation and λ_{b0} is the average electronic wavelength. The knowledge of the electron beam voltage and current is then used to estimate the 2×2 system matrix $\mathbf{M}$ that describes the differential equation governing the beam dynamics. Finally, the system matrix is used to find the wavenumbers of space-charge waves and consequently the reduced plasma frequency.

being intercepted, while preserving other properties a perfect electrical conductor. The gap between the two grids is chosen to be very small compared to wavelength $d_{grid} \ll \lambda_0$ to have a uniform electric field distribution along the gap and to avoid the transit-time effects for electrons. We apply an ac voltage V_{grid} with a monochromatic sinusoidal signal between the grids in order to generate an axial electric field that modulates the beam in a simple and reproducible way. We rely on three-dimensional PIC simulations implemented in CST Particle Studio to satisfy the equations for charged particles motion and Maxwell equations, which are discretized in space and time in the PIC software.

The PIC solver calculates the instantaneous speed $u_b^{tot}(z,t) = u_0 + u_b(z,t)$, and location of discrete charged macroparticles, where $u_b(z,t)$ represents the ac component of velocity. We represent the total (including dc and ac parts) equivalent kinetic voltage of a non relativistic electron beam using a one dimensional (1D) function as $v_b^{tot}(z,t) = \left[u_b^{tot}(z,t)\right]^2/(2\eta)$ which is expressed as $v_b^{tot}(z,t) = V_0 + v_b(z,t)$, where $v_b(z,t) \approx u_0 u_b(z,t)/\eta$ represents the ac modulation function. Analogously, the total beam current is $i_b^{tot}(z,t) = -I_0 + i_b(z,t)$, where$i_b(z,t)$ represents the ac modulation function, as was done in [134]. Note that the method can be applied also to relativistic beams when using $V_0 = c^2/\eta\left(\sqrt{1-(u_0/c)^2}-1\right)$ and $v_b^{tot}(z,t) = c^2/\eta\left(\sqrt{1-(u_b^{tot}/c)^2}-1\right)$, and the ac part is defined as $v_b(z,t) = v_b^{tot}(z,t) - V_0$. However relativistic beams are not considered in this chapter and the accuracy of the presented method in those cases is left to future studies.

We define a state vector that describes the ac electron beam velocity and current dynamics as

$$\boldsymbol{\psi}(z,t) = [\ v_b(z,t),\quad i_b(z,t)\ ]^T. \tag{10.1}$$

We show in Fig. 10.1b an example of the distribution of the electron beam total (ac and dc)

equivalent kinetic voltage and current calculated based on the particle's data exported from PIC simulations at steady state showing the modulation in the beam voltage and current due to the grids, where $\lambda_{0b} = u_0/f$.

At steady state, in the small-signal approximation, the state vector is monochromatic with angular frequency ω and therefore it is represented in phasor domain as [134]

$$\mathbf{\Psi}(z) = [\ V_b(z), \quad I_b(z)\ ]^T. \tag{10.2}$$

Because the problem we consider is uniform in the z-direction (due to confinement of the beam by a strong axial magnetic field), we assume that the evolution of the electron beam dynamic along the z-direction is described by a first order differential equation as

$$\frac{d\mathbf{\Psi}(z)}{dz} = -j\mathbf{M}\mathbf{\Psi}(z), \tag{10.3}$$

where $\mathbf{M}$ is the 2×2 system matrix and the $e^{j\omega t}$ time dependence is assumed.

The state vector is calculated from the data exported from PIC simulation as done in [134]. We calculate the state vector at discrete locations $\Psi(z = n\Delta_s) = \Psi_n$, where $n = 0, 1, ..N$, Δ_s is chosen to be a small position step size ($\Delta_s \leq \lambda_{0b}/3$ and $\lambda_{0b} = u_0/f$), and $N\Delta_s$ is the total length of the structure. According to (10.3), the sampled state vector should satisfy the relations

$$
\begin{aligned}
\boldsymbol{\Psi}_2 &= \mathbf{T}\boldsymbol{\Psi}_1, \qquad (10.4.1)\\
\boldsymbol{\Psi}_3 &= \mathbf{T}\boldsymbol{\Psi}_2, \qquad (10.4.2)\\
&\vdots \\
\boldsymbol{\Psi}_{N+1} &= \mathbf{T}\boldsymbol{\Psi}_N, \qquad (10.4.N)
\end{aligned}
\tag{10.4}
$$

where $\mathbf{T} = e^{-j\mathbf{M}\Delta_s}$ is the transfer matrix, $\mathbf{M}$ is related to $\mathbf{T}$ as $\mathbf{M} = j\ln(\mathbf{T})/\Delta_s$, and the state vectors Ψ_n are calculated directly from PIC simulations.

The relations in (10.4) represent $2N$ linear equations in 4 unknowns, which are the elements of the transfer matrix $\mathbf{T}$. Assuming $N > 2$, the system in (10.4) is mathematically referred to as overdetermined because the number of linear equations ($2N$ equations) is greater than the number of unknowns (4 unknowns). An approximate solution that best satisfies all the given equations in Eq. (10.4), i.e., minimizes the sums of the squared residuals, $\sum_n ||\boldsymbol{\Psi}_{n+1} - \mathbf{T}\boldsymbol{\Psi}_n||^2$ is determined like in [189, 134, 190] and is given by

$$
\mathbf{T}_{\text{best,approx.}} = \left(\mathbf{W}_2\mathbf{W}_1^T\right)\left(\mathbf{W}_1\mathbf{W}_1^T\right)^{-1}, \tag{10.5}
$$

where

$$
\mathbf{W}_1 = \begin{bmatrix} \boldsymbol{\Psi}_1, & \boldsymbol{\Psi}_2, & \ldots & \boldsymbol{\Psi}_N \end{bmatrix}, \tag{10.6}
$$

and

$$
\mathbf{W}_2 = \begin{bmatrix} \boldsymbol{\Psi}_2, & \boldsymbol{\Psi}_3, & \ldots & \boldsymbol{\Psi}_{N+1} \end{bmatrix}, \tag{10.7}
$$

are $2 \times N$ matrices.

Assuming the state vectors take the form of a wave function $\mathbf{\Psi}(z) \propto e^{-jkz}$, 10.3 is simplified to as $k\Psi = \mathbf{M}\mathbf{\Psi}$,which constitutes an eigenvalue problem. Therefore, the space-charge waves' wavenumbers are the eigenvalues of $\mathbf{M}_{\text{best}}$,

$$k = \text{eig}\left(\mathbf{M}_{\text{best}}\right), \tag{10.8}$$

where $\mathbf{M}_{\text{best}} = j\ln(\mathbf{T}_{\text{best}})/\Delta_s$, which leads to two solutions: k_1 and k_2. The PIC-based reduced plasma frequency is calculated as $\omega_{q,\text{PIC}} = u_0\text{Re}(k_2 - k_1)/2$. The associated "PIC-based" reduction factor calculated as

$$R = \omega_{q,\text{PIC}}/\omega_p \tag{10.9}$$

where $\omega_p = \sqrt{\eta I_o/(Au_0\varepsilon_0)}$ and the beam has cross-sectional area $A = \pi R_b^2$.

10.3 Illustrative Example

As an illustrative example, we consider a solid electron beam with equivalent kinetic dc voltage $V_0 = 6.7$ kV (which corresponds to $u_0 = \sqrt{2\eta V_0} = 0.16c$), beam radius $R_b = 0.5$ mm, and the beam current I_0 that is swept. The tunnel is made of a perfect electric conductor and has radius $R_t = 2$ mm and total length of 120 mm. We use two grids spaced apart with a gap of $d_{\text{grid}} = 0.2$ mm and a grid excitation voltage $V_{\text{grid}}(t) = 100\cos(2\pi ft)$ volts. An axial dc magnetic field of 1 T is used to confine the electron beam. All 3D PIC simulations in this chapter are performed using CST Particle Studio. The 3D segmentation performed in CST

uses hexahedral mesh with mesh size of approximately $\Delta_{\text{mesh}}=\lambda_{b0}/30 = 0.2$ mm calculated at $f = 10$ GHz, where $\lambda_{b0} = u_0/f$ and $u_0 = 0.16c$. The total number of charged particles used by PIC simulations to model the electron beam is approximately 10^6 particles. We run PIC simulations for a total time of t_{sim} =10 ns, where the beam dynamics in phasor domain are obtained based on the particles' data on the time period from $t = t_{\text{sim}} - \tau \rightarrow t_{\text{sim}}$, where $\tau = 1/f$ is the period of the applied sinusoidal signal.

We sweep the electron beam dc current I_0 at constant frequency of $f = 5$ GHz. We show in Fig. 10.2a the "PIC-based" dispersion relation for the space-charge wave showing the complex-valued wavenumbers k_1 and k_2 for the two space-charge modes versus beam current, calculated as the eigenvalues for the system matrix obtained based on PIC simulations, $\mathbf{M}_{\text{best}}$. Since we have lossless metals and vacuum in this example, the small imaginary part ($|\text{Im}(k)/\text{Re}(k)| < 10^{-3}$) of the wavenumbers shown in Fig. 10.2a may be attributed to numerical error in our PIC-based method. The method used to find the theoretical wavenumber (dashed-black curves in Fig. 10.2a) is based on the work by Branch and Mihran [173], which gives purely real wavenumbers. The dispersion diagram in Fig. 10.2a shows a good match between the real value of the space-charge wavenumber calculated based on the proposed method (based on Eq. 10.8) and the one calulated based on Branch and Mihran's method [173] (which is real-valued). We show in Fig. 10.2b the "PIC-based" reduction factor calculated as in (10.9).

We now compare the PIC-based result obtained from the method described above with the analytical one based on Branch and Mihran's work in [173]. According to that theory, the plasma frequency reduction factor is approximated as

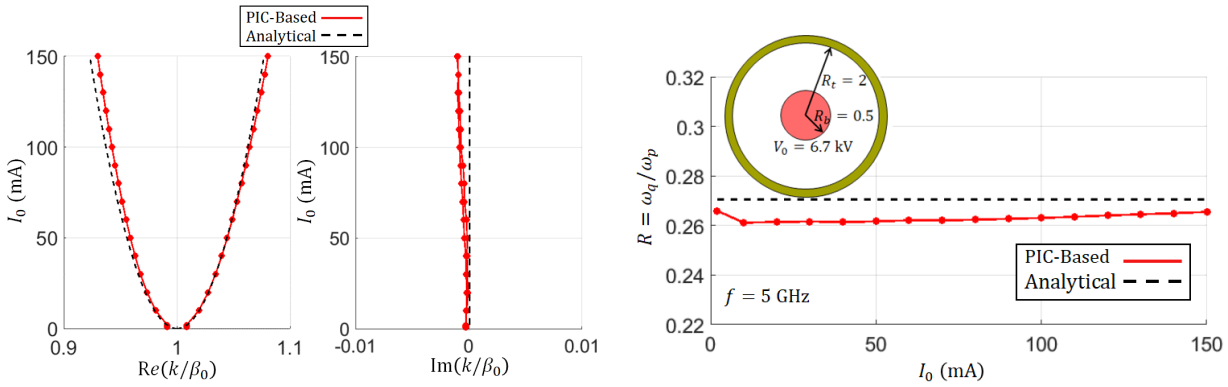

(a) (b)

Figure 10.2: (a) Dispersion relation showing the wavenumbers of the eigenmodes of the space-charge wave supported by the electron beam. Dimensions are shown in the inset of (b), with units of mm. The proposed PIC-based method is compared with the analytical results from Branch and Mihran. (b) Corresponding plasma frequency reduction factor versus beam current. Our results are in agreement with the analytical ones in (10.10) and (10.11), that show that the plasma frequency reduction factor is current independent.

$$R_{\text{Theory}} = \frac{1}{\sqrt{1 + (T/\beta_0)^2}}, \tag{10.10}$$

where $\beta_0 = \omega/u_0$ is the mean electronic phase constant and the parameter T is found by solving the following nonlinear equation [114, 173]

$$TR_b \frac{J_1(TR_b)}{J_0(TR_b)} = \beta_0 \frac{K_0(\beta_0 R_t) I_1(\beta_0 R_b) + K_1(\beta_0 R_b) I_0(\beta_0 R_t)}{K_0(\beta_0 R_b) I_0(\beta_0 R_t) - K_0(\beta_0 R_t) I_0(\beta_0 R_b)}, \tag{10.11}$$

where the various orders and kinds of Bessel functions are defined in [173]. The two real-valued wavenumbers $k_1 = \beta_0 - \omega_q/u_0$ and $k_2 = \beta_0 + \omega_q/u_0$ based on Branch and Mihran's method [173], where $\omega_q = R_{\text{Theory}}\omega_p$, are plotted in Fig. 10.2a, as "Analytical", and the reduction factor R_{Theory} is shown in Fig. 10.2b. Note that from (10.10) and (10.11), the reduction factor is independent of the beam current value I_0. However, the unreduced plasma

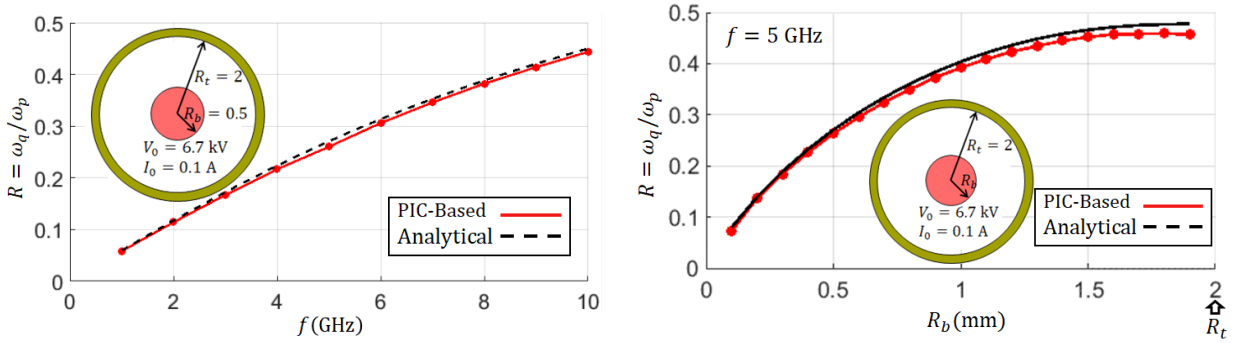

(a) (b)

Figure 10.3: Reduction factor calculated for a cylindrical beam in a metallic tunnel with geometry as shown in the insets, when (a) the frequency is swept, and (b) the beam radius is swept. The dimensions shown in the insets are in mm.

frequency and the two wavenumbers are all dependent on beam current. As expected, the reduction factor obtained by the proposed PIC-based method seems to be almost constant when varying the beam dc current. The results show a good match between the plasma frequency reduction factor obtained based on PIC simulations and that based on theoretical formulas in (10.10) and (10.11), with a maximum absolute error in R of 0.01, which is very small with respect to the reduction factor obtained theoretically. Note that when $I_0 \to 0$, the plasma frequency $\omega_p \to 0$ and therefore the two space-charge waves have wavenumbers $k_1 = k_2 = \beta_0$ as illustrated in Fig 10.2a. The dispersion relation around $I_0 = 0$ can be approximated to a quadratic polynomial as $(k - \beta_0)^2 \propto I_0$ as illustrated in Fig 10.2a, and this has a deep physical meaning as it will be discussed later on. We show in Fig. 10.3a and Fig. 10.3b the plasma frequency reduction factor when the frequency is swept at constant beam dc current of $I_0 = 100$ mA, and when the beam radius is swept at constant dc current $I_0 = 100$ mA and frequency $f = 5$ GHz, respectively. The agreement between the PIC-based solution provided in this chapter and the analytical one from (10.10) and (10.11) is excellent.

10.4 Degeneracy of the Spectrum

To provide a physical insight into the result, it is convenient to analyze the spectral properties of the system matrix $\mathbf{M}$ that describes the system as in (10.3). Following the space-charge wave theory in Ch.7 in [111] and also using the formulation presented in [169], we use the analytically determined matrix

$$\mathbf{M}_{\text{Theory}} = \begin{bmatrix} \beta_0 & \dfrac{R^2_{\text{Theory}}}{(A\omega\varepsilon_0)} \\ \beta_p^2\,(A\omega\varepsilon_0) & \beta_0 \end{bmatrix}, \tag{10.12}$$

where $\beta_p = \omega_p/u_0$ is the unreduced plasma phase constant, and the reduction factor R_{Theory} is taken from (10.10). The theoretical wavenumbers of the space-charge waves are found as the eignvalues of the system matrix $\mathbf{M}_{\text{Theory}}$, $k_1 = \beta_0 - \omega_q/u_0$ and $k_2 = \beta_0 + \omega_q/u_0$ which agree with the space-charge wavenumber expressions found in [114, 173, 174], and correspond to those already plotted in Fig. 10.2a. The ac electron kinetic energy and the ac beam current of the two space-charge waves are described by the two eigenvetors of the matrix (10.12) as $\Psi_1 = \begin{bmatrix} -R_{\text{Theory}}/\left(\beta_p A\omega\varepsilon_0\right), & 1 \end{bmatrix}^T$ and $\Psi_2 = \begin{bmatrix} R_{\text{Theory}}/\left(\beta_p A\omega\varepsilon_0\right), & 1 \end{bmatrix}^T$.

We know that when two eigenvectors coalesce, the system experiences an exceptional point of degeneracy (EPD) of order 2, where the system matrix is not diagonalizable and is instead similar to a Jordan block of order 2, as explained in [102, 169, 208, 15]. Therefore, the eigenmodes experience an algebraic linear behavior, besides the usual phase propagation along z. At an EPD where the space charge waves are degenerate (i.e., when $k_1 = k_2 = \beta_0$), the beam ac voltage is expressed as $V_b(z) = (u_1 + u_2 z)e^{-j\beta_0 z}$, whereas away from the EPD, it is expressed as $V_b(z) = e^{-j\beta_0 z}(u_1 e^{-j\beta_q z} + u_2 e^{j\beta_q z})$. The point $I_0 = 0$ in Fig. 10.2a represents an EPD, and indeed, in its proximity the two wavenumbers follow the law $(k - \beta_0)^2 \propto I_0$. A

vanishing I_0 indicates the absence of the beam but one can still see the physics pertaining to an EPD at regimes where I_0 is very small. The two eigenvectors also coalesce when the reduction factor R is very small, hence the system can experiences and EPD at $R = 0$. It is convenient to use a "coalescence parameter" that quantifies the vicinity of the two eigenvector to each other (i.e., to describe how close is a system's regime to an EPD). To check the coalescence parameter, we look at the angle between the two system's two eigenvectors, when the current elements are scaled by an impedance of $Z_0 = \beta_0/(A\omega\varepsilon_0)$ to have vectors that have all elements in volts, that is defined by the normalized scalar product as $\cos\theta_{12} = \mathrm{Re}\,(\Psi_1 \cdot \Psi_2)\,/\,(\parallel \Psi_1 \parallel \parallel \Psi_1 \parallel)$. The coalescence parameter is here calculated as

$$\sin(\theta_{12}) = \frac{2R\left(\frac{\omega_p}{\omega}\right)}{1 + R^2\left(\frac{\omega_p}{\omega}\right)}, \tag{10.13}$$

and it describes how close the two eigenvectors of the system are to coalescing (i.e., when the systems experiences an EPD), which occurs when $\sin\theta_{12} = 0$, i.e., when either $R = 0$ or $\omega_p = 0$. Indeed, in regimes where the plasma frequency is very small with respect to the operating frequency, the system is very close to an EPD. We show in Fig. 10.4 the space-charge wave behavior when the system is very close to EPD, i.e., for a case where the plasma frequency is $f_p = 0.11$ GHz and the operating frequency f =5 GHz, where a beam dc current $I_0 = 1$ mA is used. The ac beam equivalent voltage and current decays and grows, respectively, linearly, along z. This behavior is different from other cases where the EPD does not occur, as shown in Fig. 10.1b for example.

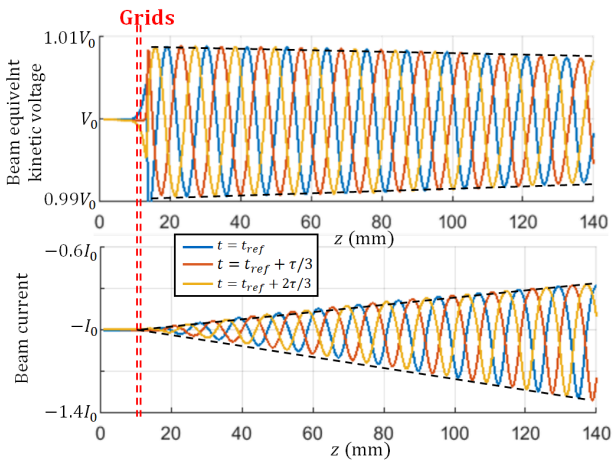

Figure 10.4: An example of electron beam dynamics when the system is very close to an EPD. The distribution of the electron beam total equivalent kinetic voltage and current decays and grows algebraically, respectively, along the z direction.

10.5 Conclusion

A method to determine the reduction factor for single stream electron beam flowing inside of a tunnel has been demonstrated using a novel technique. Our method is based on analyzing the data obtained from time-domain 3D PIC simulations, hence it accounts for all the physical aspects of the problem. Our model is general and can be applied to several other geometries supporting electron beams that are different from the one used here for demonstration purposes. The proposed method seems precise since the calculated reduction factor is in good agreement with the one obtained analytically for cylindrically-shaped electron beam flowing inside a cylindrical metallic tunnel [173]. Since the proposed method is just based on 3D PIC simulations, it can be utilized to study electron beams in complex-shaped beam tunnels, where no theoretical model yet exists, or even for electron beams made of multiple streams as in [202, 203, 201].

Chapter 11

Analytical Solution of the Space-Charge Waves in a Two-Streams Cylindrical Electron Beam

We present an analytical method to compute the wavenumbers and electric fields associated to the eigenmodes of space-charge waves that are supported by a two-streams electron beam, consisting of a solid inner cylindrical stream and a co-axial outer annular stream, both of which are contained within a cylindrical metallic tunnel. The analytical method accounts for the interaction between the two streams and with the beam-tunnel walls and can be used to model the complex wavenumbers associated with the two-stream instability effect.

11.1 Motivation and State of the Art

Vacuum electron devices with high power and broad bandwidth have a competitive edge in various applications, such as electronic countermeasures, satellite communication, plasma diagnostics, and high-resolution radars [209, 137]. Lately, the designers of microwave tubes have faced many difficult design challenges, such as reducing operating voltages and minimizing the weight and dimensions of the devices and their power supplies. In addition, with the high demand for vacuum electronics applications that operate at high frequency, the dimensions of these devices are being reduced and at the same time electron beams with high current density are also required to obtain high output power [136]. There are some technical limitations to increasing both the output power and the operating frequency. The product Pf^2 (P is output power and f is frequency) of the state-of-the-art vacuum electronics follows an increasing linear trend with time [210]. However, it is not certain how long vacuum electronic devices will continue to follow this trend. A promising engineering solution to continue improving the performance of vacuum electronic devices is the use of multiple electron beams [211, 212].

The interaction of multi-stream electron beams has been studied theoretically for years. Many authors have also proposed the multiple beam concept since the 1940s for use in electron beam devices. As a pioneer in this field, Pierce studied the double-stream amplifiers [213]. Then, Swift-Hook analyzed the validity of the theory of double stream amplification [214]. As an early work in this topic, beam-beam interaction in concentric-beam dual-mode TWTs is presented in [215] and then investigated in more detail for various kinds of TWTs in [212]. Chen analyzed the conversion mechanism from the kinetic energy of electron beams to electromagnetic wave energy in the two-stream amplifier and how the efficiency of a two-stream instability amplifier increases with the use of relativistic beam velocities [216]. Wave coupling in multiple beam TWTs to increase the power level of vacuum electronic devices has also been studied in [217]. On the other hand, many works have begun exploring and

showing realistic structures for multi-beam generation. In [218], Zavadil proposed a dual-cathode electron gun incorporating an annular hollow beam cathode, concentric and co-planar with a solid beam cathode. Some work has used multiple cathode sources to produce multiple electron beams in low-power microwave sources where each cathode is powered by two separate power supplies at different voltages [219, 220]. Also, there has been some work published in the past that uses conventional vacuum electron beam device concepts to generate multiple electron beams [221, 222, 223, 224, 220]. Finally, multiple electron beam generation with comparable currents and different energies from a single cathode for high power applications has been comprehensively studied recently in [203, 202].

Modern communications' increasing range and data handling requirements have given rise to a need for microwave tubes with power output and bandwidth capabilities that greatly exceed those of present-day state-of-the-art single-stream electron beam devices. The multiple-beam concept was developed to address this need and was applied to a resonant klystron [225], which was demonstrated to be capable of an order of magnitude higher power output than single-beam devices using the same electron beam. Then the development of multi-beam klystron to provide low operating voltages, high power, low noise, and the possibility of larger operating bandwidth is further studied in many papers such as [226, 211, 227]. Recently many research papers have focused on electron beam devices that utilize multiple electron streams, namely, multi-beam folded waveguide structures [228, 229, 230, 231], two-stream gyrotron TWT amplifiers [232], staggered dual-beam waveguides [233, 234, 235, 236], dual-beam sine waveguide TWTs [237, 238], and other unique TWT configurations [239, 240, 241, 242, 243]. The aforementioned devices can employ the advantages of two-stream and potentially more than two-stream electron beams to improve the output power significantly, and/or increase the bandwidth for various applications such as telecommunication and high-resolution radar.

The problem of space-charge waves in an electron beam is a topic of interest since such waves are excited and utilized in a variety of electron tubes. These tubes may be used to generate,

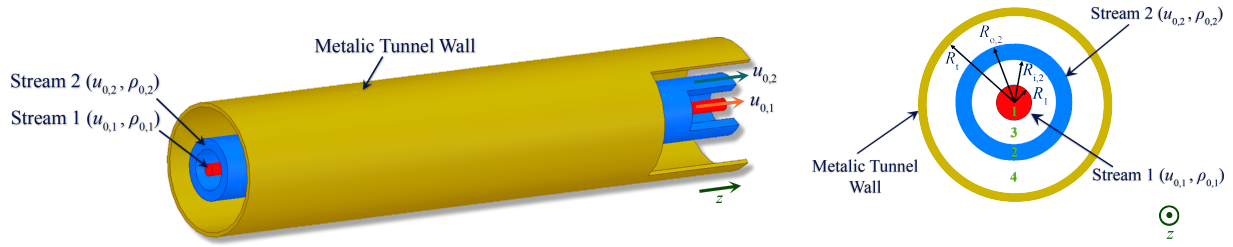

(a) (b)

Figure 11.1: (a) Double stream electron beam with distinct dc speed and charge density. We show in (b) the transverse cross section for the double stream system where the area inside of the tunnel is divided into four homogeneous regions. Stream 1 (the inner stream) exists in region 1, whereas stream 2 (the outer stream) exists in region 2. Regions 3 and 4 are vacuum space.

amplify, and detect signals. Ramo studied the propagation of space-charge waves for the case of a single electron beam propagating within a metallic beam tunnel [114]. The theory of Ramo was extended upon in [173], where they defined the plasma frequency reduction factor and considered the case of an annular electron beam within a cylindrical metallic tunnel. Here, we extend the work of Ramo for the case of two electron beams within a metallic tunnel. We consider an electron beam that is composed of solid and hollow co-axial streams. Knowledge of the complex propagation constants of space-charge waves within this two-stream system may be useful for designing and analyzing two-stream instability amplifiers and two-stream TWTs, which depend strongly on the geometric configuration of the two-stream electron beam.

11.2 Formulation

11.2.1 Problem Description

The electron beam is assumed to be made of two concentric streams: stream 1 (the inner stream) is solid with a circular cross section and it exists for $0 \leq r \leq R_1$; stream 2 (the outer stream, co-axial with stream 1) has an annular cross section and it exists for $R_{\mathrm{i},2} \leq r \leq R_{\mathrm{o},2}$. The beam tunnel is assumed to be cylindrical with radius R_{t} and made of the perfect electric conductor (PEC), as shown in Fig. 11.1. It is convenient to use cylindrical coordinates (r, θ, z) to represent both the beam and the electromagnetic fields.

The two streams are assumed to possess uniform dc charge densities of $\rho_{0,1}$ and $\rho_{0,2}$, in both transverse and longitudinal directions. The axial dc magnetic field is assumed to be strong enough to confine each of the two streams such that all charges travel in the axial direction only (a common simplifying assumption seen in other linear beam tube work such as [114, 106, 213, 113, 116]) with dc velocities $u_{0,1}$ and $u_{0,2}$ for stream 1 and stream 2, respectively. Analogously, the existence of a strong axial dc magnetic field leads also to the assumption that the ac modulation in the velocity of electrons is only in the axial direction. Therefore, the radial and the azimuthal components of electron velocities are assumed to be vanishing [114, 106, 213, 113, 116]. Our goal is to find the eigenmodes that represent the space-charge waves in this configuration. The propagating space charge waves consist of modulation in the beam's volumetric charge density and axial velocity, as well as its associated n electromagnetic fields, all of which are proportional to the wave function $e^{j(\omega t - kz)}$ in phasor domain. As another simplifying assumption, we only consider modes with azimuthal symmetry; therefore, we assume that $\partial/\partial\theta = 0$ of any quantity. However, the presented formalism could be generalized also to find modes that do not possess azimuthal symmetry. Nevertheless, the case with azimuthal symmetry is the most important one in practice for TWTs operation since it may be challenging to excite those that do not have azimuthal symmetry. Therefore, the instantaneous total (both dc and ac components) axial velocity and volumetric charge density for each stream are written as

$$
\begin{aligned}
u_1(r,z,t) &= u_{0,1} + \Re\left(u_{\mathrm{m},1}(r)e^{j\omega t - jkz}\right), \\
u_2(r,z,t) &= u_{0,2} + \Re\left(u_{\mathrm{m},2}(r)e^{j\omega t - jkz}\right),
\end{aligned}
\tag{11.1}
$$

$$
\begin{aligned}
\rho_1(r,z,t) &= \rho_{0,1} + \Re\left(\rho_{\mathrm{m},1}(r)e^{j\omega t - jkz}\right), \\
\rho_2(r,z,t) &= \rho_{0,2} + \Re\left(\rho_{\mathrm{m},2}(r)e^{j\omega t - jkz}\right),
\end{aligned}
\tag{11.2}
$$

where $u_{\mathrm{m},1}(r)$, $u_{\mathrm{m},2}(r)$, $\rho_{\mathrm{m},1}(r)$ and $\rho_{\mathrm{m},2}(r)$ are the radial distributions of the stream velocities and charge densities expressed in phasor domain, the subscript '0' denotes the dc component, 'm' denotes ac modulation component, '1' and '2' denote stream 1 and stream 2, respectively. The total radial-dependent volumetric charge density inside the tunnel is expressed as a piecewise function as

$$
\rho(r,z,t) = \begin{cases}
\rho_1(r,z,t), & 0 \le r \le R_1 \\
\rho_2(r,z,t), & R_{\mathrm{i},2} \le r \le R_{\mathrm{o},2} \\
0, \text{ otherwise}
\end{cases}
\cdot
\tag{11.3}
$$

We assume that the ac modulation of each of the electron beam streams is small compared to the corresponding dc part. Therefore, under this small-signal approximation, the electron beam streams have current densities in the axial direction ($\mathbf{J}_1 = J_1\hat{\mathbf{z}}$ and $\mathbf{J}_2 = J_2\hat{\mathbf{z}}$) in the form of

$$
\begin{aligned}
J_1(r,z,t) &= u_1(r,z,t)\rho_1(r,z,t) \approx J_{0,1} + \Re\left(J_{\mathrm{m},1}(r)e^{j\omega t - jkz}\right), \\
J_2(r,z,t) &= u_1(r,z,t)\rho_1(r,z,t) \approx J_{0,2} + \Re\left(J_{\mathrm{m},2}(r)e^{j\omega t - jkz}\right),
\end{aligned}
\tag{11.4}
$$

where the dc current densities of stream 1 and stream 2 are $J_{0,1} = \rho_{0,1}u_{0,1}$ and $J_{0,2} = \rho_{0,2}u_{0,2}$, and the ac current densities of stream 1 and stream 2 are $J_{\mathrm{m},1}(r) = \rho_{0,1}u_{\mathrm{m},1}(r) + u_{0,1}\rho_{\mathrm{m},1}(r)$ and $J_{\mathrm{m},2}(r) = \rho_{0,2}u_{\mathrm{m},2}(r) + u_{0,2}\rho_{\mathrm{m},2}(r)$, respectively. The total currents for stream 1 and stream 2 are found using integration over each of the transverse cross sections of the stream regions as $i_1(z,t) = \iint_{A_1} J_1(r,z,t)dA$ and $i_2(z,t) = \iint_{A_2} J_2(r,z,t)dA$, where $A_1 = \pi R_1^2$ and $A_2 = \pi\left(R_{o,2}^2 - R_{i,2}^2\right)$ are the cross-sectional areas of region 1 and 2, respectively . This integration yields

$$
\begin{aligned}
i_1(z,t) &= -I_{0,1} + \Re\left(I_{m,1}e^{j\omega t - jkz}\right), \\
i_2(z,t) &= -I_{0,2} + \Re\left(I_{m,2}e^{j\omega t - jkz}\right),
\end{aligned}
\tag{11.5}
$$

where $I_{0,1} = A_1\rho_{0,1}u_{0,1}$ and $I_{0,2} = A_2\rho_{0,2}u_{0,2}$ are the dc currents of stream 1 and stream 2, respectively, and $I_{m,1}$ and $I_{m,2}$ are the ac currents of stream 1 and stream 2 in phasor domain, respectively.

The electromagnetic fields associated to the two-stream electron beam are represented using the electric scalar potential and magnetic vector potential which are expressed as

$$
\phi(r,z,t) = \Re\left(f_\phi(r)e^{j\omega t - jkz}\right), \tag{11.6}
$$

$$\mathbf{A}(r,z,t) = \Re\left(f_A(r)e^{j\omega t - jkz}\right)\ \hat{\mathbf{z}}. \tag{11.7}$$

where $\hat{\mathbf{z}}$ is the unit vector in the z direction. The magnetic vector potential has only an axial component (in the z direction) because we assume only the longitudinal component of current modulation is present (we neglect current directions that are not longitudinal because of the assumption of a very high dc magnetic field). Note that here we use the International System of Units (SI) in the following analysis, whereas CGS units were used in [114]. The electric and magnetic fields in the structure are expressed in terms of the scalar electric potential and vector magnetic potential as $\mathbf{E} = -\nabla\phi - d\mathbf{A}/dt$ and $\mathbf{H} = \nabla \times \mathbf{A}/\mu_0$, where we use the Lorentz gauge to define the divergence of $\mathbf{A}$ as $\nabla \cdot \mathbf{A} = -j\omega\varepsilon\mu\phi$ (Ch. 6 in [244]).

Because the tunnel region is not homogeneously filled, we represent the radially-dependent, piecewise electric scalar potential function $f_\phi(r)$ in Eq. (11.6) as

$$f_\phi(r) = \begin{cases} f_{\phi,1}(r),\ 0 \le r \le R_1 \\ f_{\phi,3}(r),\ R_{\mathrm{o},1} \le r < R_{\mathrm{i},2} \\ f_{\phi,2}(r),\ R_{\mathrm{i},2} \le r < R_{\mathrm{o},2} \\ f_{\phi,4}(r),\ R_{\mathrm{o},2} \le r < R_{\mathrm{t}} \end{cases}. \tag{11.8}$$

The time-domain electric and magnetic fields (which do not depend on θ due to our assumption of azimuthal symmetry) are then given by

$$
\begin{aligned}
E_r(r,z,t) &= \Re\left(-f'_\phi(r)e^{j\omega t-jkz}\right), \\
E_z(r,z,t) &= \Re\left(\left(j\frac{k^2-j\omega^2\mu\varepsilon}{k}\right)f_\phi(r)e^{j\omega t-jkz}\right). \\
H_\theta(r,z,t) &= \Re\left(-\frac{\omega\mu\varepsilon}{k}f'_\phi(r)e^{j\omega t-jkz}\right),
\end{aligned}
\tag{11.9}
$$

whereas the rest of time-varying field components are vanishing, i.e., $E_\theta = H_r = H_z = 0$.

11.2.2 Governing Equations

We start by writing Newton's second law that describes the equations of motion for each stream individually. The basic equations that govern the charges' longitudinal motion are

$$
m\frac{du_1}{dt} = -eE_{z,1}, \tag{11.10}
$$

$$
m\frac{du^{s2}}{dt} = -eE_{z,2}, \tag{11.11}
$$

where $E_{z,1}$ and $E_{z,2}$ are the longitudinal electric fields that stream 1 and stream 2 experience in each of the regions denoted by '1' and '2', respectively (See Fig. 11.1), $m = 9.109\times10^{-31}$ kg is the rest mass of an electron, and $e = +1.602\times10^{-19}$ C is the elementary charge. The longitudinal electric fields$E_{z,1}$ and $E_{z,2}$ are determined using the formula $\mathbf{E} = -\nabla\phi - d\mathbf{A}/dt$, considering the expressions for the scalar electric potential found at each of region 1 and region 2 as we will discuss later. Each electron flow should be continuous and there should not be any leakage or accumulation of charges. Therefore, the continuity equation for each

stream is written as $\nabla \cdot \mathbf{J}_1 = -\partial\rho_1/\partial t$ and $\nabla \cdot \mathbf{J}_2 = -\partial\rho_2/\partial t$ which is simplified as

$$\frac{\partial\left(\rho_1 u_1\right)}{\partial z} = -\frac{\partial\rho_1}{\partial t}, \tag{11.12}$$

$$\frac{\partial\left(\rho_2 u_2\right)}{\partial z} = -\frac{\partial\rho_2}{\partial t}. \tag{11.13}$$

Furthermore, the scalar electric potential and vector magnetic potential have relations

$$\nabla \cdot \mathbf{A} = -\mu\varepsilon\frac{d\phi}{dt}, \tag{11.14}$$

$$\left(\nabla^2 + \omega^2\mu_0\varepsilon_0\right)\phi = -\frac{\rho}{\varepsilon_0}. \tag{11.15}$$

11.2.3 Boundary Conditions

Since the tunnel region is not homogeneously filled, we solve the differential equations of Eqs. (11.10) and (11.11) separately in each region, as was done in [114]. Aside from the fact that the potential function should be finite, we enforce that the potential function and its derivative are continuous across the boundaries between the regions illustrated in Fig. 11.1 as

$$
\begin{aligned}
f_{\phi,1}(R_1) = f_{\phi,3}(R_1), \quad & f'_{\phi,1}(r)\Big|_{r=R_1} = f'_{\phi,3}(r)\Big|_{r=R_1}, \\
f_{\phi,3}(R_{\mathrm{i},2}) = f_{\phi,2}(R_{\mathrm{i},2}), \quad & f'_{\phi,3}(r)\Big|_{r=R_{\mathrm{i},2}} = f'_{\phi,2}(r)\Big|_{r=R_{\mathrm{i},2}}, \\
f_{\phi,2}(R_{\mathrm{o},2}) = f_{\phi,4}(R_{\mathrm{o},2}), \quad & f'_{\phi,2}(r)\Big|_{r=R_{\mathrm{o},2}} = f'_{\phi,4}(r)\Big|_{r=R_{\mathrm{o},2}}.
\end{aligned}
\tag{11.16}
$$

Due to the assumption that a tunnel is made of PEC, we also enforce that the potential function vanishes at the tunnel walls

$$
f_{\phi,4}(R_{\mathrm{t}}) = 0. \tag{11.17}
$$

In the following section, we find the solution of the potential functions at each region. Then, we enforce boundary conditions to find the eigenmode solution of waves that are supported by the studied structure.

11.3 Modal Dispersion Equation

The general solutions of the potential as a function of radius in each region shown in Fig. 11.1 are found separately based on the derivation in Appendix A. We write the radially-dependent electric potential function in (11.8) in the form of

$$
f_{\phi,1}(r) = c_1 J_0(T_1 r), \tag{11.18}
$$

$$f_{\phi,3}(r) = c_2 K_0(\tau r) + c_3 I_0(\tau r), \tag{11.19}$$

$$f_{\phi,2}(r) = c_4 J_0(T_2 r) + c_5 Y_0(T_2 r), \tag{11.20}$$

$$f_{\phi,4}(r) = c_6 K_0(\tau r) + c_7 I_0(\tau r), \tag{11.21}$$

where c_n ($n = 1$ to 7) are arbitrary constants that are to be found to satisfy boundary conditions. The parameters T_1 and T_2 in the arguments of the above Bessel functions correspond to the regions inside of the electron streams, and the parameter τ corresponds to the regions outside of the electron streams, defined as

$$T_1^2 = \left(k^2 - k_0^2\right)\left(\frac{\left(\beta_{\mathrm{p},1}\right)^2 - \left(k - \beta_0\right)^2}{\left(k - \beta_0\right)^2}\right), \tag{11.22}$$

$$T_2^2 = \left(k^2 - k_0^2\right)\left(\frac{\left(\beta_{\mathrm{p},2}\right)^2 - \left(k - \beta_0\right)^2}{\left(k - \beta_0\right)^2}\right), \tag{11.23}$$

$$\tau^2 = \left(k^2 - k_0^2\right), \tag{11.24}$$

where $\beta_{\mathrm{p},1} = \sqrt{\eta\rho_1/\varepsilon_0}/u_{0,1}$ and $\beta_{\mathrm{p},2} = \sqrt{\eta\rho_2/\varepsilon_0}/u_{0,2}$ are the plasma phase constants of stream 1 and stream 2, and $\eta = e/m = 1.758829 \times 10^{11}$ C/kg is the charge to mass ratio of an electron. Note that we did not consider the Bessel's function of second kind (Neumann's function) in $f_{\phi,1}(r)$ because the electric potential should be finite at $r = 0$ and $Y_0(T_1 r)$ has singularity at $r = 0$. When the boundary conditions in Eqs. (11.16) and (11.17) are enforced , they may be written in matrix form as $\underline{\mathbf{M}}\mathbf{c} = \mathbf{0}$, where $\mathbf{c} = \begin{bmatrix} c_1, & c_2, & c_3 & c_4, & c_5, & c_6, & c_7 \end{bmatrix}^{\mathrm{T}}$ (T denotes transpose function) and the matrix $\underline{\mathbf{M}}$ is defined as

$$\underline{\mathbf{M}} = \begin{bmatrix} J_0(T_1R_1) & -K_0(\tau R_1) & -I_0(\tau R_1) & 0 & 0 & 0 & 0 \\ T_1 J_0'(T_1R_1) & -\tau K_0'(\tau R_1) & -\tau I_0'(\tau R_1) & 0 & 0 & 0 & 0 \\ 0 & K_0(\tau R_{\mathrm{i},2}) & I_0(\tau R_{\mathrm{i},2}) & -J_0(T_2R_{\mathrm{i},2}) & -Y_0(T_2R_{\mathrm{i},2}) & 0 & 0 \\ 0 & \tau K_0'(\tau R_{\mathrm{i},2}) & \tau I_0'(\tau R_{\mathrm{i},2}) & -T_2 J_0'(T_2R_{\mathrm{i},2}) & -T_2 Y_0'(T_2R_{\mathrm{i},2}) & 0 & 0 \\ 0 & 0 & 0 & J_0(T_2R_{\mathrm{o},2}) & Y_0(T_2R_{\mathrm{o},2}) & -K_0(\tau R_{\mathrm{o},2}) & -I_0(\tau R_{\mathrm{o},2}) \\ 0 & 0 & 0 & T_2 J_0'(T_2R_{\mathrm{o},2}) & T_2 Y_0'(T_2R_{\mathrm{o},2}) & -\tau K_0'(\tau R_{\mathrm{o},2}) & -\tau I_0'(\tau R_{\mathrm{o},2}) \\ 0 & 0 & 0 & 0 & 0 & K_0(\tau R_{\mathrm{t}}) & I_0(\tau R_{\mathrm{t}}) \end{bmatrix}. \quad (11.25)$$

A solution exists when one finds k such that $\det(\underline{\mathbf{M}}) = 0$. The matrix $\underline{\mathbf{M}}$ is badly scaled when using the imaginary part of the wavenumber k, where Bessel's functions will be extremely large or small. Therefore, it will be beyond the precision of the numerical methods used to solve such a nonlinear system. To overcome this issue, we follow the same procedure as [114], which reduces the number of equations describing the boundary conditions until only one remain. As explained in Appendix B, we reduce the seven equations that describe the system of two streams numerically since it would be difficult to do so analytically.

11.4 Illustrative Examples

As an illustrative example, we consider an electron beam consisting of two streams that have equivalent kinetic dc voltages of $V_{0,1} = 7$ kV and $V_{0,2} = 6$ kV , corresponding to average electron speeds of $u_{0,1} = 0.164c$ and $u_{0,2} = 0.152c$, respectively, from the relativistic relation

$V_0 = c^2/\eta \left(\sqrt{1-(u_0/c)^2} - 1 \right)$. Stream 1 is circular in cross section and has an outer radius $R_1 = 0.1$ mm and stream 2 is annular in cross section, with inner and outer radii $R_{\text{i},2} = 1$ mm and $R_{\text{o},2} = 1.1$ mm, respectively. The metallic tunnel is made of a PEC and has an inner radius $R_t = 2$ mm, as illustrated in Fig. 11.1.

We show in Fig. 11.2a the characteristic equation (defined in Appendix B) in log scale when the real and imaginary parts of k are swept at a fixed frequency of $f = 5$ GHz, and the dc currents of stream 1 and stream 2 are $I_{0,1} = A_1 \rho_{0,1} u_{0,1} = 50$ mA and $I_{0,2} = A_2 \rho_{0,2} u_{0,2} = 50$ mA, respectively, corresponding to dc charge densities of $\rho_{0,1} = 0.0325$ C/m^3 and $\rho_{0,2} = 0.00166$ C/m^3 for streams 1 and 2, respectively. The roots of the characteristic equation correspond to locations in Fig. 11.2a where the characteristic equation tends to zero (shown by dark blue). We label the four modes in Fig. 11.2a that correspond to the dominant modes of the system, where the potential function $f_\phi(r)$ appears continuous with radius. Modes in Fig. 11.2a that are not labeled have potential functions with abrupt transitions in the r coordinate. The mode profiles for the four dominant modes labeled in Fig. 11.2a are shown in Fig. 11.2b, Fig. 11.2c, Fig. 11.2d and Fig. 11.2e.

In Fig. 11.3, we obtain the four modes of the two-stream system when the dc current of stream 2 is swept, the dc current of stream 1 is held constant at $I_{0,1} = 50$ mA, the frequency is fixed at $f = 5$ GHz, and the equivalent kinetic voltages are held constant at $V_{0,1} = 7$ kV and $V_{0,2} = 6$ kV. This study is used to verify the validity of the method we use to find the modes. When the dc current of stream 2 approaches zero, this is equivalent to a case where stream 1 only exists in the tunnel. Therefore, one sees two conventional plasma modes with wavenumber described as $k = \beta_{0,1} \pm \beta_{q,1}$, where $\beta_{q,1} = R_{sc}\omega_{p,1}/u_{0,1}$, and R_{sc} is the plasma frequency reduction factor, calculated using the method shown in [173]. Moreover, stream 2 would have a vanishing plasma frequency $\omega_{p,2} \to 0$ and two identical

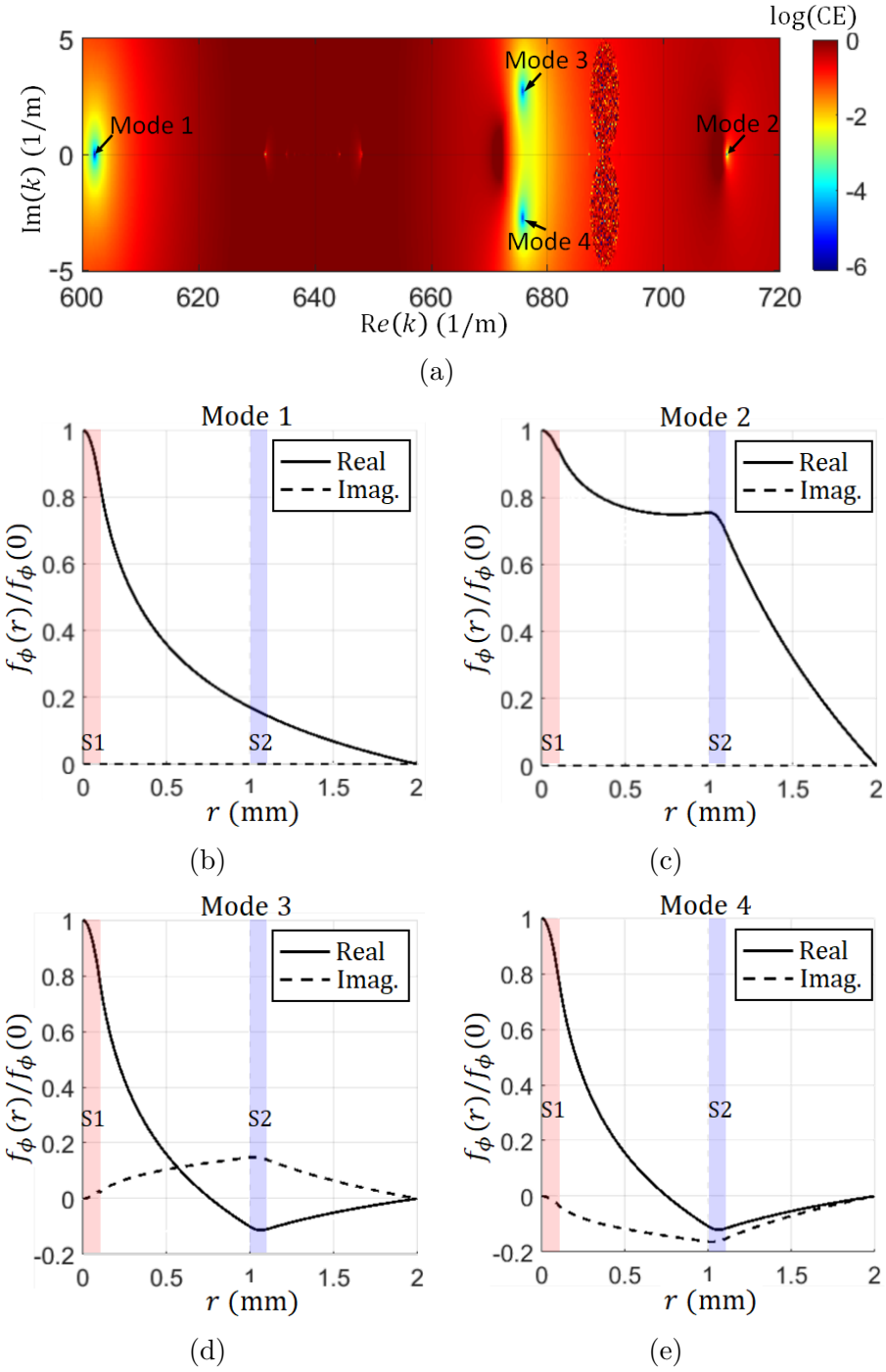

Figure 11.2: (a) Characteristic equation versus complex wavenumber k. The labeled points where CE $\rightarrow 0$ represents solution of the system. (b)-(e) Normalized potential profiles corresponding to the modes labeled in (a). The radial distribution of the potential function confirms the validity of the solution because one can observe the continuity of the potential function and its derivative at the edges of the electron streams and the vanishing potential at the tunnel walls. The shaded regions in (b)-(e) represent the radial locations ofstream 1 and stream 2.

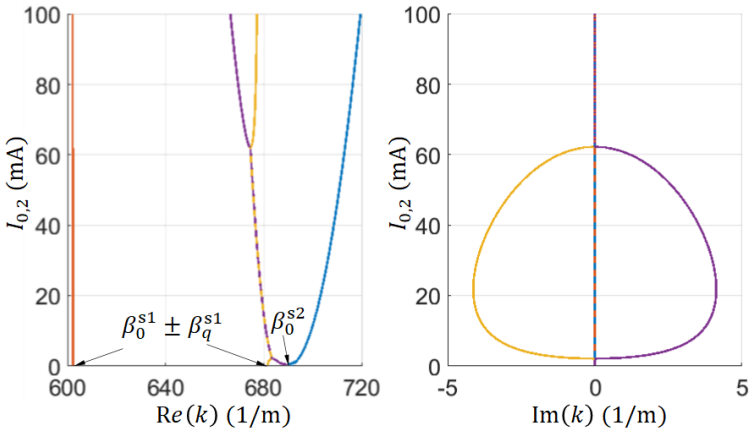

Figure 11.3: Modal dispersion diagram showing space charge wavenumber as a function of stream 2 current

wavenumbers with $k = \beta_{0,2}$. Figure 11.3 shows that there exist two transition points close to $I_{0,2} = 2.5$ mA and $I_{0,2} = 60$ mA, between which, growing space-charge waves can occur due to two-stream instability, which happens when there is a sufficient velocity difference between electron streams and sufficient stream currents, as predicted in [213, 200] using an abstract theoretical model.

To understand the conditions resulting in this instability, we have swept both dc currents of stream 1 and stream 2 at a fixed frequency of 5 GHz and fixed equivalent kinetic voltages of $V_{0,1} = 7$ kV and $V_{0,2} = 6$ kV, and we monitored the imaginary part of the growing mode to observe the parameter space where instability occurs. We show in Fig. 11.4 the absolute value of the imaginary part of wavenumber for the mode that exhibits a growing instability. Note that the boundary between the region where the wavenumber has zero imaginary part and the region where the imaginary component is non-zero is a transition point, or exceptional point of degeneracy, as labeled in Fig. 11.4 (white dashed lines). Figure 11.4 indicates that the amplification occurs only for certain combinations of stream 1 and stream 2 currents for a given freqeuncy and beam parameters.

We repeat the previous study when both dc voltages of stream 1 and stream 2 are swept at a fixed frequency of 5 GHz and the beam currents are held constant at $I_{0,1} = 50$ mA and $I_{0,2} =$

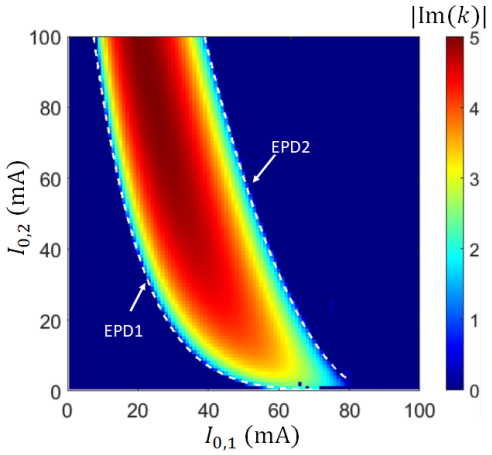

Figure 11.4: Contour showing transition boundaries (labeled EPD1 and EPD2), where the imaginary part of the space-charge wavenumber becomes nonzero and two-stream instability occurs for different combinations of stream dc currents.

50 mA. We show in Fig. 11.5 the absolute value of the imaginary part of the wavenumber for the mode that exhibits a growing instability. Note that instability occurs when either stream 1 has a higher dc voltage stream 2 or vice versa. For the studied range of stream 1 and stream 2 dc voltages in Fig. 11.5, one finds that instability occurs when the difference between the equivalent kinetic dc voltages of the two streams is 1 kV $< |V_{0,1} - V_{0,2}| <$ 1.5 kV.

We show the modal dispersion relation for the two-stream system in Fig. 11.6a when the operating frequency is swept while the beam currents are held constant at $I_{0,1} = 50$ mA and $I_{0,2} = 50$ mA and the equivalent stream voltages are held constant at $V_{0,1} = 7$ kV and $V_{0,2} = 6$ kV. The figure shows that the amplification resulting from the two-stream instability occurs from dc up to threshold frequency which is 15 GHz for this case (note that the cutoff frequency of a circular waveguide of radius $R_t = 2$ mm is approximately 44 GHz). For the case of a two-stream instability amplifier, it is potentially beneficial to have a growing instability up to a threshold frequency that is below the cutoff frequency of a circular waveguide, since the device will be less susceptible to regenerative oscillations or backward-wave oscillations, as explained in [216].

Finally, we study the effect of the coupling of the two streams on the dispersion of the modes.

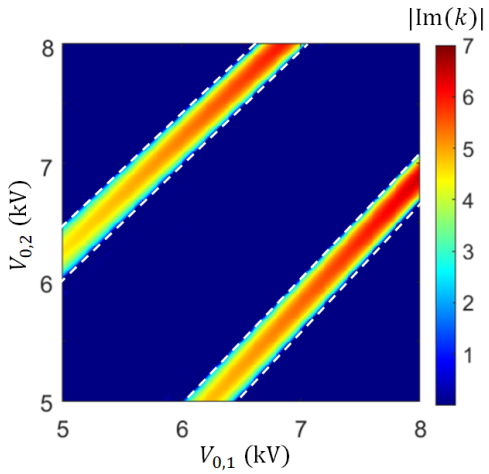

Figure 11.5: Contour showing transition boundaries where the imaginary part of the space-charge wavenumber becomes nonzero and two-stream instability occurs for different combinations of stream dc voltages. White dashed lines indicate transition boundaries where the imaginary part of the space charge wavenumber becomes nonzero and two-stream instability occurs.

The coupling is controlled in this example by sweeping the inner radius of stream 2 while keeping the $R_{o,2} - R_{i,2} = 0.1$ mm and $R_1 = 0.1$ mm. We show the dispersion relation for the two streams' four modes in Fig. 11.6b when the operating frequency is 5 GHz, the currents of the streams are $I_{0,1} = 50$ mA and $I_{0,1} = 50$ mA and the equivalent kinetic voltages of the streams are $V_{0,1} = 7$ kV and $V_{0,2} = 6$ kV.

11.5 Conclusion

We have analytically studied the space-charge waves that are supported by electron beam with two streams. We have found the dispersion characteristics and distributions for potential function associated with the modes. The results showed that the electron beam with two streams can exhibit instability where it supports modes that are growing resulting in amplification. We also found that instability occurs only for specific combinations of the

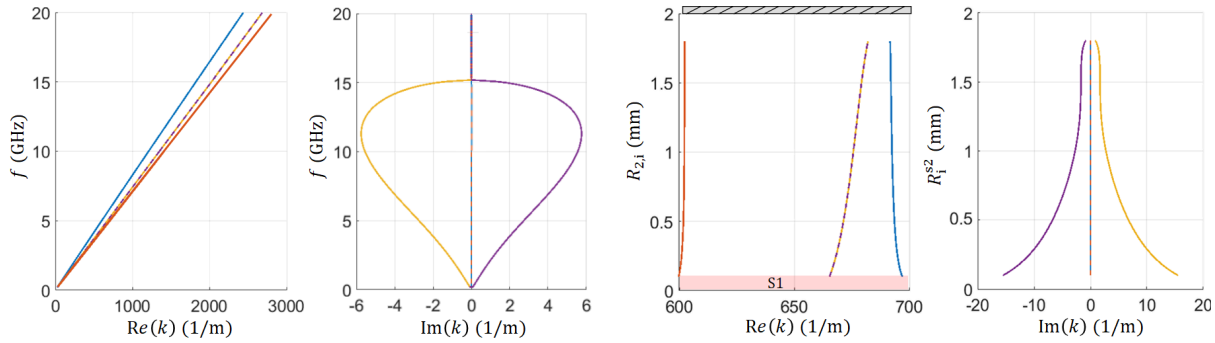

Figure 11.6: (a) Modal dispersion relation showing complex space charge wavenumber as a function of frequency. (b) Modal dispersion relation showing space charge wavenumber as a function of the inner radius of stream 2. The shaded region S1 indicates the radii where stream 1 exists.

streams dc current and dc equivalent kinetic voltages. Moreover, the amplification resulting form instability increases when the two streams are closer to each other. The finding in this work can be potentially used to make amplifiers based two stream instability or to develop TWTs that use double stream electron beam.

Bibliography

[1] Dmitry Oshmarin, Farshad Yazdi, Mohamed A.K. Othman, Jeff Sloan, Mohammad Radfar, Michael M. Green, and Filippo Capolino. New oscillator concept based on band edge degeneracy in lumped double-ladder circuits. *IET Circuits, Devices and Systems*, 13(7):950–957, jul 2019, doi: 10.1049/iet-cds.2018.5048.

[2] Ahmed F Abdelshafy, Dmitry Oshmarin, Mohamed AK Othman, Michael M Green, and Filippo Capolino. Distributed degenerate band edge oscillator. *IEEE Transactions on Antennas and Propagation*, 69(3):1821–1824, 2020.

[3] Dmitry Oshmarin, Ahmed F Abdelshafy, Alireza Nikzamir, Michael M Green, and Filippo Capolino. Experimental demonstration of a new oscillator concept based on degenerate band edge in microstrip circuit. *arXiv:2109.07002*, 2021.

[4] Mohamed AK Othman, Mehdi Veysi, Alexander Figotin, and Filippo Capolino. Low starting electron beam current in degenerate band edge oscillators. *IEEE Transactions on Plasma Science*, 44(6):918–929, 2016.

[5] Ahmed F Abdelshafy, Mohamed AK Othman, Farshad Yazdi, Mehdi Veysi, Alexander Figotin, and Filippo Capolino. Electron-beam-driven devices with synchronous multiple degenerate eigenmodes. *IEEE Transactions on Plasma Science*, 46(8):3126–3138, 2018.

[6] Banaful Paul, Niru K Nahar, and Kubilay Sertel. Frozen mode in coupled silicon ridge waveguides for optical true time delay applications. *JOSA B*, 38(5):1435–1441, 2021.

[7] John L Volakis and Kubilay Sertel. Narrowband and wideband metamaterial antennas based on degenerate band edge and magnetic photonic crystals. *Proceedings of the IEEE*, 99(10):1732–1745, 2011.

[8] Venkata Ananth Tamma, Alexander Figotin, and Filippo Capolino. Concept for pulse compression device using structured spatial energy distribution. *IEEE Transactions on Microwave Theory and Techniques*, 64(3):742–755, 2016.

[9] Mohamed AK Othman, Farshad Yazdi, Alex Figotin, and Filippo Capolino. Giant gain enhancement in photonic crystals with a degenerate band edge. *Physical Review B*, 93(2):024301, 2016.

[10] Hamidreza Ramezani, S Kalish, I Vitebskiy, and Tsampikos Kottos. Unidirectional lasing emerging from frozen light in nonreciprocal cavities. *Physical Review Letters*, 112(4):043904, 2014.

[11] Mehdi Veysi, Mohamed AK Othman, Alexander Figotin, and Filippo Capolino. Degenerate band edge laser. *Physical Review B*, 97(19):195107, 2018.

[12] M I Vishik and L A Lyusternik. The solution of some perturbation problems for matrices and selfadjoint or non-selfadjoint differential equations i. *Russian Mathematical Surveys*, 15(3):1–73, jun 1960, doi: 10.1070/rm1960v015n03abeh004092.

[13] P. Lancaster. On eigenvalues of matrices dependent on a parameter. *Numerische Mathematik*, 6(1):377–387, dec 1964, doi: 10.1007/bf01386087.

[14] Alexander P. Seyranian. Sensitivity analysis of multiple eigenvalues. *Journal of Structural Mechanics*, 21(2):261–284, jan 1993, doi: 10.1080/08905459308905189.

[15] Tosio Kato. *Perturbation Theory for Linear Operators*. Springer-Verlag New York Inc., New York, 1966, doi: 10.1007/978-3-662-12678-3.

[16] Michael V Berry. Physics of nonhermitian degeneracies. *Czechoslovak Journal of Physics*, 54(10):1039–1047, 2004.

[17] Carl M Bender and Stefan Boettcher. Real spectra in non-Hermitian Hamiltonians having PT symmetry. *Physical Review Letters*, 80(24):5243, 1998.

[18] Carl M Bender. Making sense of non-hermitian hamiltonians. *Reports on Progress in Physics*, 70(6):947, 2007.

[19] Ali Mostafazadeh. Exact pt-symmetry is equivalent to hermiticity. *Journal of Physics A: Mathematical and General*, 36(25):7081, 2003.

[20] Viktar S Asadchy, Mohammad Sajjad Mirmoosa, Ana Díaz-Rubio, Shanhui Fan, and Sergei A Tretyakov. Tutorial on electromagnetic nonreciprocity and its origins. *Proceedings of the IEEE*, 108(10):1684–1727, 2020.

[21] A Ruschhaupt, F Delgado, and JG Muga. Physical realization of-symmetric potential scattering in a planar slab waveguide. *Journal of Physics A: Mathematical and General*, 38(9):L171, 2005.

[22] R El-Ganainy, KG Makris, DN Christodoulides, and Ziad H Musslimani. Theory of coupled optical PT-symmetric structures. *Optics Letters*, 32(17):2632–2634, 2007.

[23] A Guo, GJ Salamo, D Duchesne, R Morandotti, M Volatier-Ravat, V Aimez, GA Siviloglou, and DN Christodoulides. Observation of PT symmetry breaking in complex optical potentials. *Physical Review Letters*, 103(9):093902, 2009.

[24] Mohamed AK Othman, Vincenzo Galdi, and Filippo Capolino. Exceptional points of degeneracy and p t symmetry in photonic coupled chains of scatterers. *Physical Review B*, 95(10):104305, 2017.

[25] R. Seydel. *Practical Bifurcation and Stability Analysis*. Springer-Verlag New York Inc., New York, 1994.

[26] David G Schaeffer and Ian Stewart. *Singularities and groups in bifurcation theory*. Berlin, Germany: Springer-Verlag, 1985.

[27] E Hernández, A Jáuregui, A Mondragón, and L Nellen. Degeneracy of resonances: Branch point and branch cuts in parameter space. *International Journal of Theoretical Physics*, 46(6):1666–1701, 2007.

[28] E Hernández, A Jáuregui, and A Mondragón. Exceptional points and non-hermitian degeneracy of resonances in a two-channel model. *Physical Review E*, 84(4):046209, 2011.

[29] Alexander B Yakovlev and George W Hanson. On the nature of critical points in leakage regimes of a conductor-backed coplanar strip line. *IEEE Transactions on Microwave Theory and Techniques*, 45(1):87–94, 1997.

[30] George W Hanson and Alexander B Yakovlev. An analysis of leaky-wave dispersion phenomena in the vicinity of cutoff using complex frequency plane singularities. *Radio Science*, 33(4):803–819, 1998.

[31] Alexander B Yakovlev and George W Hanson. Analysis of mode coupling on guided-wave structures using morse critical points. *IEEE Transactions on Microwave Theory and Techniques*, 46(7):966–974, 1998.

[32] Alexander B Yakovlev and George W Hanson. Fundamental modal phenomena on isotropic and anisotropic planar slab dielectric waveguides. *IEEE Transactions on Antennas and Propagation*, 51(4):888–897, 2003.

[33] George W Hanson, Alexander B Yakovlev, Mohamed AK Othman, and Filippo Capolino. Exceptional points of degeneracy and branch points for coupled transmission lines—Linear-algebra and bifurcation theory perspectives. *IEEE Transactions on Antennas and Propagation*, 67(2):1025–1034, 2019.

[34] Tarek Mealy, Ahmed F. Abdelshafy, and Filippo Capolino. The degeneracy of the dominant mode in rectangular waveguide. In *Proceedings USNC/URSI National Radio Science Meeting*. Boulder, Colorado, USA, Jan. 2019.

[35] Alexander Figotin and Ilya Vitebskiy. Electromagnetic unidirectionality in magnetic photonic crystals. *Physical Review B*, 67(16):165210, 2003.

[36] Alex Figotin and Ilya Vitebskiy. Slow light in photonic crystals. *Waves in Random and Complex Media*, 16(3):293–382, 2006.

[37] Alex Figotin and Ilya Vitebskiy. Slow wave phenomena in photonic crystals. *Laser & Photonics Reviews*, 5(2):201–213, 2011.

[38] Shachar Klaiman, Uwe Günther, and Nimrod Moiseyev. Visualization of branch points in PT-symmetric waveguides. *Physical Review Letters*, 101(8):080402, 2008.

[39] Christian E Rüter, Konstantinos G Makris, Ramy El-Ganainy, Demetrios N Christodoulides, Mordechai Segev, and Detlef Kip. Observation of parity–time symmetry in optics. *Nature Physics*, 6(3):192–195, 2010.

[40] Mohamed AK Othman and Filippo Capolino. Theory of exceptional points of degeneracy in uniform coupled waveguides and balance of gain and loss. *IEEE Transactions on Antennas and Propagation*, 65(10):5289–5302, 2017.

[41] Ahmed F Abdelshafy, Mohamed AK Othman, Dmitry Oshmarin, Ahmad T Almutawa, and Filippo Capolino. Exceptional points of degeneracy in periodic coupled waveguides and the interplay of gain and radiation loss: Theoretical and experimental demonstration. *IEEE Transactions on Antennas and Propagation*, 67(11):6909–6923, 2019.

[42] Alexander Figotin and Ilya Vitebskiy. Oblique frozen modes in periodic layered media. *Physical Review E*, 68(3):036609, 2003.

[43] Alex Figotin and Ilya Vitebskiy. Gigantic transmission band-edge resonance in periodic stacks of anisotropic layers. *Physical Review E*, 72(3):036619, 2005.

[44] Alex Figotin and Ilya Vitebskiy. Frozen light in photonic crystals with degenerate band edge. *Physical Review E*, 74(6):066613, 2006.

[45] Claudius Locker, Kubilay Sertel, and John L Volakis. Emulation of propagation in layered anisotropic media with equivalent coupled microstrip lines. *IEEE Microwave and Wireless Components Letters*, 16(12):642–644, 2006.

[46] Justin R Burr, Nadav Gutman, C Martijn de Sterke, Ilya Vitebskiy, and Ronald M Reano. Degenerate band edge resonances in coupled periodic silicon optical waveguides. *Optics Express*, 21(7):8736–8745, 2013.

[47] Mohamed Y Nada, Mohamed AK Othman, and Filippo Capolino. Theory of coupled resonator optical waveguides exhibiting high-order exceptional points of degeneracy. *Physical Review B*, 96(18):184304, 2017.

[48] Mohamed AK Othman, Xuyuan Pan, Georgios Atmatzakis, Christos G Christodoulou, and Filippo Capolino. Experimental demonstration of degenerate band edge in metallic periodically loaded circular waveguide. *IEEE Transactions on Microwave Theory and Techniques*, 65(11):4037–4045, 2017.

[49] Tarek Mealy and Filippo Capolino. General conditions to realize exceptional points of degeneracy in two uniform coupled transmission lines. *IEEE Transactions on Microwave Theory and Techniques*, 68(8):3342–3354, 2020.

[50] Lars H Frandsen, Andrei V Lavrinenko, Jacob Fage-Pedersen, and Peter I Borel. Photonic crystal waveguides with semi-slow light and tailored dispersion properties. *Optics express*, 14(20):9444–9450, 2006.

[51] Alex Figotin and Ilya Vitebskiy. Slow-wave resonance in periodic stacks of anisotropic layers. *Physical Review A*, 76(5):053839, 2007.

[52] Andrey A Sukhorukov, Andrei V Lavrinenko, Dmitry N Chigrin, Dmitry E Pelinovsky, and Yuri S Kivshar. Slow-light dispersion in coupled periodic waveguides. *JOSA B*, 25(12):C65–C74, 2008.

[53] Matthew B Stephanson, Kubilay Sertel, and John L Volakis. Frozen modes in coupled microstrip lines printed on ferromagnetic substrates. *IEEE Microwave and Wireless Components Letters*, 18(5):305–307, 2008.

[54] Gokhan Mumcu, Kubilay Sertel, and John L Volakis. Lumped circuit models for degenerate band edge and magnetic photonic crystals. *IEEE Microwave and Wireless Components Letters*, 20(1):4–6, 2009.

[55] Mohamed Y Nada, Tarek Mealy, and Filippo Capolino. Frozen mode in three-way periodic microstrip coupled waveguide. *IEEE Microwave and Wireless Components Letters*, 31(3):229–232, 2020.

[56] Raed Almhmadi and Kubilay Sertel. Frozen-light modes in 3-way coupled silicon ridge waveguides. In *2019 United States National Committee of URSI National Radio Science Meeting (USNC-URSI NRSM)*, pages 1–2, Boulder, CO, USA, 2019.

[57] Mohamed AK Othman, Venkata Ananth Tamma, and Filippo Capolino. Theory and new amplification regime in periodic multimodal slow wave structures with degeneracy interacting with an electron beam. *IEEE Transactions on Plasma Science*, 44(4):594–611, 2016.

[58] Leopold B Felsen and Nathan Marcuvitz. *Radiation and scattering of waves*. John Wiley & Sons, Hoboken, NJ, USA, 1994.

[59] N Marcuvitz and J Schwinger. On the representation of the electric and magnetic fields produced by currents and discontinuities in wave guides. i. *Journal of Applied Physics*, 22(6):806–819, 1951.

[60] Carl D. Meyer. *Matrix analysis and applied linear algebra*. Philadelphia, PA, USA: SIAM, 2001.

[61] Nicholas Higham. *Functions of matrices : theory and computation*. Philadelphia, PA, USA: SIAM, 2008.

[62] Mohamed Y Nada, Mohamed AK Othman, Ozdal Boyraz, and Filippo Capolino. Giant resonance and anomalous quality factor scaling in degenerate band edge coupled resonator optical waveguides. *Journal of Lightwave Technology*, 36(14):3030–3039, 2018.

[63] Hamidreza Kazemi, Mohamed Y. Nada, Tarek Mealy, Ahmed F. Abdelshafy, and Filippo Capolino. Exceptional points of degeneracy induced by linear time-periodic variation. *Physical Review Applied*, 11:014007, Jan 2019.

[64] Gokhan Mumcu, Kubilay Sertel, and John L Volakis. Miniature antenna using printed coupled lines emulating degenerate band edge crystals. *IEEE Transactions on Antennas and Propagation*, 57(6):1618–1624, 2009.

[65] Mohamed AK Othman and Filippo Capolino. Demonstration of a degenerate band edge in periodically-loaded circular waveguides. *IEEE Microwave and Wireless Components Letters*, 25(11):700–702, 2015.

[66] Tianyu Zheng, Massimiliano Casaletti, Ahmed F Abdelshafy, Filippo Capolino, Zhuoxiang Ren, and Guido Valerio. Design of substrate integrated waveguides supporting degenerate band-edge resonances. In *2019 13th European Conference on Antennas and Propagation (EuCAP)*, Krakow, Poland, 2019, pp. 1-3.

[67] C. Locker, K. Sertel, and J. L. Volakis. Emulation of propagation in layered anisotropic media with equivalent coupled microstrip lines. *IEEE Microwave and Wireless Components Letters*, 16(12):642–644, 2006.

[68] Jeff T Sloan, Mohamed AK Othman, and Filippo Capolino. Theory of double ladder lumped circuits with degenerate band edge. *IEEE Transactions on Circuits and Systems I: Regular Papers*, 65(1):3–13, 2018.

[69] Farshad Yazdi, Mohamed AK Othman, Mehdi Veysi, Alexander Figotin, and Filippo Capolino. A new amplification regime for traveling wave tubes with third-order modal degeneracy. *IEEE Transactions on Plasma Science*, 46(1):43–56, 2017.

[70] Tarek Mealy, Ahmed F Abdelshafy, and Filippo Capolino. The degeneracy of the dominant mode in rectangular waveguide. In *2019 United States National Committee of URSI National Radio Science Meeting (USNC-URSI NRSM)*, pages 1–2. IEEE, 2019.

[71] Clayton R Paul. *Analysis of multiconductor transmission lines*. Hoboken, NJ, USA: Wiley, 2008.

[72] Islam A Eshrah, Ahmed A Kishk, Alexander B Yakovlev, and Alien W Glisson. Evanescent rectangular waveguide with corrugated walls: A composite right/left-handed metaguide. In *Microwave Symposium Digest, 2005 IEEE MTT-S International*, Long Beach, CA, 2005, p. 4.

[73] Heeso Noh, Jin Yang, Ilya Vitebskiy, Alex Figotin, and Hui Cao. Giant resonances near the split band edges of two-dimensional photonic crystals. *Physical Review A*, 82(1):013801, 2010.

[74] Behzad Razavi. A study of phase noise in cmos oscillators. *IEEE Journal of Solid-State Circuits*, 31(3):331–343, 1996.

[75] George V Eleftheriades, Ashwin K Iyer, and Peter C Kremer. Planar negative refractive index media using periodically lc loaded transmission lines. *IEEE Transactions on Microwave Theory and Techniques*, 50(12):2702–2712, 2002.

[76] Christophe Caloz and Tatsuo Itoh. *Electromagnetic metamaterials: transmission line theory and microwave applications*. Hoboken, NJ, USA: Wiley, 2004.

[77] Nil Apaydin, Lanlin Zhang, Kubilay Sertel, and John L Volakis. Experimental validation of frozen modes guided on printed coupled transmission lines. *IEEE Transactions on Microwave Theory and Techniques*, 60(6):1513–1519, 2012.

[78] Tarek Mealy and Filippo Capolino. Exceptional points of degeneracy with indirect bandgap induced by mixing forward and backward propagating waves. *arXiv:2205.06844*, 2022.

[79] Amnon Yariv. Coupled-mode theory for guided-wave optics. *IEEE Journal of Quantum Electronics*, 9(9):919–933, 1973.

[80] Amos Hardy and William Streifer. Coupled mode theory of parallel waveguides. *Journal of Lightwave Technology*, 3(5):1135–1146, 1985.

[81] Yubo Li, Xianxin Guo, Li Chen, Chao Xu, Jianyi Yang, Xiaoqing Jiang, and Minghua Wang. Coupled mode theory under the parity-time symmetry frame. *Journal of Lightwave Technology*, 31(15):2477–2481, 2013.

[82] Ramy El-Ganainy, Konstantinos G Makris, Mercedeh Khajavikhan, Ziad H Musslimani, Stefan Rotter, and Demetrios N Christodoulides. Non-hermitian physics and pt symmetry. *Nature Physics*, 14(1):11–19, 2018.

[83] Carl D Meyer. *Matrix Analysis and Applied Linear Algebra*, volume 71. Philadelphia, PA, USA: SIAM, 2000.

[84] E Hammerstad and O Jensen. Accurate models for microstrip computer-aided design. In *1980 IEEE MTT-S International Microwave Symposium Digest*, pages 407–409. IEEE, 1980.

[85] Manfred Kirschning and Rolf H Jansen. Accurate wide-range design equations for the frequency-dependent characteristic of parallel coupled microstrip lines. *IEEE Transactions on Microwave Theory and Techniques*, 32(1):83–90, 1984.

[86] R Mittra and S Laxpati. Propagation in a wave guide with glide reflection symmetry. *Canadian Journal of Physics*, 43(2):353–372, 1965.

[87] ALEXANDER Hessel, Ming Hui Chen, ROBERT CM Li, and ARTHUR A Oliner. Propagation in periodically loaded waveguides with higher symmetries. *Proceedings of the IEEE*, 61(2):183–195, 1973.

[88] Mohammad Bagheriasl, Oscar Quevedo-Teruel, and Guido Valerio. Bloch analysis of artificial lines and surfaces exhibiting glide symmetry. *IEEE Transactions on Microwave Theory and Techniques*, 67(7):2618–2628, 2019.

[89] Fatemeh Ghasemifard, Martin Norgren, Oscar Quevedo-Teruel, and Guido Valerio. Analyzing glide-symmetric holey metasurfaces using a generalized floquet theorem. *IEEE Access*, 6:71743–71750, 2018.

[90] Qiao Chen, Francisco Mesa, Xiaoxing Yin, and Oscar Quevedo-Teruel. Accurate characterization and design guidelines of glide-symmetric holey ebg. *IEEE Transactions on Microwave Theory and Techniques*, 68(12):4984–4994, 2020.

[91] Javier Martínez, Angela Coves, Francisco Mesa, and Oscar Quevedo-Teruel. Passband broadening of sub-wavelength resonator-based glide-symmetric siw filters. *AEU-International Journal of Electronics and Communications*, 125:153362, 2020.

[92] Boules A Mouris, Armando Fernández-Prieto, Ragnar Thobaben, Jesús Martel, Francisco Mesa, and Oscar Quevedo-Teruel. On the increment of the bandwidth of mushroom-type ebg structures with glide symmetry. *IEEE Transactions on Microwave Theory and Techniques*, 68(4):1365–1375, 2020.

[93] Tarek Mealy and Filippo Capolino. Degenerate distributed feedback photonic structure with double grating exhibiting degenerate band edge. *arXiv:2205.05639*, 2022.

[94] Andrey A. Sukhorukov, C. J. Handmer, C. Martijn de Sterke, and M. J. Steel. Slow light with flat or offset band edges in few-mode fiber with two gratings. *Optics Express*, 15(26):17954–17959, 2007.

[95] Nadav Gutman, Lindsay C. Botten, Andrey A. Sukhorukov, and C. Martijn de Sterke. Degenerate band edges in optical fiber with multiple grating: efficient coupling to slow light. *Optics Letter*, 36(16):3257–3259, 2011.

[96] Michael G Wood, Justin R Burr, and Ronald M Reano. Degenerate band edge resonances in periodic silicon ridge waveguides. *Optics Letters*, 40(11):2493–2496, 2015.

[97] H Kogelnik and CV Shank. Coupled-wave theory of distributed feedback lasers. *Journal of Applied Physics*, 43(5):2327–2335, 1972.

[98] Hooshang Ghafouri-Shiraz. *Distributed feedback laser diodes and optical tunable filters*. John Wiley & Sons: Chichester, England, 2003.

[99] Shyh Wang. Principles of distributed feedback and distributed bragg-reflector lasers. *IEEE Journal of Quantum Electronics*, 10(4):413–427, 1974.

[100] John J Degnan. The waveguide laser: A review. *Applied physics*, 11(1):1–33, 1976.

[101] Nadav Gutman, C Martijn de Sterke, Andrey A Sukhorukov, and Lindsay C Botten. Slow and frozen light in optical waveguides with multiple gratings: Degenerate band edges and stationary inflection points. *Physical Review A*, 85(3):033804, 2012.

[102] Tarek Mealy, Ahmed F Abdelshafy, and Filippo Capolino. Exceptional point of degeneracy in a backward-wave oscillator with distributed power extraction. *Physical Review Applied*, 14(1):014078, 2020.

[103] WD Heiss, M Müller, and I Rotter. Collectivity, phase transitions, and exceptional points in open quantum systems. *Physical Review E*, 58(3):2894, 1998.

[104] S Bittner, B Dietz, Uwe Günther, HL Harney, M Miski-Oglu, A Richter, and F Schäfer. PT -symmetry and spontaneous symmetry breaking in a microwave billiard. *Physical Review Letters*, 108(2):024101, 2012.

[105] David Bohm and Eugene P Gross. Theory of plasma oscillations. A. Origin of medium-like behavior. *Physical Review*, 75(12):1851, 1949.

[106] JR Pierce. Waves in electron streams and circuits. *Bell System Technical Journal*, 30(3):626–651, 1951.

[107] Robert C Hansen. *Phased array antennas*, volume 213. John Wiley & Sons, NJ, USA, 2009.

[108] Warren L Stutzman and Gary A Thiele. *Antenna theory and design*. John Wiley & Sons, NY, USA, 2012.

[109] Wei Wang, Shun-Shi Zhong, Yu-Mei Zhang, and Xian-Ling Liang. A broadband slotted ridge waveguide antenna array. *IEEE Transactions on Antennas and Propagation*, 54(8):2416–2420, Aug 2006.

[110] Horace Richard Johnson. Backward-wave oscillators. *Proceedings of the IRE*, 43(6):684–697, 1955.

[111] Shulim E Tsimring. *Electron beams and microwave vacuum electronics*. John Wiley & Sons, Hoboken, NJ, USA, 2007.

[112] Mohamed AK Othman, Mehdi Veysi, Alexander Figotin, and Filippo Capolino. Giant amplification in degenerate band edge slow-wave structures interacting with an electron beam. *Physics of Plasmas*, 23(3):033112, 2016.

[113] JR Pierce. Theory of the beam-type traveling-wave tube. *Proceedings of the IRE*, 35(2):111–123, 1947.

[114] Simon Ramo. Space charge and field waves in an electron beam. *Physical Review*, 56(3):276, 1939.

[115] Rudolf Kompfner. The traveling-wave tube as amplifier at microwaves. *Proceedings of the IRE*, 35(2):124–127, 1947.

[116] Lan Jen Chu and John David Jackson. Field theory of traveling-wave tubes. *Proceedings of the IRE*, 36(7):853–863, 1948.

[117] Venkata Ananth Tamma and Filippo Capolino. Extension of the pierce model to multiple transmission lines interacting with an electron beam. *IEEE Transactions on Plasma Science*, 42(4):899–910, 2014.

[118] AS Gilmour. *Klystrons, traveling wave tubes, magnetrons, crossed-field amplifiers, and gyrotrons*. Artech House, Norwood, MA, USA, 2011.

[119] Richard W Ziolkowski and Ehud Heyman. Wave propagation in media having negative permittivity and permeability. *Physical Review E*, 64(5):056625, 2001.

[120] AP Seyranian, ON Kirillov, and AA Mailybaev. Coupling of eigenvalues of complex matrices at diabolic and exceptional points. *Journal of Physics A: Mathematical and General*, 38(8):1723–1740, 2005.

[121] David R Jackson and Arthur A Oliner. Leaky-wave antennas. *Modern Antenna Handbook*, pages 325–367, 2008.

[122] Aaron Welters. On explicit recursive formulas in the spectral perturbation analysis of a jordan block. *SIAM Journal on Matrix Analysis and Applications*, 32(1):1–22, 2011.

[123] LR Walker. Starting currents in the backward-wave oscillator. *Journal of Applied Physics*, 24(7):854–859, 1953.

[124] Tarek Mealy, Ahmed F Abdelshafy, and Filippo Capolino. High-power x-band relativistic backward-wave oscillator with exceptional synchronous regime operating at an exceptional point. *Physical Review Applied*, 15(6):064021, 2021.

[125] M Liertzer, Li Ge, A Cerjan, AD Stone, Hakan E Türeci, and S Rotter. Pump-induced exceptional points in lasers. *Physical Review Letters*, 108(17):173901, 2012.

[126] T. Mealy, A. F. Abdelshafy, and F. Capolino. Backward-wave oscillator with distributed power extraction based on exceptional point of degeneracy and gain and radiation-loss balance. In *2019 International Vacuum Electronics Conference (IVEC)*, pages 1–2, Busan, South Korea, 2019, doi: 10.1109/IVEC.2019.8745292.

[127] AS Gilmour. *Principles of traveling wave tubes*. Artech House, Norwood, MA, USA, 1994.

[128] Baruch Levush, Thomas M Antonsen, Alan Bromborsky, W-R Lou, and Yuval Carmel. Theory of relativistic backward-wave oscillators with end reflectors. *IEEE Transactions on Plasma Science*, 20(3):263–280, 1992.

[129] SH Chen, KR Chu, and TH Chang. Saturated behavior of the gyrotron backward-wave oscillator. *Physical Review Letters*, 85(12):2633, 2000.

[130] Larald D Moreland, Edl Schamiloglu, W Lemke, SD Korovin, VV Rostov, AM Roitman, Kyle J Hendricks, and TA Spencer. Efficiency enhancement of high power vacuum bwo's using nonuniform slow wave structures. *IEEE Transactions on Plasma Science*, 22(5):554–565, 1994.

[131] Zheng-Hong Li. Investigation of an oversized backward wave oscillator as a high power microwave generator. *Applied Physics Letters*, 92(5):054102, 2008.

[132] Jun Zhang, Hui-Huang Zhong, Zhenxing Jin, Ting Shu, Shengguang Cao, and Shengyue Zhou. Studies on efficient operation of an x-band oversized slow-wave hpm generator in low magnetic field. *IEEE Transactions on Plasma Science*, 37(8):1552–1557, 2009.

[133] Peter Andrew Sturrock. Kinematics of growing waves. *Physical Review*, 112(5):1488, 1958.

[134] Tarek Mealy and Filippo Capolino. Traveling wave tube eigenmode solution for beam-loaded slow wave structure based on particle-in-cell simulations. *IEEE Transactions on Plasma Science*, 50(3):635–648, 2022.

[135] Tarek Mealy, Ahmed F. Abdelshafy, and Filippo Capolino. High-power backward-wave oscillator using folded waveguide with distributed power extraction operating at an exceptional point. *IEEE Transactions on Electron Devices*, pages 1–8, 2021, doi:10.1109/TED.2021.3082812.

[136] John H Booske. Plasma physics and related challenges of millimeter-wave-to-terahertz and high power microwave generation. *Physics of Plasmas*, 15(5):055502, 2008.

[137] John H Booske, Richard J Dobbs, Colin D Joye, Carol L Kory, George R Neil, Gun-Sik Park, Jaehun Park, and Richard J Temkin. Vacuum electronic high power terahertz sources. *IEEE Transactions on Terahertz Science and Technology*, 1(1):54–75, 2011.

[138] Carter M Armstrong. The truth about terahertz. *IEEE Spectrum*, 49(9):36–41, 2012.

[139] Colin D Joye, Alan M Cook, Jeffrey P Calame, David K Abe, Alexander N Vlasov, Igor A Chernyavskiy, Khanh T Nguyen, Edward L Wright, Dean E Pershing, Takuji Kimura, et al. Demonstration of a high power, wideband 220-GHz traveling wave amplifier fabricated by UV-LIGA. *IEEE transactions on electron devices*, 61(6):1672–1678, 2014.

[140] Carter M Armstrong, Richard Kowalczyk, Andrew Zubyk, Kevin Berg, Clark Meadows, Danny Chan, Thomas Schoemehl, Ramon Duggal, Nora Hinch, Richard B True, et al. A compact extremely high frequency MPM power amplifier. *IEEE Transactions on Electron Devices*, 65(6):2183–2188, 2018.

[141] C. M. Armstrong. These vacuum devices stood guard during the cold war, advanced particle physics, treated cancer patients, and made the beatles sound better. *IEEE Spectrum*, 57(11):30–36, 2020.

[142] YM Shin, JK So, KH Jang, JH Won, A Srivastava, ST Han, GS Park, JH Kim, SS Chang, RK Sharma, et al. Experimental investigation of 95 GHz folded waveguide backward wave oscillator fabricated by two-step LIGA. In *2006 IEEE International Vacuum Electronics Conference held Jointly with 2006 IEEE International Vacuum Electron Sources*, pages 419–420. IEEE, 2006.

[143] Sean Sengele, Hongrui Jiang, John H Booske, Carol L Kory, Daniel W Van der Weide, and R Lawrence Ives. Microfabrication and characterization of a selectively metallized W-band meander-line TWT circuit. *IEEE transactions on electron devices*, 56(5):730–737, 2009.

[144] Richard Dobbs, Albert Roitman, Peter Horoyski, Mark Hyttinen, Dan Sweeney, Brian Steer, Khanh Nguyen, Edward Wright, David Chernin, Alex Burke, et al. Design and fabrication of terahertz extended interaction klystrons. In *35th International Conference on Infrared, Millimeter, and Terahertz Waves*, pages 1–3. IEEE, 2010.

[145] Jinjun Feng, Dapeng Ren, Hanyan Li, Ye Tang, and Junyi Xing. Study of high frequency folded waveguide BWO with MEMS technology. *Terahertz Science and Technology*, 4(4):164–180, 2011.

[146] Colin D Joye, Alan M Cook, Jeffrey P Calame, David K Abe, Alexander N Vlasov, Igor A Chernyavskiy, Khanh T Nguyen, and Edward L Wright. Microfabrication and cold testing of copper circuits for a 50-watt 220-GHz traveling wave tube. In *Terahertz, RF, Millimeter, and Submillimeter-Wave Technology and Applications VI*, volume 8624, page 862406. International Society for Optics and Photonics, 2013.

[147] JJ Choi, CM Armstrong, F Calise, AK Ganguly, RH Kyser, GS Parks, RK Parker, and F Wood. Experimental observation of coherent millimeter wave radiation in a folded waveguide employed with a gyrating electron beam. *Physical Review Letters*, 76(22):4273, 1996.

[148] Sudeep Bhattacharjee, John H Booske, Carol L Kory, Dan W Van Der Weide, Steve Limbach, Sean Gallagher, John D Welter, Mike R Lopez, Ronald M Gilgenbach, R Lawrence Ives, et al. Folded waveguide traveling-wave tube sources for terahertz radiation. *IEEE Transactions on Plasma Science*, 32(3):1002–1014, 2004.

[149] Khanh T Nguyen, Alexander N Vlasov, Lars Ludeking, Colin D Joye, Alan M Cook, Jeffrey P Calame, John A Pasour, Dean E Pershing, Edward L Wright, Simon J Cooke, et al. Design methodology and experimental verification of serpentine/folded-waveguide TWTs. *IEEE Transactions on Electron Devices*, 61(6):1679–1686, 2014.

[150] Jinchi Cai, Linlin Hu, Huaibi Chen, Xiao Jin, Guowu Ma, and Hongbin Chen. Study on the increased threshold current in the development of 220-GHz folded waveguide backward-wave oscillator. *IEEE Transactions on Microwave Theory and Techniques*, 64(11):3678–3685, 2016.

[151] Anisullah Baig, Diana Gamzina, Takuji Kimura, John Atkinson, Calvin Domier, Branko Popovic, Logan Himes, Robert Barchfeld, Mark Field, and Neville C Luhmann. Performance of a nano-CNC machined 220-GHz traveling wave tube amplifier. *IEEE Transactions on Electron Devices*, 64(5):2390–2397, 2017.

[152] GX Shu, Huabi Yin, Liang Zhang, JP Zhao, Guo Liu, ADR Phelps, AW Cross, and Wenlong He. Demonstration of a planar W-band, kW-level extended interaction oscillator based on a pseudospark-sourced sheet electron beam. *IEEE Electron Device Letters*, 39(3):432–435, 2018.

[153] Damien FG Minenna, Frédéric André, Yves Elskens, Jean-François Auboin, Fabrice Doveil, Jérôme Puech, and Élise Duverdier. The traveling-wave tube in the history of telecommunication. *The European Physical Journal H*, 44(1):1–36, 2019.

[154] Xiang Li, Xuejiao Huang, Storm Mathisen, Rosa Letizia, and Claudio Paoloni. Design of 71–76 GHz double-corrugated waveguide traveling-wave tube for satellite downlink. *IEEE Transactions on Electron Devices*, 65(6):2195–2200, 2018.

[155] Huarong Gong, Yubin Gong, Tao Tang, Jin Xu, and Weng-Xiang Wang. Experimental investigation of a high-power Ka-band folded waveguide traveling-wave tube. *IEEE Transactions on Electron Devices*, 58(7):2159–2163, 2011.

[156] John Robinson Pierce. *Traveling-wave tubes*. New York, NY, USA: Van Nostrand, 1950.

[157] James W Gewartowski and Hugh A Watson. *Principles of electron tubes*. New York, NY, USA: Van Nostrand, 1965.

[158] James Benford, John A Swegle, and Edl Schamiloglu. *High power Microwaves*. CRC press, Boca Raton, FL,USA, 2007.

[159] John H Booske and Mark C Converse. Insights from one-dimensional linearized pierce theory about wideband traveling-wave tubes with high space charge. *IEEE Transactions on Plasma Science*, 32(3):1066–1072, 2004.

[160] LA Vainshtein. Electron waves in retardation (slow-wave) systems. 1. general theory. *Soviet Physics-Technical Physics*, 1(1):119–134, 1956.

[161] VM Pikunov and IA Chernyavskii. Electron wave resonances in the cherenkov-type microwave device. *Journal of Communications Technology and Electronics*, 43(3):292–298, 1998.

[162] VM Pikunov and IA Chernjavsky. Amplification and generation microwaves in cherenkov relativistic device. *Radiotekhnika I Elektronika*, 37(11):2041–2050, 1992.

[163] SK Datta, SUM Reddy, BN Basu, and KU Limaye. A novel lagrangian simulation technique for helix traveling-wave tubes. *Microwave and Optical Technology Letters*, 18(4):308–310, 1998.

[164] TM Antonsen and Baruch Levush. Traveling-wave tube devices with nonlinear dielectric elements. *IEEE Transactions on Plasma Science*, 26(3):774–786, 1998.

[165] YD Joo, GS Park, and AK Sinha. Development of a simplified one-dimensional nonlinear helix traveling wave tube code based on the lagrangian disk model. *Journal-korean Physical Society*, 44(2):1313–1317, 2004.

[166] Abhijit Jassem, YY Lau, David P Chernin, and Patrick Y Wong. Theory of traveling-wave tube including space charge effects on the circuit mode and distributed cold tube loss. *IEEE Transactions on Plasma Science*, 48(3):665–668, 2020.

[167] Hanwen Tian, Zhigang Lu, Wei Shao, Zhanliang Wang, Jialu Ma, Tenglong He, Huarong Gong, Zhaoyun Duan, Tao Tang, Yanyu Wei, et al. 3-d fast nonlinear simulation for beam–wave interaction of sheet beam traveling-wave tube. *IEEE Transactions on Electron Devices*, 66(3):1504–1511, 2019.

[168] Hanwen Tian, Ningjie Shi, Zhanliang Wang, Shaomeng Wang, Zhaoyun Duan, Huarong Gong, Zhigang Lu, Claudio Paoloni, Jinjun Feng, and Yubin Gong. Improved model for beam–wave interaction with ohmic losses and reflections of sheet beam traveling wave tubes. *IEEE Transactions on Electron Devices*, 68(6):2977–2983, 2021.

[169] Kasra Rouhi, Robert Marosi, Tarek Mealy, Ahmed F Abdelshafy, Alexander Figotin, and Filippo Capolino. Exceptional degeneracies in traveling wave tubes with dispersive slow-wave structure including space-charge effect. *Applied Physics Letters*, 118(26):263506, 2021.

[170] Richard G Carter. Determination of the interaction impedance of helix slow-wave structures. In *2000 International Vacuum Electronics Conference (IVEC)*, pages 1–2, Monterey, CA, USA, 2000, doi:10.1109/OVE:EC.2000.847509.

[171] Zhaoyun Duan, Yubin Gong, Yanyu Wei, Wenxiang Wang, and Minzhi Huang. Analysis of the dispersion characteristic and interaction impedance of a tape helix slow wave structure with novel supporting mode. *International journal of electronics*, 91(5):309–318, 2004.

[172] Anurag Srivastava and V Latha Christie. Design of a high gain and high efficiency W-band folded waveguide TWT using phase-velocity taper. *Journal of Electromagnetic Waves and Applications*, 32(10):1316–1327, 2018.

[173] GM Branch and TG Mihran. Plasma frequency reduction factors in electron beams. *IRE Transactions on Electron Devices*, 2(2):3–11, 1955.

[174] Subrata Kumar Datta and Lalit Kumar. A simple closed-form formula for plasma-frequency reduction factor for a solid cylindrical electron beam. *IEEE Transactions on Electron Devices*, 56(6):1344–1346, 2009.

[175] John M Dawson. Particle simulation of plasmas. *Reviews of Modern Physics*, 55(2):403, 1983.

[176] D Tskhakaya, K Matyash, R Schneider, and F Taccogna. The particle-in-cell method. *Contributions to Plasma Physics*, 47(8-9):563–594, 2007.

[177] Thomas M Antonsen Jr and Baruch Levush. *CHRISTINE: A Multifrequency Parametric Simulation Code for Traveling Wave Tube Amplifiers.* Naval Research Lab, Washington, DC, USA, 1997.

[178] David Chernin, Thomas M Antonsen, Alexander N Vlasov, Igor A Chernyavskiy, Khanh T Nguyen, and Baruch Levush. 1-d large signal model of folded-waveguide traveling wave tubes. *IEEE Transactions on Electron Devices*, 61(6):1699–1706, 2014.

[179] Igor A Chernyavskiy, Thomas M Antonsen, Alexander N Vlasov, David Chernin, Khanh T Nguyen, and Baruch Levush. Large-signal 2-(D modeling of folded-waveguide traveling wave tubes. *IEEE Transactions on Electron Devices*, 63(6):2531–2537, 2016.

[180] John G Wohlbier, John H Booske, and Ian Dobson. The multifrequency spectral eulerian (MUSE) model of a traveling wave tube. *IEEE Transactions on Plasma Science*, 30(3):1063–1075, 2002.

[181] Thomas M Antonsen, Alexander N Vlasov, David P Chernin, Igor A Chernyavskiy, and Baruch Levush. Transmission line model for folded waveguide circuits. *IEEE Transactions on Electron Devices*, 60(9):2906–2911, 2013.

[182] Victor A Solntsev. Beam–wave interaction in the passbands and stopbands of periodic slow-wave systems. *IEEE Transactions on Plasma Science*, 43(7):2114–2122, 2015.

[183] Igor A Chernyavskiy, Thomas M Antonsen, John C Rodgers, Alexander N Vlasov, David Chernin, and Baruch Levush. Modeling vacuum electronic devices using generalized impedance matrices. *IEEE Transactions on Electron Devices*, 64(2):536–542, 2017.

[184] Vadim Jabotinski, David Chernin, Thomas M Antonsen, Alexander N Vlasov, and Igor A Chernyavskiy. Calculation and application of impedance matrices for vacuum electronic devices. *IEEE Transactions on Electron Devices*, 66(5):2409–2414, 2019.

[185] Damien FG Minenna, Artem G Terentyuk, Frédéric André, Yves Elskens, and Nikita M Ryskin. Recent discrete model for small-signal analysis of traveling-wave tubes. *Physica Scripta*, 94(5):055601, 2019.

[186] Nathan Marcuvitz. *Waveguide handbook*. New York: McGraw-Hill, 1951.

[187] Robert E Collin. *Field theory of guided waves*. John Wiley & Sons, Hoboken, NJ, USA, 1990.

[188] George Elmer Forsythe. Computer methods for mathematical computations. *Prentice-Hall series in automatic computation*, Englewood Cliffs, NJ, USA, 1977.

[189] Gareth Williams. Overdetermined systems of linear equations. *The American Mathematical Monthly*, 97(6):511–513, 1990.

[190] Howard Anton and Chris Rorres. *Elementary linear algebra: applications version*. John Wiley & Sons, Hoboken, NJ, USA, 2013.

[191] Tarek Mealy, Robert Marosi, and Filippo Capolino. Reduced plasma frequency calculation based on particle-in-cell simulations. *arXiv:2205.05806*, 2022.

[192] Lewi Tonks and Irving Langmuir. Oscillations in ionized gases. *Physical Review*, 33(2):195, 1929.

[193] WC Hahn. Small signal theory of velocity-modulated electron beams. *General Electric Review*, 42(6):258–270, 1939.

[194] PK Tien, LR Walker, and VM Wolontis. A large signal theory or traveling-wave amplifiers. *Proceedings of the IRE*, 43(3):260–277, 1955.

[195] David H Simon, Patrick Wong, David Chernin, YY Lau, B Hoff, Peng Zhang, CF Dong, and Ronald M Gilgenbach. On the evaluation of pierce parameters c and q in a traveling wave tube. *Physics of Plasmas*, 24(3):033114, 2017.

[196] Patrick Wong, Peng Zhang, and John Luginsland. Recent theory of traveling-wave tubes: a tutorial-review. *Plasma Research Express*, 2(2):023001, 2020.

[197] GM Branch, TG Mihran, W Neugebauer, and WJ Pohl. Space-charge wavelengths in electron beams. *IEEE Transactions on Electron Devices*, 14(7):350–357, 1967.

[198] GS Vorob'ev, A Ya Kirichenko, AI Tsvyk, and LI Tsvyk. Experimental determination of reduced plasma frequency of an electron flux. *Radiophysics and Quantum Electronics*, 33(10):854–859, 1990.

[199] JR Pierce. Double-stream amplifiers. *Proceedings of the IRE*, 37(9):980–985, 1949.

[200] John R Pierce and William B Hebenstreit. A new type of high-frequency amplifier. *The Bell System Technical Journal*, 28(1):33–51, 1949.

[201] Alexander Figotin. *An Analytic Theory of Multi-stream Electron Beams in Traveling Wave Tubes*. World Scientific, 2021.

[202] Khandakar Nusrat Islam, LD Ludeking, Andrey D Andreev, Salvador Portillo, Ahmed MN Elfrgani, and Edl Schamiloglu. Modeling and simulation of relativistic multiple electron beam generation with different energies from a single-cathode potential for high-power microwave sources. *IEEE Transactions on Electron Devices*, 2022.

[203] KN Islam and E Schamiloglu. Multiple electron beam generation with different energies and comparable currents from a single cathode potential for high power traveling wave tubes (twts). *Journal of Applied Physics*, 131(4):044901, 2022.

[204] Charles K Birdsall, George R Brewer, and Andrew V Haeff. The resistive-wall amplifier. *Proceedings of the IRE*, 41(7):865–875, 1953.

[205] Tyler Rowe, Nader Behdad, and John H Booske. Metamaterial-enhanced resistive wall amplifier design using periodically spaced inductive meandered lines. *IEEE Transactions on Plasma Science*, 44(10):2476–2484, 2016.

[206] Tyler Rowe, John H Booske, and Nader Behdad. Metamaterial-enhanced resistive wall amplifiers: Theory and particle-in-cell simulations. *IEEE Transactions on Plasma Science*, 43(7):2123–2131, 2015.

[207] Patrick Forbes, Nader Behdad, and John H Booske. Effective-medium modeling of a meanderline metamaterial-enhanced resistive wall amplifier circuit for particle-in-cell simulations. *IEEE Transactions on Plasma Science*, 49(9):2700–2708, 2021.

[208] Alexander Figotin. Exceptional points of degeneracy in traveling wave tubes. *Journal of Mathematical Physics*, 62(8):082701, 2021.

[209] Joe X Qiu, Baruch Levush, John Pasour, Allen Katz, Carter M Armstrong, David R Whaley, Jack Tucek, Kenneth Kreischer, and David Gallagher. Vacuum tube amplifiers. *IEEE Microwave Magazine*, 10(7):38–51, 2009.

[210] Robert K Parker, Richard H Abrams, Bruce G Danly, and Baruch Levush. Vacuum electronics. *IEEE Transactions on Microwave Theory and Techniques*, 50(3):835–845, 2002.

[211] AS Pobedonostev, EA Gelvich, MI Lopin, AM Alexeyenko, AA Negirev, and BV Sazonov. Multiple-beam microwave tubes. In *1993 IEEE MTT-S International Microwave Symposium Digest*, pages 1131–1134. IEEE, 1993.

[212] LI GAN YUAN-LONG MO SHENG and LIU GANG. Multi-beam twt with active power combining. *International Journal of Electronics*, 84(6):647–657, 1998.

[213] JR Pierce. Double-stream amplifiers. *Proceedings of the IRE*, 37(9):980–985, 1949.

[214] DT Swift-Hook. Validity of the theory of double stream amplification. *Physical Review*, 118(1):1, 1960.

[215] G Dohler, D Gagne, and D Zavadil. Beam-beam interactions in concentric-beam dual-mode twt's. In *1980 International Electron Devices Meeting*, pages 169–172. IEEE, 1980.

[216] Chiping Chen. Efficiency scaling law for the two-stream amplifier. *Physics of Plasmas*, 3(8):3107–3110, 1996.

[217] Gregory S Nusinovich, Simon J Cooke, Moti Botton, and Baruch Levush. Wave coupling in sheet-and multiple-beam traveling-wave tubes. *Physics of Plasmas*, 16(6):063102, 2009.

[218] David A Zavadil. Dual beam dual mode twt. In *1974 International Electron Devices Meeting (IEDM)*, pages 209–211. IEEE, 1974.

[219] AV Hollenberg. Experimental observation of amplification by interaction between two electron streams. *Bell System Technical Journal*, 28(1):52–58, 1949.

[220] D Neben, K Bishofberger, Vitaly Pavlenko, and Nikolai Yampolsky. A co-axial electron gun to generate millimeter-wave rf using the two-stream instability. *Review of Scientific Instruments*, 92(5):053301, 2021.

[221] LEON S Nergaard. Analysis of a simple model of a two-beam growing-wave tube. *RCA Review*, 9(585):19–8, 1948.

[222] Andrew V Haeff. The electron-wave tube-a novel method of generation and amplification of microwave energy. *Proceedings of the IRE*, 37(1):4–10, 1949.

[223] Jennifer M Butler and CB Wharton. Twin traveling-wave tube amplifiers driven by a relativistic backward-wave oscillator. *IEEE Transactions on Plasma Science*, 24(3):884–894, 1996.

[224] Bruce E Carlsten, Kip A Bishofberger, and Rickey J Faehl. Compact two-stream generator of millimeter-and submillimeter-wave radiation. *Physics of Plasmas*, 15(7):073101, 2008.

[225] MR Boyd, RA Dehn, JS Hickey, and TG Mihran. The multiple-beam klystron. *IRE Transactions on Electron Devices*, 9(3):247–252, 1962.

[226] WJ Pohl. The design and demonstration of a wide-band multiple-beam traveling-wave klystron. *IEEE Transactions on Electron Devices*, 12(6):351–368, 1965.

[227] Yaogen Ding, Bin Shen, Shaomin Shi, and Jin Cao. S-band multibeam klystron with bandwidth of 10%. *IEEE Transactions on Electron Devices*, 52(5):889–894, 2005.

[228] Shengmei Yan, Wei Su, Yajun Wang, and Ao Xu. Design and theoretical analysis of multibeam folded waveguide traveling-wave tube for subterahertz radiation. *IEEE Transactions on Plasma Science*, 43(1):414–421, 2014.

[229] Sheng-mei Yan, Wei Su, and Guo-liang Zhang. Design and fabrication of a submillimeter multi-beam folded waveguide structure. *Optoelectronics Letters*, 13(1):33–37, 2017.

[230] Wenxin Liu, Ke Li, Pengpeng Gao, Chao Zhao, Xin Guo, and Zhaochuan Zhang. Nonlinear theory for beam-wave interactions of two electron beams with higher order te20 mode in serpentine waveguide traveling wave amplifier. *Physics of Plasmas*, 25(12):123106, 2018.

[231] Ningjie Shi, Hexin Wang, Duo Xu, Zhanliang Wang, Zhigang Lu, Huarong Gong, Diwei Liu, Zhaoyun Duan, Yanyu Wei, and Yubin Gong. Study of 220 ghz dual-beam overmoded photonic crystal-loaded folded waveguide twt. *IEEE Transactions on Plasma Science*, 47(6):2971–2978, 2019.

[232] Yunyuan Yang and Wu Ding. A two-stream gyrotron traveling wave tube amplifier. *Physics of Plasmas*, 6(11):4328–4332, 1999.

[233] Young-Min Shin, Larry R Barnett, and Neville C Luhmann Jr. Strongly confined plasmonic wave propagation through an ultrawideband staggered double grating waveguide. *Applied Physics Letters*, 93(22):221504, 2008.

[234] Anthony Gee and Young-Min Shin. Gain analysis of higher-order-mode amplification in a dielectric-implanted multi-beam traveling wave structure. *Physics of Plasmas*, 20(7):073106, 2013.

[235] Wei Shao, Duo Xu, Zhanliang Wang, Huarong Gong, Zhigang Lu, Zhaoyun Duan, Yanyu Wei, Yubin Gong, and Sheel Aditya. Stacked dual beam electron optical system for thz integrated wideband traveling wave tube. *Physics of Plasmas*, 26(6):063106, 2019.

[236] Jun Yang, Ke Cai, Guangsheng Deng, Zhiping Yin, Jiufu Ruan, Fei Cai, and Yong Fang. A staggered double-vane slow-wave structure with double sheet electron beams for 340 ghz traveling wave tube. *Journal of Electromagnetic Waves and Applications*, 33(12):1632–1643, 2019.

[237] Zhigang Lu, Meiling Zhu, Kesen Ding, Ruidong Wen, Weihua Ge, Zhanliang Wang, Tao Tang, Huarong Gong, and Yubin Gong. Investigation of double tunnel sine waveguide slow-wave structure for terahertz dual-beam twt. *IEEE Transactions on Electron Devices*, 67(5):2176–2181, 2020.

[238] Jinjing Luo, Jin Xu, Pengcheng Yin, Ruichao Yang, Lingna Yue, Zhanliang Wang, Lin Xu, Jinjun Feng, Wenxin Liu, and Yanyu Wei. A 340 ghz high-power multi-beam overmoded flat-roofed sine waveguide traveling wave tube. *Electronics*, 10(23):3018, 2021.

[239] Hexin Wang, Zhanliang Wang, Xinyi Li, Tenglong He, Duo Xu, Huarong Gong, Tao Tang, Zhaoyun Duan, Yanyu Wei, and Yubin Gong. Study of a miniaturized dual-beam twt with planar dielectric-rods-support uniform metallic meander line. *Physics of Plasmas*, 25(6):063113, 2018.

[240] Gennadiy V Torgashov, Roman A Torgashov, Vladimir N Titov, Andrey G Rozhnev, and Nikita M Ryskin. Meander-line slow-wave structure for high-power millimeter-band traveling-wave tubes with multiple sheet electron beam. *IEEE Electron Device Letters*, 40(12):1980–1983, 2019.

[241] Zheng Wen, Jirun Luo, Ying Li, Wei Guo, Min Zhu, and Fang Zhu. A concentric arc meander line sws for low voltage, high efficiency, and wide bandwidth v-band twt with dual sheet beam. *IEEE Transactions on Plasma Science*, 49(6):1842–1847, 2021.

[242] Jiacai Liao, Guoxiang Shu, Jingcong He, Junchen Ren, Jujian Lin, Junzhe Deng, Zhiwei Chang, Biaogang Xu, Cunjun Ruan, and Wenlong He. A terahertz band te20 mode input/output coupling structure for dual-sheet-beam traveling-wave tubes. *IEEE Transactions on Plasma Science*, 2022.

[243] Roman A Torgashov, Andrey G Rozhnev, and Nikita M Ryskin. Design study on a multiple-tunnel meander-line slow-wave structure for a high-power v-band traveling-wave tube. *IEEE Transactions on Electron Devices*, 2022.

[244] Constantine A Balanis. *Advanced engineering electromagnetics*. John Wiley & Sons, 2012.

Appendix A

General Solution of the Scalar Electric Potential Function

A.1 Region with Moving Electrons (Stream Region)

Here, we provide the basic steps to find the general solution that satisfies the differential equation for the electron beam and the electromagnetic dynamics. For the studied region, the electrons are assumed to be traveling only in the axial direction with uniform dc velocity u_0 and uniform dc charge density ρ_0 that are radially independent due to a strong external axial magnetic field which confines the beam. We assume that the electron beam and the electromagnetic dynamics follow a wave function that involves modulation in the beam axial speed and charge density in cylindrical coordinates as

$$u(r,z,t) = u_0 + \Re\left(u_{\mathrm{m}}(r)e^{j\omega t - jkz}\right), \tag{A.1}$$

$$\rho(r,z,t) = \rho_0 + \Re\left(\rho_{\mathrm{m}}(r)e^{j\omega t - jkz}\right), \tag{A.2}$$

$$\phi(r,z,t) = \Re\left(f_\phi(r)e^{j\omega t - jkz}\right), \tag{A.3}$$

$$\mathbf{A}(r,z,t) = \Re\left(f_A(r)e^{j\omega t - jkz}\right)\mathbf{a}_z. \tag{A.4}$$

Starting from the divergence relation of the magnetic vector potential $\nabla \cdot \mathbf{A} = -\mu\varepsilon d\phi/dt$, one finds that

$$f_A(r) = \frac{\omega\mu\varepsilon}{k} f_\phi(r), \tag{A.5}$$

The axial electric field component is found using the relation $\mathbf{E} = -\nabla\phi - d\mathbf{A}/dt$, which yields that

$$E_z = -\frac{d\phi}{dz} - \frac{d\left(\mathbf{A}\cdot\mathbf{a}_z\right)}{dt} = \Re\left(\left(jkf_\phi(r) - j\omega f_A(r)\right)e^{j\omega t - jkz}\right), \tag{A.6}$$

We use the relation in Eq. (A.5) to simplify Eq. (A.6) as

$$E_z = \Re\left(\left(j\frac{k^2 - j\omega^2\mu\varepsilon}{k}\right) f_\phi(r) e^{j\omega t - jkz}\right), \tag{A.7}$$

The second law of Newton that describes the equation of motion for electrons is written as $m\, d\mathbf{u}/dt = -e\mathbf{E}$. The total derivative of the velocity of the electrons is expressed in the phasor domain as

$$\frac{du}{dt} = \frac{\partial u}{\partial t} + u_0 \frac{\partial u}{\partial z} = \Re\left(\left(j\omega - jku_0\right) u_{\mathrm{m}}(r) e^{j\omega t - jkz}\right), \tag{A.8}$$

By enforcing the second law of Newton, we find the relation between the velocity and electric potential functions as

$$u_{\mathrm{m}}(r) = \frac{\eta}{u_0} \frac{k_0^2 - k^2}{k\,(k - \beta_0)} f_\phi(r), \tag{A.9}$$

where $k_0 = \omega\sqrt{\mu_0\epsilon_0}$ is the free space wavenumber and $\beta_0 = \omega/u_0$. Moreover, we consider the continuity equation or conservation of charge,

$$\frac{\partial\left(\rho u\right)}{\partial z} = -\frac{\partial \rho}{\partial t}, \tag{A.10}$$

which is then simplified to

$$\rho_{\mathrm{m}}(r) = \frac{k\rho_0}{u_0\left(\beta_0 - k\right)} u_{\mathrm{m}}(r). \tag{A.11}$$

Using Eqs. (A.9) and (A.11), one finds the relation between the charge and the potential functions as

$$\rho_{\mathrm{m}}(r) = -\frac{\eta\rho_0}{u_0^2} \frac{k_0^2 - k^2}{\left(k - \beta_0\right)^2} f_\phi(r). \tag{A.12}$$

Finally, the Poisson's equation that governs the scalar electric potential $\left(\nabla^2 + k_0^2\right)\phi = -\rho/\varepsilon$ is simplified to

$$\frac{d^2 f_\phi(r)}{dr^2} + \frac{1}{r}\frac{df_\phi(r)}{dr} + \gamma^2 f_\phi(r) = 0, \tag{A.13}$$

where

$$\gamma^2 = \left(k_0^2 - k^2\right)\left(1 - \frac{\eta\rho_0}{\varepsilon u_0^2} \frac{1}{\left(k - \beta_0\right)^2}\right). \tag{A.14}$$

We consider the case where the studied region has moving electrons as generally studied above. The expression in Eq. (A.14) is rewritten as

$$\gamma^2 = T^2 = \left(k^2 - k_0^2\right)\left(\frac{\beta_{\mathrm{p}}^2 - \left(k-\beta_0\right)^2}{\left(k-\beta_0\right)^2}\right). \tag{A.15}$$

where $\beta_p = \omega_p/u_0$, and $\omega_p = \sqrt{\eta\rho_0/\varepsilon_0}$ is the plasma frequency. The term $(k^2 - k_0^2)$ is written as $\omega^2\left(1/v^2 - 1/c^2\right)$ and therefore it is positive because the charge waves velocity v should be comparable to the speed of the electrons which can not exceed the speed of light. The term $\beta_{\mathrm{p}}^2 - \left(k-\beta_0\right)^2$ is also positive assuming that charge wave has wavenumber that is expressed in terms of a plasma frequency reduction factor less than 1, i.e., $k = \beta_0 + R_{sc}\beta_p$, where $R_{sc} < 1$, which yields $\beta_{\mathrm{p}}^2 - \left(k-\beta_0\right)^2 = \beta_{\mathrm{p}}^2\left(1 - R_{sc}^2\right)$. Therefore, The real part of the expression in Eq. (A.15) is positive assuming that $k > k_0$ and $|k - \beta_0| < \beta_{\mathrm{p}}$. Therefore, the general solution of the differential equation in Eq. (A.13) is written in term of Bessel's functions as

$$f_\phi(r) = a_1 J_0(Tr) + a_2 Y_0(Tr), \tag{A.16}$$

where a_1 and a_2 are arbitrary constants, J_0 is Bessel function of the first kind and order zero and Y_0 is the Bessel function of the second kind (Neumann's function) of order zero.

A.2 Empty Region (Vacuum)

Here, we consider the case where the studied region is empty, i.e., it does not involve charges. We assume that the scalar electric potential follows a wave function as

$$\phi(r,z,t) = \Re\left(f_\phi(r)e^{j\omega t - jkz}\right). \tag{A.17}$$

The Poisson's equation that governs the scalar electric potential is $(\nabla^2 + k_0^2)\,\phi = 0$ and it is expanded as

$$\frac{d^2 f_\phi(r)}{dr^2} + \frac{1}{r}\frac{df_\phi(r)}{dr} - \tau^2 f_\phi(r) = 0, \tag{A.18}$$

where

$$\tau^2 = k^2 - k_0^2. \tag{A.19}$$

The real part of the expression in Eq. (A.19) is positive because the term $(k^2 - k_0^2)$ is expressed as $\omega^2\,(1/v^2 - 1/c^2)$ which is positive because the charge waves velocity v should be comparable to the speed of the electrons which cannot exceed the speed of light.

For this case, the general solution of the differential equation in Eq. (A.13) is the modified Bessel function and it is written in the form of

$$f_\phi(r) = b_1 I_0(\tau r) + b_2 K_0(\tau r), \tag{A.20}$$

where b_1 and b_2 are arbitrary constants, I_0 is the modified Bessel function of the first kind and order zero, and K_0 is the modified Bessel function of the second kind and order zero.

Appendix B

Characteristic Equation Definition and Mode Profile

Here we show the steps we used to find solutions to the system of equations in $\underline{\mathbf{M}}\mathbf{c} = \mathbf{0}$, where $\mathbf{c} = \begin{bmatrix} c_1, & c_2, & c_3 & c_4, & c_5, & c_6, & c_7 \end{bmatrix}^{\mathrm{T}}$ and the matrix $\underline{\mathbf{M}}$ is given in Eq. (11.25). Once we assume the stream parameters and the radii of the structure, the only unknowns we are left with are the 7 constants in $\mathbf{c}$ and the wavenumber k. First, we assume that the potential function is normalized such that $f_\phi(r = 0) = 1$, and therefore $c_1 = 1$.

Then, for a given wavenumber k, one finds the rest of the constants of the system by solving the last 6 equations described in $\underline{\mathbf{M}}\mathbf{c} = \mathbf{0}$, which yields

$$\begin{bmatrix} c_2 \\ c_3 \\ c_4 \\ c_5 \\ c_6 \\ c_7 \end{bmatrix} = \begin{bmatrix} \tau K_0'(\tau R_1) & \tau I_0'(\tau R_1) & 0 & 0 & 0 & 0 \\ K_0(\tau R_{\mathrm{i},2}) & I_0(\tau R_{\mathrm{i},2}) & -J_0(T_2 R_{\mathrm{i},2}) & -Y_0(T_2 R_{\mathrm{i},2}) & 0 & 0 \\ \tau K_0'(\tau R_{\mathrm{i},2}) & \tau I_0'(\tau R_{\mathrm{i},2}) & -T_2 J_0'(T_2 R_{\mathrm{i},2}) & -T_2 Y_0'(T_2 R_{\mathrm{i},2}) & 0 & 0 \\ 0 & 0 & J_0(T_2 R_{\mathrm{o},2}) & Y_0(T_2 R_{\mathrm{o},2}) & -K_0(\tau R_{\mathrm{o},2}) & -I_0(\tau R_{\mathrm{o},2}) \\ 0 & 0 & T_2 J_0'(T_2 R_{\mathrm{o},2}) & T_2 Y_0'(T_2 R_{\mathrm{o},2}) & -\tau K_0'(\tau R_{\mathrm{o},2}) & -\tau I_0'(\tau R_{\mathrm{o},2}) \\ 0 & 0 & 0 & 0 & K_0(\tau R_{\mathrm{t}}) & I_0(\tau R_{\mathrm{t}}) \end{bmatrix}^{-1} \begin{bmatrix} T_1 J_0'(T_1 R_1) \\ 0 \\ 0 \\ 0 \\ 0 \\ 0 \end{bmatrix} \tag{B.1}$$

Reaching this stage, we found the 7 constants in $\mathbf{c}$ which satisfy six out of the seven boundary

conditions. The next step is that we solve to find the last unknown k that will satisfy the first boundary condition as

$$\mathrm{CE} = |J_0(T_1 R_1) - c_2 K_0(\tau R_1) - c_3 I_0(\tau R_1)| = 0. \tag{B.2}$$

We find solutions of k by looking for wavenumbers (complex) that guarantee that equation (B.2) is satisfied, which implicitly guarantees that the remaining equations are also satisfied, since c_2 and c_3 are found based on satisfying the rest of the boundary conditions.

The mode profile in Fig. 11.2a are found based the constants calculated from Eq. (B.1) with $c_1 = 1$ to have a normalized electric potential at the center of the beam as $f_\phi(r = 0) = 1$.